crystals

Special Issue Reprint

Crystallization of High Performance Metallic Materials (2nd Edition)

Edited by
Wangzhong Mu and Chao Chen

mdpi.com/journal/crystals

MDPI

Crystallization of High Performance Metallic Materials (2nd Edition)

Crystallization of High Performance Metallic Materials (2nd Edition)

Guest Editors

Wangzhong Mu
Chao Chen

MDPI

Basel • Beijing • Wuhan • Barcelona • Belgrade • Novi Sad • Cluj • Manchester

Guest Editors

Wangzhong Mu
Department of Materials Science and Engineering
KTH Royal Institute of Technology
Stockholm
Sweden

Chao Chen
College of Materials Science and Engineering
Taiyuan University of Technology
Taiyuan
China

Editorial Office
MDPI AG
Grosspeteranlage 5
4052 Basel, Switzerland

This is a reprint of the Special Issue, published open access by the journal *Crystals* (ISSN 2073-4352), freely accessible at: https://www.mdpi.com/journal/crystals/special_issues/2570V36CKU.

For citation purposes, cite each article independently as indicated on the article page online and as indicated below:

Lastname, A.A.; Lastname, B.B. Article Title. *Journal Name* **Year**, *Volume Number*, Page Range.

ISBN 978-3-7258-6131-6 (Hbk)
ISBN 978-3-7258-6132-3 (PDF)
https://doi.org/10.3390/books978-3-7258-6132-3

Contents

About the Editors

Wangzhong Mu

Wangzhong Mu is an associate professor at the Royal Institute of Technology (KTH), Department of Materials Science and Engineering, and a visiting professor at Key Lab EPM, Northeastern University. He received both a Docent (Assoc. Prof./Reader) qualification and a Ph.D. degree from KTH. Moreover, he has worked at McMaster University (Canada), Tohoku University (Japan), and Ferritico AB (Sweden). He has close collaboration with the Max Planck Institute of Sustainable Materials (Dusseldorf, Germany), Hanyang University (Korea), Montan University Leoben (Austria), etc. His research interests include (i) particle behaviors in metals, (ii) sustainable metallurgy, (iii) artificial intelligence (AI)-based material design, etc. He has served as a PI for over 15 national-level and EU-level research grants, published over 70 peer-reviewed journal articles, and contributed over 20 plenary/keynote/invited lectures at international conferences.

Chao Chen

Chao Chen is an Associate Professor at the College of Materials Science and Engineering, Taiyuan University of Technology. He completed his PhD degree in Materials Science and Engineering at the KTH Royal Institute of Technology in 2015. He is a member of the Academic Committee on Metallurgical Reaction Engineering of the Chinese Society for Metals, and a member of the National Academic Committee on Metallurgical Processes and Theories of the Metallurgical Physical Chemistry Division of the Chinese Society for Metals. His research interests include research on key technologies for the production of special steel stainless steel; computational fluid dynamics (CFD) simulations of complex fluid flows in industrial processes; physical simulation and mathematical modeling of metallurgical processes; and the preparation and application of catalysts for hydrogen production from electrolyzed water.

crystals

MDPI

Editorial

Crystallization of High Performance Metallic Materials (2nd Edition)

Chao Chen [1,*] and Wangzhong Mu [2,3,*]

[1] College of Materials Science and Engineering, Taiyuan University of Technology, Taiyuan 030024, China
[2] Key Laboratory of Electromagnetic Processing of Materials (Ministry of Education), School of Metallurgy, Northeastern University, Shenyang 110819, China
[3] Department of Materials Science and Engineering, KTH Royal Institute of Technology, Brinellvägen 23, SE-100 44 Stockholm, Sweden
* Correspondence: chenchao@tyut.edu.cn (C.C.); wmu@kth.se (W.M.)

1. Introduction

Crystallization generally refers to the material processing in which a solid phase nucleates within a liquid or solid matrix. In metallic materials, crystallization encompasses both the nucleation and growth of a new solid phase during initial solidification and the subsequent solid-state phase transformations [1].

With the rapid development of electric vehicle (EV) technologies [2], the demand for non-oriented silicon steel is steadily rising due to its widespread use in new energy EV drive motors [3,4]. Research on the manufacturing processes of non-oriented silicon steels has become a hot topic [5–8]. In this Special Issue (SI), three contributed papers (Contributions 3, 4, and 9) [9–11] focus specifically on this subject. These studies investigate the influence of annealing temperature and cold rolling reduction rate on the microstructure, texture, and magnetic properties of non-oriented silicon steel [9,10]. Another active research area concerns the addition of rare earth elements into non-oriented silicon steels [11–17], with one study in this issue examining inclusions throughout the production and smelting processes [11]. In relation to rare earth additions, this SI also includes a paper (Contribution 3) on the effect of erbium addition in aluminum alloys [18,19].

Stainless steel represents another important class of high-performance metallic materials [20–25]. In this Special Issue, one paper (Contribution 8) focuses on the plastic deformation behavior of AISI 304 stainless steel [26–31]. Another study (Contribution 10) investigates laser cladding of AISI 904L stainless steel and Co-based composite coatings [32–34]. Continuous casting and solidification of stainless steel remain challenging processes [35–39]; accordingly, a further paper in this SI (Contribution 6) examines key parameters in the continuous casting of steel [40–44].

This SI also covers the topic of crystal plasticity [45–50], which is reviewed in Contribution 1 [51]. Additionally, Contribution 7 presents a modeling study on the sealing performance and fatigue behavior of sealing rings made by Inconel 718 alloy [52]. Separately, a review paper (Contribution 2) systematically summarizes recent advances in enhancing the antibacterial properties [53,54] of magnesium alloys through alloying strategies [55].

Followed by the first edition of SI *Crystallization of High Performance Metallic Materials* [1]. This Special Issue explores crystallization behaviors in various high-performance metallic materials. It compiles comprehensive research on these behaviors, aiming to elucidate the correlations between processing, structure, and properties in engineering materials.

2. An Overview of Published Articles

This Special Issue attracted a number of submissions on crystallization behaviors in metallic alloys. Ten high-quality papers were accepted after the peer-review process. The contributions and their descriptions are listed in Table 1.

Table 1. Summary of the published contributions.

No. of Contribution	Research Area	Focus	Type of Research
1	Crystal plasticity	Applications and challenges	Review paper
2	Magnesium alloy	Antibacterial effect and mechanism	Review paper
3	Erbium added 2024 aluminum alloy	Microstructures and mechanical properties	Experimental study
4	2.4% Si non-oriented silicon steel	Effects of annealing temperature on the microstructure, texture, and magnetic properties	Experimental study
5	3.0%Si-0.8%Al-0.3%Mn non-oriented silicon steel	Effects of cold rolling reduction rate on microstructure, texture and magnetic properties	Experimental study
6	SFQ590 steel and continuous casting mold slag	Effects of casting speed, argon injection rate, and mold flux properties on the fluid flow and heat transfer	Computational fluid dynamics study
7	W-shaped metallic sealing rings by Inconel 718	Modeling on the sealing performance and fatigue behavior	Numerical model study
8	Cold-Rolled AISI 304 Stainless Steel	Effect of plastic deformation and temperature on the formation of mechanically induced martensite and hardness	Experimental study
9	3.1% Si non-oriented silicon steel with addition of rare earth	the morphology, composition, and size distribution of inclusions throughout the smelting process	Experimental study and thermodynamics calculation
10	AISI 904L stainless steel and Co-based composite coatings	Laser cladding of the composite coatings	Experimental study

Contribution 1 provides a concise review of crystal plasticity (CP), tracing its progress from conceptual origins to its current applications. It establishes CP as a validated methodology for simulating complex material responses under demanding loading conditions. Acknowledging ongoing model development, the review highlights parameter calibration as a primary challenge for physics-based simulations and offers valuable data tables with indicative values to guide this process.

Contribution 2 summarizes recent advances in enhancing the antibacterial properties of magnesium alloys via alloying. It details the efficacy of various alloy systems and elaborates on the underlying mechanisms. This work is anticipated to furnish a foundational basis for designing novel biodegradable magnesium alloys with integrated antibacterial functions, thereby accelerating their clinical adoption.

Contribution 3 examines the impact of trace erbium (Er) additions on the microstructure and mechanical properties of 2024 aluminum alloy. Utilizing powder metallurgy techniques, for example, high-energy ball milling, cold isostatic pressing and microwave sintering and characterization via optical microscopy (OM) and scanning electron mi-

croscopy (SEM), this study offers relevant insights for developing high-performance aluminum alloys targeted for automotive structural components.

Contribution 4 studied the cold-rolled non-oriented silicon steel sheets with a Si content of 2.4 wt.%, which was produced by continuous and reversible cold rolling. The influence of annealing temperature on the microstructure, texture, and magnetic properties were studied by optical microscopy, an X-ray diffractometer, and a magnetic property measuring instrument.

Contribution 5 focused on the 3.0%Si-0.8%Al-0.3%Mn non-oriented silicon steel. This paper performed a X-ray diffraction (XRD) and electron backscatter diffraction (EBSD) study on the effects of cold rolling reduction on the microstructure, recrystallization behavior, and magnetic properties of the silicon steel. With the reduction rates of 78%, 85% and 87% in the cold rolled sheet, noting narrowed deformation bands, fewer shear bands, and increased grain boundary fractions, which collectively govern recrystallization and magnetic performance.

Contribution 6 employs a 3D numerical model to analyze how casting speed, argon injection flow rate, and mold flux properties govern fluid flow and heat transfer in a continuous casting mold. It proposes an optimized set of parameters to stabilize these phenomena, thereby reducing slab defects and enhancing process stability.

Contribution 7 analyzes the sealing performance and fatigue behavior of W-shaped metallic seals with different microstructures. It introduces an innovative simulation technique that uses temperature conduction to model gradient structures, mitigating interface stress concentration in finite element modeling (FEM) analysis. The findings inform the design and manufacturing process optimization for high-performance sealing rings.

Contribution 8 probes the effects of plastic deformation and temperature on strain-induced martensite formation and associated hardening in AISI 304 stainless steel. It confirms the transformation sequence $\gamma \rightarrow \varepsilon \rightarrow \alpha'$, with accelerated kinetics at lower temperatures and higher strains, providing a basis for tailoring mechanical properties through thermomechanical processing.

Contribution 9 tracks the evolution of inclusion morphology, composition, and size distribution during the industrial production of 3.1% Si non-oriented silicon steel. The study demonstrates that rare earth treatment effectively modifies Al_2O_3 inclusions into $REAlO_3$ and RE_2O_2S types and promotes the aggregation of AlN to form composite inclusions.

Contribution 10 employed the laser cladding technology to enhance and restore component surfaces, thereby contributing to extended service life. In this work, single-layer and multi-layer Co-based composite coatings reinforced with WC–CoCr–Ni powder were deposited onto AISI 904L stainless steel substrates via laser cladding. The phase composition of the fabricated coatings was analyzed by X-ray diffraction (XRD), while the microstructure and elemental distribution were characterized using scanning electron microscopy (SEM) coupled with energy dispersive X-ray spectroscopy (EDX). Further evaluations were conducted to determine the hardness, wear resistance, and corrosion behavior of the coatings. Analysis and comparison revealed that coating performance improved with increasing thickness, which was generally attributed to a reduced iron (Fe) content within the coating microstructure.

3. Summary

This current Special Issue (SI) collects research contributions with the topics of solidification and continuous casting, crystal plasticity and recrystallization during deformation, laser cladding of the composite coatings, and non-metallic inclusions as well as mechanical properties evolution of different engineering materials, e.g., non-oriented silicon steels, stainless steels, Inconel alloys, aluminum alloys, etc. Both experimental and simulation

studies with the crystallization topics have been reported in different papers. In addition, two review articles on crystal plasticity and antibacterial properties of magnesium alloys are presented in this issue. A third Volume of the SI with the same topic is online now. https://www.mdpi.com/journal/crystals/special_issues/75042MN87Z (accessed on 13 November 2025). It is aiming to collect more contributions regarding different topics of crystallization of materials.

Author Contributions: Writing—original draft preparation, C.C.; writing—review and editing, W.M. and C.C. All authors have read and agreed to the published version of the manuscript.

Funding: This research received no external funding.

Acknowledgments: C.C. and W.M. would like to acknowledge all the authors, the anonymous reviewers, and the Special Issue editor.

Conflicts of Interest: The authors declare no conflicts of interest.

List of Contributions :

1. Loukadakis, V.; Papaefthymiou, S. Advancements in and Applications of Crystal Plasticity Modelling of Metallic Materials. *Crystals* **2024**, *14*, 883. https://doi.org/10.3390/cryst14100883.
2. Song, Q.; Yang, L.; Yi, F.; Chen, C.; Guo, J.; Qi, Z.; Song, Y. Antibacterial Pure Magnesium and Magnesium Alloys for Biomedical Materials—A Review. *Crystals* **2024**, *14*, 939. https://doi.org/10.3390/cryst14110939.
3. Qin, T.; Fan, B.; Yu, J.; Bu, C.; Zhang, J. Effect of Erbium Micro-Additions on Microstructures and Properties of 2024 Aluminum Alloy Prepared by Microwave Sintering. *Crystals* **2024**, *14*, 382. https://doi.org/10.3390/cryst14040382.
4. Shao, K.; Niu, Y.; Pei, Y.; Qiao, J.; Pan, H.; Wang, H. Effects of Continuous Rolling and Reversible Rolling on 2.4% Si Non-Oriented Silicon Steel. *Crystals* **2024**, *14*, 824. https://doi.org/10.3390/cryst14090824.
5. Guo, F.; Niu, Y.; Fu, B.; Qiao, J.; Qiu, S. Influence Mechanisms of Cold Rolling Reduction Rate on Microstructure, Texture and Magnetic Properties of Non-Oriented Silicon Steel. *Crystals* **2024**, *14*, 853. https://doi.org/10.3390/cryst14100853.
6. Ding, Z.; Wang, C.; Wang, X.; Xiao, P.; Zhu, L.; Wang, S. The Influence of Process and Slag Parameters on the Liquid Slag Layer in Continuous Casting Mold for Large Billets. *Crystals* **2025**, *15*, 388. https://doi.org/10.3390/cryst15050388.
7. Zhao, P.; Tuo, L.; Zhang, H.; Sun, Z.; Ren, S.; Yuan, G.; Zheng, Z. Analysis of Fatigue Performance of Metallic Components with Gradient Microstructures. *Crystals* **2025**, *15*, 602. https://doi.org/10.3390/cryst15070602.
8. Burja, J.; Lindič, J.; Šetina Batič, B.; Nagode, A. Temperature-Dependent Martensitic Transformation in Cold-Rolled AISI 304 Stainless Steel. *Crystals* **2025**, *15*, 652. https://doi.org/10.3390/cryst15070652.
9. Xue, L.; Li, X.; Wang, T.; Zhao, Q.; Wang, H.; Wang, J.; Lin, W.; Niu, X.; Mu, W.; Chen, C. Analysis of Inclusions in the Entire Smelting Process of High-Grade Rare Earth Non-Oriented Silicon Steel. *Crystals* **2025**, *15*, 779. https://doi.org/10.3390/cryst15090779.
10. Anghel, I.-M.; Pascu, A.; Hulka, I.; Woelk, D.H.; Uțu, I.-D.; Mărginean, G. Characterization of Cobalt-Based Composite Multilayer Laser-Cladded Coatings. *Crystals* **2025**, *15*, 970. https://doi.org/10.3390/cryst15110970.

References

1. Mu, W.; Chen, C. Crystallization of High-Performance Metallic Materials. *Crystals* **2025**, *15*, 147. [CrossRef]
2. Irfan, M. Assessing Consumers' Behavioral Intention and Willingness to Pay for Electric Vehicles: An Evidence from China. *J. Compr. Bus. Adm. Res.* **2024**, *1*, 2–11. [CrossRef]
3. Kubota, T. Recent Progress on Non-oriented Silicon Steel. *Steel Res. Int.* **2005**, *76*, 464–470. [CrossRef]
4. Oda, Y.; Kohno, M.; Honda, A. Recent development of non-oriented electrical steel sheet for automobile electrical devices. *J. Mag. Mag. Mater.* **2008**, *320*, 2430–2435. [CrossRef]
5. Jiao, H.T.; Xu, Y.B.; Zhao, L.Z.; Misra, R.D.K.; Tang, Y.C.; Liu, D.J.; Hu, Y.; Zhao, M.J.; Shen, M.X. Texture evolution in twin-roll strip cast non-oriented electrical steel with strong Cube and Goss texture. *Acta Mater.* **2020**, *199*, 311–325. [CrossRef]

6. Jiao, H.T.; Xie, X.X.; Hu, Y.; Liu, D.J.; Tang, Y.C.; Zhao, L.Z. Enhanced {100} recrystallization texture in strip-cast nonoriented electrical steel by two-stage annealing. *Steel Res. Int.* **2023**, *94*, 2200633. [CrossRef]
7. Jiao, H.T.; Wu, W.S.; Hou, Z.B.; Xie, X.X.; Tang, Y.C.; Misra, R.D.K.; Liu, D.J.; Hu, Y.; Zhao, L.Z. Ultrastrong {100} texture in twin-roll strip cast non-oriented electrical steel through two-step annealing. *Scri. Mater.* **2024**, *243*, 115998. [CrossRef]
8. Xu, N.; Liang, Y.F.; Zhang, C.Y.; Wang, Z.; Wang, Y.L.; Ye, F.; Lin, J.P. Development of strong Goss texture in ultra-thin high silicon steel with excellent magnetic properties fabricated by two-stage rolling. *Int. J. Miner. Metall. Mater.* **2025**, *32*, 1595–1606. [CrossRef]
9. Shao, K.; Niu, Y.; Pei, Y.; Qiao, J.; Pan, H.; Wang, H. Effects of Continuous Rolling and Reversible Rolling on 2.4% Si Non-Oriented Silicon Steel. *Crystals* **2024**, *14*, 824. [CrossRef]
10. Guo, F.; Niu, Y.; Fu, B.; Qiao, J.; Qiu, S. Influence Mechanisms of Cold Rolling Reduction Rate on Microstructure, Texture and Magnetic Properties of Non-Oriented Silicon Steel. *Crystals* **2024**, *14*, 853. [CrossRef]
11. Xue, L.; Li, X.; Wang, T.; Zhao, Q.; Wang, H.; Wang, J.; Lin, W.; Niu, X.; Mu, W.; Chen, C. Analysis of Inclusions in the Entire Smelting Process of High-Grade Rare Earth Non-Oriented Silicon Steel. *Crystals* **2025**, *15*, 779. [CrossRef]
12. Wang, H.J.; Niu, Y.; Ling, H.T.; Qiao, J.L.; Zhang, Y.L.; Zhong, W.; Qiu, S.T. Effects of rare earth La–Ce alloying treatment on modification of inclusions and magnetic properties of W350 non-oriented silicon steel. *Metals* **2023**, *13*, 626. [CrossRef]
13. Wang, H.J.; Niu, Y.H.; Ling, H.T.; Qiao, J.L.; Zhang, Y.L.; Zhong, W.; Qiu, S.T. Modification of rare earth Ce on inclusions in W350 non-oriented silicon steel. *Metals* **2023**, *13*, 453. [CrossRef]
14. Guo, Z.; Li, X.; Liu, Y.; Zheng, Y.; Zhu, L.; Zhang, Y.; Sun, H.; Feng, J.; Cao, R. Effect of Rare Earth Yttrium on Inclusion Characteristics of Grain-Oriented Silicon Steel. *Crystals* **2023**, *13*, 896. [CrossRef]
15. Wang, T.; Chen, C.; Mu, W.Z.; Xue, L.Q.; Cao, J.Q.; Lin, W.M. Analysis of inclusions in whole smelting process of non-oriented silicon steel 23W1700 by rare earth treatment. *Iron Steel* **2024**, *59*, 92–103. [CrossRef]
16. Liu, X.J.; Yang, J.C.; Ren, H.P.; Jia, X.B.; Zhang, M.Y.; Yang, C.Q. Effect of solute Ce, Mn, and Si on mechanical properties of silicon steel: Insights from DFT calculations. *J. Iron Steel Res. Int.* **2024**, *31*, 700–709. [CrossRef]
17. Ren, Q.; Hu, Z.Y.; Liu, Y.X.; Zhang, W.C.; Gao, Z.Q.; Zhang, L.F. Effect of lanthanum on inclusions in non-oriented electrical steel slabs. *J. Iron Steel Res. Int.* **2024**, *31*, 1680–1691. [CrossRef]
18. Shi, Z.M.; Wang, Q.; Zhao, G.; Zhang, R. Effects of Erbium modification on the microstructure and mechanical properties of A356 aluminum alloys. *Mater. Sci. Eng.* **2015**, *A626*, 102–107. [CrossRef]
19. Lei, X.; Zhang, Z.; Dong, H.; Wang, C.; Du, X. Effect of erbium on microstructure and mechanical properties of Al-Si-Mg-Cu alloy. *Mater. Und Werkst.* **2020**, *51*, 1389–1397. [CrossRef]
20. Lo, K.H.; Shek, C.H.; Lai, J.K.L. Recent developments in stainless steels. *Mater. Sci. Eng. R Rep.* **2009**, *65*, 39–104. [CrossRef]
21. Lai, J.K.L.; Lo, K.H.; Shek, C.H. *Stainless Steels: An Introduction and Their Recent Developments*; Bentham Science Publishers: Sharjah, United Arab Emirates, 2012; p. 4. [CrossRef]
22. San-Martin, D.; Celada-Casero, C.; Vivas, J.; Capdevila, C. Stainless steels. In *High-Performance Ferrous Alloys*; Rana, R., Ed.; Springer Nature: Cham, Switzerland, 2021; pp. 459–566. [CrossRef]
23. Chen, C.; Xue, Z.; Mu, W. Advanced Stainless Steel—From Making, Shaping, Treating to Products. *Materials* **2025**, *18*, 4730. [CrossRef] [PubMed]
24. Li, F.K.; Liu, C.S.; Wang, Y.; Zhang, H.; Li, J.; Lu, Y.Y.; Xiong, L.; Ni, H.W. Effect of inclusion and microstructure transformation on corrosion resistance of 316L stainless steel after isothermal heat treatment. *J. Iron Steel Res. Int.* **2025**, *32*, 2133–2151. [CrossRef]
25. Zhang, Z.Q.; Liao, X.; Ren, Z.K.; Wang, Z.H.; Liu, Y.X.; Wang, T.; Huang, Q.X. Effect of two-pass rolling of textured roll and polished roll on surface topography and mechanical properties of 316L stainless steel ultra-thin strip. *J. Iron Steel Res. Int.* **2025**, *32*, 186–197. [CrossRef]
26. Kowalska, J.; Witkowska, M. The Influence of Cold Deformation and Annealing on Texture Changes in Austenitic Stainless Steel. *Adv. Sci. Technol. Res. J.* **2024**, *18*, 143–158. [CrossRef]
27. He, C.; Zhu, X.; Hu, C.; Dong, H.; Wan, X.; Liu, E.; Li, G.; Wu, K. Processing an 18Cr-8Ni Austenitic Stainless Steel Without the Dilemma of the Strength and Ductility Trade-Off. *JOM* **2024**, *76*, 829–842. [CrossRef]
28. Song, Y.; Li, Y.; Lu, J.; Hua, L.; Gu, Y.; Yang, Y. Strengthening and toughening mechanisms of martensite-bainite microstructure in 2 GPa ultra-high strength steel during hot stamping. *Sci. China Technol. Sci.* **2025**, *68*, 1520201. [CrossRef]
29. Li, P.C.; Wang, T.; Zhao, C.C.; Liu, Q.; Huang, Q.X. Effect of ceramic work rolls on surface roughness of rolled SUS304 ultra-thin strips. *J. Iron Steel Res. Int.* **2024**, *31*, 1704–1718. [CrossRef]
30. Zhu, L.; Sun, C.Y.; Wang, B.Y.; Zhou, J. Cross wedge rolling deformation law and bonding mechanism of 304 stainless steel/Q235 carbon steel bimetallic shaft. *J. Iron Steel Res. Int.* **2024**, *31*, 2423–2437. [CrossRef]
31. Guo, X.W.; Ren, Z.K.; Wu, H.; Chai, Z.; Zhang, Q.; Wang, T.; Huang, Q.X. Effect of annealing on microstructure and synergistic deformation of 304/TC4 composite plates with corrugated interface. *J. Iron Steel Res. Int.* **2025**, *32*, 2434–2451. [CrossRef]
32. Anghel, I.-M.; Uțu, I.-D.; Pascu, A.; Hulka, I.; Woelk, D.H.; Mărginean, G. Microstructure and properties of Co-based laser cladded composite coatings. *Mater. Test.* **2024**, *66*, 665–674. [CrossRef]

33. Poloczek, T.; Lont, A.; Górka, J. The structure and properties of laser-cladded Inconel 625/TiC composite coatings. *Materials* **2023**, *16*, 1265. [CrossRef] [PubMed]
34. Yu, Y.; Ding, W.; Wang, X.; Mo, D.; Chen, F. Study on Microstructure and Wear Resistance of Multi-Layer Laser Cladding Fe901 Coating on 65 Mn Steel. *Materials* **2025**, *18*, 3505. [CrossRef] [PubMed]
35. Hammar, O.; Svensson, U. *Solidification and Casting of Metals*; The Metal Society: London, UK, 1997; p. 401.
36. Pang, J.C.; Qian, G.Y.; Pang, S.; Ma, W.H.; Cheng, G.G. Design of a submerged entry nozzle for optimizing continuous casting of stainless steel slab. *J. Iron Steel Res. Int.* **2023**, *30*, 2229–2241. [CrossRef]
37. Wang, Y.; Chen, C.; Ren, R.J.; Xue, Z.X.; Wang, H.Z.; Zhang, Y.Z.; Wang, J.X.; Wang, J.; Chen, L.; Mu, W.Z. Ferrite formation and decomposition in 316H austenitic stainless steel electro slag remelting ingot for nuclear power applications. *Mater. Charact.* **2024**, *218*, 114581. [CrossRef]
38. Wang, Y.; Chen, C.; Yang, X.Y.; Zhang, Z.R.; Wang, J.; Li, Z.; Chen, L.; Mu, W.Z. Solidification modes and delta-ferrite of two types 316L stainless steels: A combination of as-cast microstructure and HT-CLSM research. *J. Iron Steel Res. Int.* **2025**, *32*, 426–436. [CrossRef]
39. Xue, Z.; Yang, K.; Li, Y.; Pei, C.; Hou, D.; Zhao, Q.; Wang, Y.; Chen, L.; Chen, C.; Mu, W. The Influence of Heat Treatment Process on the Residual Ferrite in 304L Austenitic Stainless Steel Continuous Casting Slab. *Materials* **2025**, *18*, 3724. [CrossRef]
40. Ding, Z.; Wang, C.; Wang, X.; Xiao, P.; Zhu, L.; Wang, S. The Influence of Process and Slag Parameters on the Liquid Slag Layer in Continuous Casting Mold for Large Billets. *Crystals* **2025**, *15*, 388. [CrossRef]
41. Li, G.; Tu, L.; Wang, Q.; Zhang, X.; He, S. Fluid Flow in Continuous Casting Mold for Ultra-Wide Slab. *Materials* **2023**, *16*, 1135. [CrossRef]
42. Wang, T.J.; Li, K.; Li, S.H.; Wang, L.J.; Yang, J.; Feng, L.H. Asymmetric flow behavior of molten steel in thin slab continuous casting mold. *Metall. Mater. Trans. B* **2023**, *54*, 3542–3553. [CrossRef]
43. Wang, Z.D.; Liu, J.R.; Heng, C.; Sun, H.; Wang, Y.Z. Effect of SEN Asymmetric Clogging on Mold Level Fluctuation and Mold Slag Distribution During Continuous Casting. *Metall. Mater. Trans. B* **2024**, *55*, 2932–2947. [CrossRef]
44. Wang, J.L.; Yang, Y.K.; Zhu, J.Y.; Wang, W.A.; Niu, L.; Li, X.M. Numerical simulation of nozzle structure to improve eccentric mold electromagnetic stirring in a round bloom mold. *J. Iron Steel Res. Int.* **2024**, *31*, 2173–2185. [CrossRef]
45. Van Houtte, P. Crystal Plasticity Based Modelling of Deformation Textures. In *Microstructure and Texture in Steels*; Springer: London, UK, 2009.
46. Shiraiwa, T.; Briffod, F.; Enoki, M. Prediction of Fatigue Crack Initiation of 7075 Aluminum Alloy by Crystal Plasticity Simulation. *Materials* **2023**, *16*, 1595. [CrossRef] [PubMed]
47. Abd El-Aty, A.; Ha, S.; Xu, Y.; Hou, Y.; Zhang, S.-H.; Alzahrani, B.; Ali, A.; Ahmed, M.M.Z. Coupling Computational Homogenization with Crystal Plasticity Modelling for Predicting the Warm Deformation Behaviour of AA2060-T8 Al-Li Alloy. *Materials* **2023**, *16*, 4069. [CrossRef]
48. Li, J.; Wu, X.; Jiang, H. Crystal Plasticity Finite Element Simulation of Grain Evolution Behavior in Aluminum Alloy Rolling. *Materials* **2024**, *17*, 3749. [CrossRef]
49. Shveykin, A.; Trusov, P.; Romanov, K. Stability of Crystal Plasticity Constitutive Models: Observations in Numerical Studies and Analytical Justification. *Metals* **2024**, *14*, 947. [CrossRef]
50. Frydrych, K.; Tomczak, M.; Papanikolaou, S. Crystal Plasticity Parameter Optimization in Cyclically Deformed Electrodeposited Copper—A Machine Learning Approach. *Materials* **2024**, *17*, 3397. [CrossRef]
51. Loukadakis, V.; Papaefthymiou, S. Advancements in and Applications of Crystal Plasticity Modelling of Metallic Materials. *Crystals* **2024**, *14*, 883. [CrossRef]
52. Zheng, Z.; Zhao, P.; Zhan, M.; Li, H.; Lei, Y.; Fu, M.W. Understanding of the Fatigue Crack Nucleation in Metallic Sealing Rings by Explicitly Incorporating the Deformation History from Manufacturing to Service. *Int. J. Fatigue* **2022**, *164*, 107174. [CrossRef]
53. Mahmoudi, P.; Akbarpour, M.R.; Lakeh, H.B.; Jing, F.; Hadidi, M.R.; Akhavan, B. Antibacterial Ti-Cu implants: A critical review on mechanisms of action. *Mater. Today Bio* **2022**, *17*, 100447. [CrossRef]
54. Liu, S.; Guo, H.J. A short review of antibacterial Cu-bearing stainless steel: Antibacterial mechanisms, corrosion resistance, and novel preparation techniques. *J. Iron Steel Res. Int.* **2024**, *31*, 24–45. [CrossRef]
55. Song, Q.; Yang, L.; Yi, F.; Chen, C.; Guo, J.; Qi, Z.; Song, Y. Antibacterial Pure Magnesium and Magnesium Alloys for Biomedical Materials—A Review. *Crystals* **2024**, *14*, 939. [CrossRef]

crystals

MDPI

Review

Advancements in and Applications of Crystal Plasticity Modelling of Metallic Materials

Vasilis Loukadakis and Spyros Papaefthymiou *

Laboratory of Physical Metallurgy, Division of Metallurgy & Materials Technology, School of Mining and Metallurgical Engineering, National Technical University of Athens, 9, Iroon Polytechniou St., 15780 Athens, Greece; vloukadakis@metal.ntua.gr

* Correspondence: spapaef@metal.ntua.gr; Tel.: +30-2107724710

Abstract: Integrated Computational Materials Engineering (ICME) is a set of methodologies utilized by researchers and engineers assisting the study of material behaviour during production processes and/or service. ICME aligns with societal efforts for the twin green and digital transitions while improving the sustainability and cost efficiency of relevant products/processes. A significant link of the ICME chain, especially for metallic materials, is the crystal plasticity (CP) formulation. This review examines firstly the progress CP has made since its conceptualization and secondly the relevant thematic areas of its utilization and portraits them in a concise and condensed manner. CP is a proven tool able to capture complex phenomena and to provide realistic results, while elucidating on the material behaviour under complex loading conditions. To this end, a significant number of formulations falling under CP, each with their unique strengths and weaknesses, is offered. It is a developing field and there are still efforts to improve the models in various terms. One of the biggest struggles in setting up a CP simulation, especially a physics-based one, is the definition of the proper values for the relevant parameters. This review provides valuable data tables with indicative values.

Keywords: crystal plasticity; materials modelling; deformation mechanisms; simulation parameters

1. Introduction

Nowadays, the twin green and digital transitions force society to change products, processes, and "lifestyle", targeting circularity and taking action towards raw material preservation. Integrated Computational Materials Engineering (ICME) is aligned with these goals as it can be applied in the development of new alloys while addressing the improvement in sustainability and cost efficiency of alloys/products, taking into consideration all requirements from their design and processing to their service.

Gradually, with the development of computer processing power, the complexity of systems and geometries has significantly increased to the point where ICME approaches today have become more realistic even for materials/systems of great complexity.

This dynamic environment creates a need for developing materials and processes guided by a deep understanding of the mechanisms and phenomena occurring on a microscopic level. This can be achieved through the coupling of different computational approaches. Such approaches, involving among other things the thermodynamic behaviour of the system and the deformation behaviour of the material, need to occur in fast, cost-effective, and sustainable development cycles. The structural design process needs to expand now to also include the material instead of narrowly focusing on the geometry of the part, as has been the case [1].

ICME provides improved understanding of the mechanics of the material, through which two main aspects of a material's lifecycle are addressed, namely the production process and the operational behaviour. The potential benefits of utilizing ICME in the process optimization are as follows: (i) development of products with higher added value, (ii) process optimization resulting in reduced energy consumption, and lastly, (iii) improved

product properties, which also target reduced raw material consumption. On the other hand, through the understanding of the behaviour during service, the requirements that the microstructure needs to meet become more clear, potentially leading to light-weight design and increased safety without compromising on the part's life. At the same time, the operating conditions for materials constantly gets more demanding. Additionally, to tailor the properties of materials to their respective applications, microstructures are becoming more complex. Another emerging challenge derives from circularity. The increasing level of impurities from scrap, following the recycling rates of materials, may negatively affect the microstructure through the build-up of residual elements, with some of them being critical for the integrity of the microstructure.

These potential benefits highlight the alignment between the adaptation of ICME approaches and the Sustainable Development Goals set by the United Nations, namely goals 4—Quality Education; 8—Decent work and economic growth; 9—Industry, innovation and infrastructure; 12—Responsible consumption and production; and 17—partnerships for the goals.

There are several methodologies under the umbrella of ICME. These can either focus on the "process–microstructure" (e.g., phase field) or the "microstructure–properties" (e.g., crystal plasticity) relations. The coupling of the two approaches allows the consecutive study of the effect of a process on the microstructure (e.g., thermal treatment) and then the use of the affected microstructure as input and prediction of its mechanical properties, enabling the tailoring of the properties to each application. Indeed, these approaches have been a subject of study for decades, with examples such as the Hall–Petch effect [2,3] and the work of Rhines [4], where critical microstructural parameters, such as the volume fraction of phases, have been connected with the mechanical properties. CP modelling falls under the microstructure–properties category [5], allowing the impact of factors such as the β-precipitation of AA6061 on mechanical properties to be obtained [6], yet it can also be used to examine the effect of mechanical loading on grains.

The CP approach is based on two fundamental axioms. Firstly, each grain is considered a continuum, and secondly, the total deformation is controlled by the interaction of the active slip systems of each grain. The latter is identified as the most important differentiator between CP and the other computational approaches [7]. Yu et al. [8] attribute the significance of the CP methodology to (i) its strong mathematical foundations, (ii) the correlation between slip systems and geometry, and lastly (iii) the high-fidelity algorithms solving such problems. These factors, in combination with the knowledge accumulated around continuum solid mechanics [9], and CP's lower costs when compared to physical experiments [10], have enabled the prediction of mechanical properties in relation to microstructural characteristics under complex loading conditions [11], making CP a widely used tool to study the mechanical responses of alloys [8], such as the deformation mechanics, e.g., during metal forming processes [12–15] or Forming Limit Diagrams, FLDs [10,16]. Additionally, when CP is coupled with other methodologies, the frameworks can expand to capture more phenomena such as the behaviour under cyclic loading [17]. This enables an enhanced understanding of how the material behaves during service and how to effectively tailor the process. Through this understanding, the development of complex, tailored materials with desired/advanced mechanical properties can be realized [16].

As mentioned, the deformation of each grain is influenced by the orientation of the slip systems in relationship with the applied load. Polycrystalline materials have grains with different orientations. This combination of the different orientations present in the material is known as crystallographic texture. This affects how the applied loading influences the material's total deformation due to the synergetic slip of all the grains deformed. This explains why the quantification and study of anisotropy, especially in relation to crystal texture, is of importance [18,19].

Texture is measured in reference to a coordination system (c.s.). Usually, the selection is between the three commonly used c.s., which are as follows [20]:

i. The c.s. defined by the deformation axes (e.g., for the case of rolling the RD (rolling direction), TD (transverse direction), and the ND (normal direction).
ii. The c.s. based on the crystallography, which rotates along the grains during deformations. This is especially useful for single-crystal systems.
iii. An external c.s. free of deformation, which is used for simplicity purposes (e.g., x, y, z).

Modern CP models, utilizing either a Finite Element Solver (FEM) or a Spectral Element Solver (SEM), can successfully predict, among others, the TRIP and TWIP effects of HSLA steels and the fatigue behaviour of dual-phase Ti-alloys [21] and Co-Cr alloys [22]. Other applications include adiabatic shear banding of FCC crystals [23] and the effect of grain size on the flow stress [24], with more models being tested even today, indicatively [25,26], and even the effect of activated slip systems on fatigue behaviour [27]. Additionally, it is often the case that the research is focused, e.g., [28], on micro-mechanical testing. This is a result of three main factors. Firstly, models need validation tests on single crystals, secondly, due to the lesser complexity of the system, they have lower computational cost, and, lastly, conducting physical experiments, under controlled conditions, on this scale is complex. Mechanical testing on single crystals is rarely preferred and most models rely on macroscopical quantities, such as stress–strain curves, for validation [29].

The importance of the CP methodology today is evidence by the breadth of research topics and alloying systems. Indicatively, some recent subjects of study, categorized by material, are as follows:

i. Aluminium (Al) alloys: The effect of grain topology on crack propagation for aerospace-grade materials [30], modelling of the Continuous Dynamic Recrystallization (CDRX) [31], and the behaviour of such alloys under cyclic compression loading [32], as well as their behaviour under high-cycle fatigue following 3D printing [33]. Moreover, they have been successfully utilized to study warm forming conditions [34] and even the Bauschinger effect on single crystals [35].
ii. Iron (Fe) and steel alloys: The effect of non-metallic inclusion on the steel failure, e.g., of a 16MnCrS5 steel, has been studied [36]. The effect of martensite on forming has been studied [10,14]. Deep drawing of dual-phase (DP) steels [37], sintering of transformation-induced plasticity (TRIP) [38], and twinning-induced plasticity (TWIP) [39] steels have also been subjects of study. Recently, a formulation modification was proposed for studying the effect of the grain size and the slip system interaction in austenitic stainless steels [40]. Another example is the study of the behaviour of an austenitic steel under multiaxial loading [41].
iii. Magnesium (Mg) alloys: The evolution of twin formation [42,43], the effect of heat treatments on the mechanical behaviour of the twins [44], the evolution [45] and effect [46] of twins in low-cycle fatigue conditions, as well as the effect of grain size on texture evolution under mechanical loading have been studied [47]. Cheng et al. expanded a model for it to be able to capture the effect of hotspots in the local deformation of twin bands [48]. A recent review detailing the applications for Mg alloys can be found in [49].
iv. Titanium (Ti) alloys: The anisotropic plastic deformation of commercial alloys has been studied [50]. The behaviour of dual-phase Ti-alloys has also been studied [21]. Additionally, the results regarding the micro-mechanic response of a TNM alloy have been validated through nano-indentation [51]. Results from CP modelling have also been compared to High-Resolution EBSD (Electron Back-Scatter Diffraction) and High-Resolution DIC (Digital Image Correlation) during micro-slip [52] and stress/strain localization [53]. Another difficulty in simulating the response of highly anisotropic materials is the effect of kink bands during forming, for which an approach for Ti alloys has been proposed [54]. Lastly, the texture evolution during cold forming has also been studied, e.g., [55].
v. Nickel (Ni) super-alloys: The effect of nano-indentation on the distribution of dislocation density of a single-crystal [56], mechanical testing on specimens produced

by direct casting [57], applying the weak link methodology in order to evaluate the fatigue behaviour of the material, while taking into account the part size [58], multiaxial fatigue behaviour [59], and the effect of grain size on fatigue behaviour have been studied [60]. Apart from fatigue behaviour, the creep behaviour has also been studied, e.g., [61,62].

vi. Other alloys: The behaviour of copper (Cu) alloy oligo-crystals under mechanical shock [63], the effect of additive manufacturing on the evolutions of residual stresses of tungsten (W) alloys [64], the low-cycle fatigue behaviour of cobalt–chromium (CoCr) alloys [22], and, lastly, the evolution of texture during severe plastic deformation (SPD) in high-entropy alloys through an expansion of the Taylor model have also been studied.

However, despite the constant progress of CP and the utility of its results, determining the input parameters is still a matter of study [9,26].

This review is structured as follows: After the introduction to the subject (Section 1), the motivation for this work and our contribution to the field is presented (Section 2). This contribution does not only reflect on how the crystal plasticity methodology has evolved over the years (Section 3), but in addition provides a discussion regarding the proper model selection including the constitutive equations (phenomenological or physics-based), the solver (Finite Elements or Fast Fourier Transformations), and the most used packages (Section 4). Then, carefully selected parameters crucial for the execution of a CP simulation, which are absolutely necessary for every researcher working in the field, are gathered, assessed, and coded in very handy table form (Section 5). Furthermore, the required critical steps (i.e., geometry, material, and loading conditions) for a successful simulation execution also considering important parameters affecting the process are presented and discussed as well. Finally, this work concludes with our closing remarks (Section 6).

2. Motivation and Contribution

Crystal plasticity (CP) has significantly evolved since its conceptualization. What began as a tool for studying the deformation of single crystals under uniaxial deformation has become capable of capturing complex phenomena in multiphase polycrystals, even in materials with a gradient crystal structure under complex loading conditions, while at the same time improving computational efficiency and accuracy. There are several papers that perform a review on CP and relevant methodologies, indicatively, Beyerlein et al. [65] reviewed extensively the various models and the difference in their mathematical formulation, Lucarini et al. [66] followed a very detailed, textbook-like approach in explaining Fast Fourier Transformations in relation to micro-mechanics, Yaghoobi et al. [49] details the challenges of magnesium alloy modelling and highlights the relevant literature, whereas, Roters et al. [67] showcased the extent of the possible applications. These reviews provide the reader with a detailed description of the mathematical formulation and mostly focus on literature directly relevant to the specific subject. This review differentiates from those mentioned above (and similar approaches) in the following aspects:

i. It systematically presents the evolution and recent advancements of the CP method through selected milestones and applications with an emphasis on metallic crystalline materials while providing explanation of the basic formulations; in-depth mathematical analysis is omitted.
ii. It is designed to be as short as possible while showcasing most of the critical aspects of running a CP simulation and providing relevant resources.

3. Evolvement of Crystal Plasticity Approaches

Taylor [68] described the slip of single-crystal materials and he was the first to present crystal plasticity in 1982 [69]. By 1993, Beaudoin et al. [70] were already using three-dimensional (3D) models. Figure 1 [71–78] highlights some, non-exhaustive, milestones in the evolution of the mathematical models describing the plastic behaviour of materials from the first mention of dislocations up to today. The formulations connecting plastic

and hardening behaviours to dislocations only became accepted in 1986 by Estren and Kubin [79]. The dislocations were introduced in the study of polycrystalline materials by Arsenlis et al. [80] in the early 21st century and quickly started developing [81]. These early adaptations restricted dislocation movement across multiple grains [81], with this limitation to be overcome by Ma, Roters, and Raabe [82,83].

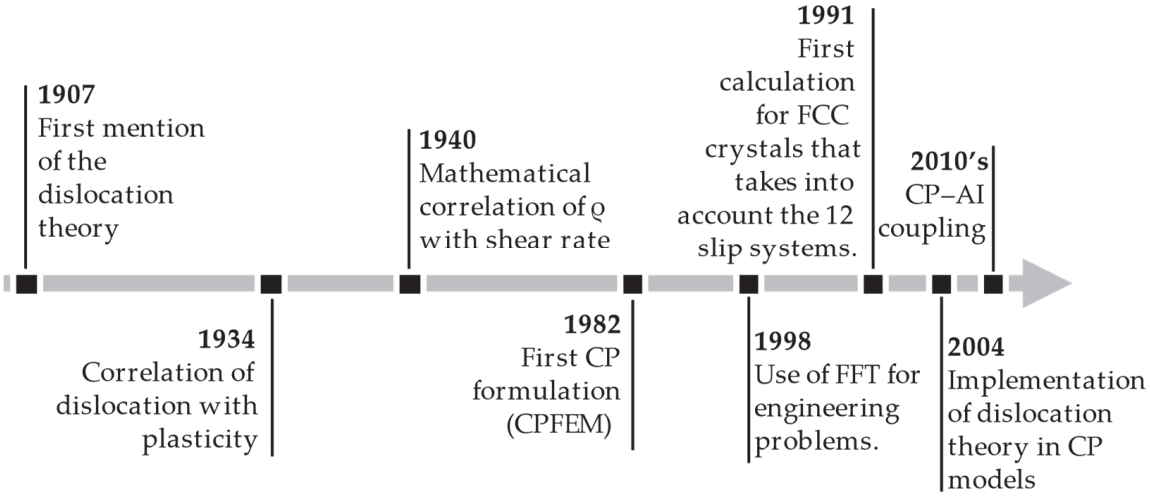

Figure 1. Evolution of the understanding and mathematical description of the deformation mechanisms in polycrystalline materials, through eight milestones.

The first attempts to utilize CP were restricted to simple geometries and significant assumptions were made to simplify the problem. Gradually, the complexity of the systems and geometries has significantly increased to the point where they have become realistic even for more complex materials. The evolvement of CP models is partly dependent on atomic-scale models, since their results can help improve the CP formulation. This can be seen by the expansion of the phenomenological models to include BCC materials [84,85], from FCC where they were originally applied. Additionally, through atomic-scale studies, it was proven that the work-hardening of FCC metals was mainly affected by the collinear dislocation interaction [86], i.e., the result of attraction of dislocations moving on the same slip plane. This created a need to incorporate the dislocation interaction into CP models, resulting in what is now known as physics-based CP. Parameters from various scales, such as dislocations, are used in a statistical manner to calculate the final macroscopic deformation and stress distribution. Due to such parameters being statistically integrated, instead of being explicitly studied, physics-based CP still falls under continuum solid mechanics (mesoscale modelling). The interaction of mobile dislocations with dislocation forests was studied via a multiscale approach, combining the dislocation density with the resolved shear stress on each slip system [87]. This was followed by efforts to capture the effect of deformation-induced heat on the material behaviour for small deformations [88]. CP is also a capable tool for the study of gradient crystal materials [89,90].

There are currently three multiscale modelling approaches to study alloys [91]. Firstly, the embedded approach, according to which the lower-scale models are embedded in the higher-order ones, which has high accuracy and is often used in physics-based CP. According to the hierarchical approach, a separate model is used at each scale and the outputs of lower scales are iteratively used as input for the higher scales, and lastly, the Adaptive Sampling Method (ASM) according to which, the lower-scale models executed only once, and their results are used in many different scenarios.

Heterogeneities within the material have been successfully studied, firstly by Hashin et al. [92] using a framework for homogenized and fully elastic (linear) microstructural models [93]. A shift from the iso-strain homogenization scheme to the Relaxed Grain Cluster (RGC) model [94,95] can allow the study of the interaction between the grains

within the representative volume element (RVE). RGC is a homogenization technique used to reduce the computational cost while retaining sufficient information [95] at an improved speed [94]. This is achieved through clustering grain behaviour under mechanical loading yet allowing a degree of freedom to minimize the energy of the cluster. The impact of the homogenization scheme on texture evolution was studied by Eisenlohr et al. [96].

3.1. General Taxonomy of Crystal Plasticity Models

There are many ways to categorize crystal plasticity models. A branch of the categories described by Trusov et al. [97] are depicted in Figure 2. They can be categorized as follows: Statistical, which is better suited for uniformly deformed volumes [98–100], Self-Consistent, which can study steady-state deformation [65], and Direct models, which are mostly used for nonuniform deformations [97]. The Self-Consistent approach was considered separate to crystal plasticity [101] until Lebensohn et al. [102] integrated them. Each approach can follow a local or a non-local approach while calculating the critical shear stress. The local approach takes into account the stress applied in each calculation point, whereas the non-local approach utilizes either [103] the deformation gradient (e.g., [24,81,104]) or continuum dislocation dynamics (e.g., [56,105–112]).

Taking the strain gradient into consideration, studying the effect of the RVE size on the results is allowed. Furthermore, non-local strain-based models can be further categorized as lower or higher order, depending on the formulation of the boundary conditions [53,54]. Lastly, they are described as mean or full field (e.g., [113]) by the selection of the solver, as discussed in Section 4.2. Utilization of a full-field formulation translates to the ability to study local heterogeneities in the macroscopical mechanical behaviour of the materials [114] and a prediction of localized stresses [18].

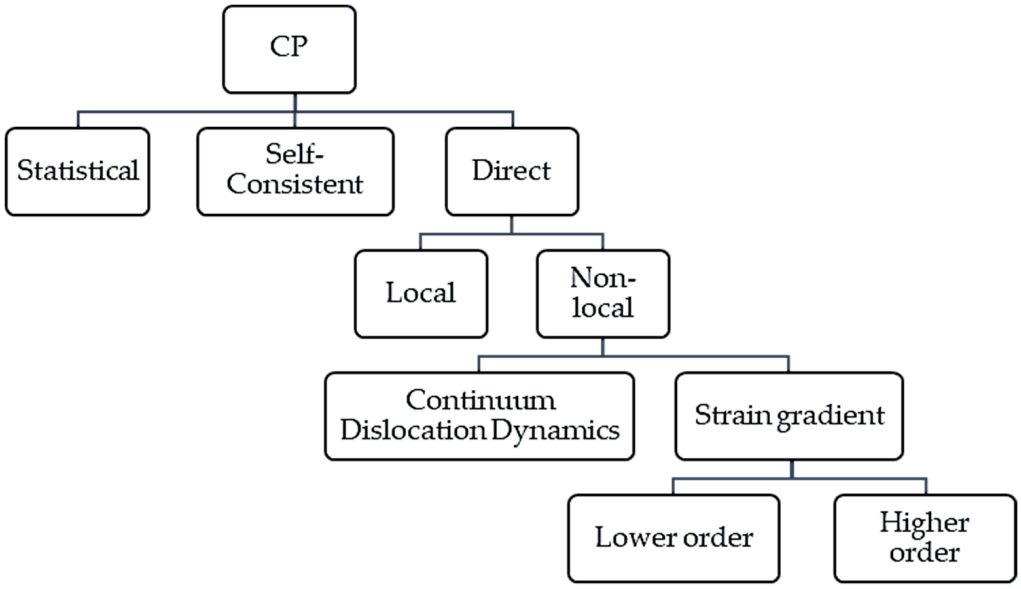

Figure 2. Categorization of crystal plasticity models.

3.2. Approaches for Further Improvement of CP

The CP framework is constantly being upgraded and optimized in its ability to utilize and predict complex phenomena, e.g., [25,26]. Other approaches for improvement can be categorized as follows:

i. Improving execution time and accuracy. As mentioned, CP problems can be solved with either a FEM approach or a FFT approach. The CP-FFT methodology is significantly faster, mostly due to the low mesh sensitivity and the mathematical formulation. However, efforts have been made to further improve their computational efficiency [115] and accuracy [116]. Ling et al. [117] decreased the mesh sensitivity

of the FEM solvers, allowing the application of a coarser grid while retaining result accuracy and indirectly accelerating the calculation process. Other efforts are focused on the optimization of resource allocation [118] via the modification of CP to run on a GPU and creating a hybrid CPU-GUP architecture to increase computational efficiency, while others focus on simplifying the FFT controls [114]. Zecevic et al. [119] introduced an LS-EVP-FFT (large-strain elasto-viscoplastic) model, which allows for increased accuracy in quantifying the effect of anisotropy on the creation of hotspots, through the modification of Green's operator and introduction of more grids per material point. Admal et al. [120] depicted grain boundaries as a special category of geometrically necessary dislocations (GNDs) to better depict their impact. Recently, Romanov et al. [11] presented a statistical model, thus reducing execution time, capable of studying the ECAP test. Another topic of interest is the evaluation of the stability of the developed models [121,122].

ii. Combining the CPFEM and CPFFT approaches. Yu et al. [8] combined the two solvers (FEM and FFT), allowing the expansion of possible applications. Alharbi et al. [123] used the results of the FFT approach as input for the CPFEM, achieving faster results.

iii. Optimizing input geometry. Apart from the geometry and the number of grains, an important parameter of the RVE file has proven to be the total volume of the synthetic microstructure [124,125]. This topic will be discussed in detail in Section 5.1.

iv. Streamlining the parameter identification process. This can be achieved through in situ tensile tests [126] or genetic algorithms [127]. Furthermore, some CP models are being designed to be material-independent [26] to increase the spectrum of potential applications.

v. Creation of tailored models. To achieve higher accuracy, some models are being created to be tailored to specific materials, e.g., [26], where a material-invariant approach of mesoscale parameters has been proposed, or processes, e.g., for the effect of the hardening parameters on the crystallographic texture evolution during the rolling of aluminium alloys [128].

vi. Other efforts focus on expanding the field of potential applications, e.g., to other crystal systems by accounting for the dislocation slip and twinning of Hexagonal Closed Packed (HCP) systems [129] or even capturing the effect of sample size to the yield stress through an embedded, sub-routine for Discrete Dislocation Dynamics in a CPFEM model [28].

3.3. Coupling CP to Machine Learning Algorithms

A different approach is the utilization of Artificial Intelligence (AI) and machine learning (ML) methodologies in conjunction with crystal plasticity modelling. A description of such approaches can be found in [130], but they will not be discussed in detail here. The usage of these approaches in the field of materials modelling is expected to grow [131]. One of the most important issues preventing their widespread application [132] is the volume of data needed for training and validation [127]. The coupling of these tools with CP usually has one of the following goals:

i. Model calibration. This approach can solve one of the most important issues of applying CP models, the determination of the correct values for the input parameters. Among others, Galan Lopez et al. [18], Chakraborty et al. [19], Plowman et al. [10], and Sedighiani et al. [127] have all performed a calibration of the input parameters needed for CP simulations through an ML algorithm, applied to data from tensile testing. A similar approach was followed by Sahoo et al. [29] for the phenomenological model. There are examples of calibration being performed under cyclic loading conditions [133].

ii. Improved accuracy while maintaining the computation cost. Due to the increasing complexity of the Partial Differential Equations (PDEs), resulting from raising the accuracy and realism of the models, the implementation of such an approach is also expected to show an increase in the following years [134]. Adopting methodologies such as Convolutional Neural Networks (CNNs) can result in a reduction in the computational cost of macroscopic properties by 99% when compared to a two-dimensional (2D) CP simulation [135]. Applying Deep Neural Networks (DNNs) for the local response of an FFT solver, carried out by Mianroodi et al. [134], lead to an acceleration in the time needed for obtaining the results by $\times$8300 times for heterogeneous materials. Another example of achieving high accuracy, while maintaining a low computational cost, is the prediction of the local response in industrial aluminium alloys using a CNN-CPFEM methodology [136].
iii. Surrogate modelling. Some indicative works are the one of Saidi et al. [137], in which they utilized the Taylor model to train an ML algorithm for the rolling of aluminium alloys. Khorrami et al. [138] calibrated a CNN model for tensile tests with results from VSPC (Viscoplastic Crystal plasticity), and accurately predicted the von Mises stresses.

4. Methodologies

This section discusses the main difference in the formulation of phenomenological CP models and physics-based CP models, includes a comparison between the Fast Fourier Transformation (FFT) and the Finite Element (FEM) solvers, and, lastly, refers to some indicative commonly used CP packages.

4.1. Phenomenological and Physics-Based CP

Regardless of the chosen model category, the shear rate of each slip system is correlated with the deformation of the whole volume under consideration. Equation (1) [20] provides the formulation for the speed of the plastic deformation gradient (L_p), where m is the vector normal to the slip system, a represents the slip system, n is the total number of independent slip systems (i.e., 12 for FCC, 5 for BCC, and 3 for HCP), and $\dot{\gamma}^{\alpha}$ is the shear rate of the ath slip system.

$$L_p = \sum_{a=1}^{n} \dot{\gamma}^{\alpha} \cdot m^{\alpha} \otimes n^{\alpha} \tag{1}$$

The expression of the shear rate is one of the most fundamental differences between the phenomenological and the physics-based formulations. For the phenomenological models, the shear rate is given by Equation (2). In Equation (2), the variable m differs from the one in Equation (1) as it a case-specific parameter with no physical meaning, modified to achieve the best fit with experimental observations.

$$\dot{\gamma}^{\alpha} = \dot{\gamma}_0 \cdot \left| \frac{\tau^{\alpha}}{\tau_c^{\alpha}} \right|^{\frac{1}{m}} \cdot \sinh(\tau^{\alpha}) \tag{2}$$

τ_C^{α} is the critical shear stress on the slip plane, while τ^{α} is the saturation shear stress [139] and a is the number of slip systems in the crystal.

On the other hand, the realism provided by the formulation incorporating physics laws leads to a more a more complex expression, with a significant number of parameters [127]. An example of such a formulation is the work of Kords [140], shown in Equation (3). It can be seen that, additionally to stress-related terms, it includes quantities such as the dislocation density (ρ) and speed (v_0), the burger vector (b), solid solution activation energy (Q_s), the Bolman's constant (k_B), and temperature (T), plus two parameters (p, q) controlling dislocation movement behaviour. Most of these terms have their own mathematical formulation, resulting in more parameters being involved.

$$\dot{\gamma} = \rho \cdot b_s \cdot v_0 \cdot e^{\left[-\frac{Q_s}{k_B \cdot T} \cdot \left\{ 1 - \left(\frac{|\tau_{eff}|}{\tau_{sol}} \right)^{p_s} \right\}^{q_s} \right]} \cdot \mathrm{sgn}(\tau) \tag{3}$$

Considering complex interactions, even in a statistical manner, is a computationally expensive process. The mathematical foundations for reducing the cost of capturing the dislocation movement in CP modelling were laid by Arsenlis et al. [105] and Ganghoffer et al. [141], who developed differential equations for the calculation of the dislocations, with higher degrees of freedom. Later, Ma, Roters, and Raabe [142] suggested an alternative, which is more efficient under complex loads. Subsequent developments further enhanced the accuracy of dislocation movement [56].

Physics-based CP models, although they can receive input parameters (e.g., atomic volume and dislocation density) from lower scales (i.e., atomic scale), still examine the grain as a continuum body. Phenomena such as dislocation interaction are considered in a statistical manner [143] instead of being individually tracked. Thus, just like phenomenological models, physics-based ones also fall under the mesoscale modelling category, since they consider each grain a continuum.

4.2. FEM vs. Spectral Methods

As mentioned, each of the CP models can be solved either with the FEM or with a spectral approach (FFT), which was proposed as an alternative [144], resulting in CPFFT and CPFEM categories. Even though FFT was suggested relatively early, its use on polycrystalline materials is rather new, firstly proposed by Lebensohn [145], from where it was expanded to anisotropic materials with significant texture [91]. Spectral solvers (FFT) have two main basic advantages over the FEM [146], which are as follows [25,115,147–149]:

i. Computational efficiency: They are faster, by around an order of magnitude, and can therefore achieve higher resolution/grid density on the RVE at the same time.
ii. Due to their low mesh sensitivity, they enable the use of a coarser grid without sacrificing result accuracy [93,146]. An example of this is [38], where they used one calculation point per grain.

On the other hand, these benefits involve some trade-offs that need to be considered for each case. Firstly, due to the periodic boundary conditions applied it is difficult to study the materials near the free surfaces. This is a result of the fact that the volume under study is virtually extended infinitely around itself in three-dimensional space [150].

To demonstrate the periodic boundary conditions, Figure 3 shows an RVE created based on the Voronoi methodology containing 30 grains with a grid of 500^3 voxels visualized through ParaView [151,152] (Figure 3a). Grain morphology is also shown (Figure 3b–d) whereas in Figure 3e,f, a face of the original RVE is repeated in space. Since the material is constantly in contact with other identical volumes, RVEs studied under the periodic conditions' assumptions have no free surfaces.

To overcome the limitation introduced by the lack of free surfaces, Maiti and Eisenlohr [153] proposed to enclose the RVE of interest in another material, simulating the interaction with the free surface, resulting, however, in a significantly more complex RVE. Additionally, it can only work with the use of a normal/regular (x = z = y) grid [154,155] and the remeshing processes have proven to be rather complex [156]. It should be noted that the issue regarding the grid sensitivity of the FEM solver can in some cases be overcome by utilizing the micro-morphic crystal plasticity technique [23]. A more detailed comparison of the approaches can be found in [157].

4.3. Indicative Available CP Packages

A significant number of CP-related software/codes exist, with research groups trying to develop in-house/custom packages, with some of them being openly available. The most widely used, to the best of the authors knowledge, are as follows:

i. DAMASK, developed by the Max Plank Institute for Sustainable Materials GmbH—R&D centre, released in 2011 [67,158].
ii. PRISMS, developed by the University of Michigan [159,160].
iii. CAPSUL and FFTMAD, both developed by the IMDEA Research centre, released in 2012 [161,162].

iv. ρ-CP, co-developed by the Indian Institute of Technology and Georgia Institute of Technology, released in 2023 [163].
v. AMITEX_FFTP, developed by the coalition Maison de la Simulation, consisting of the French National Centre for Scientific Research, the French Alternative Energies and Atomic Energy Commission (CEA), Université Paris-Saclay, and Université Versailles Saint-Quentin, also released in 2023 [164].
vi. Other packages available in the literature are the ones found in [66,104,165] as well as in [166], implementing CPFFT and CPFEM, respectively [167].

Table 1 provides a concise overview of the packages in terms of (i) the solver used, FEM vs FFT as previously discussed, (ii) the formulation used, phenomenological or physics based, and, lastly, (iii) if they are open access or require a commercial licence.

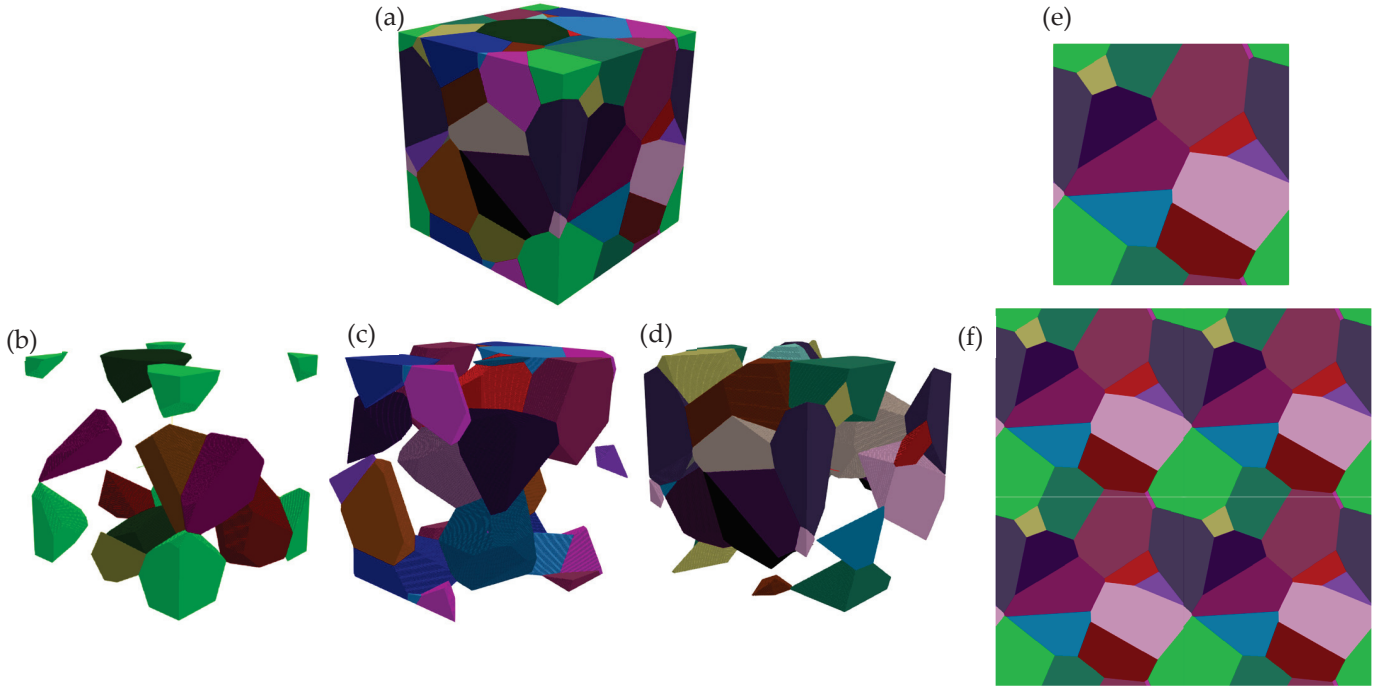

Figure 3. (**a**) An RVE consisting of 30 grains based on the Voronoi method. (**b**–**d**) Indicative grain groups shown for the purpose of highlighting the grain morphology in the 3D space. (**e**) A face of the RVE. (**f**) The face of the RVE shown in (**e**), laid in a 2 × 2 space. Colour variations correspond to grain number, as read by the program, and not to texture.

Table 1. Comparison between the selected packages.

	Solver		**Formulation**		**Access**
	FEM	**FFT**	**Phenomenological**	**Physics-Based**	**Open Access (OA)/ Commercial Licence (CL)**
PRISMS	X		X		OA
CAPSUL	X		X	X	CL
FFTMAD		X			OA/CL
ρ-CP	X			X	OA
AMITEX		X			OA
DAMASK	X	X	X	X	OA

5. Critical Aspects for CP Simulations

This section is focused on the most critical aspects of setting up a CP simulation. These aspects include the RVE dimensions, the parameters that describe the material behaviour, and the loading conditions.

5.1. RVE Modelling

5.1.1. RVE Creation

Proper selection of geometry-related parameters is the first, and crucial [18], step towards the design of the synthetic microstructure. The most common ways to create an RVE are either through (i) a 1:1 representation based on data provided by techniques such as serial sectioning [124], Atom Probe Tomography (APT), 3D EBSD, assisted by software, such as NEPER [168], DREAM 3D [169], and Voro++ [170], through the cellular automata approach [124] or (ii) creating the RVE based on typical data obtained by standard metallography procedures, via the aforementioned software, most commonly utilizing the Voronoi methodology [171]. These two approaches are not interchangeable in their results. Indicatively, Tu et al. [22] studied the effect of the grain morphology of the RVE under fatigue and found that the RVEs with an accurate morphology had a 10% better fit with the experiments in comparison to Voronoi-based microstructures. As explained in [93], the experimentally produced RVEs have some deviation in capturing grain-boundary-related phenomena, whereas the computationally calculated RVEs mostly consider grain boundaries to be planes. Moreover, during serial sectioning, the information between the sections is lost [124].

There are studies regarding measurement accuracy, e.g., [172–174] through focused ion beam-scanning electron microscopy (FIB-SEM) and automation for larger scales and APT [175] for smaller scales, which, however, greatly increases the cost of the RVE extraction. An extended review on advanced Microstructure Characterization and Reconstruction (MCR) techniques was performed by Bostanabad et al. [176].

5.1.2. RVE Size

A critical parameter when designing the RVE is the size. Specifically, small volumes, depending on the formulation used, may behave like oligo-crystals, losing information about the interaction between grain and phase boundaries, while large volumes have a higher computational cost [177]. For most cases focusing on deformation, a volume of a few hundreds of grains can suffice [24] or equivalently an edge of the RVE equal to a few hundred micrometres [128]. Studies involving statistical quantities (e.g., crystallographic texture) require a significantly larger number of grains [155].

Size also incorporates the thickness of the RVE. Macroscopically, there is evidence [178] suggesting that the fit with the validation points may be sufficient regardless of the thickness. However, the thickness can influence the accuracy on a local level, especially when the comparison is between a 2D and a 3D volume [179–181]. Mirhosseini et al. [182] schematically demonstrate the effect of the size for 2D and 3D RVEs with grains in the range between 9 and 225 and from 8 to 125, respectively. Specifically, it was shown that 3D RVEs require less grains in total for a similar accuracy. An approach for transferring the results of 2D experiments to the 3D space is described in the recent work of Tseng et al. [179]. The effect of the selected size on the calculated mechanical properties, as well as the differences between RVEs and statistical RVEs (S-RVEs or SVEs), is discussed in [183].

For each case, the proper size needs to be determined a posteriori through a dependency analysis [124], especially in the cases of fatigue analysis, where size has been found to have a significant impact on the accuracy of the fatigue prediction [58]. This means using progressively larger volumes until the results become stable.

5.1.3. Grid Density

Grid, or mesh, density refers to the number of calculation points within the volume of a given RVE. The required grid density mostly depends on the scale of interest. Specifically,

if focus of the study is on macro-mechanical properties (e.g., stress–strain curves) a few calculation points per grain are considered enough, whereas at the mesoscale 10^2–10^3 [156] calculation points per grain would be needed, significantly increasing calculation time.

Texture as a statistical quantity is considered macroscopical and, thus, it is considered to be mesh-independent if there are calculation points in all grains. Yet, Yu et al. [184] observed that when utilizing only some of the original voxels as an RVE (an approach called sub-modelling), effectively increasing the resolution in this area, the prediction of micro-texture and in grain variations was enhanced.

A grid sensitivity analysis is required to determine the proper grid size of each system. Moreover, due to the heterogenous nature of the local deformation and strain localization, the grid is subjected to degradation [156]. To counter this, an adaptive remeshing approach, i.e., changing the mesh along with RVE size, has been proposed.

5.2. Material Related Input Parameters

Defining the input parameters (calibration) for the simulations remains a challenging [9,26,29] and time-consuming task [185]. Some parameters, such as self-diffusion, can be easily found in the relevant literature, e.g., [186], whereas others have proven to be more difficult. This is due to their dependency on loading conditions and material properties [26,187], chemistry, e.g., [21], as well as on the methodology/formulation utilized.

The efforts made to surpass these challenges [127,188] and their quantification can be considered to be a separate field of study [19]. Zeng et al. [189] quantified the effect of each parameter of their model. Moreover, for some models, e.g., [127], it has been proven that each one of the various parameters for the physics-based model takes a single value for each case. As was discussed in Section 4.1, the use of physics-based models entails the quantification of a significant number of parameters. The parameters used in such models can be categorized as follows:

i. Dislocation-Related Parameters. Here, included are parameters such as the dislocation density per dislocation type, the dislocation glide and transmissivity, and various other parameters that assist with the statistical representation of the dislocations.
ii. Thermodynamical Parameters. These can be related to the solid solution, the diffusion, etc.
iii. General Parameters. These can be, for example, the mechanical parameters of the material.
iv. Case-specific parameters need to be calibrated for each case (fitted to experimental data). Parameters that do not necessarily have a physical meaning need to be fitted in each specific case, accounting both for the material and the process.

One of the most difficult-to-measure parameters is the dislocation density, usually measured in m/m^3 [190]. It is the carrier of plastic deformation [20] and thus heavily influences the mechanical response of the material. Some formulations, e.g., [140], differentiate between edge and screw dislocations and further divide them into dipolar (immobile) and monopolar (mobile) dislocation density as well as positive and negative. In one study [105], monopolar ρ is also found as GNDs (Geometrically Necessary Dislocations), while the dipoles are found as SSDs (statistically stored dislocations).

Their importance is not restricted to mechanics, since phenomena such as grain growth are heavily dependent on them. Recently, their effect on static recrystallization has been studied through a coupling of crystal plasticity with phase field [191]. Phase field modelling for nickel super alloys revealed that under high values of shear stresses, their movement speed is constant, whereas for lower values, it was found to be periodic [192].

Wang et al. [190] calculated the dislocation density for cold-rolled aluminium alloys through the Taylor model and compared their results to experimental measurements via Transmission electron microscopy (TEM), with a deviation of 30%. Significant change, around 500%, in their population as the forming progresses is also observed.

Table 2 summarizes some of the experimental methods and techniques used for calculating specific parameters, based on the earlier categorization. Parameters that lack a

physical meaning, usually non-dimensional, such as the energy barrier profile constants, can be determined through macroscopic (e.g., comparing the texture after the applied deformation and stress—strain curves) or microscopic (e.g., using Digital Image Correlation, DIC, to compare the stresses developed) tests until the result agrees with experimental results. Parameters referring to lower scales, such as kink width, are more difficult to measure experimentally and require access to equipment such as APT. Most of the required parameters can also be calculated from atomistic simulations such as ab initio or molecular dynamics. An example of parameter calculations through the ab initio approach is [193].

Table 2. Indicative required equipment for the measurement of the values of parameters used by physics-based CP models.

	Tensile Test	**Nanoindentation**	**XRD**	**Elec. Cond.**	**EDS**	**Diffusion Couple**	**TEM/High Resolution**	**Atom Probe Tom.**	**Atomic Force Mi.**	**Fitting**	**Atomic-Level Simulation**
Elastic constants		X									X
Dislocation core radius							X				X
Atomic volume			X								X
Attempt frequency				X							X
Mean free P path							X			X	X
Width (double kink)			X				X		X		X
Drag coefficient											X
Solid solution activation energy						X					X
Atomic concentration					X						
Transmissivity parameters										X	
Energy for dislocation climb	X										X
Peierls stress		X									X
Minimum dislocation density of the material							X				X
Starting dislocation density							X				X
Fitting parameters										X	
Energy required for a solute atom to move								X			X
Contribution of edge dislocations to the multiplication of dislocations										X	X
Dislocation interaction			X				X		X		X
Poisson's ratio	X										X

Experimentally determined parameters necessary for physics-based CP simulation execution are difficult to achieve. Alternative possible approaches to calibrate the models are as follows: (i) an iterative one, either via hand or via a dedicated algorithm until the results demonstrate good fit with experimental validation points such as the stress–strain curve, (ii) use machine learning algorithms to approximate the values of the required

parameters, and (iii) finding relevant data in the available literature. The manual–iterative approach is extremely time-consuming, especially for formulations that have a significant number of required inputs. The automated–iterative approach seems to provide a good balance of cost–benefit, yet the, limited, available codes may be designed for a different formulation and, thus, require some basic programming skills. Arguably, the faster approach is the machine learning, albiet it requires significant amounts of data. Lastly, a dedicated literature review requires a significant investment of time in order to properly retrieve valuable data.

Table 3 shows indicative articles providing the values used for the various parameters organized by material. The parameters included in these articles are also compared to each other to highlight the variance they may exhibit for the same material. Table 4 provides indicative literature for the BCC- Fe, BCT-Fe (α and α' respectively) and the BCC-Ti (β), whereas the Table 5, provides similar information for FCC-Al (α).

Table 3. Indicative references per alloy category.

Alloy Category	**Indicative References**
Fe and Steel	[13,36,139,179,194]
Ti	[21,114]
Ni	[24,56]
Cu	[24,25,63,87,195–199]
Al	[6,24,30,114,128,140,187,200–205]

Table 4. Indicative crystal plasticity parameters for Fe (BCC—BCT) and β-Ti (BCC).

Parameter		**α-Fe**	**α′-Fe**		**β-Ti**		
First elastic stiffness constant with normal strain	C_{11}	233.3	417.4	[13,195]	160	[114]	GPa
				[36]	135	[21]	
Second elastic stiffness constant with normal strain	C_{12}	135.5	242.4	[13,179]	87	[114]	GPa
		235.5		[36]	113	[21]	
First elastic stiffness constant with shear strain	C_{44}	128.0	211.1	[13,179]	54	[114]	GPa
				[36]	54.9	[21]	
Shear strain rate	$\dot{\gamma}_0$	0.001	0.001	[13]	0.001	[114]	s^{-1}
		0.56		[36]			
Initial shear resistance on [111]	$S_0^{[111]}$	95	406	[13,179]			MPa
				[36]			
Saturation shear resistance on [111]	$S_\infty^{[111]}$	222	873	[13,179]			MPa
				[36]			
Initial shear resistance on [112]	$S_0^{[112]}$	96	457	[13,179]			MPa
				[36]			
Saturation shear resistance on [112]	$S_\infty^{[112]}$	412	971	[13,179]			MPa
				[36]			
Slip hardening parameter/ self-hardening coefficient	h_0	1.0	563	[13,179]	0.1		GPa
				[36]			
Interaction hardening parameter/hardening matrix	$h_{\alpha,\beta}$	1.0	1.0	[13,179]			-
				[36]			

Table 4. *Cont.*

Parameter		**α-Fe**	**α′-Fe**		**β-Ti**		
Stress exponent	N	20	20	[13,179]			-
		3		[36]			
m = strain rate sensitivity component	1/m				20	[114]	-
Curve fitting parameter	W	2.0	2.0	[13,179]			-
				[36]			
Critical resolved shear stress	τ_c^{β}						
Initial slip hardness	${\tau_0}^{\alpha}$				60	[114]	MPa
					120×10^3	[21]	
Saturation value of slip resistance	τ_s				450	[114]	MPa
Hardening exponent	A				2.25	[114]	-
(Self and coplanar slip systems)	q_{ab}						-
(Non-coplanar slip systems)	q_{ab}				1.4	[114]	-
Burgers vector	B				2.86×10^{-10}	[21]	m
Reference dislocation velocity	v_0				10^{-3}	[21]	m s^{-1}
Exponent	P				0.71	[21]	
	Q				1.1	[21]	
Total initial dislocation density	ρ_0				10^{+13}	[21]	m^{-2}
Critical radius for edge annihilation	R_e				11.5	[21]	nm
Critical radius for screw annihilation	R_s				58	[21]	nm
Strength interaction coefficients	g_0				0.5	[21]	-
	g_1				0.5	[21]	-
	g_2				0.8	[21]	-
	g_3				0.8	[21]	-
	g_4				0.8	[21]	-
	g_5				0.8	[21]	-
	g_6				0.8	[21]	-
Segment length interaction coefficients	h_0				0.0	[21]	-
	h_1				0.0	[21]	-
	h_2				0.2	[21]	-
	h_3				0.02	[21]	-
	h_4				0.01	[21]	-
	h_5				0.18	[21]	-
	h_6				0.02	[21]	-
Free energy of activation	F_0				3.1×10^{-23}	[21]	J K^{-1}

Table 5. Indicative parameters for aluminium alloys.

Description	Symbol	Values	Reference	Units
First elastic stiffness constant with normal strain	C_{11}	106.75	[114,128,140]	GPa
		100	[127]	
		108	[24,203]	
		108.2	[204]	
Second elastic stiffness constant with normal strain	C_{12}	60.41	[114,128,140]	GPa
		60	[127]	
		61.3	[24,203,204]	
First elastic stiffness constant with shear strain	C_{44}	28.34	[114,128,140]	GPa
		30	[127]	
		28.0	[24]	
		28.5	[203,204]	
Isotropic shear modulus	M	26.27	[140]	GPa
		25.0	[24,203]	
Poisson ratio	ν	0.345	[140]	-
Burger vector	b	0.286	[24,140,200,205]	nm
Atomic volume	Ω	0.017	[140]	nm^3
		1.7×10^{-29}	[200]	
Shear strain rate	$\dot{\gamma}_0$	0.001	[19,114,127,128,204]	/s
		400	[205]	
Slip hardening parameter/self-hardening coefficient	h_0	75	[114]	MPa
		400	[19]	
		190	[204]	
		80	[127]	
Stress exponent	N			-
m = strain rate sensitivity component	1/m	20	[114,127]	-
		60	[204]	
		25	[19]	
		20	[187]	
		6.66		
		4		
		333.33	[187]	
		5.88		
Curve fitting parameter	W			-
Slip resistance	τ_0	30	[127]	MPa
		58.5	[205]	
		47	[204]	
		31	[19]	
Critical resolved shear stress	τ_c^{β}	31	[128]	MPa

Table 5. *Cont.*

Description	Symbol	Values	Reference	Units
Saturation value of slip resistance	τ_s	63	[19,114,128]	MPa
		95	[204]	
		60	[127]	
Hardening exponent	a	2.25	[19,114,128]	-
		2	[127]	
(Self and coplanar slip systems)	q_{ab}	1	[128]	-
(Non-coplanar slip systems)	q_{ab}	1.4	[128]	-
Latent/self-hardening ratio		1.4	[204]	
Minimum edge dipole separation	$\breve{d}_e$	1.6	[140]	nm
		1×10^{-9}	[200]	m
Minimum screw dipole separation	$\breve{d}_s$	10	[140]	nm
		1×10^{-9}	[200]	m
Dislocation multiplication constant	λ_0	60	[140]	
		100	[200]	
Edge contribution to multiplication	k_1	0.1	[140]	
Initial overall dislocation density	ρ_0	6×10^{10}	[140]	m^{-2}
Self-diffusivity (at T = 300 K)	D_{SD}	7×10^{-29}	[140]	$m^2\ s^{-1}$
Solid solution activation energy	Q_{Sol}	1.25	[140]	eV
Activation energy for dislocation climb	Q_{cl}	3×10^{-19}	[200]	
Solid solution concentration	c_{at}	1.5×10^{-6}	[140]	
Solid solution size	d_{obst}	0.572	[140]	nm
Peierls stress	τ_P	0.1	[140]	MPa
Double kink width	w_k	2.86	[140]	nm
Energy barrier profile constants	p	1	[140]	
		0.233	[205]	
	q	2	[205]	
		1	[140]	
Attack frequency	ν_α	50	[140]	GHz
Dislocation viscosity	η	0.01	[140]	Pa s
Edge jog formation factor	k_3	1	[140]	

5.3. Macroscopic Loading Conditions

Information about the loading conditions, the deformation (F), the applied stresses (P), and their rates ($\dot{F}$, $\dot{P}$) is also required. An example of such input is the following, where the macroscopic load is applied steadily for the duration of the experiment:

$$F = \begin{bmatrix} x & \mathbb{R} & \mathbb{R} \\ \mathbb{R} & x & \mathbb{R} \\ \mathbb{R} & \mathbb{R} & x \end{bmatrix} \quad P = \begin{bmatrix} \mathbb{R} & x & x \\ x & \mathbb{R} & x \\ x & x & \mathbb{R} \end{bmatrix}$$

In the tables above, $\mathbb{R}$ stands for a known real number and x means that the value is undefined and to be determined by the algorithm. It should be noted that these matrices refer to the macroscopic values of strain and pressure applied to the material. For example, a

tensile test with a known enforced total deformation (ε_{tot}) along one axis can be formulated as follows [154]:

$$F = \begin{bmatrix} \varepsilon_{tot} & 0 & 0 \\ 0 & x & 0 \\ 0 & 0 & x \end{bmatrix} \quad P = \begin{bmatrix} x & x & x \\ x & 0 & x \\ x & x & 0 \end{bmatrix}$$

Alternatively, the process can be described by the applied strain rate $(\dot{\varepsilon})$ through the rate of the strain gradient $(\dot{F})$.

During flat rolling, the material deforms in two directions. The rolling direction (RD) and in the Normal to the rolling direction (ND). Macroscopically, it is not subjected to shearing, nor is the width of the plate affected. Thus, the proper formulation would be as follows:

$$F = \begin{bmatrix} \varepsilon_{RD} & 0 & 0 \\ 0 & 0 & 0 \\ 0 & 0 & \varepsilon_{ND} \end{bmatrix}$$

By defining all the nine elements of the deformation matrix, all the elements of the stress matrix should be left undefined. For more complex metal forming processes, e.g., extrusion, these matrices can be calculated through FEM simulations.

6. Closing Remarks

Since its introduction, crystal plasticity has widened its spectrum of applications from FCC single crystals under tensile testing to realistic, multiphase polycrystalline materials under multiaxial loading conditions. The range of the possible applications have piqued the interest of the scientific community, as has become evident through the volume of relevant published work, as well as by the variety of models that have been developed. Yet, there is a need for further improvement of the models to reduce their computational costs, to overcome remaining limitations, to further increase their accuracy, to streamline their set up, to reduce the difficulty of their calibration, and to link them with other models.

It is evident that CP simulations can provide valuable insight into the material behaviour and the impact of micromechanics during forming processes or for fatigue damage. For each case, the selection of the proper type of CP and solver are the first steps that need to be guided by a deep understanding of the process and the assumptions each choice inevitably entails. Each formulation comes with its own set of parameters that need to be determined either experimentally or via an extensive literature review. Regarding the solver (FFT or FEM), the choice is guided by the area of interest. For complex geometries or free surfaces, the FEM solver is usually best suited, compromising, however, the execution speed. For achieving reliable results, proper dependency analysis for the RVE size and mesh density also need to be performed. The selection of the constitutive model,, i.e., phenomenological or physics-based, relies on (i) the area of interest, since for macroscopical phenomena the phenomenological approach is significantly faster and delivers reliable results, whereas for local phenomena the physics-based models seems to be better suited, and (ii) the overall modelling approach, since the models incorporating parameters with physical meaning can be better integrated with various models covering all length scales.

One of the biggest struggles of implementing ICME solutions is the calibration of the models utilized. The first adopters of these methodologies did highlight the importance of creating repositories for the values of the various parameters used. This is also the case for CP. Despite the fact that increasingly more authors publish their parameters, there is a lack of a widespread repository or review articles providing this information per material and process. This should be weighed against the competitive advantage of having in-house databases for the material/processes, which as discussed are not as easy to produce. Utilizing machine learning raises the issue of proper data storage, labelling where needed, and of course it usually requires a significant amount of data. On the other hand, when possible, its use can significantly accelerate the R&D cycle.

Finally, regarding Sustainable Development, CP has a lot to offer. As a challenging field of study, researchers utilizing CP need to be highly trained (SDG 4). Its application can help optimize industrial processes (SDG 9) creating new job positions in the industry (SDG 8) and reducing the environmental footprint of the product (SDG 12 and SDG 13). CP is often provided as a service from research centers to the industry (SDG 17) and its exact impact, qualitative or quantitative, must be calculated for each case individually.

Author Contributions: Conceptualization, S.P.; methodology, S.P. and V.L.; formal analysis, V.L.; investigation, V.L.; resources, S.P.; data curation, V.L.; writing—original draft preparation, V.L.; writing—review and editing, S.P.; visualization, V.L.; supervision, S.P. All authors have read and agreed to the published version of the manuscript.

Funding: This research received no external funding.

Data Availability Statement: No new data were created.

Acknowledgments: The authors would like to thank M. Bouzouni, S. Papadopoulou, V. Karamitros, and F. Tsiolis for taking time to review the manuscript and for their valuable comments.

Conflicts of Interest: The authors declare no conflicts of interest.

References

1. The Minerals, Metals & Materials Society. *Integrated Computational Materials Engineering (ICME): Implementing ICME in the Aerospace, Automotive, and Maritime Industries*; TMS: Warrendale, PA, USA, 2013.
2. Hall, E.O. The Deformation and Ageing of Mild Steel: III Discussion of Results. Proceedings of the Physical Society. *Sect. B* **1951**, *64*, 747.
3. Petch, N.J. The Cleavage Strength of Polycrystals. *J. Iron Steel Inst.* **1953**, *174*, 25–28.
4. Rhines, F.N. Microstructure-property relationships in materials. *Metall. Trans. A* **1977**, *8A*, 127–133. [CrossRef]
5. Diehl, M.; Wang, D.; Liu, C.; Miaroodi, J.R.; Han, F.; Ma, D.; Kok, P.J.; Roters, F.; Shanthraj, P. Solving Material Mechanics and Multuphysics Problems of Metals with Complex Microstructures Using DAMASK—The Dusseldorf Advanced Material Simulation Kit. *Adavanced Eng. Mater.* **2020**, *22*, 201901044.
6. Wang, H.; Lee, H.-W.; Kang, S.-H.; Kim, D.-K. Crystal Plasticity Finite Element Analyses on the Formability of AA6061 Aluminum Alloy with Different Ageing Treatments. *Metals* **2024**, *14*, 503. [CrossRef]
7. Asaro, R.J. Micromechanics of Crystals and Polycrystals. *Adv. Appl. Mech.* **1983**, *23*, 1–115.
8. Yu, Q.; Martinez, E.; Segurado, J.; Marian, J. A stochastic solver based on the residence time algorithm for crystal plasticity models. *Comput. Mech.* **2021**, *68*, 1369–1384. [CrossRef]
9. Roters, F.; Eisenlohr, P.; Bieler, T.R.; Raabe, D. *Crystal Plasticity Finite Element Methods*; Wiley-VHC Verlang GmbH & Co. KGaA: Weinheim, Germany, 2012.
10. Plowman, A.; Jedrasiak, P.; Jailin, T.; Crowther, P.; Mishra, S.; Shanthraj, P.; Quinta de Fonseca, J. A novel integrated framework for reproducible formability predictions using virtual materials testing [version 1; peer review: Approved with reservations]. *Mater. Open Res.* **2023**, *2*, 2. [CrossRef]
11. Romanov, K.; Shveykin, A.; Trusov, P. Advanced Statistical Crystal Plasticity Model: Description of Copper Grain Structure Refinement during Equal Channel Angular Pressing. *Metals* **2023**, *13*, 953. [CrossRef]
12. Yuan, M.; Paradiso, S.; Meredig, B.; Niezgoda, S.R. Machine Learning–Based Reduce Order Crystal Plasticity Modeling for ICME Applications. *Integr. Mater. Manuf. Innov.* **2018**, *7*, 214–230. [CrossRef]
13. Qayyum, F.; Guk, S.; Kawalla, R.; Prahl, U. On Attempting to Create a Virtual Laboratory for Application-Oriented Microstructural Optimization of Multi-Phase Materials. *Appl. Sci.* **2021**, *11*, 1506. [CrossRef]
14. Hussein, T.; Umar, M.; Qayyum, F.; Guk, S.; Prahl, U. Micromechanical Effect of Martensite Attributes on Forming Limits of Dual-phase steels investigated by crystal plasticity. *Crystals* **2022**, *12*, 155. [CrossRef]
15. Li, J.; Wu, X.; Jiang, H. Crystal Plasticity Finite Element Simulation of Grain Evolution Behavior in Aluminum Alloy Rolling. *Materials* **2024**, *17*, 3749. [CrossRef]
16. Qayyum, F.; Guk, S.; Prahl, U. Applications of Crystal Plasticity in Forming Technologies. *Crystals* **2022**, *12*, 1466. [CrossRef]
17. Auth, K.L.; Brouzoulis, J.; Ekh, M. A thermodynamic framework for ductile phase-field fracture and gradient-enhanced crystal plasticity. *Eur. J. Mech.—A/Solids* **2024**, *108*, 105418. [CrossRef]
18. Galan-Lopez, J.; Hidalgo, J. Use of the Correlation between Grain Size and Crystallographic Orientation in Crystal Plasticity Simulations: Application to AISI 420 Stainless Steel. *Crystals* **2020**, *10*, 819. [CrossRef]
19. Chakraborty, A.; Eisenlohr, P. Evaluation of an inverse methodology for estimating constitutive parameters in face-centered cubic materials from single crystal indentations. *Eur. J. Mech. A/Solids* **2017**, *66*, 114–124. [CrossRef]

20. Roters, F.; Eisenlohr, P.; Hantcherli, L.; Tjahjanto, D.; Bieler, T.; Raabe, D. Overview of constitutive laws, kinematics, homogenization and multiscale methods in crystal plasticity finite-element modeling: Theory, experiments, applications. *Acta Mater.* **2009**, *58*, 1152–1211. [CrossRef]
21. Hemery, S.; Villechaise, P.; Banerjee, D. Microplasticity at Room Temperature in α/β Titanium Alloys. *Metall. Mater. Trans. A* **2020**, *51*, 4931–4969. [CrossRef]
22. Tu, Y.; Leen, S.B.; Harrison, N.M. A high-fidelity crystal-plasticity finite element methodology for low-cycle fatigue using automatic electron backscatter diffraction scan conversion: Application to hot-rolled cobalt–chromium alloy. *J. Mater. Desing Appl.* **2021**, *235*, 1901–1924. [CrossRef]
23. Phalke, V.; FOrest, S.; Chang, H.-J.; Roos, A. Adiabatic shear banding in FCC metallic single and poly-crystals using a micromorphic crystal plasticity approach. *Mech. Mater.* **2022**, *169*, 104288. [CrossRef]
24. Haouala, S.; Lucarini, S.; LLorca, J.; Segurado, J. Simulation of the Hall-Petch effect in FCC polycrystals by means of strain gradient crystal plasticity and FFT homogenization. *J. Mech. Phys. Solids* **2020**, *134*, 103755. [CrossRef]
25. Jeong, J.; Voyiadjis, G.Z. A physics-based crystal plasticity model for the prediction of the dislocation densities in micropillar compression. *J. Mech. Phys. Solids* **2022**, *167*, 105006. [CrossRef]
26. Dindarlou, S.; Castalluccio, G.M. Substructure-sensitive crystal plasticity with material-invariant parameters. *Int. J. Plast.* **2022**, *155*, 103306. [CrossRef]
27. Xie, C.; Sun, T.; Li, L.; Zheng, Z. Effect of Microstructure on Fatigue Damage Accumulation in 7075 Aluminum Alloy Subjected to a Single Compressive Overload. *Metals* **2024**, *14*, 980. [CrossRef]
28. Zhang, Z.; Tong, Z.; Jiang, X. Development of the Concurrent Multiscale Discrete-Continuum Model and Its Application in Plasticity Size Effect. *Crystals* **2022**, *12*, 329. [CrossRef]
29. Sahoo, S.K.; Dhinwal, S.S.; Vu, V.Q.; Toth, L.S. A new macroscopic strain hardening function based on microscale crystal plasticity and its application in polycrystal modeling. *Mater. Sci. Eng. A* **2021**, *823*, 141634. [CrossRef]
30. Grant, C.; Aboura, Y.; Burnett, T.L.; Prangnell, P.; Shanthraj, P. Computational study of the geometrical influence of grain topography on short crack propagation in AA7XXX series alloys. *Materialia* **2023**, *29*, 101798. [CrossRef]
31. Chen, S.F.; Li, D.Y.; Zhang, S.H.; Han, H.N.; Lee, H.W.; Lee, M.G. Modelling continuous dynamic recrystallization of aluminum alloys based on the polycrystal plasticity approach. *Int. J. Plast.* **2020**, *131*, 102710. [CrossRef]
32. Shiraiwa, T.; Broffod, F.; Enoki, M. Prediction of Fatigue Crack Initiation of 7075 Aluminum Alloy by Crystal Plasticity Simulation. *Materials* **2023**, *16*, 1595. [CrossRef]
33. Luo, Z.; Li, D.; Ojha, A.; Lai, W.-J.; Engler-Pinto, C.; Li, Z.; Peng, Y. Prediction of high cycle fatigue strength for additive manufactured metals by defects incorporated crystal plasticity modeling. *Mater. Sci. Eng. A* **2023**, *870*, 144832. [CrossRef]
34. El-Athy, A.A.; Ha, S.; Xu, Y.; Hou, Y.; Zhang, S.-H.; Alzahrani, B.; Ali, A.; Ahmed, M.M.Z. Coupling Computational Homogenization with Crystal Plasticity Modelling for Predicting the Warm Deformation Behaviour of AA2060-T8 Al-Li Alloy. *Materials* **2023**, *16*, 4069. [CrossRef] [PubMed]
35. Aria, A.I.; Holmedal, B.; Manik, T.; Marthinsen, K. A Full-Field Crystal Plasticity Study on the Bauschinger Effect Caused by Non-Shearable Particles and Voids in Aluminium Single Crystals. *Metals* **2024**, *14*, 424. [CrossRef]
36. Qayyum, F.; Umar, M.; Elagin, V.; Kirschner, M.; Hoffmann, F.; Guk, S.; Prahl, U. Influence of Non-Metallic Inclusions on Local Deformation and Damage Behavior of Modified 16MnCrS5 Steel. *Crystals* **2022**, *12*, 281. [CrossRef]
37. Tjahjanto, D.D.; Eisenlohr, P.; Roters, F. Multiscale deep drawing analysis of dual-phase steels using grain cluster-based RGC schemedi. *Model. Simul. Mater. Sci. Eng.* **2015**, *23*, 045005. [CrossRef]
38. Qayyum, F.; Guk, S.; Pruger, S.; Schmidtchen, M.; Saenko, I.; Kiefer, B.; Kawalla, R.; Prahl, U. Investigating the local deformation and transformation behavior of sintered X3CrMnNi16-7-6 TRIP steel using a calibrated crystal plasticity-based numerical simulation model. *Int. J. Mater. Res.* **2020**, *111*, 392–404. [CrossRef]
39. Khan, R.; Pervez, T.; Alfozan, A.; Qamar, S.Z.; Mohsin, S. Numerical Modeling and Simulations of Twinning-Induced Plasticity Using Crystal Plasticity Finite Element Method. *Crystals* **2022**, *12*, 930. [CrossRef]
40. Agious, D.; Kareer, A.; Al Mamun, A.; Truman, C.; Collins, D.M.; Mostafavi, M.; Knowles, D. A crystal plasticity model that accounts for grain size effects and slip system interactions on the deformation of austenitic stainless steels. *Int. J. Plast.* **2022**, *152*, 103249. [CrossRef]
41. Biswas, A.; Kurtulan, D.; Ngeru, T.; Guzman, A.A.; Hanke, S.; Hartmaier, A. Mechanical Behavior of Austenitic Steel under Multi-Axial Cyclic Loading. *Metals* **2023**, *16*, 1367. [CrossRef]
42. Wu, P.D.; Guo, X.Q.; Qiao, H.; Lloyd, D.J. A constitutive model of twin nucleation, propagation and growth in magnesium crystals. *Mater. Sci. Eng. A* **2015**, *625*, 140–145. [CrossRef]
43. Zhang, H.; Jerusalem, A.; Salvati, E.; Papadaki, C.; Fong, K.S.; Song, X.; Korsunsky, A.M. Multi-scale mechanisms of twinning-detwinning in magnesium alloy AZ31B simulated by crystal plasticity modeling and validated via in situ synchrotron XRD and in situ SEM-EBSD. *Int. J. Plast.* **2019**, *119*, 43–56. [CrossRef]
44. Ganesan, S.; Yaghoobi, M.; Githens, A.; Chen, Z.; Daly, S.; Allison, J.E. The effects of heat treatment on the response of WE43 Mg alloy: Crystal plasticity finite element simulation and SEM-DIC experiment. *Int. J. Plast.* **2021**, *137*, 102917. [CrossRef]
45. Abdolvand, H.; Majkut, M.; Oddershede, J.; Schmidt, S.; Lienert, U.; Diak, B.J.; Withers, P.J.; Daymondd, M.R. On the daformation twinning of Mg AZ31B: A three-dimensional synchrotron X-ray diffraction experiment and crystal plasticity finite element model. *Int. J. Plast.* **2015**, *70*, 77–97. [CrossRef]

46. Wu, L.; Agnew, S.; Ren, Y.; Brown, D.; Clausen, B.; Stoica, G.; Wenk, H.; Liaw, P. The effects of texture and extension twinning on the low-cycle fatigue behavior of a rolled magnesium alloy, AZ31B. Mater. *Sci. Eng. A* **2010**, *527*, 70057–77067. [CrossRef]
47. Ravaji, B.; Joshi, S.P. A crystal plasticity investigation of grain size-texture interaction in magnesium alloys. *Acta Mater.* **2021**, *208*, 116743. [CrossRef]
48. Cheng, J.; Hu, X.; Bong, H.J.; Ghosh, S.; Sun, X. A finite element formulation for deformation twinning induced strain localization in polycrystal magnesium alloys. *Comput. Mater. Sci.* **2021**, *190*, 110323. [CrossRef]
49. Yaghoobi, M.; Voyiadjis, G.Z.; Sundararaghavan, V. Crystal Plasticity Simulation of Magnesium and Its Alloys: A Review of Recent Advances. *Crystlas* **2021**, *11*, 435. [CrossRef]
50. Hama, T.; Kobuki, A.; Takuda, H. Crystal-plasticity finite-element analysis of anisotropic deformation behavior in a commercially pure titanium Grade 1 sheet. *Int. J. Plast.* **2017**, *91*, 77–108. [CrossRef]
51. Yin, B.; Xue, X.; Zhang, M.; Deng, T.; Li, J.; Tang, B. Parameter identification and pileup behavior of TiAl alloy through nanoindentation and crystal plasticity simulation. *J. Alloys Compd.* **2023**, *948*, 169743. [CrossRef]
52. Zhang, Z.; Lunt, D.; Abdolvand, H.; Wilkinson, A.J.; Preuss, M.; Dunne, F.P. Quantitative investigation of micro slip and localization in polycrystalline materials under uniaxial tension. *Int. J. Plast.* **2018**, *108*, 88–106. [CrossRef]
53. Agius, D.; Cram, D.; Hutchinson, C.; Preuss, M.; Sterjovski, Z.; Wallbrink, C. An experimental and computational study into strain localisation in beta-annealed Ti-6Al-4V. *Mater. Sci. Eng.* **2023**, *45*, 4–11. [CrossRef]
54. Marano, A.; Gélébart, L.; Forest, S. FFT-based simulations of slip and kink bands formation in 3D polycrystals: Influence of strain gradient crystal plasticity. *J. Mech. Phys. Solids* **2021**, *149*, 104295. [CrossRef]
55. Mahadule, D.; Demiral, M.; Mulki, H.; Khatirkar, R.K. Experiments and Crystal Plasticity Finite Element Simulations of Texture Development during Cold Rolling in a Ti-15V-3Cr-3Sn-3Al Alloy. *Crystals* **2023**, *13*, 137. [CrossRef]
56. Reuber, C.; Eisenlohr, P.; Roters, F.; Raabe, D. Dislocation density distribution around an indent in single-crystalline nickel: Comparing nonlocal crystal plasticity finite-element predictions with experiments. *Acta Mater.* **2014**, *71*, 333–348. [CrossRef]
57. Sancho, R.; Segurado, J.; Erica, B.; Perez-Martin, M.-J.; Galvez, F. Crystal-Plasticity-Finite-Element Modeling of the Quasi-Static and Dynamic Response of a Directionally Solidified Nickel-Base Superalloy. *Materials* **2020**, *13*, 2990. [CrossRef]
58. Lucarini, S.; Segurado, J. An upscaling approach for micromechanics based fatigue: From RVEs to specimens and component life prediction. *Int. J. Fract.* **2020**, *223*, 93–108. [CrossRef]
59. Zhang, Y.; Zhang, X.; Wang, J.; Ren, X.; Wang, X.; Chen, R.; Yue, Z. High cycle fatigue life prediction model based on crystal plasticity and continuum damage mechanics for Ni-based single crystal superalloys under a multiaxial stress state. *Int. J. Plast.* **2023**, *162*, 103526. [CrossRef]
60. Cruzado, A.; Lucarini, S.; Llorca, J.; Segurado, J. Crystal plasticity simulation of the effect grain size on the fatigue behavior of polycrystalline Inconel 718. *Int. J. Fatigue* **2018**, *113*, 236–245. [CrossRef]
61. Skamniotis, C.; Grilli, N.; Cocks, A.C. Crystal plasticity analysis of fatigue-creep behavior at cooling holes in single crystal Nickel based gas turbine blade components. *Int. J. Plast.* **2023**, *166*, 103589. [CrossRef]
62. Keshavarz, S.; Campell, C.E.; Reid, A.C.E. Multi-Scale Crystal Plasticity Model of Creep Responses in Nickel-Based Superalloys. *Materials* **2022**, *15*, 4447. [CrossRef]
63. Luscher, D.J.; Bronkhorst, C.A.; Alleman, C.N.; Addessio, F.L. A model for finite-deformation nonlinear thermomechanical response of single crystal copper under shock conditions. *J. Mech. Phys. Solids* **2013**, *61*, 1877–1894. [CrossRef]
64. Wang, C.; Li, Z.J.; Ji, C.Q.; Gao, S.W.; Cui, Y.N. Crystal plasticity analysis of the evolutions of temperature, stress and dislocation in additively manufactured tungsten. *Int. J. Refract. Met. Hard Mater.* **2023**, *110*, 106041. [CrossRef]
65. Beyerlein, I.J.; Knezevic, M. Review of microstructure and micromechanism-based constitutive modeling of polycrystals with a low-symmetry crystal structure. *J. Mater. Res.* **2018**, *33*, 3711–3738. [CrossRef]
66. Lucarini, S.; Upadhyay, M.; Segurado, J. FFT based approaches in micromechanics: Fundamentals, methods and applications. *Model. Simul. Mater. Sci. Eng.* **2021**, *30*, 023002. [CrossRef]
67. Roters, F.; Diehl, M.; Shanthraj, P.; Eisenlohr, P.; Reuber, C.; Wong, S.L.; Maiti, T.; Ebrahimi, A.; Hochrainer, T.; Fabritius, H.-O.; et al. DAMASK—The Dusseldorf Advanced Material Simulation Kit for modeling multi-physics crystal plasticity, thermal, and damage phenomena from single crystal up to the component scale. *Comput. Mater. Sci.* **2019**, *158*, 420–478. [CrossRef]
68. Taylor, G.I.; Elam, C.F. The distortion of an aluminium crystal during a tensile test. Proceedings of the Royal Society of London A: Mathematical. *Phys. Eng. Sci.* **1923**, *102*, 126–135.
69. Taylor, G. The Mechanism of Plastic Deformation of Crystals. Part I. Theoretical. *Proc. R. Soc. Lond. Ser. A* **1934**, *145*, 362–387.
70. Beaudoin, A.J.; Mathur, K.K.; Dawson, P.R.; Johnson, G. Three-Dimensional Deformation Process Simulation with Explicit use of Polyctystal Plasticity Models. *Int. J. Plast.* **1993**, *9*, 833–860. [CrossRef]
71. Volterra, V. Sur l'équilibre des corps élastiques multiplement connexes. *Ann. Sci. Ec. Norm. Super.* **1907**, *24*, 401–517. [CrossRef]
72. Orwan, E. Problems of plastic gliding. *Proc. Phys. Soc.* **1940**, *52*, 8–22. [CrossRef]
73. Becker, R.; Butler, J.F.; Hu, H.; Lalli, L.A. Analysis of an aluminum single crystal with unstable initial orientation (001) [111] in channel die compression. *Metall. Trans. A* **1991**, *22*, 45–58. [CrossRef]
74. Becker, R. Analysis of texture evolution in channel die compression—I. Effects of grain interaction. *Acta Metall.* **1991**, *39*, 1211–1230. [CrossRef]
75. Orowan, E. Zur Kristallplastizität, I.–III. *Z. Phys.* **1934**, *89*, 605–659. [CrossRef]
76. Polanyi, M. Über eine Art Gitterstörung, die einen Kristall plastisch machen könnte. *Z. Phys.* **1934**, *89*, 660–664. [CrossRef]

77. Peirce, D.; Asaro, R.J.; Needleman, A. An analysis of nonuniform and localized deformation in ductile single crystals. *Acta Metall.* **1982**, *30*, 1087–1119. [CrossRef]
78. Moulinec, H.; Suquet, P. A numerical method for computing the overall response of nonlinear composites 64j 3 Crystal Plasticity Modeling with complex microstructure. *Comput. Methods Appl. Mech. Eng.* **1998**, *157*, 69–94. [CrossRef]
79. Estrin, Y.; Kubin, L.P. Local strain hardening and nonuniformity of plastic deformation. *Acta Metall.* **1986**, *34*, 2455–2664. [CrossRef]
80. Arsenlis, A.; Parks, D.M. Modeling the evolution of crystallographic dislocation density in crystal plasticity. *J. Mech. Phys. Solids* **2002**, *50*, 1979–2009. [CrossRef]
81. Evers, L.P.; Brekelmans, W.A.; Geers, M. Non-local crystal plasticity model with intrinsic SSD and GND effects. *J. Mech. Phys. Solids* **2004**, *52*, 23792401. [CrossRef]
82. Ma, A.; Roters, F.; Raabe, D. Studying the effect of grain boundaries in dislocation density based crystal-plasticity finite elements simulations. *Int. J. Solids Struct.* **2006**, *43*, 7287–7303. [CrossRef]
83. Ma, A.; Roters, F.; Raabe, D. On the consideration of interactions between dislocations and grain boundaries in crystal plasticity finite element modeling—Theory, experiments and simulations. *Acta Mater.* **2006**, *54*, 2181–2194. [CrossRef]
84. Ito, K.; Vitek, V. Atomistic study of non-Schmid effects in the plastic yielding of BCC metals. *Philos. Mag. A* **2001**, *81*, 1387–1407. [CrossRef]
85. Vitek, V.; Mrovec, M.; Bassani, J. Influence of non-glide stresses on plastic flow: From atomistic to continuum modeling. *Mat. Sci. Eng. A* **2004**, *365*, 31–37. [CrossRef]
86. Madec, R.; Devincre, B.; Kubin, L.; Hoc, T.; Rodney, D. The role of collinear interaction in dislocation-induced hardening. *Science* **2003**, *301*, 1879–1882. [CrossRef] [PubMed]
87. Kubin, L.; Devincre, B.; Hoc, T. Modeling dislocation storage rates and mean free paths in face-centered cubic crystals. *Acta Mater.* **2008**, *56*, 6040–6049. [CrossRef]
88. Bertram, A.; Krawietz, A. On the introduction of thermoplasticity. *Acta Mech.* **2012**, *223*, 2257–2268. [CrossRef]
89. Zheng, Z.; Li, X.; Xu, D.; Lu, L.; Gao, H.; Zhu, T. Gradient plasticity in gradient nano-grained metals. *Extrem. Mech. Lett.* **2016**, *8*, 213–219. [CrossRef]
90. Xiao, M.; Yao, J.; Huang, C. Fracture Model of Al–Cu Alloys with Gradient Crystals Based on Crystal Plasticity. *Metals* **2024**, *14*, 694. [CrossRef]
91. Van Houttee, P.; Kanjarla, A.K.; Van Bael, A.; Seefeldt, M.; Delannay, L. Multiscale modelling of the plastic anisotropy and deformation texture of polycrystalline materials. *Eur. J. Mech. A/Solids* **2006**, *25*, 634–648. [CrossRef]
92. Hashin, Z.; Shtrikman, S. A variational approach to the theory of the elastic behaviour of multiphase materials. *Mech. Phys. Solids* **1963**, *11*, 127–140. [CrossRef]
93. Segurado, J.; Lebensohn, R.A.; LLorca, J. Computational Homogenization of Polycrystals. *Adv. Appl. Mech.* **2018**, *51*, 1–114.
94. Tjahjanto, D.D.; Eisenlohr, P.; Roters, F. A novel grain cluster-based homogenization scheme. *Model. Simul. Mater. Sci. Eng.* **2009**, *18*, 015006. [CrossRef]
95. Tjahjanto, D.; Eisenlohr, P.; Roters, F. Relaxed Grain Cluster (RGC) Homogenization Scheme. *Int. J. Mater. Form.* **2009**, *2*, 939–942. [CrossRef]
96. Eisenlohr, P.; Tjahjanto, D.D.; Hochrainer, T.; Roters, F.; Raabe, D. Comparison of texture evolution in fcc metals predicted by various grain cluster homogenization schemes. *Int. J. Mater. Res.* **2009**, *100*, 500–509. [CrossRef]
97. Trusov, P.; Shveykin, A.; Kondratev, N. Some Issues on Crystal Plasticity Models Formulation: Motion Decomposition and Constitutive Law Variants. *Crystals* **2021**, *11*, 1392. [CrossRef]
98. Habraken, A.M. Modelling the plastic anisotropy of metals. *Arch. Comput. Methods Eng.* **2004**, *11*, 3–96. [CrossRef]
99. Van Houtte, P. Crystal Plasticity Based Modelling of Deformation Textures. In *Microstructure and Texture in Steels*; Springer: London, UK, 2009.
100. Zhang, K.; Holmedal, B.; Hopperstad, O.S.; Dumoulin, S.; Gawad, J.; Van Bael, A.; Van Houtte, P. Multi-level modelling of mechanical anisotropy of commercial pure aluminium plate: Crystal plasticity models, advanced yield functions and parameter identification. *Int. J. Plast.* **2015**, *66*, 3–30. [CrossRef]
101. Petkov, M.P.; Hu, J.; Tarleton, E.; Cocks, A.C. Comparison of self-consistent and crystal plasticity FE approaches for modelling the high-temperature deformation of 316H austenitic stainless steel. *Int. J. Solids Struct.* **2019**, *171*, 54–80. [CrossRef]
102. Lebensohn, R.A.; Turner, P.A.; Signorelli, J.W.; Canova, G.R.; Tomé, N.C. Calculation of intergranular stresses based on a large-strain viscoplastic self-consistent polycrystal model. *Model. Simul. Mater. Sci. Eng.* **1998**, *6*, 447. [CrossRef]
103. Zhang, X.; Zhao, J.; Kang, G.; Zaiser, M. Geometrically necessary dislocations and related kinematic hardening in gradient grained materials: A nonlocal crystal plasticity study. *Int. J. Plast.* **2023**, *163*, 103553. [CrossRef]
104. Gurtin, M.E. A gradient theory of single-crystal viscoplasticity that accounts for geometrically necessary dislocations. *J. Mech. Phys. Solids* **2002**, *50*, 5–32. [CrossRef]
105. Arsenlis, A.; Parks, D.M.; Becker, R.; Bulatov, V.V. On the evolution of crystallographic dislocation density in non-homogenously deforming crystals. *J. Mech. Phys. Solids* **2004**, *52*, 1213–1246. [CrossRef]
106. Groma, I.; Csikor, F.F.; Zaiser, M. Spatial correlations and higher-order gradient terms in a continuum description of dislocation dynamics. *Acta Mater.* **2003**, *51*, 1271–1281. [CrossRef]

107. Hochraine, T.; Sandfeld, S.; Zaise, M.; Gumbusch, P. Continuum dislocation dynamics: Towards a physical theory of crystal plasticity. *J. Mech. Phys. Solids* **2014**, *63*, 167–178. [CrossRef]
108. Leung, H.S.; Leung, P.S.S.; Cheng, B.; Ngan, A.H.W. A new dislocation-density-function dynamics scheme for computational crystal plasticity by explicit consideration of dislocation elastic interactions. *Int. J. Plast.* **2015**, *67*, 1–25. [CrossRef]
109. Lim, H.; Lee, M.G.; Kim, J.H.; Adams, B.L.; Wagoner, R.H. Simulation of polycrystal deformation with grain and grain boundary effects. *Int. J. Plast.* **2011**, *27*, 1328–1354. [CrossRef]
110. Luscher, D.J.; Mayer, J.R.; Mourad, H.M.; Hunter, A.; Kenamond, M.A. Coupling continuum dislocation transport with crystal plasticity for application to shock loading conditions. *Int. J. Plast.* **2016**, *76*, 11–129. [CrossRef]
111. Mayer, J.R.; Mourad, H.M.; Darby, J.L.; Abigail, H.; Kenamond, M.A. Numerical implementation of a crystal plasticity model with dislocation transport for high strain rate applications. *Model. Simul. Mater. Sci. Eng.* **2016**, *24*, 045013. [CrossRef]
112. Wulfinghoff, S.; Böhlke, T. Gradient crystal plasticity including dislocation-based work-hardening and dislocation transport. *Int. J. Plast.* **2015**, *69*, 152–169. [CrossRef]
113. Lebensohn, R.A. PoPolycrystal Plasticity Models Based on Green's Functions: Mean-Field Self-Consistent and Full-Field Fast Fourier Transform Formulations. In *Handbook of Materials Modeling*; Springer: London, UK, 2018.
114. Dadhich, R.; Alankar, A. A modular spectral solver for crystal plasticity. *Int. J. Plast.* **2022**, *156*, 103328. [CrossRef]
115. Lucarini, S.; Segurado, J. DBFFT: A displacement based FFT approach for non-linear homogenization of the mechanical behavior. *Int. J. Eng. Sci.* **2019**, *144*, 103131. [CrossRef]
116. Lucarini, S.; Segurado, J. On the accuracy of spectral solvers for micromechanics based fatigue modeling. *Comput. Mech.* **2019**, *63*, 365–382. [CrossRef]
117. Ling, C.; Forest, S.; Besson, J.; Tanguy, B.; Latourte, F. A reduced micromorphic single crystal plasticity model at finite deformations. Application to strain localization and void growth in ductile metals. *Int. J. Solids Struct.* **2018**, *134*, 43–69. [CrossRef]
118. Knezevic, M.; Savage, D.J. A high-performance computational framework for fast crystal plasticity simulations. *Comput. Mater. Sci.* **2014**, *83*, 101–106. [CrossRef]
119. Zecevic, M.; Lebensohn, A.R.; Capolungo, L. New large-strain FFT-based formulation and its application to model strain localization in nano-metallic laminates and other strongly anisotropic crystalline materials. *Mech. Mater.* **2022**, *166*, 104208. [CrossRef]
120. Admal, N.C.; Po, G.; Marian, J. Diffuse-interface polycrystal plasticity: Expressing grain boundaries as geometrically necessary dislocations. *Mater. Theory* **2017**, *1*, 6. [CrossRef]
121. Shveikin, A.I.; Trusov, P.V.; Romanov, K.A. On an Approach to Numerical Estimation of the Stability of Multilevel Constitutive Models of Materials. *Contin. Comput. Mech.* **2021**, *14*, 61–76. [CrossRef]
122. Shveikin, A.; Trusov, P.; Romanov, K. Stability of Crystal Plasticity Constitutive Models: Observations in Numerical Studies and Analytical Justification. *Metals* **2024**, *14*, 947. [CrossRef]
123. Alharbi, H.F.; Kalidindi, S.R. Crystal plasticity finite element simulations using a database of discrete Fourier transforms. *Int. J. Plast.* **2015**, *66*, 71–84. [CrossRef]
124. Bargmann, S.; Klusemann, B.; Markmann, J.; Schnabel, J.; Schneider, K.; Soyarslan, C.; Wilmers, J. Generation of 3D representative volume elements for heterogeneous materials: A review. *Prog. Mater. Sci.* **2018**, *96*, 322–384. [CrossRef]
125. Harris, W.; Chiu, W. Determining the representative volume element size for three-dimensional microstructural material characterization. Part 1: Predictive models. *J. Power Sources* **2015**, *282*, 552–561. [CrossRef]
126. Bertin, M.; Du, C.; Hoefnagels, J.P.; Hild, F. Crystal plasticity parameter identification with 3D measurements and Integrated Digital Image Correlation. *Acta Mater.* **2016**, *116*, 321–331. [CrossRef]
127. Sedighiani, K.; Diehl, M.; Traka, K.; Roters, F.; Sietsma, J.; Raabe, D. An efficient and robust way to determine material parameters of crystal plasticity constitutive laws from macro-scale stress-strain curves. *Int. J. Plast.* **2020**, *134*, 102779. [CrossRef]
128. Cantergiani, E.; Falkinger, G.; Mitsche, S.; Theissing, M.; Klitschke, S.; Roters, F. Influence of Strain Rate Sensitivity on Cube Texture Evolution in Aluminium Alloys. *Metall. Mater. Trans. A* **2022**, *53*, 2832–2860. [CrossRef]
129. Patel, M.; Paudel, Y.; Mujahid, S.; Rhee, H.; El Kadiri, H. Self-Consistent Crystal Plasticity Modeling of Slip-Twin Interactions in Mg Alloys. *Crystals* **2023**, *13*, 653. [CrossRef]
130. Mirzoev, A.A.; Gelchinski, B.R.; Rempel, A.A. Neural Network Prediction of Interatomic Interaction in Multielement Substances and High-Entropy Alloys: A Review. *Dokl. Phys. Chem.* **2022**, *504*, 51–77. [CrossRef]
131. Papaefthymiou, S.; Bouzouni, M.; Loukadakis, V. Opportunities of AI and ICME in Metals Recycling, Production and Processing. *Mater. Proc.* **2021**, *5*, 49. [CrossRef]
132. Maurizi, M.; Gao, C.; Berto, F. Predicting stress, strain and deformation fields in materials and structures with graph neural networks. *Sci. Rep.* **2022**, *12*, 21834. [CrossRef] [PubMed]
133. Frydrych, K.; Tomczak, M.; Papanikolaou, S. Crystal Plasticity Parameter Optimization in Cyclically Deformed Electrodeposited Copper—A Machine Learning Approach. *Materials* **2024**, *17*, 3397. [CrossRef]
134. Mianroodi, J.R.; Siboni, N.H.; Raabe, D. Teaching solid mechanics to artificial intelligence—A fast solver for heterogeneous materials. *NPJ Comput. Mater.* **2021**, *7*, 99. [CrossRef]
135. Frankel, A.; Tachida, K.; Jones, R. Prediction of the evolution of the stress field of polycrystals undergoing elastic-plastic deformation with a hybrid neural network model. *Mach. Learn. Sci. Technol.* **2020**, *1*, 035005. [CrossRef]

136. Ibragimova, O.; Brahme, A.; Muhammad, W.; Connolly, D.; Levesque, J.; Inal, K. A convolutional neural network based crystal plasticity finite element framework to predict localised deformation in metals. *Int. J. Plast.* **2022**, *157*, 103374. [CrossRef]
137. Saidi, P.; Pirgazi, H.; Sanjari, M.; Tamimi, S.; Mohammadi, M.; Beland, L.K.; Daymond, M.R.; Tamblyn, I. Deep learning and crystal plasticity: A preconditioning approach for accurate orientation evolution prediction. *Comput. Methods Appl. Mech. Eng.* **2022**, *389*, 114392. [CrossRef]
138. Khorrami, M.S.; Mianroodi, J.R.; Siboni, H.N.; Goyal, P.; Svendsen, B.; Benner, P.; Raabe, D. An artificial neural network for surrogate modeling of stress fields in viscoplastic polycrystalline materials. *NPJ Comput. Mater.* **2023**, *9*, 37. [CrossRef]
139. Eres-Castellanos, A.; Hidalgo, J.; Morales-Rivas, L.; Caballero, F.G.; Garcia-Mateo, C. The role of plastic strains on variant selection in ausformed bainitic microstructures studied by finite elements and crystal plasticity simulations. *J. Mater. Res. Technol.* **2021**, *13*, 1416–1430. [CrossRef]
140. Kords, C. *On the Role of Dislocation Transport in the Constitutive Description of Crystal Plasticity*; RWTH Aachen: Aachen, Germany, 2013.
141. Ganghoffer, J.; Brekelmans, W.; Geers, M. Distribution based model for the grain boundaries in polycrystalline plasticity. *Eur. J. Mech. A Solids* **2008**, *27*, 737–763. [CrossRef]
142. Ma, A.; Roters, F.; Raabe, D. A dislocation density based constitutive model for crystal-plasticity FEM including geometrically necessary dislocations. *Acta Mater.* **2006**, *54*, 2169–2179. [CrossRef]
143. Bertin, N.; Sills, R.B.; Cai, W. Frontiers in the Simulation of Dislocations. *Annu. Rev. Mater. Res.* **2020**, *50*, 437–464. [CrossRef]
144. Shanthraj, P.; Eisenlohr, P.; Diehl, M.; Roters, F. Numerical robust spectral methods for crystal plasticity simulations of heterogeneous meterials. *Int. J. Plast.* **2015**, *66*, 31–45. [CrossRef]
145. Lebensohn, R.A. N-site modeling of a 3D viscoplastic polycrystal using fast Fourier transformation. *Acta Mater.* **2001**, *49*, 2723–2737. [CrossRef]
146. Lucarini, S.; Segurado, J. An algorithm for stress and mixed control in galerkin-based fft homogenization. *Int. J. Numer. Methods Eng.* **2019**, *119*, 797–805. [CrossRef]
147. Roterz, F.; Diehl, M.; Eisenlohr, P.; Raabe, D. Crystal Plasticity Modeling. In *Microstructural Design of Advanced Engineering Materials*; Wiley-VCH: Hoboken, NJ, USA, 2013; pp. 41–67.
148. Roters, F.; Eisenlohr, P.; Kords, C.; Tjahjano, D.D.; Diehl, M.; Raabe, D. DAMASK: The Düsseldorf Advanced MAterial Simulation Kit for studying crystal plasticity using an FE based or a spectral numerical solver. *Procedia IUTAM* **2012**, *3*, 3–10. [CrossRef]
149. Eisenlohr, P.; Diehl, M.; Lebensohn, R.; Roters, F. A spectral method solution to crystal elasto-viscoplasticity at finite strains. *Int. J. Plast.* **2013**, *46*, 37–53. [CrossRef]
150. Moulinec, H.; Suquet, P. A fast numerical method for computing the linear and nonlinear mechanical properties of composites. *Mecahnics Solids—Paris Acad. Sci.* **1994**, *3218*, 1417–1423.
151. Ahrens, J.; Geveci, B.; Law, C. ParaView: An End-User Tool for Large Data Visualization. In *Visualization Handbook*; Elsevier: Amsterdam, The Netherlands, 2005.
152. Ayachit, U. *The ParaView Guide: A Parallel Visualization Application*; Kitware: Clifton Park, NY, USA, 2015.
153. Maiti, T.; Eisenlohr, P. Fourier-based spectral method solution to finite strain crystal plasticity with free surfaces. *Scr. Mater.* **2018**, *145*, 37–40. [CrossRef]
154. Diehl, M.; Niehuesbernd, J.; Bruder, E. Quantifying the Contribution of Crystallographic Texture and Grain Morphology on the Elastic and Plastic Anisotropy of bcc Steel. *Metals* **2019**, *9*, 1252. [CrossRef]
155. Mangal, A.; Holm, E.A. Applied machine learning to predict stress hotspots I: Face centered cubic materials. *Int. J. Plast.* **2018**, *111*, 122–134. [CrossRef]
156. Sedighiani, K.; Shah, V.; Traka, K.; Diehl, M.; Roters, F.; Sietsma, J.; Raabe, D. Large-deformation crystal plasticity simulation of microstructure and microtexture evolution through adaptive remeshing. *Int. J. Plast.* **2021**, *146*, 103078. [CrossRef]
157. Ortolano, J.M.; Hernandez, J.A.; Oliver, J. *A Comparative Study on Homogenization Strategies for Multi-Scale Analysis of Materials*; International Center for Numerical Methods in Engineering: Barcelona, Spain, 2013.
158. Max-Planck-Institut für Eisenforschung GmbH. DAMASK. Max-Planck-Institut für Eisenforschung GmbH, 2011–2023. [Online]. Available online: https://damask.mpie.de/index.html (accessed on 2 June 2023).
159. Yaghoobi, M.; Ganesan, S.; Sundar, S.; Lakshmanan, A.; Rudraraju, S.; Allison, J.E.; Sundararaghavan, V. PRISMS-Plasticity: An open-source crystal plasticity finite element software. *Comput. Mater. Sci.* **2019**, *169*, 109078. [CrossRef]
160. PRISMS Center, "Software," University of Michigan, [Online]. Available online: http://www.prisms-center.org/#/ctools/software (accessed on 2 June 2023).
161. Segurado, J.; Llorca, J. Simulation of the deformation of polycrystalline nanostructured Ti by computational homogenization. *Comput. Mater. Sci.* **2013**, *76*, 3–11. [CrossRef]
162. Javier, S.; Javier, L.; Sergio, L.; Aitor, C.; Sarra, H.; Vicente, H. CAPSUL. IMDEA Materiales and Universidad Politécnica de Madrid, 2012–2023. [Online]. Available online: https://materials.imdea.org/capsul/ (accessed on 2 June 2023).
163. Patra, A.; Chaudhary, S.; Pai, N.; Ramgopal, T.; Khandelwal, S.; Rao, A.; McDowell, D.L. ρ-CP: Open source dislocation density based crystal plasticity framework for simulating temperature- and strain rate-dependent deformation. *Comput. Mater. Sci.* **2023**, *224*, 112182. [CrossRef]
164. Gelebart, L. AMITEX_FFTP. Maison de la Simulation, [Online]. Available online: https://amitexfftp.github.io/AMITEX/index.html (accessed on 2 June 2023).

165. Lebensohn, R.A.; Kanjarla, A.K.; Eisenlohr, P. An elasto-viscoplastic formulation based on fast Fourier transforms for the prediction of micromechanical fields in polycrystalline materials. *Int. J. Plast.* **2012**, *32–33*, 59–69. [CrossRef]
166. Tran, A.; Wildey, T.; Lim, H. Microstructure-sensitive uncertainty quantification for crystal plasticity finite element constitutive models using stochastic collocation methods. *Frontier* **2022**, *9*, 915254. [CrossRef]
167. Eghtesad, A.; Luo, Q.; Shang, S.-L.; Lebensohn, R.A.; Knezevic, M.; Liu, Z.-K.; Beese, A.M. Machine learning-enabled identification of micromechanical stress and strain hotspots predicted via dislocation density-based crystal plasticity simulations. *Int. J. Plast.* **2023**, *166*, 103646. [CrossRef]
168. Quey, R.; Kasemer, M. The Neper/FEPX project: Free/open-source polycrystal generation, eformation simulation and post-processing. In *IOP Conference Series Materials Science and Engineering*; IOP Publishing: Bristol, UK, 2022; Volume 1249.
169. Groeber, M.A.; Jackson, M.A. DREAM.3D: A Digital Representation Environment for the Analysis of Microstructure in 3D. *Integr. Mater. Manuf. Innov.* **2014**, *3*, 56–72. [CrossRef]
170. Rycroft, C.H. Voro++: A three-dimensional Voronoi cell library in C++. *Chaos* **2009**, *19*, 041111. [CrossRef]
171. Vittorietti, M.; Kok, P.J.; Sietsma, J.; Li, W.; Jongbloed, G. General framework for testing Poisson-Voronoi assumption for real microstructures. *Appl Stoch. Models Bus Ind.* **2020**, *36*, 604–627. [CrossRef]
172. Münch, B.; Gesser, P.; Holzer, L.; Flatt, R. FIB-nanotomography of particulate systems Part II: Particle recognition and effect of boundary truncation. *J. Am. Ceram. Soc.* **2006**, *89*, 2586–2595. [CrossRef]
173. Jørgensen, P.; Hansen, K.; Larsen, R.; Bowen, J. A framework for automatic segmentation in three dimensions of microstrural tomography data. *Ultramicroscopy* **2010**, *110*, 216–218. [CrossRef]
174. Spowart, J.; Mullens, H.; Puchala, B. Collecting and analyzing microstructures in three dimensions: A fully automated approach. *JOM* **2003**, *55*, 35–37. [CrossRef]
175. Kelly, T.; Miller, M. Atom Probe Tomography. *Rev. Scient. Instrum.* **2007**, *78*, 031101. [CrossRef]
176. Bostanabad, R.; Zhang, Y.; Li, X.; Kearney, T.; Brinson, L.C.; Apley, D.W.; Liu, W.K.; Chen, W. Computational microstructure characterization and reconstruction: Review of the state-of-the-art techniques. *Prog. Mater. Sci.* **2018**, *95*, 1–41. [CrossRef]
177. Chatterjee, K.; Echlin, M.; Kasemer, M.; Callahan, P.; Pollock, T.; Dawson, P. Prediction of tensile stiffness and strength of Ti-6Al-4V using instantiated volume elements and crystal plasticity. *Acta Mater.* **2018**, *157*, 21–32. [CrossRef]
178. Gallardo-Basile, F.-J.; Naunheim, Y.; Roters, F.; Diehl, M. Lath Martensite Microstructure Modeling: A High-Resolution Crystal Plasticity Simulation Study. *Materials* **2021**, *14*, 691. [CrossRef]
179. Tseng, S.; Qayyum, F.; Guk, S.; Chao, C.; Prahl, U. Transformation of 2D RVE Local Stress and Strain Dstributions to 3D Observations in Full Phase Crystal Plasticity Simulations of Dual-Phase Steels. *Crystals* **2022**, *12*, 955. [CrossRef]
180. Ramazani, A.; Mukherjee, K.; Quade, H.; Prahl, U.; Bleck, W. Correlation between 2D and 3D flow curve modelling of DP steels using a microstructure-based RVE approach. *Mater. Sci. Eng. A* **2013**, *560*, 129–139. [CrossRef]
181. Qayyum, F.; Chaudhry, A.A.; Guk, S.; Schmidtchen, M.; Kawalla, R.; Prahl, U. Effect of 3D Representative Volume Element (RVE) Thickness on Stress and Strain Partitioning in Crystal Plasticity Simulations of Multi-Phase Materials. *Crystals* **2020**, *10*, 944. [CrossRef]
182. Mirhosseini, S.; Perdahcioglu, E.S.; Atzema, E.H.; van den Boogard, A.H. Response of 2D and 3D crystal plasticity models subjected to plane strain condition. *Mech. Res. Commun.* **2023**, *128*, 104047. [CrossRef]
183. Tian, X.-Y.; Zhang, H.-L.; Nong, Z.-S.; Cui, X.; Gu, Z.-H.; Liu, T.; Li, H.-M.; Arzikulov, E. Effect of Alloying on Microstructure and Mechanical Properties of AlCoCrFeNi2.1 Eutectic High-Entropy Alloy. *Materials* **2024**, *17*, 4471. [CrossRef] [PubMed]
184. Liu, Y.; Zhang, Q.; Ge, Q.; Wang, X.; Shen, Y. Improving Texture Prediction by Increasing Mesh Resolution in Submodel: A Crystal Plasticity FE Study and Experiment Verification. *Crystals* **2023**, *13*, 849. [CrossRef]
185. Frydrych, K.; Papanikolaou, S. Unambiguous Identification of Crystal Plasticity Parameters from Spherical Indentation. *Crystals* **2022**, *12*, 1341. [CrossRef]
186. Volin, T.E.; Balluffi, R.W. Annealing Kinetics of Voids and the Self-Diffusion Coefficient in Aluminum. *Phys. Stat. Sol.* **1986**, *25*, 163–173. [CrossRef]
187. Cantergiani, E.; Falkinger, G.; Roters, F. Crystal plasticity simulations of Cube in-grain fragmentation in aluminium: Influence of crystal neighbor orientation. *Int. J. Solids Struct.* **2022**, *252*, 111801. [CrossRef]
188. El Shawish, S.; Cizelj, L. Combining Single- and Poly- Crystalline Measurements for Identification of Crystal Plasticity Parameters: Application to Austenitic Stainless Steel. *Crystals* **2017**, *7*, 181. [CrossRef]
189. Zheng, X.; Kong, Y.; Chang, T.; Liao, X.; Ma, Y.; Du, Y. High-Throughput Computing Assisted by Knowledge Graph to Study the Correlation between Microstructure and Mechanical Properties of 6XXX Aluminum Alloy. *Materials* **2022**, *15*, 5296. [CrossRef]
190. Wang, S.; Zhu, Z.; Starink, M. Estimation of dislocation densities in cold rolled Al-Mg-Cu-Mn alloys by combination of yield strength data, EBSD and strength models. *J. Microsc.* **2005**, *217*, 174–178. [CrossRef]
191. Luan, Q.; Lee, J.; Zheng, J.H.; Hopper, C.; Jiang, J. Combining microstructural characterization with crystal plasticity and phase-field modelling for the study of static recrystallization in pure aluminium. *Comput. Mater. Sci.* **2020**, *173*, 109419. [CrossRef]
192. Wu, R.; Zhao, Y.; Yin, Q.; Wang, J.; Ai, X.; Wen, Z. Atomistic simulation studies of Ni-based superalloys. *J. Alloys Compd.* **2021**, *855*, 157355. [CrossRef]
193. Rodney, D.; Ventelon, L.; Clouet, E.; Pizzagalli, L.; Willaime, F. Ab initio modeling of dislocation core properties in metals and semicondactors. *Acta Mater.* **2017**, *124*, 633–659. [CrossRef]

194. Gallardo, F.; Roters, F.; Jentner, R.M.; Srivastava, K.; Scholl, S.; Diehl, M. Modeling Bainite Dual-Phase Steels: A High-Resolution Crystal Plasticity Simulation Study. *Crystals* **2023**, *13*, 673. [CrossRef]
195. Li, J.; Li, Y.; Suo, T.; Wei, Q. Numerical simulations of adiabatic shear localization in textured FCC metal based on crystal plasticity finite element method. *Mater. Sci. Eng. A* **2018**, *737*, 348–363. [CrossRef]
196. Chen, B.; Hamada, S.; Li, W.; Noguchi, H. Crystal plasticity FEM study of material and mechanical effects on damage accumulation mode of fatigue crack propagation. *Int. J. Fatigue* **2023**, *173*, 107683. [CrossRef]
197. Anderson, P.M.; Hirth, J.P.; Lothe, J. *Theory of Dislocations*, 3rd ed. Cambridge University Press: Cambridge, UK, 2017.
198. Trusov, P.; Kondratev, N.; Podsedertsev, A. Description of Dynamic Recrystallization be Means of An Advanced Statistical Multilevel Model: Grain Stracture Evolution Analysis. *Crystals* **2022**, *12*, 653. [CrossRef]
199. Roters, F. *Advaned Material Models for the Crystal Plasticity Finite Element Method*; RWTH Aachen: Aachen, Germany, 2011.
200. Queyreau, S. On the Saturation Stress of Deformed Metalsl; HAL Open Science, No. hal-03916664. 2022. Available online: https://hal.science/hal-03916664v1/file/on_the_saturation_stress_of_deformed_metals.pdf (accessed on 2 June 2023).
201. Rezaei, M.J.; Sedighi, M.; Pourbashiri, M. Developing a new method to represent the low and high angle grain boundaries by using multi-scale modeling of crystal plasticity. *J. Alloys Compd.* **2023**, *939*, 168844. [CrossRef]
202. Ta, N.; Bilal, M.U.; Hausler, I.; Saxena, A.; Lin, Y.-Y.; Schleifer, F.; Fleck, M.; Glatzel, B.; Kamachali, R.D. Simulation of the θ' Precipitation Process with Interfacial Anisotropy Effects in Al-Cu Alloys. *Materials* **2021**, *14*, 1280. [CrossRef]
203. Alankar, A.; Mastorakos, I.N.; Field, D.P. A dislocation-density-based 3D crystal plasticity model for pure aluminum. *Acta Mater.* **2009**, *57*, 5936–5946. [CrossRef]
204. Bulut, O.; Acar, S.S.; Yalcinkaya, T. The influence of thickness/grain size ratio in microforming through crystal plasticity. *Procedia Struct. Integr.* **2022**, *35*, 228–236. [CrossRef]
205. Pai, N.; Prakash, A.; Samajdar, I.; Patra, A. Study of grain boundary orientation gradients through combined experiments and strain gradient crystal plasticity modeling. *Int. J. Plast.* **2022**, *156*, 103360. [CrossRef]

crystals

MDPI

Review

Antibacterial Pure Magnesium and Magnesium Alloys for Biomedical Materials—A Review

Qingfeng Song [1], Lingzhi Yang [1], Fang Yi [2,3,*], Chao Chen [4], Jing Guo [2], Zihua Qi [2] and Yihan Song [2]

[1] School of Minerals Processing and Bioengineering, Central South University, Changsha 410083, China; 245612087@csu.edu.cn (Q.S.); yanglingzhi@csu.edu.cn (L.Y.)
[2] Xiangya School of Stomatology, Central South University, Changsha 410008, China; 8302220120@csu.edu.cn (J.G.); qizihua0922@163.com (Z.Q.); syh030104@163.com (Y.S.)
[3] Hunan Xiangya Stomatological Hospital, Central South University, Changsha 410008, China
[4] College of Materials Science and Engineering, Taiyuan University of Technology, Taiyuan 030024, China; chenchao@tyut.edu.cn
* Correspondence: yifangcsu@163.com

Abstract: Implant-related infections are one of the major challenges faced by orthopedic surgeries. Developing implants with inherent antibacterial properties is an effective strategy to address this issue. Biodegradable magnesium and magnesium alloys have become a research hotspot due to their good bioactivity, mechanical properties, biocompatibility, and excellent antibacterial ability. However, magnesium and its alloys have rapid corrosion, and the difficulty in expelling harmful magnesium ions and hydrogen gas produced by degradation from the body. This review summarizes the mainstream surface modification techniques such as laser surface modification, friction stir processing, and micro-arc oxidation, along with their impact on the antimicrobial properties of magnesium-based materials. This paper reviews the latest research progress on improving the antibacterial properties of magnesium alloys through alloying and introduces the antibacterial effects of mainstream magnesium alloys and also elaborates on the antibacterial mechanism of magnesium alloy materials. It is expected to provide more basis and insights for the design of biodegradable magnesium alloys with antibacterial properties, thereby promoting their development and clinical application.

Keywords: antibacterial property; magnesium alloys; biodegradable magnesium material; surface modifications; biomedical implants

1. Introduction

Biomaterials are materials used to diagnose, treat, repair, or replace tissues and organs of the body or to enhance their functions [1]. In contrast, bio-implantable materials are used for implantation into the human body. They interact with human biological +tissues and have strong biocompatibility. Bio-implantable materials have specialized roles in the body and can repair and replace damaged tissues and organs. Bone healing sparked the development of bio-implantable materials. People implanted materials to heal shattered bones. Antimicrobial properties and biocompatibility of bio-implantable materials are two important factors [2].

Initially, non-biodegradable implant materials such as iron and copper were chosen. After bone healing, these materials must be surgically removed. The patient's cost and risk increase with this second procedure. These compounds also inflame neighboring tissues upon implantation. People must use antibiotics to manage inflammation to prevent bacteria from causing significant injury. This may lead to bacterial resistance and, in severe cases, may even require surgery to eliminate the inflammation. These issues restricted implantable material use. To address these issues, the researchers propose a new strategy that uses a drug delivery system based on porous alloys and oxide nanotubes. These

systems can be filled with antibiotics to prevent inflammation from occurring. In the design of drug delivery systems, the application of porous nanomaterials such as porous silicon nanoparticles (pSiNPs) and mesoporous silica nanoparticles (MSNs) is also progressing. These materials could be designed as smart drug delivery systems to control drug release and reduce reliance on antibiotics [3]. Degradable implants are a better alternative to non-degradable implants. By modifying the surface and incorporating antibacterial metal elements, they can also achieve an antibacterial effect, reducing reliance on antibiotics, which is currently a hot topic of research.

Degradable implant materials can degrade independently after some time in the body. The degradation products are eliminated from the body via the kidneys, avoiding the surgical risks associated with the secondary surgical removal of traditional implanted materials [4,5] and the possibility of secondary infections. This reduces the patient's risk of new complications, which aids recovery and lowers costs. Magnesium metal is one of nature's most abundantly stored elements, with numerous sources and low prices. Magnesium alloy has excellent mechanical properties and good biocompatibility as a degradable material. And magnesium is one of the essential nutrients in the human body, participating in various metabolic processes. Therefore, magnesium-based materials are promising metal materials in the field of biomedicine.

The breakdown rate of degradable implant materials is crucial. The rate of deterioration should mirror the rate of tissue repair. It should not be too rapid to prevent function loss before completing its supportive task. And it shouldn't be too sluggish to inhibit tissue growth and healing or induce localized inflammation. Controlling the complete deterioration period of the implanted material is also necessary. Handling degradation time suits different applications. The implanted material must be mechanically robust and biocompatible. The implant also needs to be bacteria-resistant. The body can easily absorb and eliminate its breakdown products. Currently, there are specific issues with using magnesium as an implant material. In vivo, degradation is speedy [6–9], rapidly weakening mechanical characteristics. In vivo study in male Sprague-Dawley® rats showed that the degradation rate of pure Mg was initially 0.4 mm/year and was less than 0.2 mm/year at week 4 and week 12. In vitro experiments showed that when the material was placed in Dulbecco's modified eagle's medium (DMEM) supplemented with 10% fetal bovine serum (FBS), the degradation rate of pure magnesium was 0.75 ± 0.45 mm/year in the first week, and significantly decreased to 0.32 ± 0.04 mm/year after four weeks [10]. When magnesium is in the body, the antibacterial ability was weakened and reduced [11]. And the degradation process produces hydrogen accumulation in the tissue affecting tissue healing [12]. Surface alteration and alloying can fix these issues [13]. The surface modification method delays magnesium corrosion and ensures complete operation. Some specific elements can also be added in the modification process to give the implant material other unique properties [14]. Alloying is one of the known methods for improving the corrosion resistance of magnesium alloys. Various aspects of the properties of magnesium alloys can be enhanced by adding different alloying compositions. Alloying is a research priority in the biomedical field. The article describes surface modification methods, including laser surface modification technology, micro-arc oxidation (MAO), hydrothermal method, layer-by-layer assembly (LBL), electrophoretic deposition, and chemical conversion. And the article explains the principle of surface modification to enhance material properties, discussing the different antimicrobial effects of different coatings and other property improvements. Alloying can alter material characteristics and structure. Magnesium alloy characteristics depend on the elements used [15,16]. Silver, zinc, copper, tin, iron, and gallium are common antimicrobials [17,18]. As shown in Figure 1, this article begins with an overview of the basic knowledge of magnesium alloys as biomaterials, and then delves into a discussion of their advantages and disadvantages. Next, the interaction between magnesium alloys and bacteria is analyzed, which is key to understanding their biocompatibility and potential antibacterial performance. Subsequently, the specific antibacterial effects of two commonly used methods to enhance antibacterial performance (surface mod-

ification techniques and alloying) are introduced, and finally, the antibacterial mechanisms of magnesium-based materials are explored.

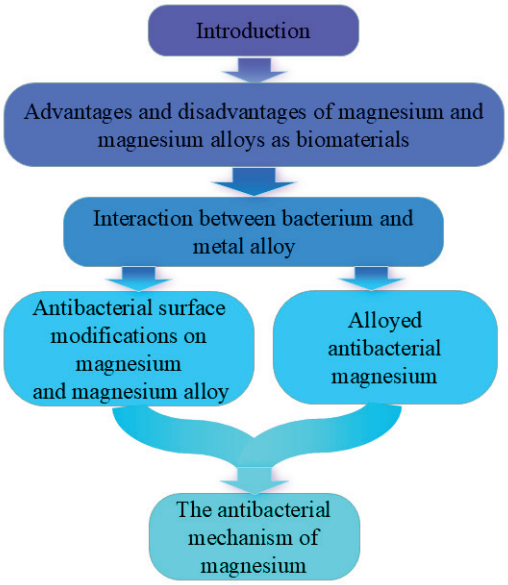

Figure 1. Introduction diagram of the article content.

2. Advantages and Disadvantages of Magnesium and Magnesium Alloys as Biomaterials

2.1. Advantages of Magnesium and Magnesium Alloys as Bioimplant Materials

For a long time, there has been extensive research on biodegradable implant materials, and magnesium and magnesium alloys have stood out among many biological implant materials due to their excellent biocompatibility, similarity to human bones, and the ability to promote osteogenesis.

The mechanical properties of magnesium are superior to those of other implant materials. Magnesium has mechanical properties similar to those of human bones, which gives it a natural advantage over traditional inert biological implant materials [19]. Magnesium has a natural advantage over traditional inert bio-implantable materials. Magnesium has a density of 1.74 g/cm^3, similar to human bone (1.75 g/cm^3) [7]. Magnesium's Young's modulus is akin to that of the human body. It can obviously avoid the stress shielding effect in the replacement of hip joint, knee joint and some fracture fixation devices. However, other conventional implant materials are difficult to avoid stress shielding directly. For example, titanium metal's modulus of elasticity (106.4 GPa) is much higher than human bone. To solve the problem of excessive mismatch between the modulus of elasticity of titanium implants and the modulus of elasticity of human bone, titanium has been made into a porous material [20]. This strategy eliminated the elastic modulus mismatch-induced stress shielding effect. However, the surface area increases after the cloth is absorbent, which significantly increases the cost of titanium surface modification. Porous titanium fabrication is complicated and difficult to mass produce. The density of stainless steel is 7.86 g/cm^3 and the elastic modulus is 110 GPa, which is also much larger than the human bone and difficult to match [12,21]. Magnesium and magnesium alloys do not have this problem, as shown in Table 1, and the mechanical properties of magnesium and magnesium alloys are a good match for bone. The density of magnesium alloys is basically controlled at 1–2 g/cm^3, and the elastic modulus is about 40 GPa [22–24], which is relatively close to the elastic modulus of human bone at 30 GPa [25]. Its low elastic -modulus can effectively reduce the stress-shielding effect of implants in the body. This makes Mg-based materials have obvious advantages in mechanical properties for some hard tissue replacements in vivo.

Magnesium has innate good biocompatibility. Magnesium is one of the nutrients required for the human body to function correctly and is involved in various metabolic

processes. Magnesium is essential for the normal physiological functioning of many tissues and organs, particularly the heart, brain, muscles, and skeletal system. And Magnesium is synthesized and associated with nucleic acids and more than thirty enzymes in the human body. Human serum magnesium ranges from 0.75–0.95 mmol/L [26]. The body fluid can destroy magnesium-based implants. Some of the magnesium is absorbed into the body, while excess is eliminated through the body's metabolic processes. Magnesium in the body also has a diastolic effect on coronary vessels [27].

Furthermore, magnesium promotes osteogenesis. Magnesium can enhance osteogenesis in the human body in at least two ways, and Nie et al. [28] reviewed and explained the mechanism of magnesium-based materials to promote osteogenesis. One method is that magnesium ions can activate the MAPK/ERK signaling pathway in vivo, which promotes bone growth, as shown in Figure 2 [29]. This signaling pathway can regulate bone development and metabolic processes of bone. The other is that magnesium ions enhance osteogenesis by modulating Wnt/β-Catenin, as shown in Figure 2 [29]. The regulating method is that magnesium ions induce the phosphorylation of GSK3 to impede GSK3 binding to β-Catenin, increasing the content level of β-Catenin. And it stimulates β-Catenin to form new bone and expedite skeletal healing.

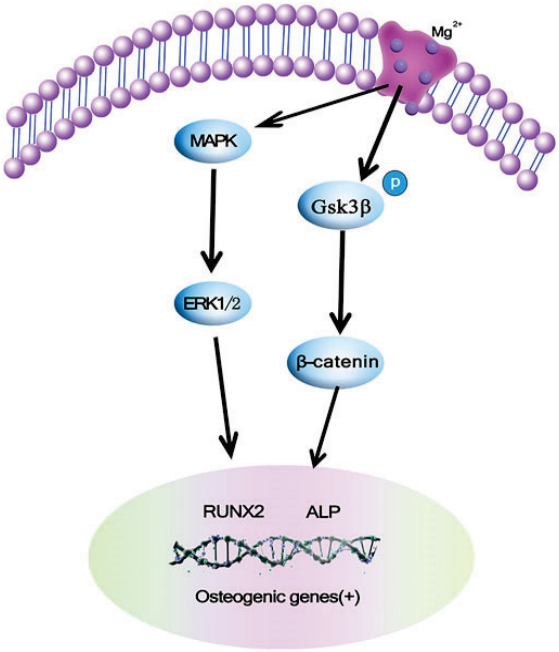

Figure 2. Schematic diagram of magnesium promoting osteogenesis [29].

Table 1. Performance parameters of bone and various implant materials (Partial reference [30]).

Sample	Density g/cm^3	Modulus of Elasticity GPa	Yield Strength (MPa)	Fracture Toughness (MPam1/2)	Corrosion Rate	Reference
Cortical bone	1.75	3–30	130–180	3–6	N/A	[7,12,21,25,31]
Pure magnesium	1.74–2.00	41–45	60–100	15–40	0.2–0.4 mm/year	[10,12,21,25]
Titanium alloy	4.4–4.5	110–117	758–1117	55–115	N/A	[12]
Ti6Al4V	4.51	110	900	N/A	Passivation, Corrosion potential −254 mV	[25,32–35]
AZ91	1.81	45	160	N/A	3.6–4.11 mm/year	[22,23,36]
WE43	1.84	44	170	N/A	5.04–6.19 mm/year	[23,37]
Mg-6Zn	N/A	42.3	169.5	N/A	2.32 ± 0.11 mm/year	[24]
Stainless steel	7.86	110	170–310	50–200	Corrosion resistant	[12,21,38]

2.2. Current Problems with Magnesium and Magnesium Alloys

Magnesium and magnesium alloys, as biomaterials for implants, still have certain issues. The main problems at present include the excessively fast corrosion rate of magnesium-based implant materials in the body, the increase in surrounding environmental alkalinity due to the production of hydroxide ions during the degradation process, and the corrosion process produces a large amount of magnesium ions and hydrogen gas, causing adverse reactions.

Magnesium's high breakdown rate in the body is an issue [19]. The corrosion degradation rate of magnesium-based implants is higher than the rate of human bone development and healing, and this causes the magnesium-based substance to degrade before the bone is supportive, losing its tissue-supporting and cell-adsorbing properties [39].

The corrosion of magnesium will increase the alkalinity of the surrounding environment. In living organisms, the corrosion of magnesium or magnesium alloys releases hydroxide ions, which raise the pH of the surroundings. Magnesium is degraded and corroded vivo via the reaction $Mg + 2H_2O = Mg(OH)_2 + H_2$. Wang et al. [20] found that soaking titanium-magnesium (Ti6Al4V-Mg) alloys in saline for two days produced enough hydroxide ions to elevate the ambient pH above 10. The high pH would surely be a significant issue for the organism. It also increases the alkalinity of the surrounding environment in the body, but much more gently than outside the body, and the body neutralizes alkaline substances produced by degradation [11]. However, it is also faced with the problem of insufficient antibacterial effect, because the antibacterial effect of magnesium mainly depends on the increase of alkalinity in the environment to kill bacteria. If the alkalinity in the body environment is not high enough, the bactericidal effect may also be affected.

At the same time, there are many magnesium ions accompanied by hydroxide ions produced. Although the human body contains a certain amount of magnesium ions, if the magnesium ion content is too high, it will cause hypermagnesemia, magnesium toxicity, and other adverse reactions. In addition to producing enormous volumes of alkaline material and magnesium ions, the corrosion process of magnesium also has hydrogen gas. One mole of magnesium creates around 22.4 L of hydrogen gas. If hydrogen generation exceeds tissue cell absorption, hydrogen will clear the implant. The collected hydrogen will also diffuse into softer and looser tissues to generate air pockets, which can interfere with wound repair and exacerbate the patient's sensation of foreign body experience. Although such cavities can be released through puncture, this is impossible in all cases. For example, in some in vivo vascular procedures, using a prick to alleviate the problem of gas cavities is not ideal [40].

3. Interaction Between Bacterium and Metal Alloy

3.1. The Role of Bacteria and Implant Materials

The antimicrobial properties of bioimplants are critical, and the ability to prevent bacterial growth and spread is essential because they significantly reduce the risk of inflammation and infection, thereby ensuring the success of the implant procedure and patient safety, as well as protecting patients from potential complications. Especially magnesium as an implant material for already infected bone tissue, such as infectious osteomyelitis, contaminated fracture wounds, etc., has obvious advantages. The antibacterial properties of magnesium-based implant materials can effectively prevent further infection and inflammation.

Biomaterials and microorganisms interact complexly. When bacteria encounter the surface of a biomaterial and begin to proliferate, two significant processes occur. The first process is the attachment of bacteria to the surface of biomaterials by some physicochemical effects or specific structures on the bacterial surface [41], which permanently change the surface's structural characteristics and physicochemical properties through their own secreted metabolites [42]. The second process is that the bacterial community produces macromolecular exopolymers on the biomaterial's surface. The macromolecular exopolymers form a biofilm to protect its structure, provide a better habitat for bacterial

development and resist external drug effects [43]. Finally, the bacteria begin to proliferate on the surface of the material.

There are two kinds of interactions between bacteria and materials. The first type is the interaction of microorganisms with metal ions in the environment. The implanted material keeps a higher concentration of metal ions in the surrounding environment. Bacteria will interact with metal ions before touching the bioimplant material [44–46]. The second type of interaction is between the bacteria and the surface of the implant material. After contacting biological material, bacteria will interact with the surface [47,48].

The interaction between alloys and bacteria is mutual; nearly half of the biochemical reactions within bacteria are catalyzed by enzymes containing metal ions. Bacteria need to maintain metal ions at an appropriate concentration to meet their normal physiological needs. Some metal ions themselves possess antibacterial properties. In a liquid environment, the surface of the alloy is constantly eroded by bacteria, causing changes in the surface structure of the alloy and producing metal ions, which in turn kill the bacteria [15,16,49–51]. At the same time, the alloy will also resist bacteria, and the strength of its antibacterial ability depends on the alloying ingredients.

3.2. The Performance of Some Mainstream Antibacterial Metals

The antimicrobial strength of bio-implantable materials depends on their type, concentration, and degradation rate in the body. The type and content of the elements in the material affect these factors. At present, many elements have antibacterial effects, including silver, aluminum, arsenic, cadmium, cobalt, chromium, copper, iron, gallium, mercury, molybdenum, manganese, nickel, lead, antimony, and zinc [17,18,52]. Among them, silver, copper, and zinc are common antibacterial implant materials. By degradation in the body and creating metal ions, these materials compounds are potent, broad-spectrum antimicrobials. The specific antimicrobial concentrations of these metals have been collated in Table 2.

Table 2. Antimicrobial properties of metal elements.

Element	Antibacterial Substances	Minimum Inhibitory Concentration (μM)	Reference
Silver	Silver ion	<1	[53,54]
Copper	Copper ion	12	[55]
Zinc	Activated oxygen	156	[56]

Magnesium also has certain antibacterial properties, but the antibacterial performance of magnesium alone as an implant material is limited. An in vitro antibacterial experiment was conducted using the spread plate method to evaluate the antibacterial rates of planktonic bacteria in culture dishes and adherent bacteria on samples. The tested bacterial species included *Escherichia coli*, *Staphylococcus epidermidis*, and *Staphylococcus aureus*. The results showed that pure magnesium has a certain antibacterial ability. On the first and third days of the test, the antibacterial effects on planktonic *E. coli* were 59.9% and 77.6%, on planktonic *S. epidermidis* were 50.8% and 72.4%, and on planktonic S. aureus were 50.3% and 70.1%. The antibacterial effects on adherent *E. coli* were 70.5% and 88.8%, on adherent *S. epidermidis* were 63.8% and 83.0%, and on adherent *S. aureus* were 65.2% and 81.4%. It can be seen that in the case of magnesium alone for antibacterial action, it has a certain inhibitory ability against adherent bacteria, with an antibacterial rate reaching 60–88%, while the antibacterial ability against planktonic bacteria is weaker, with an antibacterial rate of only 50–70% [57]. Based on the different antibacterial rates of magnesium against planktonic and adherent bacteria, the antibacterial action of magnesium mainly occurs on the material surface, belonging to the second type of interaction, whereas the antibacterial effect produced by the first type of interaction is relatively weaker.

Antimicrobial silver is fantastic. It inhibits most bacteria, fungi, and viruses. Its efficient bactericidal action renders medical surgical instruments and other items antibacterial.

Today, silver is used as an antibacterial substance in surface-modified devices rather than silver-made devices [42]. For example, Catalano et al., Aleksandrova et al., and Tiller sought to employ silver nano-ions to produce antimicrobial film coatings [58–60]. McQuillan et al. [61] found that reactive oxygen species from silver influence cell membrane function, thereby achieving antibacterial effects.

Copper degradation generates reactive oxygen species and copper ions [62]. Salah et al. [63] found that under the action of reactive oxygen species and the increasing concentration of copper ions, the bacterial membrane is severely damaged by reactive oxygen. Subsequently, copper ions and the reactive oxygen they release cause bacterial death. The DNA inside the bacteria is also destroyed as copper ions enter the cells [64].

Zinc has a medium antibacterial action. Zinc inhibits bacterial activity but does not kill bacteria [65]. Gudkov et al., Li et al., and Sirelkhatim et al. [66–68] showed that zinc oxide-based compounds are more effective at killing microbes. Especially after being made into nano-zinc oxide, the antibacterial ability is stronger.

4. Antibacterial Surface Modifications on Magnesium and Magnesium Alloy

Magnesium alloys have been shown to have the ability to promote osteogenesis and effectively avoid the stress masking effect. Because of its biodegradable properties and biocompatibility, it has a promising future in human implantable biomaterials. However, the excessive corrosion rate of magnesium alloys in vivo has always affected their application. Many factors are related to magnesium corrosion rate and biocompatibility, such as the proportion of alloying, the primary type of alloying, the technology of processing methods [69], the surface modification of magnesium alloys [70], and so on. Surface modification techniques for magnesium alloys are one of the finest solutions for improving the problem of excessive corrosion rate of magnesium alloys in vivo [70–74]. There are numerous surface modification techniques for reducing the corrosion rate of magnesium alloys. This paper focuses on several surface modification techniques for increasing antimicrobial properties, such as laser surface modification [75,76], friction stir processing (FSP) [77,78], micro-arc oxidation (MAO) method, hydrothermal method, layer-by-layer assembly (LBL) technique, electrophoretic deposition method, chemical conversion method, and sol-gel method. Representative methods are listed in Table 3. This table details the class of substrate material to which the coating is attached, the coating reference material and the antibacterial properties of the coating.

Table 3. Surface modification methods and their effects.

Method	Subject	Mixed Substances	Antimicrobial Properties	Reference
Laser surface modification	MA8 (Mg-Mn-Ce)	Nothing (superhydrophilic) or fluorosilane (superhydrophobic)	After 48 h, treated superhydrophilic samples showed a bacterial titer of 10^{-8} for both *Pseudomonas aeruginosa* and *Klebsiella pneumoniae*, with a clear antibacterial effect.	[79]
Friction stir processing	AZ91-D (Mg-9Al-1Zn)	HAP (Hydroxyapatite)	AZ91-D Mg alloy surface treated to prepare nanoscale hydroxyphosphate lime composites. Better antimicrobial properties against *Staphylococcus aureus*, *Candida albicans*, and *Aspergillus fumigatus*.	[80]
Micro-arc oxidation method	Mg-2Zn-1Gd-0.5Zr alloy	Cu	Copper ion release gives the material an antimicrobial rate of up to 96% (*S. aureus*).	[81]
	Mg-3Zn-0.5Sr alloy	Ag	Strong antimicrobial properties against *E. coli*	[82]
	AZ31 (Mg-3Al-1Zn)	TA (Tannic acid)	There were 147 CFUs of *E. coli* in the untreated alloy sample dish, while there were only 10 CFUs in the TA-coated alloy sample dish	[83]
	AZ91 (Mg-9Al-1Zn)	Ag	In the inhibition zone test of *Staphylococcus aureus*, it was found that the inhibition zone diameter of the Ag coated sample was 40 mm, and the inhibition zone of the non-Ag coated sample was 15 mm	[84]
Hydrothermal method	$Mg_{68}Zn_{28}Ca_4$(at%)	HA/ZnO (Nano-hydroxyapatite/ZnO)	In the antibacterial experiments against *Staphylococcus aureus* and *Escherichia coli*, the plate counting method was used, and the samples with HA/ZnO coating achieved an antibacterial rate of 100%.	[85]

Table 3. *Cont.*

Method	Subject	Mixed Substances	Antimicrobial Properties	Reference
Layer-by-layer assembly technology	APTMS/Mg ((3-aminopropyl)trimethoxysilane/Mg)	AgNPs	Samples coated with AgNPs on agar plates at 37 °C showed an inhibition zone diameter of 22.10 mm against *E. coli*, which is larger than the inhibition zone diameter of uncoated samples (14.86 mm).	[86]
	AZ31(Mg-3Al-1Zn)	AgNPs/PMTMS	The antimicrobial efficacy of $(AgNPs/PEI)_5$ multilayer film and $PMTMS/(AgNPs/PEI)_5$ film against S. aureus was 98.40% and 85.00%, respectively	[87]
Electrophoretic deposition method	TiO_2/MgO	Ag-Zeo-Hap (Ag-zeolite-hydroxyapatite)	The inhibition zone of the Ag-Zeo-Hap coating against *E. coli* is 3.86 mm, and the number of *E. coli* colonies in the petri dish decreased by 94%.	[88]
Chemical conversion method	AZ31B (Mg-3Al-1Zn)	$MgO-MgF_2$	Through the *E. coli* antibacterial experiment, the antibacterial rate of the alloy samples with fluoride coating reached 99.99% after 24 h.	[89]
Sol-gel method	Mg	$Mg(OH)_2$	After 30 h of sol-gel treatment, the inhibition ability of the samples against Enterobacteriaceae was significantly enhanced compared with the hydrothermal treatment materials, and the optical density of *E. coli* at 600 nm was between 0.2 and 0.3.	[90]

4.1. Laser Surface Modification

Laser surface modification technology uses a high-energy laser to treat the surface of magnesium alloy. Make the melting-solidification process happen to modify the microstructure. Laser treatment changes the surface properties of magnesium alloy. Varying the intensity and speed of the laser can obtain different forms of microstructure and surface properties. As shown in Figure 3 [91]. Emelyanenko et al. [79] used a surface laser to process the MA8 magnesium alloy. He chose *Pseudomonas aeruginosa* and *Klebsiella pneumoniae* for the antimicrobial experiments. After comparative experiments, the highly hydrophilic alloy with laser processing performed better against *Pseudomonas aeruginosa* than the MA8 standard polishing alloy. After 48 h, the antibacterial performance peaking, and the antimicrobial effect is more than 60% stronger than the original alloy. The treated material was a bit more antibacterial against *Klebsiella pneumoniae* than polishing.

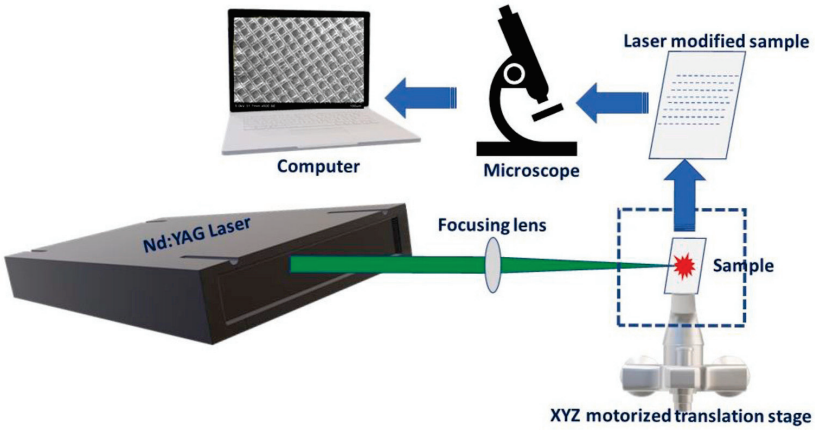

Figure 3. Laser surface modification technology [91].

4.2. Friction Stir Processing

Friction stir processing technology is derived from friction stir welding technology. Rotating the cylindrical head at high speed violently rubbed and exothermic the material surface, causing substantial plastic deformation. The surface microstructure is homogenized, refined, and densified [77]. The specific formation process is shown in Figure 4 [92]. Nasiri et al. [93] observed that homogenized dispersed particles strengthen brittle alloy components and improve magnesium alloy tensile characteristics. This method is useful for coating the surface of magnesium alloys. Kundu et al. [80] used friction-stirring composite coating on the surface of AZ91-D magnesium alloy to create hydroxyapatite

surface composites. Using *Staphylococcus aureus*, *Candida albicans*, and *Aspergillus fumigatus* as experimental strains, the material's antibacterial performance was more than three times that of the raw material. Even rubbing and stirring the material does not prepare HA composite layer. Antibacterial activity against various experimental bacteria rose by 60–90% after treatment.

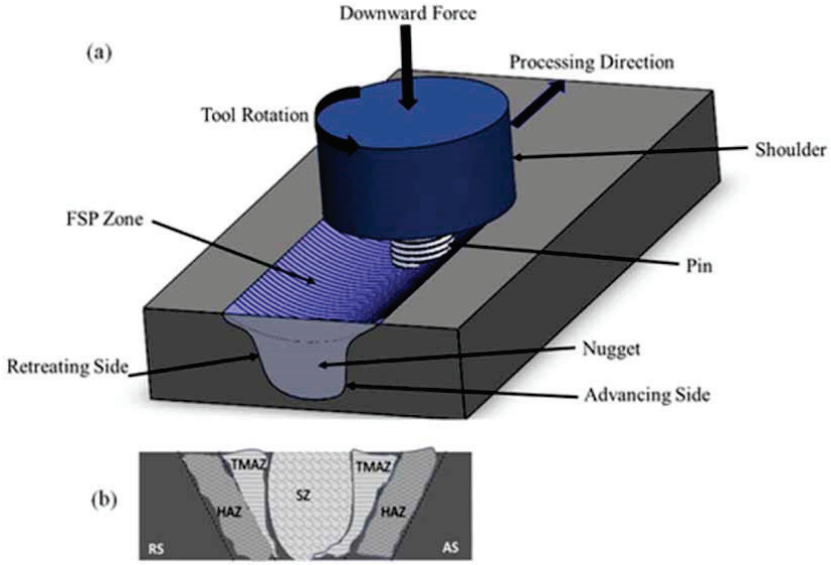

Figure 4. Schematic of (**a**) FSP and (**b**) transverse cross section view of FSPed region [92].

4.3. Micro-Arc Oxidation Method

The main principle of surface modification of micro-arc oxidation is that the metal surface grows a ceramic film layer with matrix metal oxide and electrolyte compounds as the main components under the action of instantaneous high temperature and high pressure produced by arc discharge. Figure 5 depicts the formation process of the coating, with the yellow part indicating the molten oxide, the red area denoting the reaction zone, and the green part showing the oxide after cooling and solidification [94]. Ceramic micro-arc oxidation (MAO) coating adheres well to magnesium alloys. Its surface has a distinctive porous morphology [95]. Due to their microporous topology, MAO coatings can combine more closely with other materials. And this allows the micro-arc oxide coating to be used as a base coating. Different surface-modified materials can comprise to the surface of the micro-arc oxide coating. The participation of silver, zinc, and copper elements can create antibacterial coatings. It's important to note that too much metal can harm human cells [96]. Chen et al. [81] used MAO technology to fabricate a coating containing copper on the surface of magnesium alloys. The coating was found to have good corrosion resistance, with a corrosion rate of 0.16 mm/y after two weeks. At the same time, the release of copper ions in the coating also inhibited the proliferation of bacteria, and the antibacterial rate against *Staphylococcus aureus* reached 96% after 12 h of culture. Cui et al. [83] found that adding tannic acid (TA) to MAO coating reduces micropore size and microcracks. MAO-TA coatings are thicker than MAO coatings, and TA-magnesium complexes can slow magnesium alloy corrosion. In in vitro antimicrobial testing, the TA-MAO coating increased antimicrobial ability. Silver is often added to MAO coatings to boost their antibacterial properties. Sukuroglu et al. and Chen et al. [82,84] incorporated silver into the MAO coating. In the *Staphylococcus aureus* test and the antimicrobial test for *E. coli*, almost no bacteria survive on the silver-coated surface, showing strong antimicrobial ability.

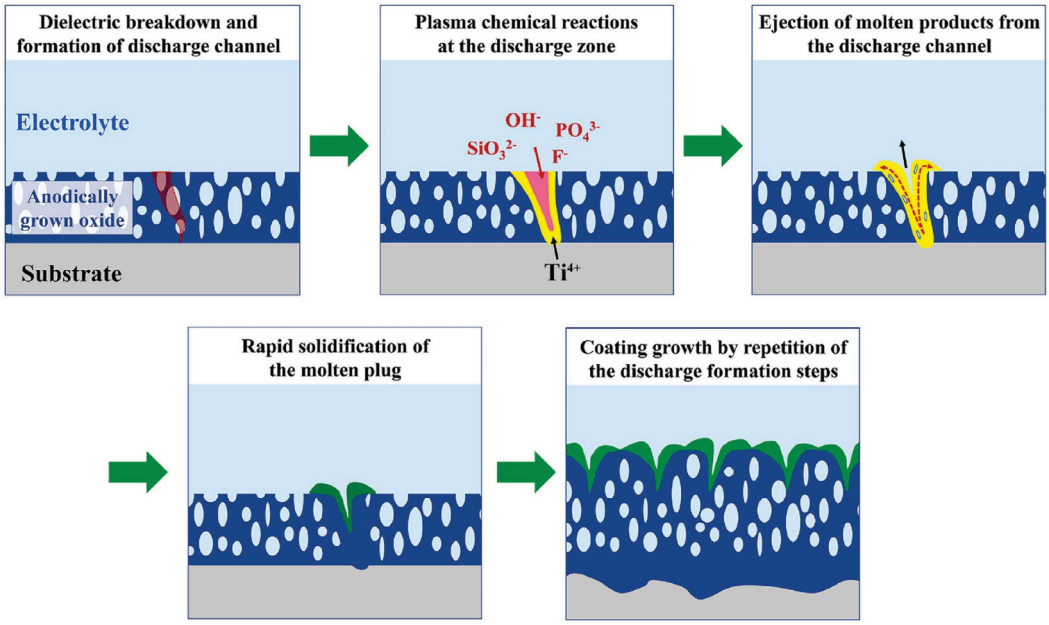

Figure 5. Formation process of micro-arc oxidation coating [94].

4.4. Hydrothermal Method

The hydrothermal method involves placing the metal in a container at high temperature and pressure. The metal surface absorbed particles from the liquid. The particles crystallize and precipitate. Precipitates produce a uniform, complete, smooth, and dense covering on the substance [97–99]. As shown in Figure 6, Ca-P and $Mg(OH)_2$ composite coatings were prepared on magnesium based materials by hydrothermal method at 120 °C [100]. This approach increases the corrosion resistance and biodegradability of magnesium alloy surface coatings [99,101–103]. Ji et al. [97] produced a dense, seamless HAp coating. The HAp coating made magnesium alloys corrosion-resistant and extended Gentamicin Sulfate (GS) release. Song et al. [99] used a hydrothermal approach to create a three μm thick magnesium hydroxide coating on the surface of magnesium-lithium alloys with outstanding corrosion resistance. Zhou et al. [85] prepared a 16 μm thick HA Nano-hydroxyapatite/ZnO coating on the surface of $Mg_{68}Zn_{28}Ca_4$ by one-step hydrothermal method. The overcoat material showed good biocompatibility and excellent corrosion resistance, and the antibacterial rate against staphylococci was close to 100% in vitro antibacterial experiments.

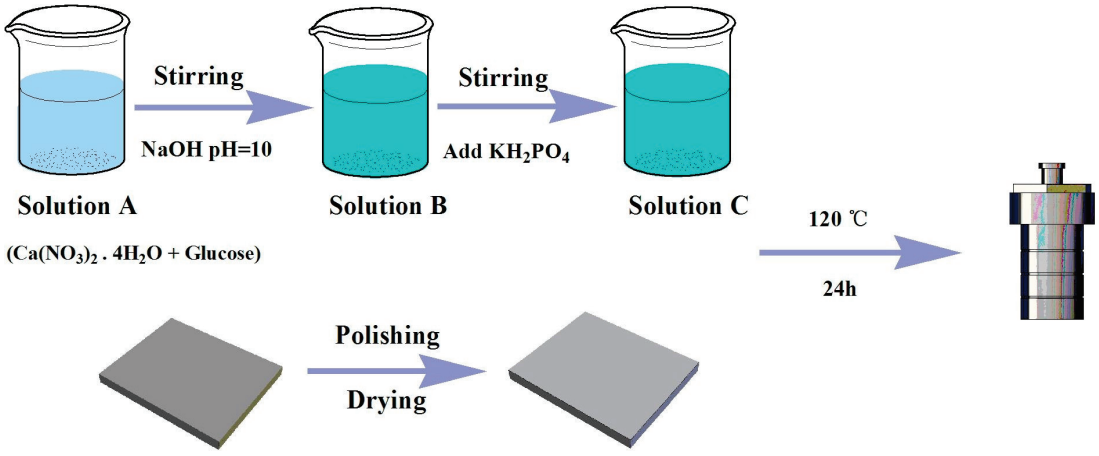

Figure 6. Schematic diagram of composite coating prepared on pure magnesium by hydrothermal method [100].

4.5. Layer-by-Layer Assembly Technology

Layer-by-layer assembly (LBL) technology enables coatings with diverse functions to be composited together [104,105]. Figure 7 illustrates the specific formation process of the layer-by-layer assembly coating, where rods and sheets of different colors correspond to one-dimensional (1D) and two-dimensional (2D) structures formed by molecules of various substances [106]. Zeng et al. [86] used a self-assembly technique to immobilize silver nanoparticles on the surface of an APTMS-modified magnesium alloy. The breakdown voltage of the treated material is −1040 mV, and the diameter of the inhibition band for *E. coli* is up to 14.86 mm. The material exhibits better corrosion resistance and excellent antimicrobial properties against *E. coli*. Zhao et al. [87] made silver nanoparticle-polysiloxane composite coatings. Composite coatings improve antibacterial and corrosion resistance. The slow-released silver ions in the coating played a major bactericidal role, and the sterilization rates of $(AgNPs/PEI)_5$ multilayer materials and $PMTMS/(AgNPs/PEI)_5$ multilayer materials against *Staphylococcus aureus* were 98.4% and 85.0%, respectively.

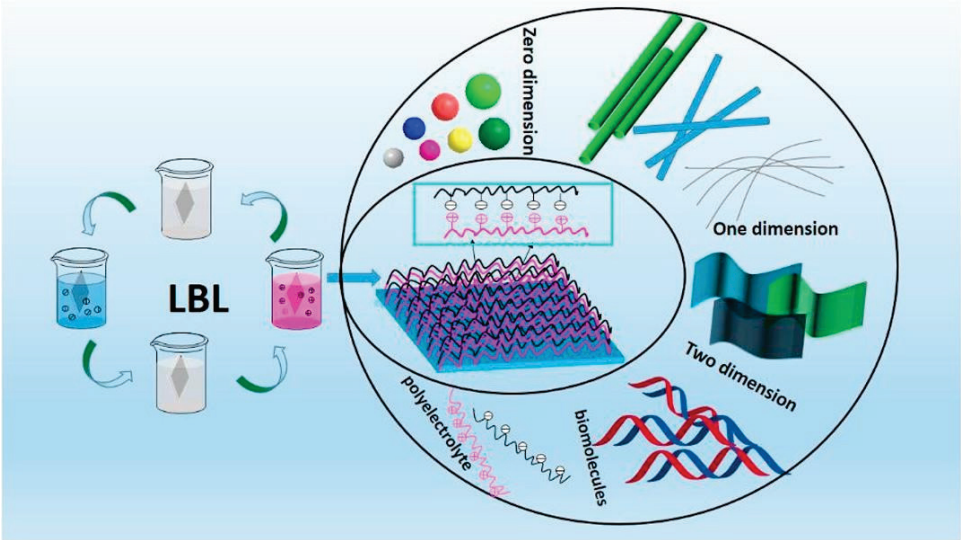

Figure 7. General scheme of the LbL process with a wide variety of assembly materials [106].

4.6. Electrophoretic Deposition Method

The electrophoretic deposition method uses direct current to transport charged ions in a suspension in a specific direction, depositing and attaching to the material's surface to form a coating. As shown in Figure 8, a voltage was used to drive the nano-silica to attach to the prototype material to form a coating [107]. The formation of a coating on Mg-based materials is similar, as long as the anode material is replaced by a Mg-based material, the electrophoretic deposition method can be used to prepare a coating on the surface of Mg-based materials. Energization period and voltage intensity affect coating properties [108]. This method offers several advantages. For instance, coating preparation is delicate and does not cause heat stress or high temperature-induced material brittleness. The coating can be applied uniformly to alloy material in all directions, recessed places, and delicate components. The coating can be adjusted from 1 μm to 100 μm. The downside is that the material must be conductive. Conductive layers must be produced before electrodeposition for non-conductive materials, which adds cost and process [13]. Bakhsheshi et al. [88] used PVD-assisted electrodeposition to complete the silver-doped zeolite hydroxyapatite (Ag-Zeo-HAp) coating on the surface of magnesium alloy with titanium dioxide coating. The corrosion potential of the material is −1540 mV and the corrosion current is $0.7 \mu A/cm^2$. And showed excellent antimicrobial rates in Petri dishes of *E. coli*, with a 94% reduction in colonies. The range of the suppression band with the Ag-Zeo-Hap coating material is 47% larger than the range without the Ag-Zeo-Hap coating material.

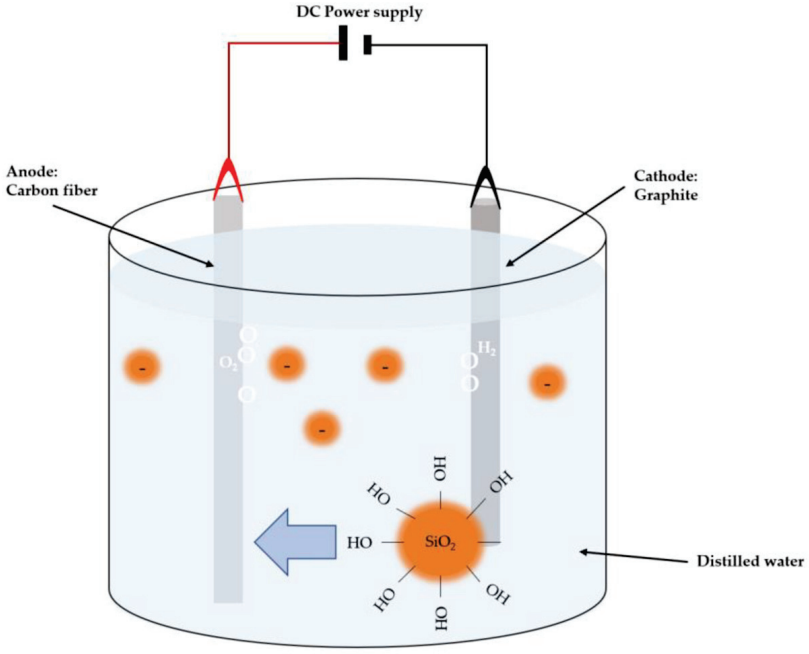

Figure 8. Schematic illustration of EPD configuration for CF surface modification [107].

4.7. Chemical Conversion Method

The chemical conversion method uses the surface of the substrate to undergo complex chemical reaction with the components in the solution, and the reaction product film is generated on the surface, as shown in Figure 9 [109]. The surface of the material reacts with phosphoric acid ions and metal ions in the solution to form a dense coating. For magnesium-based materials, complex surface reactions result in the formation of a coating of magnesium oxide, magnesium hydroxide, or other oxides and hydroxides on the surface. The chemical conversion method uses components in a solution. The surface reacts to generate magnesium oxide, magnesium hydroxide, or other oxides and hydroxides after complex interactions. This covering grows in situ. The coating has excellent adherence and a strong substrate-coating bond [110]. This method can also be used to pretreat the material for better adhesion of the outer coating to the surface of the material [111]. Yan et al. [89] successfully synthesized a fluoride coating on the surface of magnesium alloy by chemical conversion method in hydrofluoric acid, which significantly improved the corrosion resistance of the material and showed good biological activity in plasma. It has also shown a non-toxic effect in vitro experiments on BMMSCs. In the 24-h *E. coli* antibacterial test, the fluoride-coated sample had a killing rate of 99.99%.

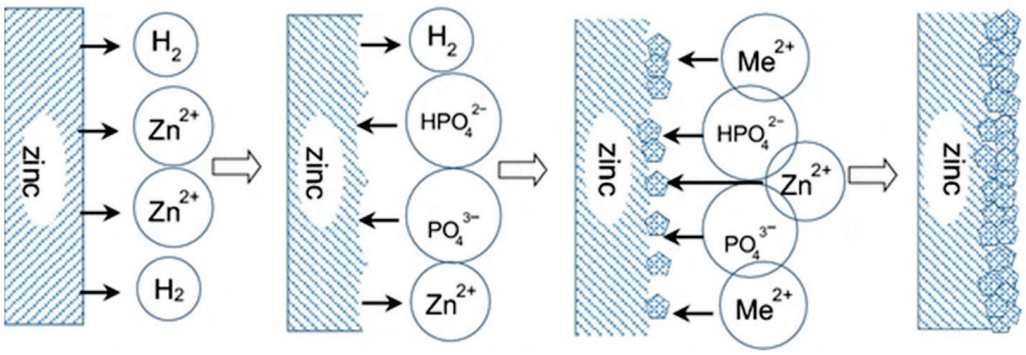

Figure 9. Zinc base material surface phosphate chemical conversion coating process diagram [109].

4.8. Sol-Gel Method

The sol-gel method does not melt the substrate and is carried out at room temperature. This method allows for simple control over the chemical composition of the film. The coating is pure and does not introduce impurities. It is well suited for complex and uneven surfaces. The coating adheres well and bonds directly with the material. However, the coating produced by this process is relatively thin. Its preparation process is shown in Figure 10 [112]. The different colored spheres in the figure represent different kinds of precursors. Tatullo et al. [90] subjected superplastically treated magnesium devices to sol-gel treatment to investigate their bioactivity and antibacterial properties. The study found that the material had excellent cell compatibility. After a seven-day L929 cell viability test, the cell survival rate was 100%, indicating that the material had very good cell activity. The antibacterial performance was also enhanced. Compared to materials treated with the hydrothermal method, materials treated with the sol-gel method showed a lower survival rate of *E. coli* in a 30-h antibacterial test, with an optical density at 600 nm of 0.2–0.3.

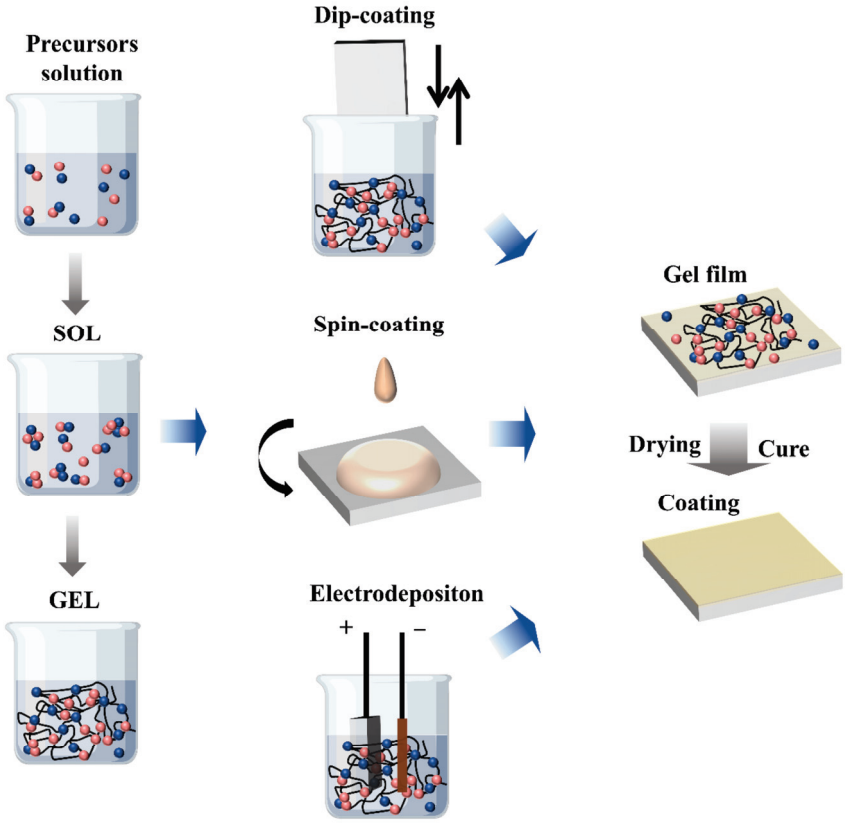

Figure 10. Schematic of steps and processes used to obtain sol-gel coatings [112].

The combined use of multiple methods can obtain superior-performance surface coatings. Shang et al. [113] used the self-assembly method (SAM) and micro-arc oxidation (MAO) to create composite coatings with more excellent corrosion resistance than MAO alone. Multi-method surface coatings on magnesium alloys function better. The combined use of the self-assembly method (SAM) and layer-by-layer assembly method (LBL) preparing chitosan-functionalized graphene oxide (GOCS)/heparin (Hep) multilayer coatings. The coating exhibits high blood compatibility and in vitro corrosion resistance.

5. Alloyed Antibacterial Magnesium

5.1. Properties of Magnesium Alloys

Magnesium bioimplants have some drawbacks. For instance, in vivo, antibacterial activities are suppressed [11], and the corrosion rate is too high [19,39]. Magnesium alloying can fully exploit the benefits of magnesium as a bioimplant material. Magnesium alloy

properties can be enhanced by incorporating various antimicrobial alloy components. Silver, copper, tin, and zinc are common antimicrobial metals in magnesium alloys. Magnesium alloying can dramatically raise the pH of the environment surrounding the implant [114] and has more extraordinary antibacterial characteristics than pure magnesium [114–118]. As element proportions increase, metallic elements' attributes alter. These magnesium alloys with antimicrobial metal components show biocompatibility comparable to pure magnesium [115,116] and better cell adhesion and proliferation promotion [114]. Alloying magnesium changes the degradation rate of the alloy. Magnesium-silver alloys have a reduced corrosion rate after treatment [117]. Many types of magnesium alloys have significantly reduced corrosion rates, such as AZ type, ZK type, WE type, etc. [119,120].

Magnesium alloys are better implant materials than pure magnesium due to their corrosion resistance, antibacterial efficiency, and biocompatibility. Many elements, including silver, copper, tin, zinc, chromium, iron, gallium, and others, can be introduced into magnesium alloys to modify their properties. Among them, silver and copper have a strong antibacterial effect and have obvious advantages over traditional antibiotics in controlling bacterial resistance. Alloying magnesium with tin, zinc or iron improves antimicrobial efficacy, and alloying metals provides a means of physical antimicrobial protection compared to injectable antibiotics, reducing the risk of development of resistance, and can provide long-lasting antimicrobial protection. Various alloys are created by combining one or more of these with magnesium. Table 4 provides specific details on the compositions, preparation methods, and antibacterial properties of mainstream magnesium alloys.

Table 4. Magnesium alloys and their effects.

Alloy	Elemental Ratios	Production Method	Antibacterial and Other Properties	Reference
Magnesia-silver alloy	Mg-4 wt% Ag	Solution treatment, aging heat treatment	The number of bacteria adhering is reduced by 50–75%, the viability of bacteria is reduced by 74–79%, and the sterilizing rate is 90%.	[115]
	Mg-6 wt% Ag	Solution treatment, T4	Bacterial survival was 18.64%. (Mix *S. aureus* and *S. epidermidis* 1 to 1)	[117]
	Mg-8 wt% Ag	Solution treatment, T4	Bacterial survival was 14.75%. High silver content showed poor osteogenic activity and degradation rate.	[117]
Magnesium-copper alloy	Mg-0.03 wt% Cu	Ingot casting method	In the 6 h anti *Staphylococcus aureus* experiment, the remaining bacterial colonies were 4.1 CFU/mL. Best bone formation ability.	[118]
	Mg-0.01 wt% Cu	Ingot casting method	Degradation rate 20 mm/year. Better antimicrobial effects against *MRSA* and *Staphylococcus epidermidis*, CFU stands for 30.3 ± 7.4, 18.7 ± 5.2, and 11.5 ± 3.8	[121]
	Mg-0.25 wt% Cu	Ingot casting method	Rapid release of copper ions, significant antibacterial effect, Rapid release of copper ions, significant antibacterial effect, CFU of *MRSA* and *Staphylococcus epidermidis* stands for 30.3 ± 7.4, 18.7 ± 5.2, and 11.5 ± 3.8	[121]
	Mg-0.5 wt% Cu	Ingot casting method	Degradation rate is more than 50 mm/year. In the 6 h anti *Staphylococcus aureus* experiment, the remaining bacterial colonies were 2.3 CFU/mL. Degradation is faster, with a 3-day degradation rate approaching 90 mm/year. Less osteogenic capacity.	[118]
Magnesia-tin alloy	Mg-1Zn-0.5Sn	Melted in an induction furnace under Ar gas protection and extruded at 300 °C.	In the antibacterial experiment, the optical density was detected at 600 nm, with the optical density of *Escherichia coli* stabilized at 0.4, and that of *Staphylococcus aureus* stabilized at 0.35.	[114]

Table 4. *Cont.*

Alloy	Elemental Ratios	Production Method	Antibacterial and Other Properties	Reference
	Mg-4Zn-xSn (x = 0, 1.0, 1.5 wt%)	Melted in an induction furnace under Ar gas protection and extruded at 300 °C.	The number of *Staphylococcus aureus* colonies in the samples with Sn group decreased by more than 50%, and the antibacterial ability was significantly improved compared to the samples without Sn group.	[122]
Magnesium-zinc alloy	Mg-5.6 wt% Zn	Metal ingot	In the test experiment of the display board method, the Mg-Zn alloy achieved a 1–3 day antibacterial rate of 72.8–96.2% against planktonic *MRSA*, and a 1–3 day antibacterial rate of 62.3–84.5% against adherent *MRSA*.	[123]
	Mg-1Ca-0.5Sr-2Zn	Melting in a high-purity graphite crucible (protected by Ar gas) and thermally extruding at 320 °C	The killing rate of *Staphylococcus aureus* is 76.9%.	[116]
	Mg-1Ca-0.5Sr-4Zn, Mg-1Ca-0.5Sr-6Zn	Melting in a high-purity graphite crucible (protected by Ar gas) and thermally extruding at 320 °C	The bactericidal rates of Mg-1Ca-0.5Sr-4Zn and Mg-1Ca-0.5Sr-6Zn against *Staphylococcus aureus* are higher than 96.6%.	[116]

5.2. Mg-Ag Alloy Properties

Magnesium-silver alloys combine silver's antibacterial qualities with magnesium's outstanding characteristics. Tie et al. [115] successfully fabricated magnesium-silver alloys with enhanced properties using solid solution and heat treatment processes. Comparing magnesium-silver alloys to glass and titanium, alloys showed antibacterial solid action. Bacteria adhering to magnesium-silver alloys were reduced by 50–75%, viability by 74–79%, and death by over 90%. Tie et al. [115] tested biocompatibility for two weeks in cellular tests. Magnesium-silver alloys provide over 95% cell adhesion and survival. Magnesium-silver alloys are more bioactive than titanium and glass. Liu et al. [117] prepared magnesium-silver alloys to enhance antibacterial properties. The alloy was found to be non-toxic to human primary osteoblasts. The corrosion rate of the alloy after T4 treatment was significantly reduced. Furthermore, the bacterial activity (a mixture of *Staphylococcus aureus* and *Staphylococcus epidermidis*) of Mg-6Ag and Mg-8Ag after T4 treatment was 18.64% and 14.75%, respectively

5.3. Mg-Cu Alloy Properties

Magnesium-copper alloys have high biocompatibility and long-lasting bactericidal characteristics. Magnesium-copper alloy kills bacteria by dissolving their biofilm and has obvious antibacterial and fungicidal capabilities [124]. Liu et al. [118] research on magnesium-copper alloys found that the alloys can stimulate angiogenesis, induce osteogenesis, and also provide long-lasting antibacterial properties. In the antibacterial experiment against *Staphylococcus aureus*, under normal pH conditions, the antibacterial effect from 3 to 72 h showed that the magnesium-copper alloy's antibacterial effect was stronger than that of pure magnesium, and the antibacterial effect became stronger as the copper content in the alloy increased. After 72 h, the *Staphylococcus aureus* colonies on both the magnesium-copper alloy and magnesium were eliminated. In a neutral pH environment, the bactericidal effect of the magnesium-copper alloy from 3 to 24 h was somewhat reduced, but it still killed the bacteria after 72 h. Li et al. [121] studied the antibacterial effects and other biological properties of magnesium-copper alloys with 0.05, 0.1, and 0.25 wt% copper content. In the 24-h antibacterial tests against *MRSA*, *Staphylococcus epidermidis*, and *Escherichia coli*, the magnesium-copper alloys performed better than titanium. The number of formed units of bacterial colonies in the Mg-0.1Cu group were 30.3 ± 7.4, 18.7 ± 5.2, and 11.5 ± 3.8, respectively. In the Mg-0.25Cu group, these numbers decreased to 8.2 ± 3.3,

4.4 ± 2.4, and 7.9 ± 2.7. At the same time, biocompatibility is good and did not cause side effects. The antibacterial effect of the magnesium-copper alloys gradually increased with the increase of copper content, which confirmed the research conclusions of Lui and his team.

5.4. Mg-Sn Alloy Properties

Tin is a vital trace element. Tin and magnesium have good solid solubility, and tin can prevent corrosion by increasing magnesium's electrode potential [114]. Zhao et al. [114] found that tin oxide and tin dioxide create a membrane on the alloy's surface as it corrodes. The membrane prevents corrosion of the alloy. Zhao et al. also observed magnesium alloys containing tin have better antibacterial characteristics. In vitro, the alloys demonstrated good biocompatibility, allowing biological cells to cling to the alloy surface and promote cell proliferation. Jiang et al. [122] studied the antibacterial activity of Mg-4Zn-xSn alloys (where the content of Sn is 0, 1.0, 1.5 wt%). The experimental results of antibacterial activity against *Staphylococcus aureus* showed that the number of bacterial units in the 1.0 Sn and 1.5 Sn groups was half that of pure magnesium after 12 h, demonstrating significant antibacterial effects.

5.5. Mg-Zn Alloy Properties

Zinc is another crucial trace element. Zinc additives in magnesium improve mechanical strength and ductility [125]. Yu et al. [123] research indicates that magnesium-zinc alloys have a good antibacterial effect on MRSA. The bactericidal rate of the samples against planktonic MRSA reached 72.8% and 96.2% on the first and third days, respectively, and the bactericidal rate against adherent MRSA reached 62.3% and 84.5%, respectively. In vitro experiments show that the alloy extract can inhibit bacterial growth. The antibacterial test against *Staphylococcus aureus* found that Mg-1Ca-0.5Sr-2Zn exhibited a relatively low kill rate of 76.9%. While the kill rates of Mg-1Ca-0.5Sr-4Zn and Mg-1Ca-0.5Sr-6Zn were higher than 96.6% [116].

6. Antibacterial Mechanisms

6.1. PH and Antibacterial

Degradation of magnesium and magnesium alloys produce hydroxide roots, raising the surrounding pH. A high pH inhibits the growth of bacteria [126]. Alkaline pH suppresses the expression of bacterial agr RNAIII [127] and hinders bacterial multiplication. The solution pH can reach 9–10 after the breakdown of magnesium-based compounds in vitro [126,128]. However, most bacteria thrive at pH 6–8 [129]. Bacterial biofilms thrive in acidic pH 5–6 environments [130]. When pH exceeds 7, biofilms of common bacteria like *Staphylococcus aureus* weaken and are easily eliminated [131]. The alkaline environment created during magnesium breakdown contributes significantly to magnesium's remarkable antibacterial ability. This idea has been supported by experiments [114,118,132–134]. Rahim et al. [135] showed that pH affects antibacterial action in magnesium-degraded supernatants. After increasing the total amount of magnesium, the supernatant had a higher pH and more pronounced bacterial suppression. However, after neutralizing the pH of the supernatant, the antimicrobial effect worsened, and the bacterial inhibitory effect of the supernatant was lost. It shows that alkalinity in the environment is crucial to antibacterial activity.

Magnesium-based alloys induce alkaline environmental changes due to deterioration process. Magnesium breakdown produces alkaline compounds. The anode oxidizes magnesium to magnesium ions. The cathode reduces water to hydrogen and hydroxide [136]. This creates alkaline magnesium hydroxide. Magnesium hydroxide forms an exterior coating on the alloy. The outer film dehydrates, forming a magnesium oxide inner film [132,137–141]. The deposited layer provides some corrosion resistance. However, anions in living organisms can react with magnesium ions [142,143]. This reaction weakens magnesium oxide and hydroxide's protective layer, making them reactive [144].

Thus, chloride ions in the environment quickly combine with magnesium hydroxide to create magnesium chloride [139,145]. This process eventually destroys the outer layer of magnesium hydroxide and exposes the inner layer of magnesium oxide. Yao [141] found that magnesium oxide reacts readily with water. The volume of the resultant magnesium hydroxide expands. The oxide coating will burst if too much magnesium oxide reacts and expands. After the oxide film breaks, the magnesium alloy corrodes. This process generates alkaline chemicals, which increase the alkalinity of the surrounding environment. Lin [133] observed that in alkaline conditions, bacteria must use considerable amounts of their hydrogen ions to neutralize ambient hydroxide ions. This would impair the bacteria's internal proton electrochemical gradient. The internal bacterial electrochemical gradient drives ATP production. Electrochemical gradient disruption restricts ATP synthesis and kills bacteria.

6.2. Biochemical Effects of Magnesium Ions on Bacteria

Another antibacterial function of magnesium implants is the usage of magnesium ions released into the environment to kill microorganisms. Magnesium ions' antibacterial action is intimately linked to their influence on bacterial biofilms [146]. Magnesium ions specifically bind to biomembranes, thereby increasing the permeability of the biomembranes and even destroying them, leading to a significant loss of cellular contents and bacterial death [147]. Magnesium ions also exert immunomodulatory effects by regulating the local immune environment, thereby producing antibacterial effects. Magnesium ions can also regulate the local immune environment to enhance the antibacterial effect. High concentrations of magnesium ions promote macrophage polarization to the bactericidal M1 type and induce the expression of two important substances, TNF-α and iNOS, in macrophages, thereby significantly increasing phagocytic activity against bacteria [148]. It is worth mentioning that in an environment with low concentrations of magnesium ions, magnesium ions can reduce the production of pro-inflammatory cytokines by macrophages by inhibiting the activation of transcription factor NF-κB, such as tumor necrosis factor α (TNF-α), interleukin 6 (IL-6), and interleukin 1β (IL-1β), thereby controlling inflammatory cell aggregation and activation, and enhancing human bone marrow mesenchymal stem cell (hBMSC) chondrogenic differentiation [149].However, magnesium ions cannot be used as the primary force for sterilization. Most bacterial cells contain magnesium ions. For some bacteria, the amount of magnesium ions in them is very high [150,151]. To kill the bacteria alone, magnesium ions must exceed the organism's magnesium ions [133].

In alkaline settings, magnesium ions have a substantially higher antibacterial capacity. Alkaline surroundings increase magnesium ions' antibacterial impact [152]. Magnesium ions and the alkaline environment magnesium creates make magnesium alloys antibacterial [133]. The bactericidal effect of magnesium ions depends on the alkaline environment [152]. Thus, alkaline conditions are necessary for magnesium alloys' antibacterial properties.

6.3. Direct Contact Sterilization

The surface of the alloy directly contacting with bacteria can destroy the bacterial membrane and structure, and it can also inhibit the bacterial adhesion to the alloy surface to achieve antibacterial effects [47,127]. Magnesium has a certain contact antibacterial ability, but its antibacterial capacity is limited. When magnesium forms alloys with other antibacterial metals or forms oxides, it exhibits better antibacterial effects. In vitro antibacterial experiments, Qin et al. used the spread plate method to test the antibacterial effects of magnesium and magnesium alloy (Mg-Nd-Zn-Zr) on *Escherichia coli*, *Staphylococcus aureus*, and *Staphylococcus epidermidis*. The results showed that pure magnesium has a good antibacterial effect on adherent bacteria, and the Mg-Nd-Zn-Zr alloy has a stronger antibacterial effect [57]. Nemanja et al. explored the antibacterial mechanism of magnesium oxide particles and found that the antibacterial activity of magnesium oxide is closely related to its surface properties, and reducing the low-coordinate oxygen atoms on the MgO surface

greatly promotes the antibacterial process of magnesium oxide. Magnesium oxide can undergo hydrolysis reactions in a liquid environment, forming defects or vacancies on the surface, which destroys the original surface of magnesium oxide. When the low-coordinate oxygen atoms on the surface of magnesium oxide are reduced, the MgO surface becomes less susceptible to water, maintaining more of the original surface. The original surface of MgO can destroy the bacterial cell wall through physical contact, causing cell content leakage and thus killing the bacteria [153]. At the same time, MgO slurry powder has shown bactericidal effects on bacteria such as *Escherichia coli*, Salmonella, and *Pseudomonas aeruginosa*, demonstrating a broad antibacterial spectrum [154].

6.4. Affects Bacterial Electron Transfer

Bacteria produce energy substance adenosine triphosphate (ATP) through respiration, which is vital for their survival. The synthesis of ATP in bacteria depends on the electrochemical gradient formed by the transfer of charged particles, and the formation and stability of the electrochemical gradient are very important for the formation, transport, and respiratory function of ATP in bacteria [155,156]. The proton electrochemical gradient is a transmembrane proton concentration difference established by the cell through the electron transport chain (ETC) during cellular respiration. In bacteria, this process usually occurs on the cytoplasmic membrane. Electrons are transferred from NADH or FADH2 to oxygen, while protons (H+) are pumped from the inside of the cell to the outside, forming a proton gradient. This gradient provides the necessary driving force for ATP synthesis [157–159]. As shown in Figure 11(4), electrochemical corrosion occurs between magnesium and other metallic elements in magnesium-based materials, causing electron transfer in the surrounding environment and producing many electrons. The yellow and blue circles in the figure represent different types of metals [48]. Studies have shown that after bacteria encounter magnesium-based materials, many protons are produced, and the proton reserve in the bacterial membrane gap is excessively consumed, thereby destroying the proton electrochemical gradient of the bacteria. The interruption of the transmembrane proton electrochemical gradient can lead to a decrease in ATP synthesis, which in turn limits the formation and maintenance of the glycocalyx, causing metabolic disorders in bacteria [160], and interfering with their normal proliferation. Ultimately, this can lead to the death of bacteria due to their inability to maintain basic life activities or resist environmental stress [161]. While the massive migration of protons also leads to the generation and transfer of many electrons, the process of electron transfer consumes hydrogen ions. Excessive consumption of hydrogen ions can affect the activity of the proton pump inside the bacteria, thus releasing a large amount of ROS [18], thereby killing the bacteria.

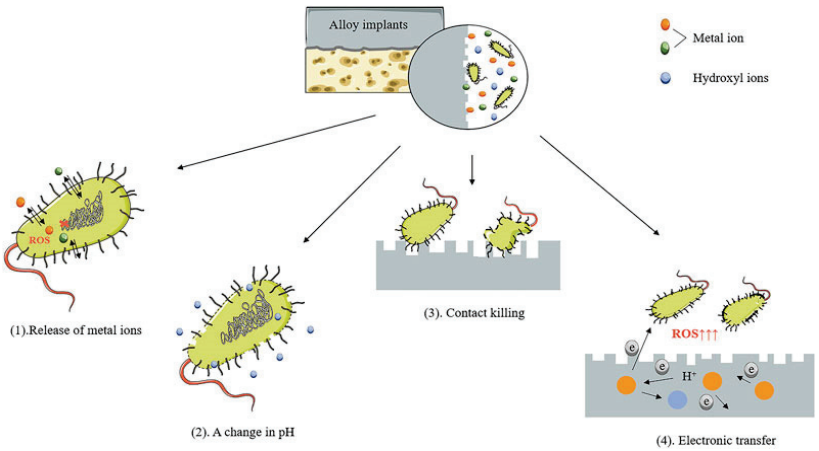

Figure 11. Four mainstream antimicrobial mechanisms for metal implants [48] The diagram describes the four primary mechanisms of alloy antibiosis, and the four mechanisms are: (**1**) release of metal ions, (**2**) a change in pH, (**3**) contact killing, and (**4**) electronic transfer.

7. Conclusions

Despite their potential, magnesium alloys face significant limitations in clinical use due to their rapid degradation rate in physiological conditions. This high corrosion rate makes it challenging to achieve a harmonious balance between biocompatibility, mechanical properties, and corrosion resistance. The future of magnesium alloy development hinges on controlling this corrosion rate effectively. Strategies such as surface modification, alloying with other elements, and other optimization methods are being explored to enhance corrosion behavior and regulate the degradation rate precisely.

Magnesium alloys possess a robust antimicrobial effect in vitro, but this efficacy is reduced in vivo, where the body's neutral environment counteracts the alkaline pH produced by degrading magnesium, thereby diminishing its antimicrobial impact [11]. To optimize magnesium-based implants for enhanced in vivo antimicrobial performance, it is essential to tailor the composition of magnesium alloys to meet the specific requirements of different implantation sites and to modify the surface of magnesium materials accordingly.

Magnesium has a strong antimicrobial effect in vitro, but this effect is weakened in vivo, and the mechanism of this lagged effect is unknown. It is now thought that the in vivo environment neutralizes the alkaline environment created by magnesium degradation products and that disrupting the alkaline environment reduces magnesium's antimicrobial effect. Studying magnesium's in vivo antimicrobial effect can help better target the environmental situation and develop magnesium-based implants with excellent vivo antimicrobial properties. The high degradation rate of magnesium alloys in the physiological environment continues to be a significant limitation for clinical applications. They are still far from achieving a good balance between biocompatibility, mechanical properties, and corrosion resistance. The focus of future development remains the control of its corrosion rate. It combines surface modification, alloying, and other optimization methods to improve corrosion behavior and precisely regulate its degradation rate.

Specific methods include but are not limited to the use of laser surface modification, micro arc oxidation and other surface modification methods, a comprehensive discussion of its modification principles and uses, the formation of a variety of methods of composite application, the collection of different methods of their respective advantages. At the same time, combined with alloying, the substrate metal is optimized, the corrosion behavior of the material is improved, and the degradation speed is accurately adjusted.

Similarly, the design of magnesium alloy should be changed to the overall design of structure and function and the development of composite materials. Specific types of alloys must be developed based on the requirements of different implantation sites to broaden the scope of magnesium alloys' application in the biomedical field. Meanwhile, the transformation of implantable magnesium-based devices is multidisciplinary. It entails material design and preparation, biological testing, and clinical evaluation. Establishing a collaborative platform between research institutes, hospitals, and businesses is necessary to promote the development and clinical application of new magnesium-based implants.

Author Contributions: Writing—original draft preparation, formal analysis, investigation resources, Q.S.; Conceptualization, writing—review and editing, funding acquisition; F.Y.; Supervision, project administration, L.Y.; Methodology, project administration, C.C.; Conceptualization, responsible for proofreading, J.G.; Data analysis, writing—review, Z.Q.; Visualization, resources, Y.S. All authors have read and agreed to the published version of the manuscript.

Funding: This research did not receive any specific grant from funding agencies in the public, commercial, or not-for-profit sectors.

Data Availability Statement: All the data presented in this review is publicly available and can be accessed through the references provided in the article.

Acknowledgments: We appreciate the valuable feedback from all reviewers and editors, as their suggestions have helped us improve the quality of the review.

Conflicts of Interest: The authors declare that they have no conflicts of interest.

References

1. Misra, R.D.K. Biomaterials. *Mater. Sci. Technol.* **2008**, *24*, 1009. [CrossRef]
2. Prakasam, M.; Locs, J.; Salma-Ancane, K.; Loca, D.; Largeteau, A.; Berzina-Cimdina, L. Biodegradable Materials and Metallic Implants—A Review. *J. Funct. Biomater.* **2017**, *8*, 44. [CrossRef] [PubMed]
3. Lee, J.; An, J.M.; Kim, J.; Bang, E.-K.; Kim, D. A hybrid formulation of porous silicon nanoparticle with carboxymethyl cellulose for enhanced drug loading. *Mater. Lett.* **2024**, *371*, 136929. [CrossRef]
4. Nassif, N.; Ghayad, I. Corrosion Protection and Surface Treatment of Magnesium Alloys Used for Orthopedic Applications. *Adv. Mater. Sci. Eng.* **2013**, 532896. [CrossRef]
5. Wang, J.-L.; Xu, J.-K.; Hopkins, C.; Chow, D.H.-K.; Qin, L. Biodegradable Magnesium-Based Implants in Orthopedics—A General Review and Perspectives. *Adv. Sci.* **2020**, *7*, 1902443. [CrossRef]
6. Bommala, V.K.; Krishna, M.G.; Rao, C.T. Magnesium matrix composites for biomedical applications: A review. *J. Magnes. Alloys* **2019**, *7*, 72–79. [CrossRef]
7. Zhou, H.; Liang, B.; Jiang, H.; Deng, Z.; Yu, K. Magnesium-based biomaterials as emerging agents for bone repair and regeneration: From mechanism to application. *J. Magnes. Alloys* **2021**, *9*, 779–804. [CrossRef]
8. Riaz, U.; Shabib, I.; Haider, W. The current trends of Mg alloys in biomedical applications—A review. *J. Biomed. Mater. Res. Part B Appl. Biomater.* **2019**, *107*, 1970–1996. [CrossRef]
9. Tian, P.; Liu, X. Surface modification of biodegradable magnesium and its alloys for biomedical applications. *Regen. Biomater.* **2015**, *2*, 135–151. [CrossRef]
10. Myrissa, A.; Agha, N.A.; Lu, Y.; Martinelli, E.; Eichler, J.; Szakács, G.; Kleinhans, C.; Willumeit-Römer, R.; Schäfer, U.; Weinberg, A.-M. In vitro and in vivo comparison of binary Mg alloys and pure Mg. *Mater. Sci. Eng. C* **2016**, *61*, 865–874. [CrossRef]
11. Hou, P.; Zhao, C.; Cheng, P.; Wu, H.; Ni, J.; Zhang, S.; Lou, T.; Wang, C.; Han, P.; Zhang, X.; et al. Reduced antibacterial property of metallic magnesium in vivo. *Biomed. Mater.* **2016**, *12*, 015010. [CrossRef]
12. Staiger, M.P.; Pietak, A.M.; Huadmai, J.; Dias, G. Magnesium and its alloys as orthopedic biomaterials: A review. *Biomaterials* **2006**, *27*, 1728–1734. [CrossRef] [PubMed]
13. Guo, X.; Hu, Y.; Yuan, K.; Qiao, Y. Review of the Effect of Surface Coating Modification on Magnesium Alloy Biocompatibility. *Materials* **2022**, *15*, 3291. [CrossRef] [PubMed]
14. Zhao, Q.; Guo, X.; Dang, X.; Hao, J.; Lai, J.; Wang, K. Preparation and properties of composite MAO/ECD coatings on magnesium alloy. *Colloids Surf. B Biointerfaces* **2013**, *102*, 321–326. [CrossRef] [PubMed]
15. Amendola, R.; Acharjee, A. Microbiologically Influenced Corrosion of Copper and Its Alloys in Anaerobic Aqueous Environments: A Review. *Front. Microbiol.* **2022**, *13*, 806688. [CrossRef]
16. Gopalakrishnan, U.; Felicita, A.S.; Mahendra, L.; Kanji, M.A.; Varadarajan, S.; Raj, A.T.; Feroz, S.M.A.; Mehta, D.; Baeshen, H.A.; Patil, S. Assessing the Potential Association Between Microbes and Corrosion of Intra-Oral Metallic Alloy-Based Dental Appliances Through a Systematic Review of the Literature. *Front. Bioeng. Biotechnol.* **2021**, *9*, 631103. [CrossRef]
17. Yasuyuki, M.; Kunihiro, K.; Kurissery, S.; Kanavillil, N.; Sato, Y.; Kikuchi, Y. Antibacterial properties of nine pure metals: A laboratory study using *Staphylococcus aureus* and *Escherichia coli*. *Biofouling* **2010**, *26*, 851–858. [CrossRef]
18. Lemire, J.A.; Harrison, J.J.; Turner, R.J. Antimicrobial activity of metals: Mechanisms, molecular targets and applications. *Nat. Rev. Microbiol.* **2013**, *11*, 371–384. [CrossRef]
19. Tan, J.; Ramakrishna, S. Applications of Magnesium and Its Alloys: A Review. *Appl. Sci.* **2021**, *11*, 6861. [CrossRef]
20. Wang, J.; Bao, Z.; Wu, C.; Zhang, S.; Wang, N.; Wang, Q.; Yi, Z. Progress in partially degradable titanium-magnesium composites used as biomedical implants. *Front. Bioeng. Biotechnol.* **2022**, *10*, 996195. [CrossRef]
21. Zhi, P.; Liu, L.; Chang, J.; Liu, C.; Zhang, Q.; Zhou, J.; Liu, Z.; Fan, Y. Advances in the Study of Magnesium Alloys and Their Use in Bone Implant Material. *Metals* **2022**, *12*, 1500. [CrossRef]
22. Agarwal, S.; Curtin, J.; Duffy, B.; Jaiswal, S. Biodegradable magnesium alloys for orthopaedic applications: A review on corrosion, biocompatibility and surface modifications. *Mater. Sci. Eng. C* **2016**, *68*, 948–963. [CrossRef] [PubMed]
23. Py, B.; Johnston, S.; Hardy, A.; Shi, Z.; Wolski, K.; Atrens, A. Quantifying the influence of calcium ion concentration on the corrosion of high-purity magnesium, AZ91, WE43 in modified Hanks' solutions. *Mater. Res. Express* **2020**, *7*, 096501. [CrossRef]
24. Zhang, S.; Zhang, X.; Zhao, C.; Li, J.; Song, Y.; Xie, C.; Tao, H.; Zhang, Y.; He, Y.; Jiang, Y.; et al. Research on an Mg–Zn alloy as a degradable biomaterial. *Acta Biomater.* **2010**, *6*, 626–640. [CrossRef] [PubMed]
25. Li, N.; Zheng, Y. Novel Magnesium Alloys Developed for Biomedical Application: A Review. *J. Mater. Sci. Technol.* **2013**, *29*, 489–502. [CrossRef]
26. Bancerz, B.; Dus-Zuchowska, M.; Cichy, W.; Matusiewicz, H. Effect of magnesium on human health. *Prz. Gastroenterol.* **2012**, *7*, 359–366. [CrossRef]
27. Zheng, D.; Upton, R.N.; Ludbrook, G.L.; Martinez, A. Acute cardiovascular effects of magnesium and their relationship to systemic and myocardial magnesium concentrations after short infusion in awake sheep. *J. Pharmacol. Exp. Ther.* **2001**, *297*, 1176–1183.
28. Nie, X.J.; Zhang, X.Y.; Lei, B.Z.; Shi, Y.H.; Yang, J.X. Regulation of Magnesium Matrix Composites Materials on Bone Immune Microenvironment and Osteogenic Mechanism. *Front. Bioeng. Biotechnol.* **2022**, *10*, 842706. [CrossRef]

29. Iezaki, T.; Onishi, Y.; Ozaki, K.; Fukasawa, K.; Takahata, Y.; Nakamura, Y.; Fujikawa, K.; Takarada, T.; Yoneda, Y.; Yamashita, Y.; et al. The Transcriptional Modulator Interferon-Related Developmental Regulator 1 in Osteoblasts Suppresses Bone Formation and Promotes Bone Resorption. *J. Bone Miner. Res.* **2016**, *31*, 573–584. [CrossRef]
30. Li, L.; Zhang, M.; Li, Y.; Zhao, J.; Qin, L.; Lai, Y. Corrosion and biocompatibility improvement of magnesium-based alloys as bone implant materials: A review. *Regen. Biomater.* **2017**, *4*, 129–137. [CrossRef]
31. Niinomi, M.; Nakai, M.; Hieda, J. Development of new metallic alloys for biomedical applications. *Acta Biomater.* **2012**, *8*, 3888–3903. [CrossRef] [PubMed]
32. Affatato, S.; Ruggiero, A.; Merola, M. Advanced biomaterials in hip joint arthroplasty. A review on polymer and ceramics composites as alternative bearings. *Compos. Part B Eng.* **2015**, *83*, 276–283. [CrossRef]
33. Oskouei, R.H.; Fallahnezhad, K.; Kuppusami, S. An Investigation on the Wear Resistance and Fatigue Behaviour of Ti-6Al-4V Notched Members Coated with Hydroxyapatite Coatings. *Materials* **2016**, *9*, 111. [CrossRef] [PubMed]
34. Bocchetta, P.; Chen, L.-Y.; Tardelli, J.D.C.; Reis, A.C.d.; Almeraya-Calderón, F.; Leo, P. Passive Layers and Corrosion Resistance of Biomedical Ti-6Al-4V and β-Ti Alloys. *Coatings* **2021**, *11*, 487. [CrossRef]
35. Li, L.; Gao, J.; Wang, Y. Evaluation of cyto-toxicity and corrosion behavior of alkali-heat-treated magnesium in simulated body fluid. *Surf. Coat. Technol.* **2004**, *185*, 92–98. [CrossRef]
36. Sikora-Jasinska, M.; Mostaed, E.; Mostaed, A.; Beanland, R.; Mantovani, D.; Vedani, M. Fabrication, mechanical properties and in vitro degradation behavior of newly developed ZnAg alloys for degradable implant applications. *Mater. Sci. Eng. C* **2017**, *77*, 1170–1181. [CrossRef]
37. Chen, Y.; Xu, Z.; Smith, C.; Sankar, J. Recent advances on the development of magnesium alloys for biodegradable implants. *Acta Biomater.* **2014**, *10*, 4561–4573. [CrossRef]
38. Eliaz, N. Corrosion of Metallic Biomaterials: A Review. *Materials* **2019**, *12*, 407. [CrossRef]
39. Pei, Y.L.; Zhang, G.N.; Zhang, C.; Wang, J.M.; Hang, R.Q.; Yao, X.H.; Zhang, X.Y. Corrosion resistance, anticoagulant and antibacterial properties of surface-functionalized magnesium alloys. *Mater. Lett.* **2019**, *234*, 323–326. [CrossRef]
40. Noviana, D.; Paramitha, D.; Ulum, M.F.; Hermawan, H. The effect of hydrogen gas evolution of magnesium implant on the postimplantation mortality of rats. *J. Orthop. Transl.* **2016**, *5*, 9–15. [CrossRef]
41. Campoccia, D.; Montanaro, L.; Arciola, C.R. A review of the biomaterials technologies for infection-resistant surfaces. *Biomaterials* **2013**, *34*, 8533–8554. [CrossRef] [PubMed]
42. Zhang, E.; Zhao, X.; Hu, J.; Wang, R.; Fu, S.; Qin, G. Antibacterial metals and alloys for potential biomedical implants. *Bioact. Mater.* **2021**, *6*, 2569–2612. [CrossRef] [PubMed]
43. Ferraris, S.; Spriano, S. Antibacterial titanium surfaces for medical implants. *Mater. Sci. Eng. C* **2016**, *61*, 965–978. [CrossRef] [PubMed]
44. Frei, A.; Verderosa, A.D.D.; Elliott, A.G.G.; Zuegg, J.; Blaskovich, M.A.T. Metals to combat antimicrobial resistance. *Nat. Rev. Chem.* **2023**, *7*, 202–224. [CrossRef]
45. Mutalik, C.; Lin, I.H.; Krisnawati, D.I.; Khaerunnisa, S.; Khafid, M.; Widodo; Hsiao, Y.-C.; Kuo, T.-R. Antibacterial Pathways in Transition Metal-Based Nanocomposites: A Mechanistic Overview. *Int. J. Nanomed.* **2022**, *17*, 6821–6842. [CrossRef]
46. Wang, X.L.; Liu, S.X.; Li, M.; Yu, P.; Chu, X.; Li, L.; Tan, G.X.; Wang, Y.J.; Chen, X.F.; Zhang, Y.; et al. The synergistic antibacterial activity and mechanism of multicomponent metal ions-containing aqueous solutions against *Staphylococcus aureus*. *J. Inorg. Biochem.* **2016**, *163*, 214–220. [CrossRef]
47. Jiao, J.; Zhang, S.; Qu, X.; Yue, B. Recent Advances in Research on Antibacterial Metals and Alloys as Implant Materials. *Front. Cell. Infect. Microbiol.* **2021**, *11*, 693939. [CrossRef]
48. Wang, N.; Ma, Y.; Shi, H.; Song, Y.; Guo, S.; Yang, S. Mg-, Zn-, and Fe-Based Alloys with Antibacterial Properties as Orthopedic Implant Materials. *Front. Bioeng. Biotechnol.* **2022**, *10*, 888084. [CrossRef]
49. Kawabe, A. Marine organisms influenced corrosion of copper alloys. *Electrochemistry* **2003**, *71*, 681–685. [CrossRef]
50. Mahmoudi, P.; Akbarpour, M.R.; Lakeh, H.B.; Jing, F.; Hadidi, M.R.; Akhavan, B. Antibacterial Ti-Cu implants: A critical review on mechanisms of action. *Mater. Today Bio* **2022**, *17*, 100447. [CrossRef]
51. Chandrangsu, P.; Rensing, C.; Helmann, J.D. Metal homeostasis and resistance in bacteria. *Nat. Rev. Microbiol.* **2017**, *15*, 338–350. [CrossRef] [PubMed]
52. Vimbela, G.V.; Ngo, S.M.; Fraze, C.; Yang, L.; Stout, D.A. Antibacterial properties and toxicity from metallic nanomaterials. *Int. J. Nanomed.* **2017**, *12*, 3941–3965. [CrossRef] [PubMed]
53. Marambio-Jones, C.; Hoek, E.M.V. A review of the antibacterial effects of silver nanomaterials and potential implications for human health and the environment. *J. Nanoparticle Res.* **2010**, *12*, 1531–1551. [CrossRef]
54. Alexander, J.W. History of the Medical Use of Silver. *Surg. Infect.* **2009**, *10*, 289–292. [CrossRef] [PubMed]
55. Zhu, L.; Elguindi, J.; Rensing, C.; Ravishankar, S. Antimicrobial activity of different copper alloy surfaces against copper resistant and sensitive *Salmonella enterica*. *Food Microbiol.* **2012**, *30*, 303–310. [CrossRef]
56. Manzoor, U.; Siddique, S.; Ahmed, R.; Noreen, Z.; Bokhari, H.; Ahmad, I. Antibacterial, Structural and Optical Characterization of Mechano-Chemically Prepared ZnO Nanoparticles. *PLoS ONE* **2016**, *11*, e0154704. [CrossRef]
57. Qin, H.; Zhao, Y.; An, Z.; Cheng, M.; Wang, Q.; Cheng, T.; Wang, Q.; Wang, J.; Jiang, Y.; Zhang, X.; et al. Enhanced antibacterial properties, biocompatibility, and corrosion resistance of degradable Mg-Nd-Zn-Zr alloy. *Biomaterials* **2015**, *53*, 211–220. [CrossRef]

58. Catalano, P.N.; Pezzoni, M.; Costa, C.; Soler-Illia, G.J.d.A.A.; Bellino, M.G.; Desimone, M.F. Optically transparent silver-loaded mesoporous thin film coating with long-lasting antibacterial activity. *Microporous Mesoporous Mater.* **2016**, *236*, 158–166. [CrossRef]
59. Aleksandrova, T.P.; Vais, A.A.; Masliy, A.I.; Burmistrov, V.A.; Gusev, A.A.; Bagavieva, S.K. Synthetic Fibers with Silver-Containing Coatings and Their Antimicrobial Properties. *Mater. Manuf. Process.* **2015**, *30*, 798–803. [CrossRef]
60. Tiller, J.C. Silver-based antimicrobial coatings. In *Polymeric Drug Delivery II: Polymeric Matrices and Drug Particle Engineering*; Svenson, S., Ed.; ACS Publications: Washington, DC, USA, 2006; pp. 215–231.
61. McQuillan, J.S.; Infante, H.G.; Stokes, E.; Shaw, A.M. Silver nanoparticle enhanced silver ion stress response in *Escherichia coli* K12. *Nanotoxicology* **2012**, *6*, 857–866. [CrossRef]
62. Ma, X.R.; Zhou, S.Y.; Xu, X.L.; Du, Q. Copper-containing nanoparticles: Mechanism of antimicrobial effect and application in dentistry-a narrative review. *Front. Surg.* **2022**, *9*, 905892. [CrossRef] [PubMed]
63. Salah, I.; Parkin, I.P.; Allan, E. Copper as an antimicrobial agent: Recent advances. *RSC Adv.* **2021**, *11*, 18179–18186. [CrossRef] [PubMed]
64. Wang, Y.G.; Li, H.Y.; Yuan, X.Y.; Jiang, Y.B.; Xiao, Z.A.; Li, Z. Review of copper and copper alloys as immune and antibacterial element. *Trans. Nonferrous Met. Soc. China* **2022**, *32*, 3163–3181. [CrossRef]
65. Almoudi, M.M.; Hussein, A.S.; Abu Hassan, M.I.; Zain, N.M. A systematic review on antibacterial activity of zinc against Streptococcus mutans. *Saudi Dent. J.* **2018**, *30*, 283–291. [CrossRef]
66. Gudkov, S.V.; Burmistrov, D.E.; Serov, D.A.; Rebezov, M.B.; Semenova, A.A.; Lisitsyn, A.B. A Mini Review of Antibacterial Properties of ZnO Nanoparticles. *Front. Phys.* **2021**, *9*, 641481. [CrossRef]
67. Li, Y.; Yang, Y.; Qing, Y.a.; Li, R.; Tang, X.; Guo, D.; Qin, Y. Enhancing ZnO-NP Antibacterial and Osteogenesis Properties in Orthopedic Applications: A Review. *Int. J. Nanomed.* **2020**, *15*, 6247–6262. [CrossRef]
68. Sirelkhatim, A.; Mahmud, S.; Seeni, A.; Kaus, N.H.M.; Ann, L.C.; Bakhori, S.K.M.; Hasan, H.; Mohamad, D. Review on Zinc Oxide Nanoparticles: Antibacterial Activity and Toxicity Mechanism. *Nano-Micro Lett.* **2015**, *7*, 219–242. [CrossRef]
69. Chen, Y.; Dou, J.; Yu, H.; Chen, C. Degradable magnesium-based alloys for biomedical applications: The role of critical alloying elements. *J. Biomater. Appl.* **2019**, *33*, 1348–1372. [CrossRef]
70. He, L.-J.; Shao, Y.; Li, S.-Q.; Cui, L.-Y.; Ji, X.-J.; Zhao, Y.-B.; Zeng, R.-C. Advances in layer-by-layer self-assembled coatings upon biodegradable magnesium alloys. *Sci. China-Mater.* **2021**, *64*, 2093–2106. [CrossRef]
71. Lin, Z.; Zhao, Y.; Zhang, Z.; Xi, Y.; Kelvin, Y. Antibacterial Properties, Hemolysis and Biocompatibility of Biodegradable Medical Magnesium Alloys. *Rare Met. Mater. Eng.* **2018**, *47*, 403–408.
72. Wu, W.; Wang, Z.; Zang, S.; Yu, X.; Yang, H.; Chang, S. Research Progress on Surface Treatments of Biodegradable Mg Alloys: A Review. *ACS Omega* **2020**, *5*, 941–947. [CrossRef] [PubMed]
73. Zheng, B.; Wang, J.; Wu, W.; Ou, J. Functionalized Coatings on Degradable Magnesium Alloys for Orthopedic Implants: A Review. *Trans. Indian Inst. Met.* **2023**, *76*, 613–627. [CrossRef]
74. Li, D.; Dai, D.; Xiong, G.; Lan, S.; Zhang, C. Composite Nanocoatings of Biomedical Magnesium Alloy Implants: Advantages, Mechanisms, and Design Strategies. *Adv. Sci.* **2023**, *10*, 2300658. [CrossRef]
75. Wu, W.L. Research progress of laser surface modification of magnesium alloys. *Lasers Eng.* **2008**, *18*, 71–84.
76. Taltavull, C.; Torres, B.; López, A.J.; Rodrigo, P.; Rams, J. Novel laser surface treatments on AZ91 magnesium alloy. *Surf. Coat. Technol.* **2013**, *222*, 118–127. [CrossRef]
77. Kumar, S.N.M.; Chethan, S.; Nikhil, T.; Dhruthi. A review on friction stir processing over other surface modification processing techniques of magnesium alloys. *Funct. Compos. Struct.* **2022**, *4*, 015006. [CrossRef]
78. Bhojak, V.; Jain, J.K.; Singhal, T.S.; Saxena, K.K.; Prakash, C.; Agrawal, M.K.; Malik, V. FRICTION STIR PROCESSING AND CLADDING: AN INNOVATIVE SURFACE ENGINEERING TECHNIQUE TO TAILOR MAGNESIUM-BASED ALLOYS FOR BIOMEDICAL IMPLANTS. *Surf. Rev. Lett.* **2023**, 2340007. [CrossRef]
79. Emelyanenko, A.M.; Domantovsky, A.G.; Kaminsky, V.V.; Pytskii, I.S.; Emelyanenko, K.A.; Boinovich, L.B. The Mechanisms of Antibacterial Activity of Magnesium Alloys with Extreme Wettability. *Materials* **2021**, *14*, 5454. [CrossRef]
80. Kundu, S.; Thakur, L. Microhardness and biological behavior of AZ91D-nHAp surface composite for bio-implants. *J. Electrochem. Sci. Eng.* **2022**, *13*, 137–147. [CrossRef]
81. Chen, J.; Zhang, Y.; Ibrahim, M.; Etim, I.P.; Tan, L.; Yang, K. In vitro degradation and antibacterial property of a copper-containing micro-arc oxidation coating on Mg-2Zn-1Gd-0.5Zr alloy. *Colloids Surf. B Biointerfaces* **2019**, *179*, 77–86. [CrossRef]
82. Chen, Y.; Dou, J.; Pang, Z.; Zheng, Z.; Yu, H.; Chen, C. Ag-containing antibacterial self-healing micro-arc oxidation coatings on Mg-Zn-Sr alloys. *Surf. Eng.* **2021**, *37*, 926–941. [CrossRef]
83. Cui, L.-Y.; Liu, H.-P.; Xue, K.; Zhang, W.-L.; Zeng, R.-C.; Li, S.-Q.; Xu, D.-k.; Han, E.-H.; Guan, S.-K. In Vitro Corrosion and Antibacterial Performance of Micro-Arc Oxidation Coating on AZ31 Magnesium Alloy: Effects of Tannic Acid. *J. Electrochem. Soc.* **2018**, *165*, C821–C829. [CrossRef]
84. Sukuroglu, E.E. Investigation of Antibacterial Susceptibility of Ag-Doped Oxide Coatings onto AZ91 Magnesium Alloy by Microarc Oxidation Method. *Adv. Mater. Sci. Eng.* **2018**, *2018*, 6871241. [CrossRef]
85. Zhou, J.; Li, K.; Wang, B.; Ai, F. Nano-hydroxyapatite/ZnO coating prepared on a biodegradable Mg-Zn-Ca bulk metallic glass by one-step hydrothermal method in acid situation. *Ceram. Int.* **2020**, *46*, 6958–6964. [CrossRef]

86. Zeng, R.; Liu, L.; Li, S.; Zou, Y.; Zhang, F.; Yang, Y.; Cui, H.; Han, E.-h. Self-Assembled Silane Film and Silver Nanoparticles Coating on Magnesium Alloys for Corrosion Resistance and Antibacterial Applications. *Acta Metall. Sin.-Engl. Lett.* **2013**, *26*, 681–686. [CrossRef]
87. Zhao, Y.; Shi, L.; Ji, X.; Li, J.; Han, Z.; Li, S.; Zeng, R.; Zhang, F.; Wang, Z. Corrosion resistance and antibacterial properties of polysiloxane modified layer-by-layer assembled self-healing coating on magnesium alloy. *J. Colloid Interface Sci.* **2018**, *526*, 43–50. [CrossRef]
88. Bakhsheshi-Rad, H.R.; Hamzah, E.; Ismail, A.F.; Aziz, M.; Karamian, E.; Iqbal, N. Bioactivity, in-vitro corrosion behavior, and antibacterial activity of silver-zeolites doped hydroxyapatite coating on magnesium alloy. *Trans. Nonferrous Met. Soc. China* **2018**, *28*, 1553–1562. [CrossRef]
89. Yan, T.; Tan, L.; Zhang, B.; Yang, K. Fluoride Conversion Coating on Biodegradable AZ31B Magnesium Alloy. *J. Mater. Sci. Technol.* **2014**, *30*, 666–674. [CrossRef]
90. Tatullo, M.; Piattelli, A.; Ruggiero, R.; Marano, R.M.; Iaculli, F.; Rengo, C.; Papallo, I.; Palumbo, G.; Chiesa, R.; Paduano, F.; et al. Functionalized magnesium alloys obtained by superplastic forming process retain osteoinductive and antibacterial properties: An in-vitro study. *Dent. Mater.* **2024**, *40*, 557–562. [CrossRef]
91. Saran, R.; Ginjupalli, K.; George, S.D.; Chidangil, S.; Unnikrishnan, V.K. LASER as a tool for surface modification of dental biomaterials: A review. *Heliyon* **2023**, *9*, e17457. [CrossRef]
92. Nasiri, Z.; Khorrami, M.S.; Mirzadeh, H.; Emamy, M. Enhanced mechanical properties of as-cast Mg-Al-Ca magnesium alloys by friction stir processing. *Mater. Lett.* **2021**, *296*, 129880. [CrossRef]
93. Patel, V.; Li, W.Y.; Vairis, A.; Badheka, V. Recent Development in Friction Stir Processing as a Solid-State Grain Refinement Technique: Microstructural Evolution and Property Enhancement. *Crit. Rev. Solid State Mater. Sci.* **2019**, *44*, 378–426. [CrossRef]
94. Cui, L.; Xue, K.; Li, S.; Zhang, F.; Liu, C.; Zeng, C. Research Progress on Antimicrobial Coatings for Biodegradable Magnesium Alloy Bone Implants. *Chin. J. Nonferrous Met.* **2021**, *31*, 3071–3092.
95. Lin, Z.; Wang, T.; Yu, X.; Sun, X.; Yang, H. Functionalization treatment of micro-arc oxidation coatings on magnesium alloys: A review. *J. Alloys Compd.* **2021**, *879*, 160453. [CrossRef]
96. Li, G.; Ma, F.; Liu, P.; Qi, S.; Li, W.; Zhang, K.; Chen, X. Review of micro-arc oxidation of titanium alloys: Mechanism, properties and applications. *J. Alloys Compd.* **2023**, *948*, 169773. [CrossRef]
97. Ji, X.-J.; Cheng, Q.; Wang, J.; Zhao, Y.-B.; Han, Z.-Z.; Zhang, F.; Li, S.-Q.; Zeng, R.-C.; Wang, Z.-L. Corrosion resistance and antibacterial effects of hydroxyapatite coating induced by polyacrylic acid and gentamicin sulfate on magnesium alloy. *Front. Mater. Sci.* **2019**, *13*, 87–98. [CrossRef]
98. Tacikowski, M.; Kaminski, J.; Rozniatowski, K.; Pisarek, M.; Jakiela, R.; Marchlewski, P.; Wierzchon, T. Improving the Properties of Composite Titanium Nitride Layers on the AZ91D Magnesium Alloy Using Hydrothermal Treatment. *Materials* **2021**, *14*, 5903. [CrossRef]
99. Song, D.; Lian, B.; Fu, Y.; Wang, G.; Qiao, Y.; Klu, E.E.; Gong, X.; Jiang, J. Dual-Layer Corrosion-Resistant Conversion Coatings on Mg-9Li Alloy via Hydrothermal Synthesis in Deionized Water. *Metals* **2021**, *11*, 1396. [CrossRef]
100. Li, L.-Y.; Cui, L.-Y.; Liu, B.; Zeng, R.-C.; Chen, X.-B.; Li, S.-Q.; Wang, Z.-L.; Han, E.-H. Corrosion resistance of glucose-induced hydrothermal calcium phosphate coating on pure magnesium. *Appl. Surf. Sci.* **2019**, *465*, 1066–1077. [CrossRef]
101. Li, K.; Wang, B.; Yan, B.; Lu, W. Preparing Ca-P coating on biodegradable magnesium alloy by hydrothermal method: In vitro degradation behavior. *Chin. Sci. Bull.* **2012**, *57*, 2319–2322. [CrossRef]
102. Miklaszewski, A.; Kowalski, K.; Jurczyk, M. Hydrothermal Surface Treatment of Biodegradable Mg-Materials. *Metals* **2018**, *8*, 894. [CrossRef]
103. Miura, K.; Kobayashi, Y.; Naito, T.; Yamada, A.; Ikarashi, A.; Hayashi, N.; Isobe, K. Influence of Chemical Pretreatments on the Effectiveness of Hydrothermal Treatment to Enhance the Pitting Corrosion Resistance of Magnesium Alloy. *J. Jpn. Inst. Met.* **2010**, *74*, 771–778. [CrossRef]
104. Cui, L.-Y.; Gao, L.; Zhang, J.-C.; Tang, Z.; Fan, X.-L.; Liu, J.-C.; Chen, D.-C.; Zeng, R.-C.; Li, S.-Q.; Zhi, K.-Q. In vitro corrosion resistance, antibacterial activity and cytocompatibility of a layer-by-layer assembled DNA coating on magnesium alloy. *J. Magnes. Alloys* **2021**, *9*, 266–280. [CrossRef]
105. Gao, F.; Hu, Y.; Li, G.; Liu, S.; Quan, L.; Yang, Z.; Wei, Y.; Pan, C. Layer-by-layer deposition of bioactive layers on magnesium alloy stent materials to improve corrosion resistance and biocompatibility. *Bioact. Mater.* **2020**, *5*, 611–623. [CrossRef]
106. Qiu, X.; Li, Z.; Li, X.; Zhang, Z. Flame retardant coatings prepared using layer by layer assembly: A review. *Chem. Eng. J.* **2018**, *334*, 108–122. [CrossRef]
107. Escorcia-Díaz, D.; García-Mora, S.; Rendón-Castrillón, L.; Ramírez-Carmona, M.; Ocampo-López, C. Advancements in Nanoparticle Deposition Techniques for Diverse Substrates: A Review. *Nanomaterials* **2023**, *13*, 2586. [CrossRef]
108. Maqsood, M.F.; Raza, M.A.; Ghauri, F.A.; Rehman, Z.U.; Ilyas, M.T. Corrosion study of graphene oxide coatings on AZ31B magnesium alloy. *J. Coat. Technol. Res.* **2020**, *17*, 1321–1329. [CrossRef]
109. Gao, Z.; Zhang, D.; Liu, Z.; Li, X.; Jiang, S.; Zhang, Q. Formation mechanisms of environmentally acceptable chemical conversion coatings for zinc: A review. *J. Coat. Technol. Res.* **2019**, *16*, 1–13. [CrossRef]
110. Hornberger, H.; Virtanen, S.; Boccaccini, A.R. Biomedical coatings on magnesium alloys—A review. *Acta Biomater.* **2012**, *8*, 2442–2455. [CrossRef]
111. Liu, Z.; Gao, W. Electroless nickel plating on AZ91 Mg alloy substrate. *Surf. Coat. Technol.* **2006**, *200*, 5087–5093. [CrossRef]

112. Li, J.; Bai, H.; Feng, Z. Advances in the Modification of Silane-Based Sol-Gel Coating to Improve the Corrosion Resistance of Magnesium Alloys. *Molecules* **2023**, *28*, 2563. [CrossRef] [PubMed]
113. Shang, W.; Wang, Y.Y.; Wen, Y.Q.; Zhan, X.Q.; Kong, D. Study on the Properties of Micro—Arc Oxidation Self—Assembled Composite coatings on Magnesium Alloy. *Int. J. Electrochem. Sci.* **2017**, *12*, 11875–11891. [CrossRef]
114. Zhao, W.; Wang, J.; Jiang, W.; Bo, Q.; Wang, Y.; Li, Y.; Jiang, D. A novel biodegradable Mg-1Zn-0.5Sn alloy: Mechanical properties, corrosion behavior, biocompatibility, and antibacterial activity. *J. Magnes. Alloys* **2020**, *8*, 374–386. [CrossRef]
115. Tie, D.; Feyerabend, F.; Mueller, W.-D.; Schade, R.; Liefeith, K.; Kainer, K.U.; Willumeit, R. Antibacterial biodegradable Mg-Ag alloys. *Eur. Cells Mater.* **2013**, *25*, 284–298. [CrossRef] [PubMed]
116. He, G.; Wu, Y.; Zhang, Y.; Zhu, Y.; Liu, Y.; Li, N.; Li, M.; Zheng, G.; He, B.; Yin, Q.; et al. Addition of Zn to the ternary Mg-Ca-Sr alloys significantly improves their antibacterial properties. *J. Mater. Chem. B* **2015**, *3*, 6676–6689. [CrossRef]
117. Liu, Z.; Schade, R.; Luthringer, B.; Hort, N.; Rothe, H.; Mueller, S.; Liefeith, K.; Willumeit-Roemer, R.; Feyerabend, F. Influence of the Microstructure and Silver Content on Degradation, Cytocompatibility, and Antibacterial Properties of Magnesium-Silver Alloys In Vitro. *Oxidative Med. Cell. Longev.* **2017**, *2017*, 8091265. [CrossRef]
118. Liu, C.; Fu, X.; Pan, H.; Wan, P.; Wang, L.; Tan, L.; Wang, K.; Zhao, Y.; Yang, K.; Chu, P.K. Biodegradable Mg-Cu alloys with enhanced osteogenesis, angiogenesis, and long-lasting antibacterial effects. *Sci. Rep.* **2016**, *6*, 27374. [CrossRef]
119. Wang, H.; Shi, Z. In vitro biodegradation behavior of magnesium and magnesium alloy. *J. Biomed. Mater. Res. Part B-Appl. Biomater.* **2011**, *98B*, 203–209. [CrossRef]
120. Huan, Z.G.; Leeflang, M.A.; Zhou, J.; Fratila-Apachitei, L.E.; Duszczyk, J. In vitro degradation behavior and cytocompatibility of Mg-Zn-Zr alloys. *J. Mater. Sci.-Mater. Med.* **2010**, *21*, 2623–2635. [CrossRef]
121. Li, Y.; Liu, L.; Wan, P.; Zhai, Z.; Mao, Z.; Ouyang, Z.; Yu, D.; Sun, Q.; Tan, L.; Ren, L.; et al. Biodegradable Mg-Cu alloy implants with antibacterial activity for the treatment of osteomyelitis: In vitro and in vivo evaluations. *Biomaterials* **2016**, *106*, 250–263. [CrossRef]
122. Jiang, W.; Wang, J.; Liu, Q.; Zhao, W.; Jiang, D.; Guo, S. Low hydrogen release behavior and antibacterial property of Mg-4Zn-xSn alloys. *Mater. Lett.* **2019**, *241*, 88–91. [CrossRef]
123. Yu, W.; Chen, D.; Ding, Z.; Qiu, M.; Zhang, Z.; Shen, J.; Zhang, X.; Zhang, S.; He, Y.; Shi, Z. Synergistic effect of a biodegradable Mg-Zn alloy on osteogenic activity and anti-biofilm ability: An in vitro and in vivo study. *RSC Adv.* **2016**, *6*, 45219–45230. [CrossRef]
124. Zhao, X.; Wan, P.; Wang, H.; Zhang, S.; Liu, J.; Chang, C.; Yang, K.; Pan, Y. An Antibacterial Strategy of Mg-Cu Bone Grafting in Infection-Mediated Periodontics. *Biomed. Res. Int.* **2020**, *2020*, 7289208. [CrossRef] [PubMed]
125. Watroba, M.; Bednarczyk, W.; Szewczyk, P.K.; Kawalko, J.; Mech, K.; Grunewald, A.; Unalan, I.; Taccardi, N.; Boelter, G.; Banzhaf, M.; et al. In vitro cytocompatibility and antibacterial studies on biodegradable Zn alloys supplemented by a critical assessment of direct contact cytotoxicity assay. *J. Biomed. Mater. Res. B Appl. Biomater.* **2023**, *111*, 241–260. [CrossRef] [PubMed]
126. Robinson, D.A.; Griffith, R.W.; Shechtman, D.; Evans, R.B.; Conzemius, M.G. In vitro antibacterial properties of magnesium metal against Escherichia coli, Pseudomonas aeruginosa and Staphylococcus aureus. *Acta Biomater.* **2010**, *6*, 1869–1877. [CrossRef]
127. Li, Y.; Liu, G.; Zhai, Z.; Liu, L.; Li, H.; Yang, K.; Tan, L.; Wan, P.; Liu, X.; Ouyang, Z.; et al. Antibacterial Properties of Magnesium In Vitro and in an In Vivo Model of Implant-Associated Methicillin-Resistant Staphylococcus aureus Infection. *Antimicrob. Agents Chemother.* **2014**, *58*, 7586–7591. [CrossRef]
128. Lock, J.Y.; Draganov, M.; Whall, A.; Dhillon, S.; Upadhyayula, S.; Vullev, V.I.; Liu, H. Antimicrobial properties of biodegradable magnesium for next generation ureteral stent applications. In Proceedings of the 2012 Annual International Conference of the IEEE Engineering in Medicine and Biology Society, San Diego, CA, USA, 28 August–1 September 2012; pp. 1378–1381. [CrossRef]
129. Padan, E.; Bibi, E.; Ito, M.; Krulwich, T.A. Alkaline pH homeostasis in bacteria: New insights. *Biochim. Biophys. Acta-Biomembr.* **2005**, *1717*, 67–88. [CrossRef]
130. Behbahani, S.B.; Kiridena, S.D.; Wijayaratna, U.N.; Taylor, C.; Anker, J.N.; Tzeng, T.-R.J. pH variation in medical implant biofilms: Causes, measurements, and its implications for antibiotic resistance. *Front. Microbiol.* **2022**, *13*, 1028560. [CrossRef]
131. Stewart, E.J.; Ganesan, M.; Younger, J.G.; Solomon, M.J. Artificial biofilms establish the role of matrix interactions in staphylococcal biofilm assembly and disassembly. *Sci. Rep.* **2015**, *5*, 13081. [CrossRef]
132. Fattah-alhosseini, A.; Molaei, M.; Nouri, M.; Babaei, K. Antibacterial activity of bioceramic coatings on Mg and its alloys created by plasma electrolytic oxidation (PEO): A review. *J. Magnes. Alloys* **2022**, *10*, 81–96. [CrossRef]
133. Lin, Z.; Sun, X.; Yang, H. The Role of Antibacterial Metallic Elements in Simultaneously Improving the Corrosion Resistance and Antibacterial Activity of Magnesium Alloys. *Mater. Des.* **2021**, *198*, 109350. [CrossRef]
134. Zhang, D.; Liu, Y.; Liu, Z.; Wang, Q. Advances in Antibacterial Functionalized Coatings on Mg and Its Alloys for Medical Use-A Review. *Coatings* **2020**, *10*, 828. [CrossRef]
135. Rahim, M.I.; Eifler, R.; Rais, B.; Mueller, P.P. Alkalization is responsible for antibacterial effects of corroding magnesium. *J. Biomed. Mater. Res. Part A* **2015**, *103*, 3526–3532. [CrossRef] [PubMed]
136. Xu, L.; Liu, X.; Sun, K.; Fu, R.; Wang, G. Corrosion Behavior in Magnesium-Based Alloys for Biomedical Applications. *Materials* **2022**, *15*, 2613. [CrossRef] [PubMed]
137. Lamaka, S.V.; Gonzalez, J.; Mei, D.; Feyerabend, F.; Willumeit-Römer, R.; Zheludkevich, M.L. Local pH and Its Evolution Near Mg Alloy Surfaces Exposed to Simulated Body Fluids. *Adv. Mater. Interfaces* **2018**, *5*, 1800169. [CrossRef]

138. Nordlien, J.H.; Ono, S.; Masuko, N.; Nis¸ancioĞlu, K. Morphology and Structure of Oxide Films Formed on Magnesium by Exposure to Air and Water. *J. Electrochem. Soc.* **1995**, *142*, 3320. [CrossRef]
139. Ascencio, M.; Pekguleryuz, M.; Omanovic, S. An investigation of the corrosion mechanisms of WE43 Mg alloy in a modified simulated body fluid solution: The influence of immersion time. *Corros. Sci.* **2014**, *87*, 489–503. [CrossRef]
140. Cui, Z.; Ge, F.; Lin, Y.; Wang, L.; Lei, L.; Tian, H.; Yu, M.; Wang, X. Corrosion behavior of AZ31 magnesium alloy in the chloride solution containing ammonium nitrate. *Electrochim. Acta* **2018**, *278*, 421–437. [CrossRef]
141. Yao, H.B.; Li, Y.; Wee, A.T.S. An XPS investigation of the oxidation/corrosion of melt-spun Mg. *Appl. Surf. Sci.* **2000**, *158*, 112–119. [CrossRef]
142. Marco, I.; Feyerabend, F.; Willumeit-Römer, R.; Van der Biest, O. Influence of Testing Environment on the Degradation Behavior of Magnesium Alloys for Bioabsorbable Implants. In *TMS2015 Supplemental Proceedings*; Springer: Berlin/Heidelberg, Germany, 2015; pp. 497–506.
143. Tie, D.; Feyerabend, F.; Hort, N.; Hoeche, D.; Kainer, K.U.; Willumeit, R.; Mueller, W.D. In vitro mechanical and corrosion properties of biodegradable Mg-Ag alloys. *Mater. Corros.* **2014**, *65*, 569–576. [CrossRef]
144. Rossrucker, L.; Samaniego, A.; Grote, J.P.; Mingers, A.M.; Laska, C.A.; Birbilis, N.; Frankel, G.S.; Mayrhofer, K.J.J. The pH Dependence of Magnesium Dissolution and Hydrogen Evolution during Anodic Polarization. *J. Electrochem. Soc.* **2015**, *162*, C333. [CrossRef]
145. Li, Z.; Gu, X.; Lou, S.; Zheng, Y. The development of binary Mg-Ca alloys for use as biodegradable materials within bone. *Biomaterials* **2008**, *29*, 1329–1344. [CrossRef] [PubMed]
146. Demishtein, K.; Reifen, R.; Shemesh, M. Antimicrobial Properties of Magnesium Open Opportunities to Develop Healthier Food. *Nutrients* **2019**, *11*, 2363. [CrossRef] [PubMed]
147. Xie, Y.; Yang, L. Calcium and Magnesium Ions Are Membrane-Active against Stationary-Phase Staphylococcus aureus with High Specificity. *Sci. Rep.* **2016**, *6*, 20628. [CrossRef]
148. Xie, K.; Wang, N.; Guo, Y.; Zhao, S.; Tan, J.; Wang, L.; Li, G.; Wu, J.; Yang, Y.; Xu, W.; et al. Additively manufactured biodegradable porous magnesium implants for elimination of implant-related infections: An in vitro and in vivo study. *Bioact. Mater.* **2022**, *8*, 140–152. [CrossRef]
149. Hu, T.; Xu, H.; Wang, C.; Qin, H.; An, Z. Magnesium enhances the chondrogenic differentiation of mesenchymal stem cells by inhibiting activated macrophage-induced inflammation. *Sci. Rep.* **2018**, *8*, 3406. [CrossRef]
150. Wolf, F.I.; Cittadini, A. Chemistry and biochemistry of magnesium. *Mol. Asp. Med.* **2003**, *24*, 3–9. [CrossRef]
151. Wolf, F.I.; Torsello, A.; Fasanella, S.; Cittadini, A. Cell physiology of magnesium. *Mol. Asp. Med.* **2003**, *24*, 11–26. [CrossRef]
152. Feng, H.; Wang, G.; Jin, W.; Zhang, X.; Huang, Y.; Gao, A.; Wu, H.; Wu, G.; Chu, P.K. Systematic Study of Inherent Antibacterial Properties of Magnesium-based Biomaterials. *ACS Appl. Mater. Interfaces* **2016**, *8*, 9662–9673. [CrossRef]
153. Anic˘ić, N.; Vukomanović, M.; Koklic˘, T.; Suvorov, D. Fewer Defects in the Surface Slows the Hydrolysis Rate, Decreases the ROS Generation Potential, and Improves the Non-ROS Antimicrobial Activity of MgO. *Small* **2018**, *14*, 1800205. [CrossRef]
154. Sawai, J.; Igarashi, H.; Hashimoto, A.; Kokugan, T.; Shimizu, M. Evaluation of Growth Inhibitory Effect of Ceramics Powder Slurry on Bacteria by Conductance Method. *J. Chem. Eng. Jpn.* **1995**, *28*, 288–293. [CrossRef]
155. Gomaa, O.M.; Costa, N.L.; Paquete, C.M. Electron transfer in Gram-positive bacteria: Enhancement strategies for bioelectrochemical applications. *World J. Microbiol. Biotechnol.* **2022**, *38*, 83. [CrossRef] [PubMed]
156. Shi, L.; Dong, H.; Reguera, G.; Beyenal, H.; Lu, A.; Liu, J.; Yu, H.-Q.; Fredrickson, J.K. Extracellular electron transfer mechanisms between microorganisms and minerals. *Nat. Rev. Microbiol.* **2016**, *14*, 651–662. [CrossRef] [PubMed]
157. Jin, G.; Qin, H.; Cao, H.; Qian, S.; Zhao, Y.; Peng, X.; Zhang, X.; Liu, X.; Chu, P.K. Synergistic effects of dual Zn/Ag ion implantation in osteogenic activity and antibacterial ability of titanium. *Biomaterials* **2014**, *35*, 7699–7713. [CrossRef]
158. Boyer, P.D. The ATP synthase—A splendid molecular machine. *Annu. Rev. Biochem.* **1997**, *66*, 717–749. [CrossRef]
159. Cao, H.; Liu, X.; Meng, F.; Chu, P.K. Biological actions of silver nanoparticles embedded in titanium controlled by micro-galvanic effects. *Biomaterials* **2011**, *32*, 693–705. [CrossRef]
160. von Ballmoos, C. Alternative proton binding mode in ATP synthases. *J. Bioenerg. Biomembr.* **2007**, *39*, 441–445. [CrossRef]
161. Trumpower, B.L.; Gennis, R.B. Energy transduction by cytochrome complexes in mitochondrial and bacterial respiration: The enzymology of coupling electron transfer reactions to transmembrane proton translocation. *Annu. Rev. Biochem.* **1994**, *63*, 675–716. [CrossRef]

crystals

MDPI

Article

Effect of Erbium Micro-Additions on Microstructures and Properties of 2024 Aluminum Alloy Prepared by Microwave Sintering

Tao Qin [1,*], Bowen Fan [1], Jincheng Yu [1], Chengwei Bu [1] and Jiukun Zhang [2]

[1] School of Mechanical Engineering, Wuxi Institute of Technology, Wuxi 214121, China
[2] Wuxi Wanling High Frequency Equipment Manufacturing Co., Ltd., Wuxi 214100, China
* Correspondence: qint@wxit.edu.cn

Abstract: The effects of rare earth erbium (Er) micro-additions on the microstructures and mechanical properties of 2024 aluminum alloy were investigated. The microstructures and fracture surfaces of specimens prepared via high-energy ball milling, cold isostatic pressing and microwave sintering were carried out by optical microscopy (OM) and scanning electron microscopy (SEM). Under the conditions of sintering heating rate of 20 min/°C and soaking time of 30 min at 490 °C, it was found that with the increase in Er addition, the grain size first decreased then increased, and it reached a minimum size of about 5 μm when the Er content was 0.6%, showing that the grains were refined. At the same time, the compactness and microhardness reached maximum levels, which were 97.6% and 94.5 HV, respectively. Moreover, the tensile strength and elongation reached the peak at 160.5 MPa and 4.4%, respectively. The dynamic mechanical response of Er/2024Al alloy with different Er content was studied through a split Hopkinson pressure bar (SHPB) at strain rates of 600 s^{-1} and 800 s^{-1}, respectively. Both at the strain rates of 600 s^{-1} and 800 s^{-1}, the dynamic yield stress of the specimens increased gradually with an increase in Er content. For the 0.6 wt.% Er specimen, the dynamic yield stress reached 371.3 MPa at a strain rate of 800 s^{-1}, which was 28.2% higher than that at a strain rate of 600 s^{-1}. When the strain rate is 800 s^{-1}, the deformation degree of the 0.6 wt.%Er specimen is 55.3%, which is 14.7% higher than for the Er-free one, and there are adiabatic shear bands formed in the 0.6 wt.%Er specimen. Through a fracture analysis of the samples, a certain number of dimples appeared in the fracture of an impact specimen, indicating that the addition of Er improved the toughness of the material. This research can provide a reference for the development and application of high-performance aluminum alloy in automotive structural materials.

Keywords: Er; microwave sintering; microstructure; mechanical properties; split Hopkinson pressure bar

1. Introduction

2024 aluminum alloy (2024Al) belongs to the aluminum–copper–magnesium series. Its composition is well balanced and possesses good comprehensive mechanical properties. It is the most widely used aluminum alloy of the 2 series aluminum alloys, it is widely used in aviation (such as in aircraft engines, structural parts, wings, etc.), power machinery, electronics, automobile manufacturing, and other fields [1,2], and it is one of the most ideal lightweight structural materials. In the 2024 aluminum alloy, Cu and Mg are the main alloying elements. In addition, there is a small amount of Mn and trace amounts of Si and Fe. The preparation methods of the alloy mainly include fusion casting and powder metallurgy. The advantages of the melt casting method are its simple process, low cost, and the ability to prepare castings with complex shapes. However, during preparation, there are inevitably defects such as component segregation, coarse grains, and interfacial reaction, etc. [3]. Being a new powder metallurgy method, microwave sintering (MWS)

can effectively avoid composition segregation, reduce interfacial reactions, promote the uniform distribution of reinforcements, refine grains, and improve solid solubility [4]. Microwave sintering has become the main method to prepare high-performance aluminum alloys [5–8].

The energy crisis and the increasingly severe environmental protection situation have put forward higher requirements for lightweight high-performance structural materials. Rare earth elements have special physical and chemical activities and can be used as an ideal adding phase. Adding an appropriate amount of rare earth elements can refine the grain, optimize the structure, and eliminate impurities, and, furthermore, it can improve the comprehensive mechanical properties of alloys or composites [9,10]. As the most widely used high-strength lightweight material, the 2024 aluminum alloy is generally added with alloying elements to improve its microstructure and mechanical properties, and the addition of rare earth elements and their oxides has been proven to be one of the most effective methods. There are three strengthening mechanisms of rare earth elements in aluminum alloy or matrix composites: solid solution strengthening, fine grain strengthening, and dispersion strengthening [11].

In recent years, researchers have tried to explore the effects of different rare earth elements on the microstructures and mechanical properties of aluminum alloys. In 2009, TSAI Y C et al. [12] tried to add a certain amount of La into the A356 aluminum alloy. When the content of La was greater than 0.6%, the breaking elongation of the alloy was significantly improved, and when the content of La reached 1.0%, the eutectic Si phase in the alloy changed from coarse slats to short fibers. In 2019, Zhong Tao et al. [13] added a small amount (0.35 wt.%) of Ce to the 3003 aluminum alloy, and the micro Vickers hardness (HV) of the alloy obtained was 56.3 HV higher than that without Ce. In 2019, Ding W W et al. [14] added the Al-10Y alloy to the 6063 aluminum alloy, and the grain of the modified alloy was obviously refined, and the microstructure became more uniform. Studies have shown that an appropriate amount of rare earth Er has a good modification effect on the eutectic Al-Si alloy, and the addition of Er improves the mechanical properties of hypoeutectic aluminum alloy more than that of rare earth La [15,16]. The rare earth Er is another effective microalloying element besides Sc in aluminum alloys [17,18], and its price is relatively low. A micro amount of Er can generate fine and dispersed Al_3Er particles in Al-Mg, Al-Mn, and Al-Zn-Mg alloys, which can effectively stabilize the substructure, inhibit recrystallization, and improve the comprehensive properties of the alloy [19]. On the premise of keeping the breaking elongation of the alloy unchanged, a small amount of Er addition can not only greatly improve the room temperature strength of pure aluminum and aluminum magnesium alloys, but can also increase the recrystallization temperature of the alloy, which is conducive to an improvement in high-temperature properties.

At present, the research on rare earth reinforced aluminum alloy mainly focuses on the fusion casting method, and on the mechanism of Y, Ce, La, and their mixtures in aluminum alloy and aluminum matrix composites. Compared to other rare earth elements such as Y, Ce, and La, the price of the rare earth element Er is more affordable, yet it has similar effects in enhancing the mechanical properties of aluminum alloys. This makes it more attractive economically. In addition, the research on adding rare earth elements to aluminum matrix composites prepared by microwave sintering is less. Different from traditional sintering methods, microwave sintering has the characteristics of uniform temperature, fast low-temperature sintering, and selective sintering. Therefore, it is necessary to explore the process of preparing a rare earth aluminum alloy by microwave sintering to further improve the properties of the aluminum alloy and its composites and develop new aluminum matrix composites. In this paper, the 2024Al-Er alloy was prepared by high energy ball milling, cold isostatic pressing, and microwave sintering, the effect of Er on the microstructure and mechanical properties was studied, and the mechanism by which the addition of Er affects the microstructure and performance of the alloy was discussed; in particular, the dynamic mechanical properties of the 2024Al-Er alloy were analyzed in detail, which provided a feasible idea for the preparation and development of a high-performance aluminum alloy.

2. Experimental Details

Commercial powders of 2024Al and Er were used as raw materials for the experiment. The particle size of the 2024Al powder was below 5 μm and that of the Er powder was below 40 μm. The morphologies of the two original powders are shown in Figure 1, and the chemical composition of 2024Al and the experimental scheme for preparing the new 2024Al-Er alloy are shown in Tables 1 and 2.

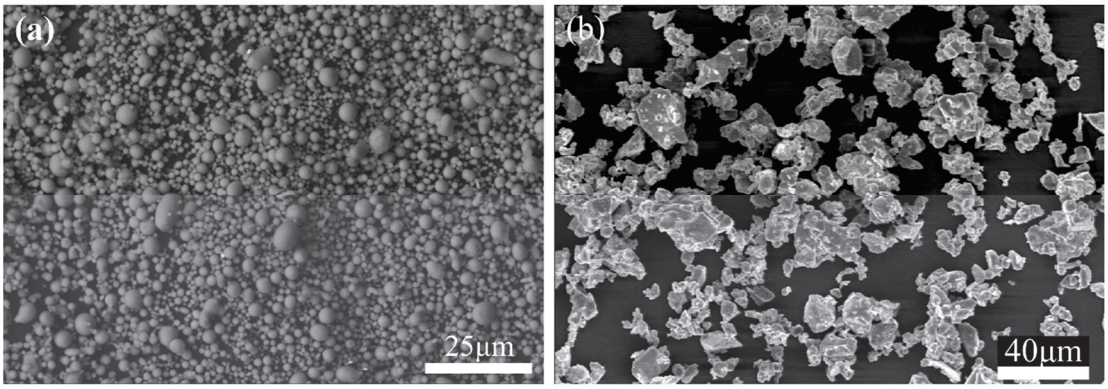

Figure 1. Morphology of the original powder: (**a**) 2024Al and (**b**) Er.

Table 1. The chemical composition of 2024Al (wt.%).

Element	Al	Cu	Mg	Mn	Si	Fe	Cr	Zn	Ti	Others
Content	Residual	3.8–4.9	1.2–1.8	0.3–0.9	≤0.5	≤0.5	≤0.1	≤0.25	≤0.15	≤0.15

Table 2. Experimental plan for the preparation of 2024Al-Er alloy (wt.%).

Serial No.	2024Al	Er
0	100.0	0
1	99.8	0.2
2	99.6	0.4
3	99.4	0.6
4	99.2	0.8

Firstly, the two powders were mixed according to the proportion of ingredients and then placed into the high-energy ball milling machine for ball milling. The ball milling process parameters are shown in Table 3.

Table 3. The ball milling process parameters.

Parameters	Level
Milling time	5 h
Alcohol-to-powder material ratio	2:3
Balls-to-materials ratio	5:1
Large balls-to-medium balls-to-small balls ratio	1:2:4

After high-energy ball milling, the evenly mixed powder was placed in a vacuum-drying oven at 60 °C for 72 h. Then, the dried powder was filled into the rubber mold, which was put into the cold isostatic press machine. The rubber mold filled with mixed powder could withstand a pressure of 300 MPa for 2 min. The pressed green bodies were sintered in the microwave sintering equipment with argon protection. The optimized microwave sintering process is demonstrated in Table 4.

Table 4. The technological parameters of microwave sintering process.

Parameters	Level
Output power	4 kW
Frequency	2.45 GHz
Heating temperature	490 °C
Heating rate	20 °C/min
Soaking time	30 min

The sintered specimens for microstructure observations were mechanically polished and then etched using Kohler reagent (2.5%HNO_3 + 1.5%HCl + 1%HF + 95%H_2O). The microstructures of the specimens were observed by the S-3400 N scanning electron microscope (SEM), and the phase analysis was performed using a D8 ADVANCE X-ray diffractometer (XRD)(BRUKER AXS GMBH, Karlsruhe, Germany).

The compactness of the 1 cm × 1 cm × 1 cm block was obtained in the experiment by means of the Archimedes principle. The actual density of the specimen can be calculated using Equation (1):

$$\rho = \frac{m_1}{m_1 - m_2} \cdot \rho_{water} \tag{1}$$

where ρ is the density of the specimen, ρ_{water} the density of distilled water used in the experiment, m_1 is the mass of the dry specimen, and m_2 is the mass of the specimen in the distilled water. The full density ρ_0 of the alloy can be calculated using Equation (2):

$$\rho_0 = \sum \rho_i \cdot v_i \tag{2}$$

where ρ_i is the theoretical density of i phase, and v_i is the volume fraction. Then, the compactness I can be calculated from Equation (3):

$$I = \frac{\rho}{\rho_0} \tag{3}$$

The dynamic compressive properties of the specimens were tested by the split Hopkinson pressure bar (SHPB). A schematic illustration of the SHPB system is presented in Figure 2. Cylindrical specimens of 8 mm diameter and 6 mm height were prepared for SHPB experiments. The specimens after a dynamic impact test were cut along the axial direction. After grinding, polishing, and etching, the microstructure changes after deformation were analyzed by OM and SEM. Moreover, the fracture morphology was observed. The effect of different Er additions on the impact deformation and failure behavior of the alloy was studied.

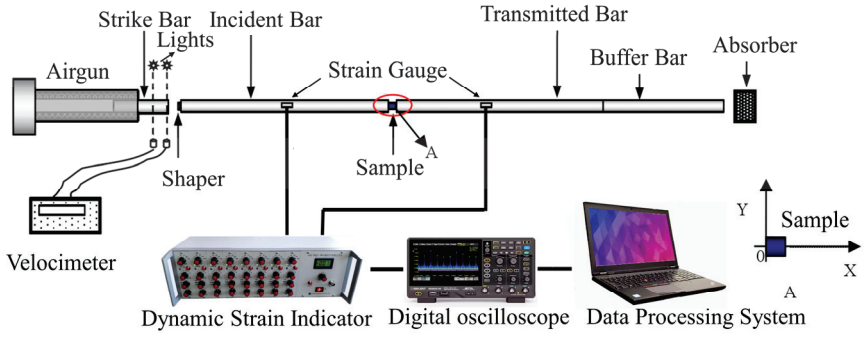

Figure 2. Schematic representation of split Hopkinson pressure bar (SHPB) system.

3. Results and Discussion

3.1. Microstructure

Figure 3 presents the SEM micrographs of the 2024Al-Er alloy with different Er contents: 0% (Figure 3a), 0.2 wt.% (Figure 3b), 0.4 wt.% (Figure 3c), 0.6 wt.% (Figure 3d), and

0.8 wt.% (Figure 3e). The Er-containing specimens showed changes in microstructure in comparison to the Er-free one.

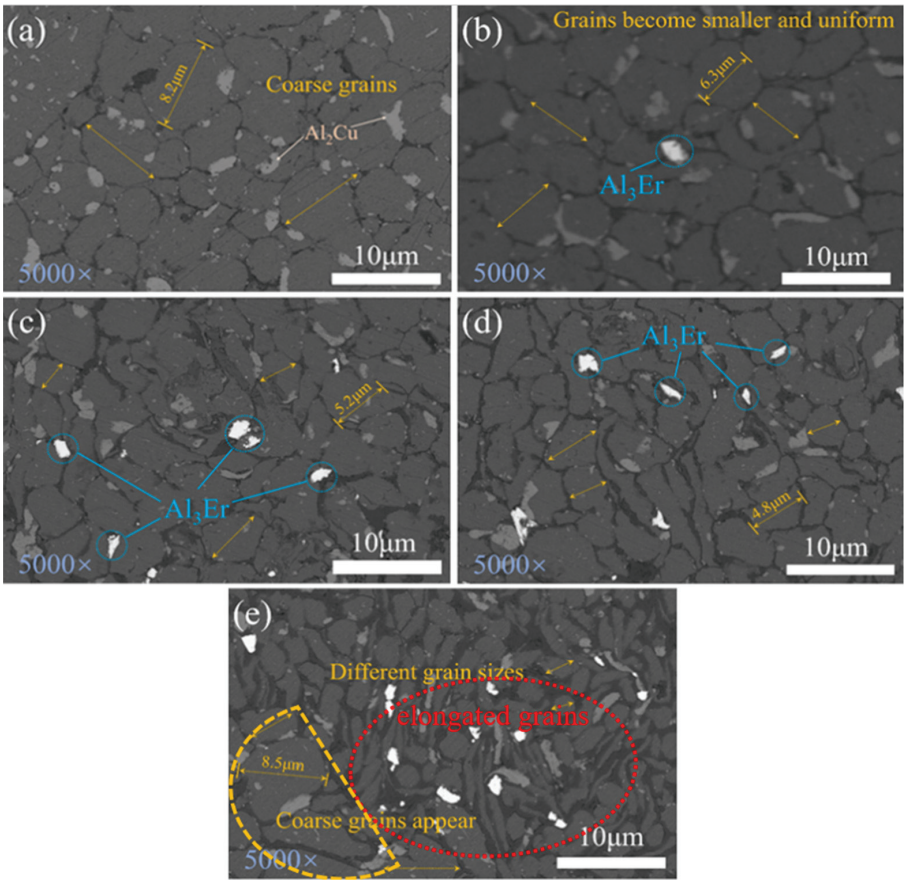

Figure 3. The SEM micrographs of 2024Al-Er alloy with different Er content: (**a**) Er-free, (**b**) 0.2 wt.%, (**c**) 0.4 wt.%, (**d**) 0.6 wt.%, and (**e**) 0.8 wt.%.

Firstly, the grain size of the specimens changed. The grain size of the Er-free specimen is large and inhomogeneous, and the diameter of large grains is about 8 μm. With the increase in Er content, the grain size decreases gradually. When Er content is 0.6 wt.%, the average grain diameter is less than 5 μm. The grain size is significantly refined, and the grain shape is relatively smooth. The grain refinement in the 2024 aluminum alloy is mainly due to the addition of Er, which reacts with the Al in the matrix and generates fine Al_3Er particles dispersed on the 2024Al matrix. These fine Al_3Er particles can pin the dislocation and sub-grain boundary of the composite, and hinder the recombination of the dislocations and the migration of the sub-grain boundary, thus delaying the nucleation and growth of the grains and playing a role in refining grains. This is similar to previous research, which has shown that Er and Al can form an Al_3Er compound. This compound has a high melting point and shares the same crystal structure as the aluminum matrix, making it suitable as a core for heterogeneous nucleation [20,21].

Secondly, the substitutional solid solution can be formed when Er is dissolved in the 2024Al matrix, which can fill the defects on the surface of the alloy phase, and it is also conducive to improving the nucleation rate, which is an important means of grain refinement. Moreover, during microwave sintering, Er can interact strongly with impurity elements Si and Fe in the 2024Al alloy, preventing them from entering the solid solution. Therefore, Er also has a certain purification effect on the grain boundary of the 2024Al alloy and can improve the toughness of the aluminum alloy [22].

When the Er content reaches 0.8 wt.% (Figure 3e), the grain size is uneven, with coarse elongated grains coexisting with fine ones and also including some coarse equiaxed grains.

Such anisotropy in grain size and shape is detrimental to the mechanical proper-ties of the alloy. According to the literature, it can be inferred that the content of Er is high, forming inclusion Al_8Cu_4Er [23], and the refining effect is weakened.

Figure 4 presents the microstructure of the 2024Al-Er alloy obtained by SEM and the EDS mapping of the typical region of the 0.6 wt.% Er alloy. The EDS energy spectrum analysis was performed on the spot marked in Figure 4a, and the results show that the ratio of the atomic numbers of Al and Er is about 3:1 (Figure 4f), which can be deduced to be the Al_3Er phase [24]. In Figure 4d, the content of the Er element in the marked area is obviously larger, which corresponds to Al_3Er phases (Figure 4a), while there is a certain amount of Er in other areas, and the distribution is relatively uniform. On the one hand, Er dissolved in the 2024 aluminum alloy matrix can form a substitutional solid solution, which plays a role in solution strengthening; on the other hand, Er and Al form a fine compound Al_3Er, which is dispersedly distributed in the 2024Al matrix. The distribution of Cu (Figure 4c) is relatively uniform, and there will be some elements gathered in a small range, mainly the Al_2Cu phase in the 2024 aluminum alloy.

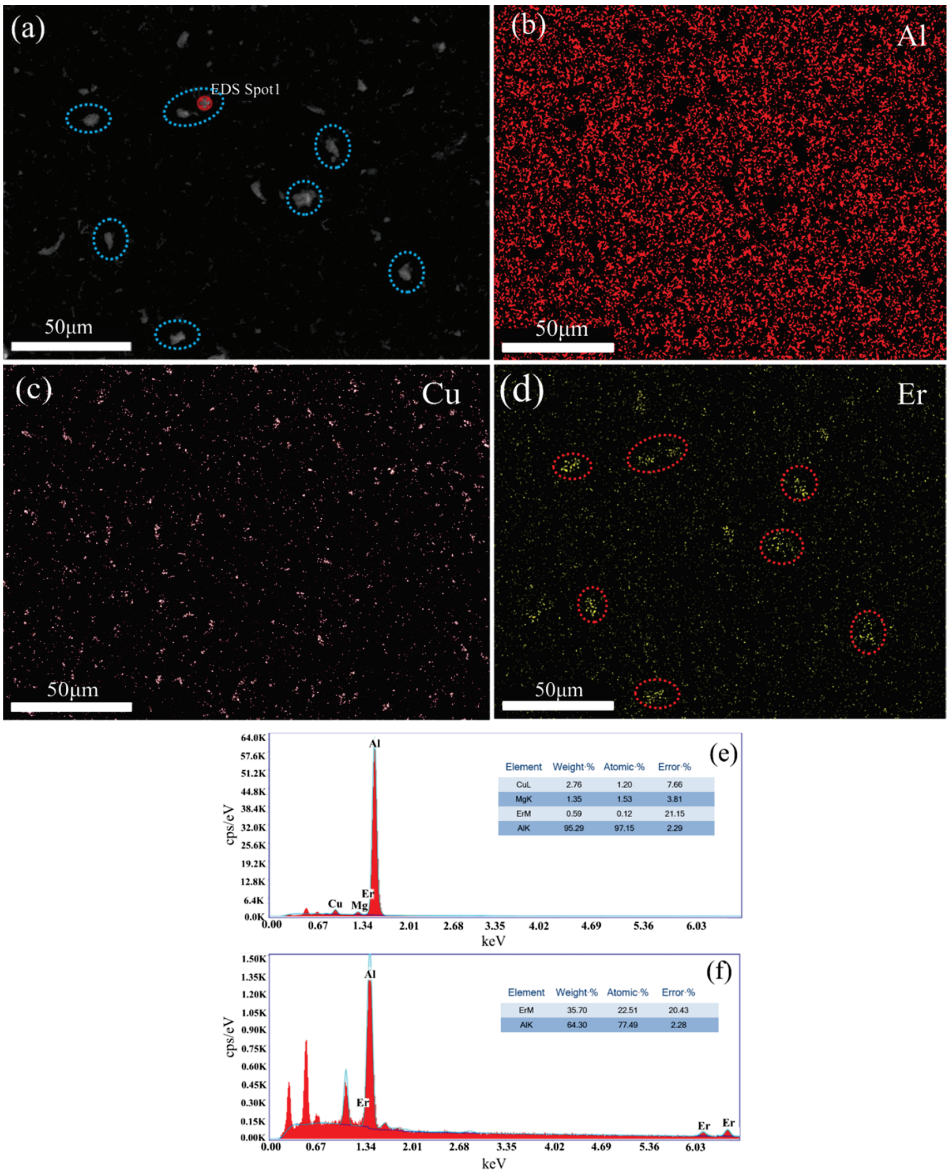

Figure 4. The microstructure of the 2024Al-Er alloy obtained by SEM and EDS mapping of the typical region of the 0.6 wt.% Er alloy: (**a**) overall view map; (**b**) Al; (**c**) Cu; (**d**) Er; (**e**) element composition of (**a**); and (**f**) element composition at spot 1.

3.2. XRD Analysis

Figure 5 shows the XRD patterns of the 2024Al-Er alloy with different Er contents. For the Er-free alloy, the XRD patterns of the specimen are only Al and Al_2Cu. As Er is added, the diffraction peak of Al_3Er appears, and its intensity increases with an increase in Er content, indicating that the number of the Al_3Er phase increases. That is to say, the addition of the Er element to the alloy does not completely exist in a solid solution form in the matrix. Part of it will be dissolved in the Al matrix for solid solution strengthening, while the other part will precipitate in the form of a fine Al_3Er phase for dispersion strengthening. Moreover, the diffraction peak of Al_8Cu_4Er is not obvious, mainly because its content is relatively low and difficult to detect. This is consistent with the change trend of the microstructure in Section 3.1.

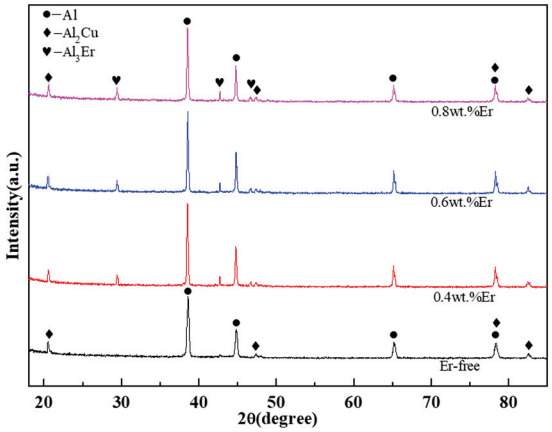

Figure 5. XRD pattern of 2024Al-Er alloy.

3.3. Compactness and Microhardness

Figure 6 shows the effect of Er content (0%, 0.2 wt.%, 0.4 wt.%, 0.6 wt.%, 0.8 wt.%) on the compactness and microhardness of the 2024Al-Er alloy. It can be seen that the Er content has a significant effect on the compactness of the alloy. When Er is not added, the compactness of the alloy is 95.7%. With the increase in Er addition (0.2 wt.%→ 0.4 wt.% →0.6 wt.%→0.8 wt.%), the compactness increases first and then decreases. When the Er content is 0.6 wt.%, the highest compactness arrived is 97.6%. The change in compactness mainly depends on the interaction between the matrix and reinforcing phase. During the sintering process, with an increase in Er content, the content of the Al_3Er phase in the matrix increases, which will enhance the ability to absorb and convert microwaves, and produce more heat, which can cause the green-body rapid heating process, and lead to a more uniform structure and higher compactness. When the Er content is 0.8%, the compactness of the alloy decreases. It is regarded, through analysis, that an interaction occurred between Er and Al, and Cu in the 2024Al matrix, meaning the Al_8Cu_4Er phase with a low melting point is formed, and closed pores are generated in a local range, making the gas difficult to discharge [25–27]. On the other hand, due to the strong enrichment ability of rare earth Er in the matrix, most of the rare earth Er will gather at the junction of the two-phase interface. Excessive rare earth Er will cause the matrix to split locally, which will deteriorate the region and make the overall mechanical properties decrease instead.

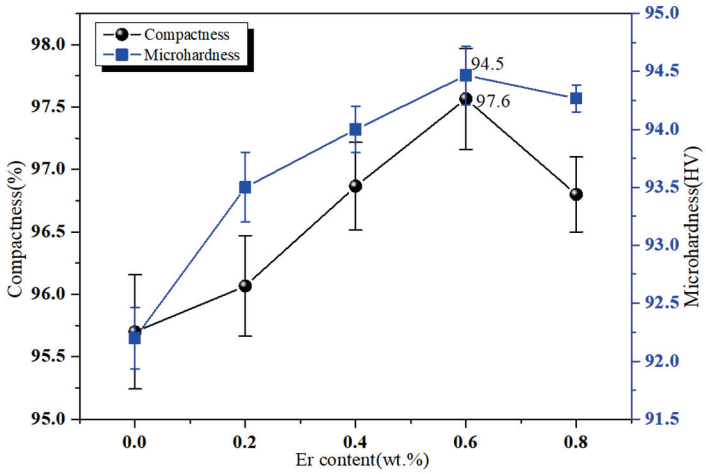

Figure 6. Dependence of compactness and microhardness of 2024Al-Er alloy with different Er content.

As shown in Figure 6, with the increase in Er content, the microhardness first increases and then decreases. When the addition of Er is 0.6%, the microhardness reaches the maximum, which is 94.5 HV, 2.5% more than for the Er-free specimen. The reason for the microhardness increase in the 2024Al-Er alloy is that Er, as a heterogeneous atom dissolved in the matrix, causing lattice distortion in the matrix, and the potential barrier of the distorted lattice increases and the ability to resist deformation increases. From the perspective of microstructure, with the increase in Er addition, the number of the second phase in the material increases, and the grain boundary increases. The dislocations on the grain boundary intertwine with each other, forming a large number of defects, leading to an improvement in the deformation resistance and hardness of the alloy. When the addition of Er reaches 0.8 wt%, the hardness decreases. This is largely due to excessive Er reacting with Cu in 2024Al to form low-melting-point Al_8Cu_4Er phases, which would cause more pores in the structure, lower compactness, and lower hardness. Wang [28] studied the effect of densification in the 2024Al alloy reinforced with high-entropy alloy (HEA) particles of FeCoNi1.5CrCu. The initial compactness of the pure 2024Al alloy was 94.6%. Upon the introduction of the HEA particles, the maximum achieved compactness was 90.8%, and the maximum microhardness of FeCoNi1.5CrCu/2024Al composite material was 93.1 HV. This indicates that under the same preparation conditions, the effect of improving Er alloying on compactness and hardness is better than that of FeCoNi1.5CrCu HEA particles.

3.4. Tensile Properties

Figure 7 shows the tensile properties of the 2024 aluminum alloy under different Er contents. It can be concluded that with the increase in Er addition, the strength and plasticity of the alloy are both improved. When the addition of Er is 0.6 wt.%, it reaches its peaks at 160 MPa and 4.5%, respectively. According to Figure 3, we can see that when the addition of Er is less than 0.6 wt.%, the grain size of the 2024 aluminum alloy is significantly refined and equiaxed, producing fine grain strengthening. As is well known, grain refinement is beneficial for both the strength and plasticity of materials. If the Er addition continues to increase, the tensile strength and elongation decrease instead. On the one hand, the grain size of the alloy becomes uneven, which affects the mechanical properties of the material; on the other hand, when the amount of Er added exceeds 0.6 wt.%, in addition to the formation of the Al_3Er phase, a portion of the AlCuEr phase may be formed, which reduces the mechanical properties of the alloy. Lei added Er to an Al-Si-Mg-Cu alloy and also found that the addition of 0.6 wt.% erbium has a greater promotion effect than an inhibition effect, and the alloy has the best mechanical properties at as-cast and heat-treatment conditions [29].

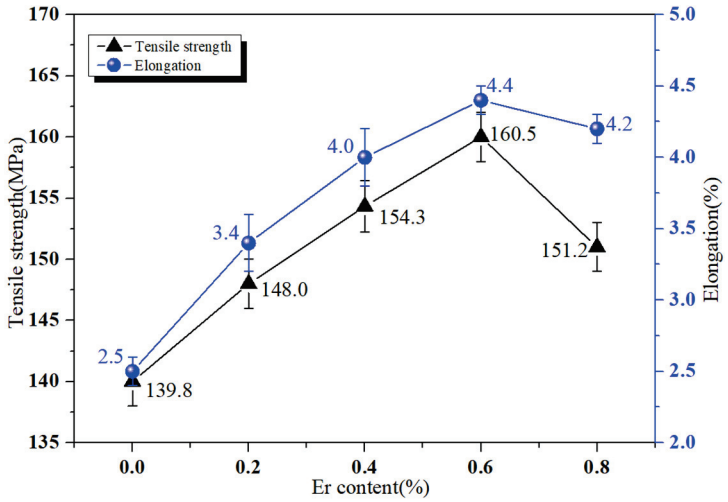

Figure 7. Dependence of tensile strength and elongation of 2024Al-Er alloy on different Er contents.

3.5. Dynamic Compression Properties

The dynamic compressive properties of the specimens were carried out on the split Hopkinson pressure bar (SHPB), as shown in Figure 2. The SHPB experimental device is mainly composed of two equal-length pressure bars, a short impact bar, and a set of impact loading devices. The strain ($\mathcal{E}_s\ (t)$), strain rate ($\dot{\mathcal{E}}_s\ (t)$), and dynamic stress ($\sigma_s\ (t)$) of the specimen are calculated from Equations (4)–(6) [30]:

$$\mathcal{E}_s\ (t) = -\frac{2C}{L}\int_0^t \mathcal{E}_R\ (t)dt \tag{4}$$

$$\dot{\mathcal{E}}_s\ (t) = -\frac{2C}{L}\mathcal{E}_R\ (t) \tag{5}$$

$$\sigma_s\ (t) = E\frac{A}{A_0}\ \varepsilon_T\ (t) \tag{6}$$

where C and E are the elastic wave velocity and elasticity modulus of the pressure bar, respectively; L is the length of the specimen before impact; A_0 and A are cross-sectional areas of pressure bar and the specimen before impact; and $\mathcal{E}_R\ (t)$ and $\varepsilon_T\ (t)$ are the obtained reflected and transmitted waves, respectively.

Figure 8 are the dynamic compression stress–strain curves of the 2024Al-Er alloy with different Er additions at strain rates of 600 s^{-1} and 800 s^{-1}. It can be learned that the stress–strain curves of the alloy are divided into elastic and plastic sections, each of which has obvious characteristics, and there is no obvious yield platform. True stress–strain curves at both strain rates show a wave-like response after yielding, indicating that dynamic recovery and dynamic recrystallization of the alloy occur. This is consistent with Xie's research, which indicates that for the SiC_p/2024Al composite, during the elastic phase, the influence of different strain rates on the elastic modulus of the composite is negligible; during the plastic phase, as the strain rate increases, the yield flow stress becomes larger, and the trend of strain hardening remains roughly the same. [31]. Upon analyzing the dynamic impact of plastic deformation, it is seen that the dynamic recovery caused by the slip of the cross spiral dislocation and the edge dislocation is limited, and the subgrain boundary is not significantly formed. The dislocation density remains high, resulting in a rapid increase in energy storage. When the storage energy of the deformed metal reaches a critical value, dynamic recrystallization occurs [32]. In addition, under the condition of high strain rate, the flow stress of the alloy has a certain fluctuation, which is caused by the inertial dispersion effect and external interference that the SHPB is difficult to avoid.

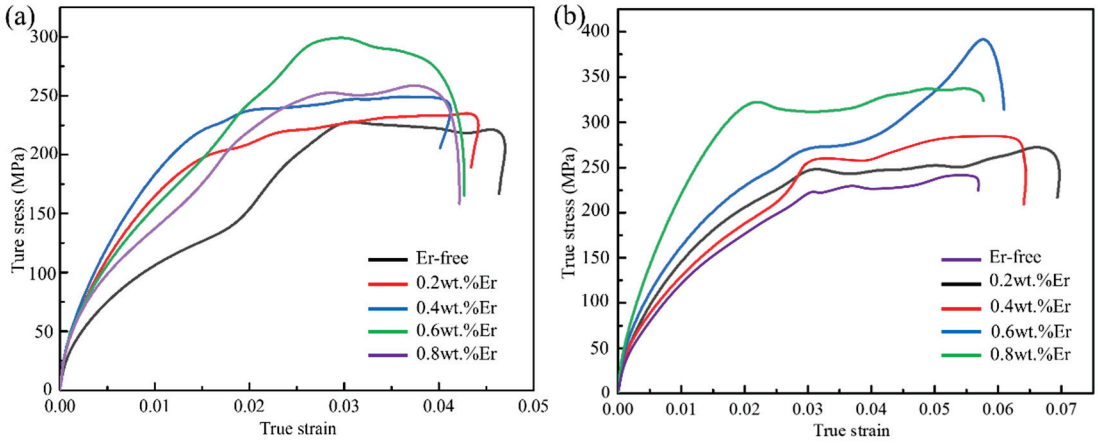

Figure 8. True stress–true strain curves obtained from the specimens with different Er content: (**a**) 600 s^{-1} and (**b**) 800 s^{-1}.

Under different strain rates, the curve coincidence degree of the elastic segment is low, and the change trend is basically consistent. Therefore, the strain rate has a certain influence on the elastic modulus of the 2024Al-Er alloy. At a strain rate of 600 s^{-1}, the dynamic yield stress of the specimens increases gradually with the increase in Er addition (Figure 8a). When the Er content is 0.6 wt.%, the dynamic yield stress reaches the maximum value of 289.6 MPa and then decreases. When the strain rate increases from 600 s^{-1} to 800 s^{-1}, the true stress–true strain curve of the Er/2024Al alloy with different Er contents generally moves upward (Figure 8b), indicating increased stress on the material, and showing the positive strain rate-strengthening effect. When the Er content is 0.6 wt.%, the dynamic yield stress reaches 371.3 MPa, an increase of 28.2% in comparison to that under a 600 s^{-1} strain rate. It can be seen from the plastic section curve that the dynamic yield stress increases with an increase in strain rate, and there is a trend of strain hardening. It is believed that the alloy with 0.6 wt.%Er has the smallest grain and the highest compactness, which is an important factor for improving the strength. Small grains are more likely to lead to dislocation packing, forming a pinning effect, and exerting the dislocation strengthening mechanism [33].

Figure 9 shows the macro deformation of 0.6 wt.% Er and Er-free specimens under different strain rates. It can be concluded that when the strain rate is 600 s^{-1}, the deformation degree of the specimen is 32.2%, and there is no obvious macroscopic damage of shear failure in the specimen. When the strain rate reaches 800 s^{-1}, the deformation degree of the two specimens is 55.3% (0.6 wt.% Er) and 48.2% (Er-free), respectively, and the specimens are seriously damaged. However, from the macroscopic morphology, the damage of the Er-free specimen is more serious, showing the characteristics of brittle fracture.

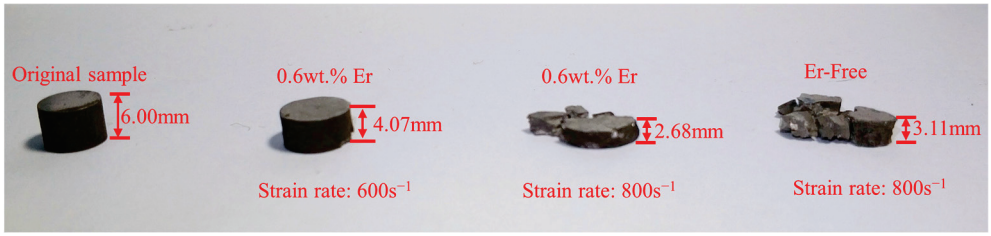

Figure 9. The macro deformation of 0.6 wt.% Er and Er-free specimens under different strain rates.

The microstructure of the 0.6 wt.%Er specimen obtained by light microscopy after dynamic shock loading is presented in Figure 10, and the strain rates are 600 s^{-1} and 800 s^{-1} respectively. When preparing the metallographic specimen, it is necessary to cut the specimen along the axis after dynamic compression and take its profile as an observation plane; i.e., the metallographic observation plane shall be parallel to the compression direction.

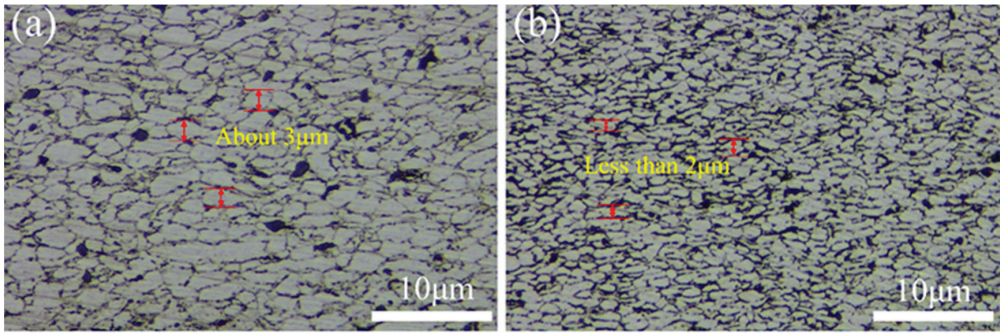

Figure 10. Optical micrographs of 0.6%Er specimens after exposure to different dynamic impact loads: (**a**) 600 s^{-1} and (**b**) 800 s^{-1}.

It is found that the microstructures of the samples vary with the impact condition. The grains are elongated in a direction perpendicular to that of the impact loading at a lower strain rate (600 s^{-1}). By analyzing the micrographs of the two samples, it is found that with the strain rate and the degree of grain refinement increasing, the elongation increases. The average grain size decreases with the increase in strain rate. This is because when the strain rate increases, the deformation time of the alloy will be shortened, resulting in grain refinement and restrained growth of recrystallized grains. In units of time, the dislocation density in grains increases faster, and the accumulated deformation storage energy is also higher, which will promote the nucleation of recrystallized grains, leading to grain refinement.

The results of scanning electron microscopic (SEM) investigation of the 0.6 wt.%Er specimen after high-strain-rate (800 s^{-1}) deformation under impact loading are presented in Figure 11. Due to instantaneous stress waves, a short standing of high-intensity stress is generated, and it is difficult to transfer the heat generated by the plastic deformation of local regions in time as the process is almost adiabatic. Local softening occurred due to temperature rise, while surrounding regions remained hardened. When further loaded, if the thermal softening conquers the strain rate hardening, the deformation will occur in a strong plastic shear band, forming an adiabatic shear band (ASB) [34].

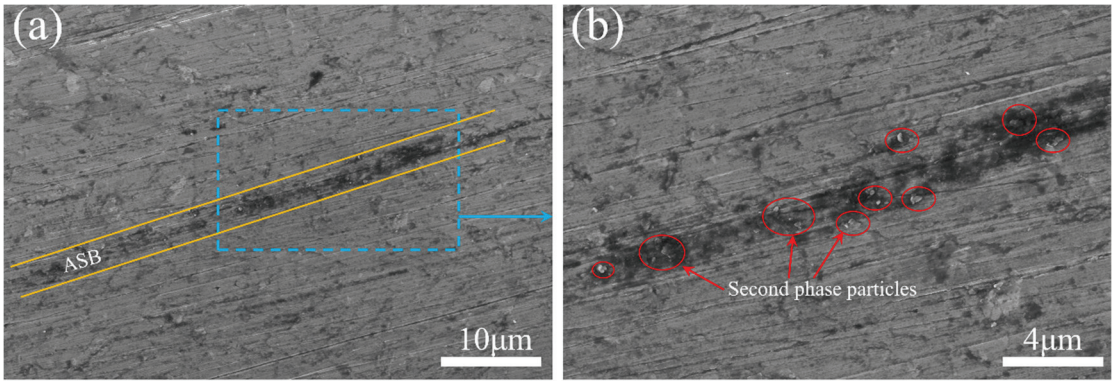

Figure 11. (**a**) The results of scanning electron microscopic investigation of the 0.6%Er specimen after high strain rate (800 s^{-1}) and (**b**) enlargement of blue wireframe area in Figure 9a.

As is known to all, the formation of localized shear bands is a unique form of microdamage in materials under impact loads, and the formation of shear bands indicates the beginning of material catastrophic failure. It is obvious that the occurrence of the heterogeneous deformation caused the formation of ASB in the alloy (Figure 11a). When excessive thermal softening leads to a decrease in load-carrying capacity and strong strain in the local region along the narrow paths, shear bands will develop. So, the ASBs can be clearly distinguished from other parts of the microstructure under SEM. The second-phase particles in the alloy are also elongated and arranged along the ASB region and become

denser than those outside the shear bands (Figure 11b). The main factor contributing to strain localization is the thermal softening of the matrix in the shear band region. Under the combined action of the pressure of the rigid matrix outside the shear band and the shear flow of the viscoplastic matrix in the shear band region, the arrangement of the second-phase particles in the shear band region is more compact. In a previous study, analogous phenomena were also observed [35].

Figure 12 presents the fracture surfaces of dynamic compression specimens. It can be clearly seen that extensive irregular cleavage planes and some cracks are apparent on the entire fracture surface of the Er-free specimen, as shown in Figure 12a. The cracks expand along the grain boundary, and the grain boundary is obvious. The polyhedron morphology of each grain is similar to the stacking of rock candy. It indicates that the fracture characteristics exhibit quasi-cleavage fracture, resulting in a low strength value of the specimen. Meanwhile, the 0.6 wt.% Er specimen exhibits some dimples, and the number of cracks is reduced. As can be seen in Figure 12b, the morphology of dimple fracture from a 0.6 wt.% Er specimen is obvious, and the dimples are slightly deep and well distributed, which results in higher mechanical properties. However, the morphology of the dimple fracture of the Er-free specimen is not evident, and the dimples are very flat and unevenly distributed. Therefore, the mechanical properties are far inferior to those of the specimen modified with 0.6 wt.% Er. This shows that the addition of Er improves the plasticity and toughness of the 2024Al alloy.

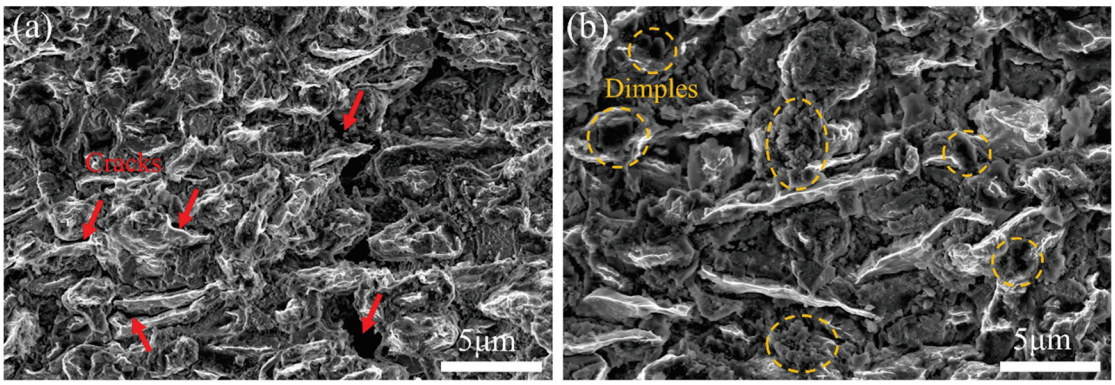

Figure 12. The SEM analysis of fracture surfaces of the dynamic compression specimens: (**a**) Er-free, (**b**) 0.6 wt.% Er addition.

In general, the propagation of cracks is always present along the direction of the small atomic bonding force. The addition of trace Er makes the microstructure homogenized and refined, which improves the plastic deformation ability of the alloy and hinders crack propagation along the grain boundary [36]. This shows that the addition of Er improves the impact toughness of the alloy. The fracture mode is no longer a simple brittle fracture, and the tendency of ductile fracture begins to appear, which is consistent with the results of a metallographic microstructure and stress–strain curves.

4. Conclusions

An Er/2024Al alloy with different Er contents was prepared by ball milling, cold isostatic pressing, and microwave sintering. The results can be summarized as follows:

(1) When the sintering temperature is 490 °C, the heating rate is 20 °C/min, and the soaking time is 30 min. Thus, the addition of Er can significantly refine the grains of the 2024Al alloy, with the main mechanism being the presence of the Al_3Er phase. This phase acts as a heterogeneous nucleation site, greatly increasing the nucleation rate. Moreover, small Al_3Er particles exert a pinning effect on dislocations and sub-grain boundaries, thereby causing a significant reduction in grain size. The grain size of the 0.6%Er specimen is about 5 μm, which is the optimal value.

(2) The mechanical properties of the 2024Al alloy were improved with the addition of Er. Due to the refinement of the grains, the compactness, strength, and toughness of the alloy were elevated. When the Er content is 0.6%, the compactness and microhardness reach maximum levels, which are 97.6% and 94.5 HV, 1.9% and 2.8% higher than those of the Er-free specimen, respectively. At the same time, the tensile strength and elongation reach the peak at 160.5 MPa and 4.4%, respectively.

(3) At both the strain rates of 600 s^{-1} and 800 s^{-1}, the dynamic yield stress of the specimens increases gradually with an increase in Er content. For the 0.6 wt.% Er specimen, the dynamic yield stress reaches 371.3 MPa at a strain rate of 800 s^{-1}, which is 28.2% higher than that under a 600 s^{-1} strain rate. The toughness of the 2024Al-0.6 wt.% Er alloy is enhanced and dimples appear, indicating that the fracture mode changes from brittle fracture to ductile fracture.

The 2024Al alloy has excellent comprehensive mechanical properties, and with the development of the aerospace industry, its requirements for comprehensive performance are constantly increasing. By conducting research on the action effect of rare earth erbium alloying on the microstructure and properties of the 2024 aluminum alloy, it is possible to further optimize the comprehensive performance of the 2024 aluminum alloy, laying the necessary theoretical and practical foundation for the development of advanced high-strength and high-toughness aluminum alloy materials.

Author Contributions: Conceptualization, T.Q.; formal analysis, J.Y.; investigation, T.Q., J.Y., and C.B.; writing—original draft preparation, T.Q.; writing—review and editing, B.F.; supervision, J.Z.; funding acquisition, B.F. All authors have read and agreed to the published version of the manuscript.

Funding: This research was funded by "The Natural Science Foundation of the Jiangsu Higher Education Institutions of China (23KJB430037)" and "Jiangsu Province Vocational College Teachers Enterprise Practice Training Project (2024QYSJ038)".

Data Availability Statement: The original contributions presented in the study are included in the article; further inquiries can be directed to the corresponding author.

Conflicts of Interest: Author J.Z. has been involved as a consultant and expert witness in Wuxi Wanling High Frequency Equipment Manufacturing Co., Ltd. The remaining authors declare that the research was conducted in the absence of any commercial or financial relationships that could be construed as a potential conflict of interest.

References

1. Zhang, H.S.; Yan, M.; Wang, H.Y.; Shen, L.T.; Dai, L.H. Determination of dynamic shear strength of 2024 aluminum alloy under shock compression. *AIP Adv.* **2016**, *6*, 045309. [CrossRef]
2. Gautam, A.; Sarkar, P.K.; Jangid, R. Ductile and Fatigue Behaviour Estimation of Lightweight High-Strength Al 2024. *Mater. Today Proc.* **2018**, *5*, 7873–7881. [CrossRef]
3. Rohatgi, P.K.; Kumar, P.A.; Chelliah, N.M.; Rajan, T.P.D. Solidification processing of cast metal matrix composites over the last 50 years and opportunities for the future. *JOM* **2020**, *72*, 2912–2926. [CrossRef]
4. Nazree, M.; Nabilla, S.; Che, Z. The effect of microwave sintering time to PM aluminum alloys. *Appl. Mech. Mater.* **2015**, *754–755*, 240–244.
5. Wang, H.; Tang, F.; Li, G.; Zhang, D.; Liu, M.; Kai, X. Microstructure and properties of B_4C_p/Al composite prepared by microwave sintering with low temperature. *Mater. Res. Express* **2020**, *7*, 096511. [CrossRef]
6. Han, Z.; Xu, L.; Guo, S.; Wu, Q.; Zhang, L.; Liu, J. Study on the microwave sintering characteristics of spherical tin-silver alloy powder. *Mater. Res. Express* **2019**, *6*, 1265k7. [CrossRef]
7. Liu, J.Q.; Wang, H.M.; Li, G.R.; Su, W.X.; Zhang, Z.B.; Zhou, Z.C.; Dong, C. Microstructure and improved plasticity of $(FeCoNi_{1.5}CrCu)_p$/Al composites subject to adjusted deep cryogenic treatment (DCT). *J. Alloys Compd.* **2022**, *895*, 162690. [CrossRef]
8. Liu, J.Q.; Wang, H.M.; Huang, Z.H.; Ma, Z.; Li, G.; Zhou, P. Enhanced strength-ductility synergy of aging treated $(FeCoNi_{1.5}CrCu)_p$/2024Al composite. *J. Alloys Compd.* **2022**, *929*, 167372. [CrossRef]
9. Gaurava, A.; Satpala, S. Influence of rare earth addition on the properties of AA6351 hybrid composites. *J. Eng. Res.* **2021**, *9*, 253–268.
10. Nazarov, S.; Rossi, S.; Bison, P. Influence of Rare Earths Addition on the Properties of Al–Li Alloys. *Phys. Met. Metallogr.* **2019**, *120*, 402–409. [CrossRef]

11. Nogita, K.; McDonald, S.D.; Dahle, A.K. Eutectic modification of Al-Si alloys with rare earth metals. *Mater. Trans.* **2004**, *45*, 323–326. [CrossRef]
12. Tsai, Y.C.; Chou, C.Y.; Lee, S.L.; Lin, C.K.; Lin, J.C.; Lim, S.W. Effect of trace La addition on the microstructures and mechanical properties of A356 (Al-7Si-0.35Mg) aluminum alloys. *J. Alloys Compd.* **2009**, *487*, 157–162. [CrossRef]
13. Zhong, T.; Zeng, G.; Xiao, M.; Qin, S.; Wan, Y. Effect of Rare Earth Ce on Microstructure and Properties of 3003 Aluminum Alloy. *Rare Met. Cem. Carbides* **2019**, *33–36*, 41.
14. Ding, W.W.; Zhao, X.Y.; Chen, T.L. Effect of rare earth Y and Al-Ti-B master alloy on the microstructure and mechanical properties of 6063 aluminum alloy. *J. Alloys Compd.* **2020**, *830*, 154685. [CrossRef]
15. Shi, Z.M.; Wang, Q.; Zhao, G.; Zhang, R. Effects of Erbium modification on the microstructure and mechanical properties of A356 aluminum alloys. *Mater. Sci. Eng.* **2015**, *A626*, 102–107. [CrossRef]
16. Li, Q.; Xia, T.; Lan, Y.; Li, P. Effects of rare earth Er addition on the microstructure and mechanical properties of Al-20Si alloy. *Mater. Sci. Eng.* **2013**, *A588*, 97–102. [CrossRef]
17. Nie, Z.; Jin, T.; Zou, J.; Fu, J.; Yang, J.; Zuo, T. Development on research of advanced rare-earth aluminum alloy. *Trans. Nonferrous Met. Soc. China* **2003**, *13*, 509–514.
18. Yang, J.; Nie, Z.; Jin, T.; Xu, G.; Fu, J.; Ruan, H.; Zuo, T. Effect of trace earth element Er on high pure Al. *Trans. Nonferrous Met. Soc. China* **2003**, *13*, 1035–1039.
19. Yu, Y.; Shi, Y.; Xia, Z. Effect of rare earth element Er on microstructure and properties of Al-Si-Cu solder alloy. *Beijing Gongye Daxue Xuebao* **2008**, *32*, 1148–1152.
20. Xing, Z.; Nie, Z.; Ji, X.; Wang, X.; Zou, J. Effect of trace element erbium and manganese on microstructure and properties of Al-Mg alloy. *Rare Met. Mater. Eng.* **2006**, *35*, 1979–1982.
21. Wu, H.; Wen, S.P.; Huang, H.; Li, B.; Wu, X.; Gao, K.; Wang, W.; Nie, Z. Effects of homogenization on precipitation of Al_3(Er, Zr) particles and recrystallization behavior in a new type Al-Zn-Mg-Er-Zr alloy. *Mater. Sci. Eng. A* **2017**, *689*, 313–322. [CrossRef]
22. Sun, W. *Behavior of Rare Earth in Aluminum Alloys*; Press of Weapon Industry: Beijing, China, 1992.
23. Hu, X.; Jiang, F.; Ai, F.; Yan, H. Effects of rare earth Er additions on microstructure development and mechanical properties of die-cast ADC12 aluminum alloy. *J. Alloys Compd.* **2012**, *538*, 21–27. [CrossRef]
24. Colombo, M.; Gariboldi, E.; Morri, A. Er addition to Al-Si-Mg-based casting alloy: Effects on microstructure, room and high temperature mechanical properties. *J. Alloys Compd.* **2017**, *708*, 1234–1244. [CrossRef]
25. Li, Y.; Liu, Z.; Ma, F.; Xia, Q. Phase constitution and growth manner at grain boundary in Al-Cu-Mg-Ag-Er alloy. *Rare Met. Mater. Eng.* **2008**, *37*, 1019–1022.
26. Nie, Z.R.; Fu, J.B.; Zou, J.X.; Jin, T.N.; Yang, J.J.; Xu, G.F.; Ruan, H.Q.; Zuo, T.Y. Advanced Aluminum Alloys Containing Rare-earth Erbium. *Mater. Forum* **2005**, *28*, 197–201.
27. Zou, M.; Ge, Z.; Qi, L.; Zhou, X.; Wei, X.; Zhang, J.; Chen, J. Effect of erbium (Er) on the hot cracking behaviour of Al-5Cu alloy. *Mater. Sci. Technol.* **2011**, *17*, 1–36. [CrossRef]
28. Wang, H.; Ren, W.; Li, G.; Wen, H.; Wang, C.; Chen, J.; Zhao, Y.; Chen, G.; Kai, X. Microstructure and properties of $FeCoNi_{1.5}CrCu$/2024Al composites prepared by microwave sintering. *Mater. Sci. Eng. A* **2021**, *801*, 140406. [CrossRef]
29. Lei, X.; Zhang, Z.; Dong, H.; Wang, C.; Du, X. Effect of erbium on microstructure and mechanical properties of Al-Si-Mg-Cu alloy. *Mater. Und Werkst.* **2020**, *51*, 1389–1397. [CrossRef]
30. Wang, J.; Dong, N.; Ma, H. Study on high speed impact deformation behaviors of Mg-1Al-4Y by SHPB. *Mater. Res. Express* **2020**, *7*, 116506. [CrossRef]
31. Xie, W.; Wang, H. Research on dynamic mechanical properties of SiC_p/2024Al composites prepared by hot-pressing sintering. *Powder Metall. Ind.* **2021**, *31*, 47–51.
32. Cai, Z.; Ji, Z.; Cui, J.; Tian, W. Deformation behaviors and microstructure evolution of 60Al-30Fe-10Bi alloy under high speed impact. *Powder Metall. Technol.* **2017**, *35*, 352–357.
33. Casati, R.; Vedani, M. Metal Matrix Composites Reinforced by Nano-Particles-A Review. *Metals* **2014**, *4*, 65–83. [CrossRef]
34. Zhang, X.; Li, H.; Li, H.; Gao, H.; Gao, Z.-G.; Liu, Y.; Liu, B. Dynamic property evaluation of aluminum alloy 2519A by split Hopkinson pressure bar. *Trans. Nonferrous Met. Soc. China* **2008**, *18*, 1–5. [CrossRef]
35. Odeshi, A.G.; Owolabi, G.M.; Singh, M.N.K.; Bassim, M.N. Dynamic shear band formation in Aluminum 6061-T6 and Aluminum 6061-T6/Al_2O_3 composites. *Mat. Sci. Eng. A Struct.* **2007**, *457*, 114–119.
36. Liu, L.; Liu, L.; Cao, F.; Yang, T.; Yin, P.Z. Effect of Er element on impact deformation and failure behaviors of 7xxx series aluminum alloy. *Ordnance Mater. Sci. Eng.* **2020**, *43*, 125–130.

crystals

MDPI

Article

Effects of Continuous Rolling and Reversible Rolling on 2.4% Si Non-Oriented Silicon Steel

Kaixuan Shao [1,2], Yuhao Niu [1,2,3], Yinghao Pei [4], Jialong Qiao [1,2,3,*], Hongbo Pan [1,2] and Haijun Wang [1,2]

[1] Anhui Key Laboratory of Low Carbon Metallurgy and Solid Waste Resource Utilization, Anhui University of Technology, Ma'anshan 243032, China; shao25802021@163.com (K.S.); niuyuhaoahut@163.com (Y.N.); 20130007@ahut.edu.cn (H.P.); whjchina@ahut.edu.cn (H.W.)
[2] School of Metallurgical Engineering, Anhui University of Technology, Ma'anshan 243032, China
[3] Iron and Steel Research Institute Co., Ltd., Beijing 100081, China
[4] Technology Center, Ma'anshan Iron and Steel Co., Ltd., Ma'anshan 243000, China; m76349@baosteel.com
* Correspondence: qiaojialong2015@126.com

Abstract: The cold-rolled non-oriented silicon steel sheets with a Si content of 2.4 wt.%, produced by continuous and reversible cold rolling, were used as the experimental material. The effects of annealing temperature on the microstructure, texture, and magnetic properties were studied by optical microscopy, an X-ray diffractometer, and a magnetic property measuring instrument. The experimental results showed that the dominant texture components at the surface of both sheets were almost the same, i.e., α and γ fibers. After annealing at 920 °C for 30 s, a complete recrystallization occurred in both sheets. When annealing below 1070 °C, the average grain sizes of continuous cold-rolled sheets were slightly higher than those of reversible cold-rolled ones. Additionally, for all specimens, the recrystallization texture components were γ fiber, as well as weak α fiber, λ fiber, and Goss texture. Additionally, the difference was the texture intensity. The iron losses of the finished products of continuous cold rolling were lower than those of the finished products of reversible cold rolling with the increase in annealing temperature, and the magnetic induction was higher than that of the finished products of reversible cold rolling.

Keywords: non-oriented silicon steel; iron loss; magnetic induction; cold rolling; texture

1. Introduction

Cold-rolled non-oriented silicon steel is a kind of Fe-Si-Al alloy with an extremely low carbon content and a total mass fraction of Si and Al ranging from approximately 1.5 to 4.0%. It is widely used as the core of medium and large motors and generators because of its ability to maintain excellent magnetic isotropy in all directions in a high-speed rotating magnetic field. In addition, it offers a higher performance price ratio compared with iron-based amorphous alloys, dual-phase materials, nanocrystalline alloys, and other core magnetic materials [1–3]. In recent years, the drive motors of new energy vehicles require non-oriented silicon steel to meet the magnetic properties of high magnetic induction, low iron loss, and low magnetostriction. At the same time, non-oriented silicon steel needs to have high mechanical properties, such as yield strength and tensile strength, to resist the deformation and fatigue fracture caused by the centrifugal force when the motor is running at a high speed [4–6].

For non-oriented silicon steel, it is typically desired to maximize {100} planes during the cold rolling and annealing process, while minimizing {111} planes as much as possible [7]. Kawamata et al. [8] used rolls with three different radii to carry out cold rolling experiments on hot-rolled sheets with two different thicknesses. The results showed that when the roller shape parameter was smaller, the development of surface γ fiber (<111>//ND) after annealing of the cold-rolled sample was suppressed, while the vicinity 0of the {100} <001> component was developed. Cheong et al. [9] studied the effects

of roll roughness on texture and magnetic properties. Compared with the rough work roll, the smooth work roll made the surface stress of the rolled piece more concentrated, resulting in sharper textures of the rolled piece. When Li et al. [10] annealed 2.8 wt.% Si non-oriented silicon steel at 1100 °C, the Goss ({110} <001>) and Cube textures ({001} <100>) were stronger and {111} <112> was weaker in the grain growth stage. With the increase in annealing time, the intensity of the Cube texture increased with the grain growth, the intensity of Goss texture decreased obviously, and the intensity of {111} <112> did not change significantly. Kestens et al. [11] used "cross rolling" to rotate the hot-rolled sheet around ND (normal direction) by 90° before cold rolling, switching RD (rolling direction) and TD (transverse direction), and finally formed a very strong Cube texture or Rotated Cube texture ({001} <110>) in the sheet.

At present, the large-scale production of cold-rolled non-oriented silicon steel mainly adopts continuous cold rolling. However, due to the reasons of manufacturing cost, work efficiency, and market demand, the non-oriented silicon steel products produced by reversible cold rolling have the characteristics of a small batch, multi-variety, and short cycle, so they also occupy a place in the user market. Most of the existing research focuses on the effect of the annealing process on the grain size, texture strength, and magnetic properties of non-oriented silicon steel under a certain cold rolling method. In addition, different grades of non-oriented silicon steel have different cold rolling reduction rates in the production process. The change in the cold rolling reduction rate will directly affect the deformation microstructure, thus affecting the formation of recrystallized grains and then changing the magnetic properties. Therefore, it is of great significance to study the effects of different cold rolling methods and cold rolling reduction rates on the deformation structure and texture, recrystallization texture evolution, and magnetic properties of non-oriented silicon steel cold-rolled sheets.

In this work, the same furnace non-oriented silicon steel produced by industrial production was selected and cold rolled to 0.35 mm by continuous and reversible cold rolling. After the same annealing process in the laboratory, the microstructure, texture, and magnetic properties of different annealed sheets were investigated. The aim is to clarify the changes of microstructure, texture, and magnetic properties of a 2.4% Si non-oriented silicon steel obtained by different cold rolling working systems after annealing.

2. Materials and Methods

The experimental material is the industrial production of the same furnace non-oriented silicon steel with a Si content of 2.4 wt.%, and the main chemical composition is shown in Table 1. The hot-rolled sheets of non-oriented silicon steel with a thickness of 2.20 mm were normalized at 900 °C for 3 min and then acid pickled in HCl aqueous solution with a volume fraction of about 10% at 60 °C for 10 min. At the end of pickling, the normalized sheets were rolled to 0.35 mm by continuous cold rolling and reversible cold rolling, respectively. The main frame of the reversible cold rolling mill mainly includes the upper and lower working rolls, sets the target reduction thickness in the mill control system, and starts the main mill to start the first pass rolling. When the strip is completely removed from the work roll, the main drive slows down and begins to reverse the next pass of rolling [12]. Then, the cold-rolled sheets were processed into Epstein square specimens with dimensions of 30 mm × 320 mm, and the annealing experiments were carried out in an RDM-180-11Q multi-atmosphere continuous annealing furnace. The specific annealing experimental processes are shown in Figure 1. The cold-rolled specimens were heated from room temperature to 800 °C at a heating rate of 20 °C·s^{-1} and held at that temperature for 180 s, then they were heated to the target process temperature for 30 s and slowly cooled to room temperature with the furnace. In addition, a dry mixed atmosphere of 20 vol.% H_2 + 80 vol.% N_2 was introduced throughout the furnace as a protective atmosphere for recrystallization annealing.

Table 1. Chemical composition of experimental raw materials (wt.%).

Elements	C	Si	Mn	P	S	Als	N	Ni	Cu	Ti	Nb
Content	0.0012	2.40	0.20	0.0008	0.0014	1.05	0.0011	0.0125	0.025	0.0023	0.0018

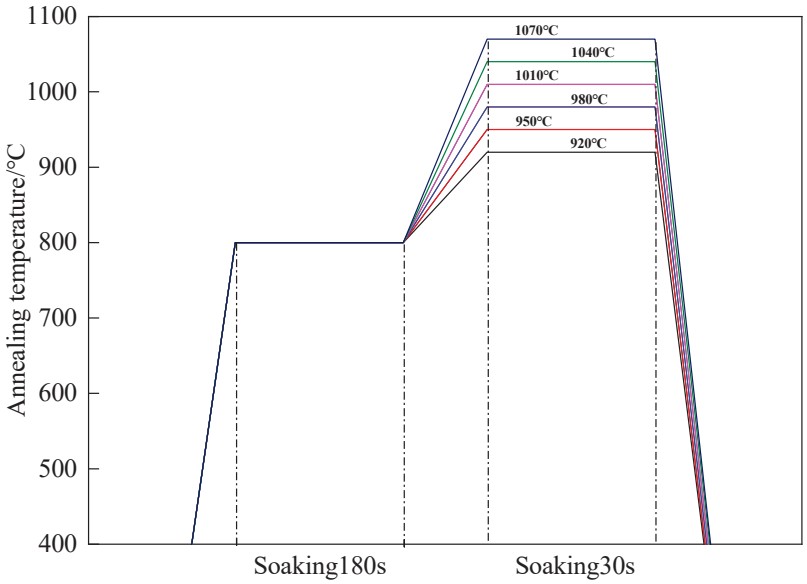

Figure 1. Laboratory annealing process diagram.

After annealing at different temperatures, the microstructures and textures of annealed sheets were observed, and the magnetic properties of the finished products were measured. The 15 mm (TD) × 20 mm (RD) specimens were used for microstructure observation. After standard grinding and polishing, the annealed samples were etched with a 5% nitric acid alcohol solution. The microstructures of the annealed sheets in the thickness direction were observed and captured on the ZEISS-200MAT metallographic microscopy (Tokyo, Japan) under 100× magnification. According to the cut-off point method in the GB/T6394-2002 metal average grain size measurement method, the image processing software Image Pro Plus 6.0 was used to measure the average grain size of the annealed specimens. Three to five fields of view were randomly selected for our statistics. In order to make the measurement results more accurate, the number of cut-off points for each specimen should reach 500. The X' Pert Pro X-ray diffractometer was used to detect the macro-textures at the surface layer of different annealed sheets of 15 mm (TD) × 20 mm (RD). The X-ray diffractometer uses a CoKα radiation source with a tube voltage of 35 kV and a tube current of 40 mA. The orientation distribution functions (ODFs) were calculated from {200}, {110}, and {211} incomplete pole-figures, and the orientation distribution function was calculated by X' Pert Texture software.

The magnetic properties were measured by the Epstein square method. Eight pieces of 30 mm (TD) × 320 mm (RD) specimens were measured on the Metron SKJ-300 magnetic performance measuring instrument (Tokyo, Japan) according to GB/T3655. The magnetic properties of the finished products after annealing at different temperatures were measured. Specifically, the iron loss at 1.5 T by 50 Hz ($P_{1.5/50}$) and magnetic induction at 5000 A·m^{-1} (B_{50}) were measured, respectively.

3. Experimental Results

3.1. Textures of Hot-Rolled and Normalized Sheets

The ODFs for the $\Phi_2 = 45^\circ$ section at the surface layer of hot-rolled and normalized sheets of 2.36% Si non-oriented silicon steel are shown in Figure 2, and the observation surface is RD-ND. The surface texture of the hot-rolled sheet is dominated by a strong Goss

texture, and it contains a weak α texture and λ texture. Due to the contact between the surface layer and the roll, the friction generates strong shear stress to form a typical Goss texture [13]. Figure 2b shows that the surface texture of the normalized sheet is similar to that of the hot-rolled sheet. The normalized sheet is mainly composed of {110} <112>~{110} <001> and {111} <110>~{111} <112>. The orientation density of the Goss texture decreases from 3.4 in the hot-rolled sheet to 3.0, but the distribution of the {111} <112> and {111} <110> textures is more concentrated than that of the hot-rolled sheet, and the texture orientation density reaches 2.1 and 1.2, respectively.

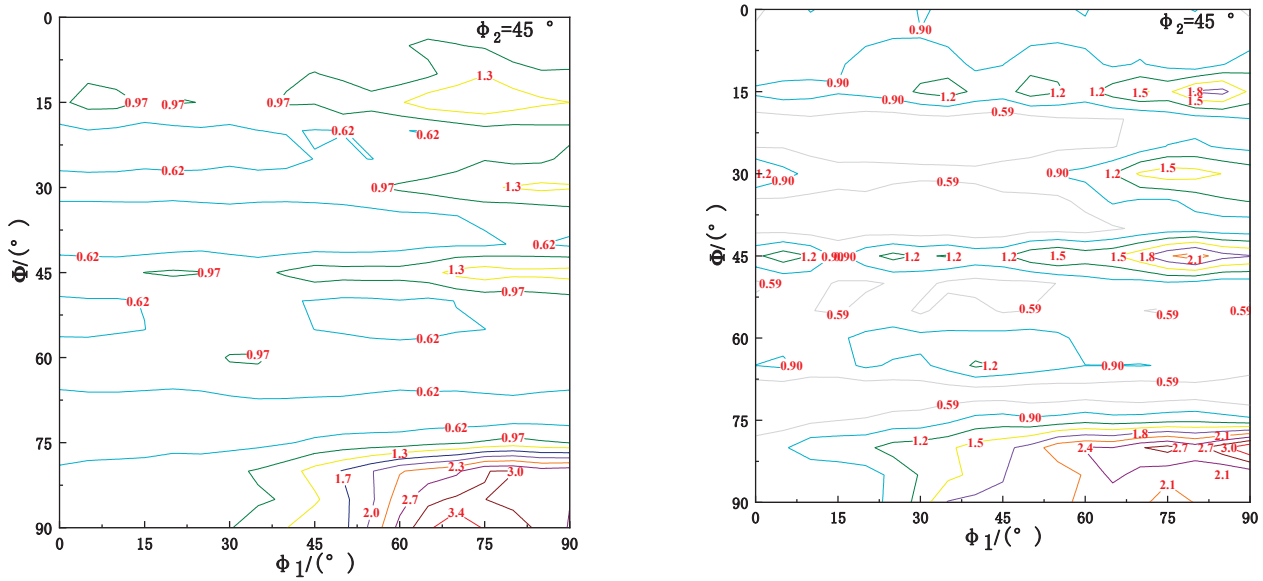

Figure 2. Textures in the surface layer of hot-rolled and normalized sheets. (**a**) Hot-rolled sheet and (**b**) normalized sheet. The numbers in the figures are texture intensities.

3.2. Microstructures and Textures of Cold-Rolled Sheets

Figure 3 shows the optical microscopy (OM) images of the continuous cold-rolled sheet and reversible cold-rolled sheet, and the observation surface is RD-ND. The microstructures of hot-rolled sheets after normalization are generally recrystallized ferrite. Due to the effect of the external load during cold rolling, the ferrite grains have undergone different degrees of deformation. The compression deformation is a fibrous mixed structure, and the grain boundaries are difficult to distinguish. According to the report of Hu et al. [14], strong α fiber (<110>//RD) and weak γ fiber were formed after the cold rolling of a normalized sheet. Due to the different chemical reaction rates of grains with different orientations during the corrosion process, the corrosion of {111} grains are the fastest. In order to preliminarily judge the intensity of each texture after cold rolling, the metallographic structure of cold-rolled sheets is observed after erosion with 4 vol.% nitric acid + 96 vol.% alcohol. In Figure 3a,b, the area with lighter color is larger, and the area with darker color is less. Therefore, it is preliminarily judged from the degree of corrosion that the γ fiber of the two cold-rolled sheets is weak, and shear bands are usually formed in the deformed γ-fiber grains, which are fishtailed in the deformed structure.

Figure 4a,b show the ODFs for the Φ = 45° section at the surface layer of normalized sheets after continuous cold rolling and reversible cold rolling, respectively. Whether it is continuous cold rolling or reversible cold rolling, the dominant components after cold rolling accumulate on the α-fiber and γ-fiber orientations, which have a typical body-centered cubic metal rolling texture. The {001} <110>, {113} <110>, and {111} <110> orientations are relatively concentrated [15]. The α-fiber intensity in cold-rolled textures is stronger than the γ-fiber intensity. The texture intensities formed by reversible cold rolling

in α fiber are stronger than those formed by continuous cold rolling, such as {001} <110> and {112} <110>, indicating that reverse cold rolling is more favorable for the formation of the α fiber. The texture types of the cold-rolled sheets by continuous and reversible cold rolling are basically the same, and both have a strong Rotated Cube texture ({001} <110>).

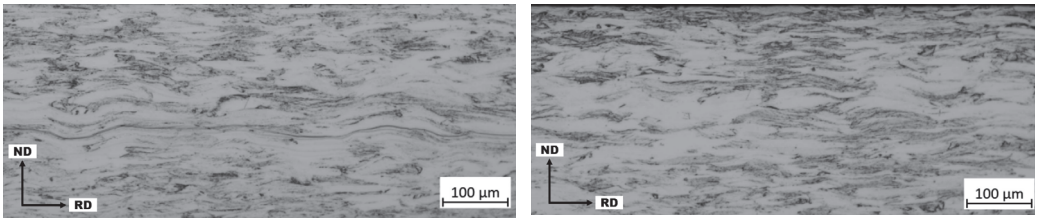

(**a**) (**b**)

Figure 3. Microstructures of continuous cold-rolled sheet and reversible cold-rolled sheet. (**a**) Continuous cold-rolled sheet and (**b**) reversible cold-rolled sheet.

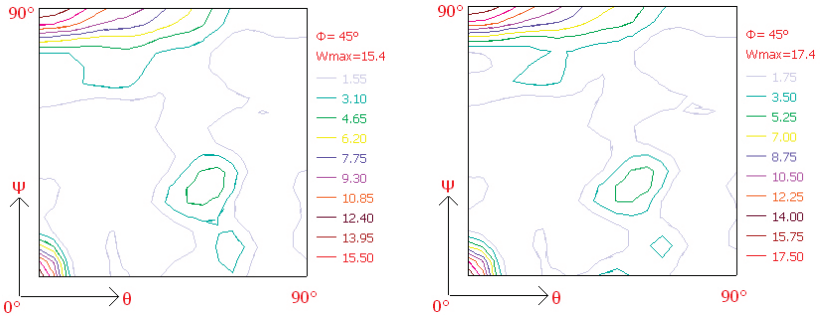

(**a**) (**b**)

Figure 4. Surface textures of continuous cold-rolled sheet and reversible cold-rolled sheet. (**a**) Continuous cold-rolled sheet and (**b**) reversible cold-rolled sheet.

3.3. Microstructures and Textures of Annealed Sheets

Figure 5 shows the microstructures of continuous cold-rolled sheets and reversible cold-rolled sheets after annealing. The grains of 2.4% Si non-oriented silicon steel annealed at 920 °C have completed recrystallization, resulting in a single ferrite structure, and some recrystallized grains have grown. After annealing at 1070 °C, the fine grains almost disappear and the microstructure uniformity is improved, but the grain size of the surface region is still slightly lower than that of the central layer [4]. Figure 6 shows the average grain size of the annealed sheets at different temperatures. The average grain sizes of the reversible cold-rolled sheets annealed at 920~950 °C are similar to those of the continuous cold-rolled annealed sheets. As the temperature gradually increases to 1010 °C, the difference of the average grain size between the two specimens at the same temperature increases. The average grain size of the reversible cold-rolled annealed sheet exceeds that of the continuous cold-rolled annealed sheet annealed at 1070 °C [16].

Table 2 shows the ODFs for the Φ = 45° section at the surface layer of continuous cold-rolled sheets and reversible cold-rolled sheets after annealing at different temperatures. The main recrystallization texture component is γ fiber with peak at {111} <112>, as well as a weak α fiber, λ fiber (<001>//ND), and Goss texture. For the annealed sheets of continuous cold rolling, with the increase in annealing temperature, the intensity of the {111} increases first and decreases, and reaches its maximum when annealed at 980 °C. The intensity of {001} <110> in the α fiber fluctuates with the increase in temperature, and it reaches maximum annealing at 980 °Cand reaches its maximum when annealed at 980 °C. The changes in the {110} and Goss textures are not obvious in the whole annealing temperature range. The intensities of the annealed sheets of reversible cold rolling are similar to those of the annealed sheets of continuous cold rolling, but the intensity of the {111} texture of the annealed sheets with reversible cold rolling reaches the maximum when

annealed at 950 °C, and the γ-fiber intensity of the two types of annealed sheets is not much different.

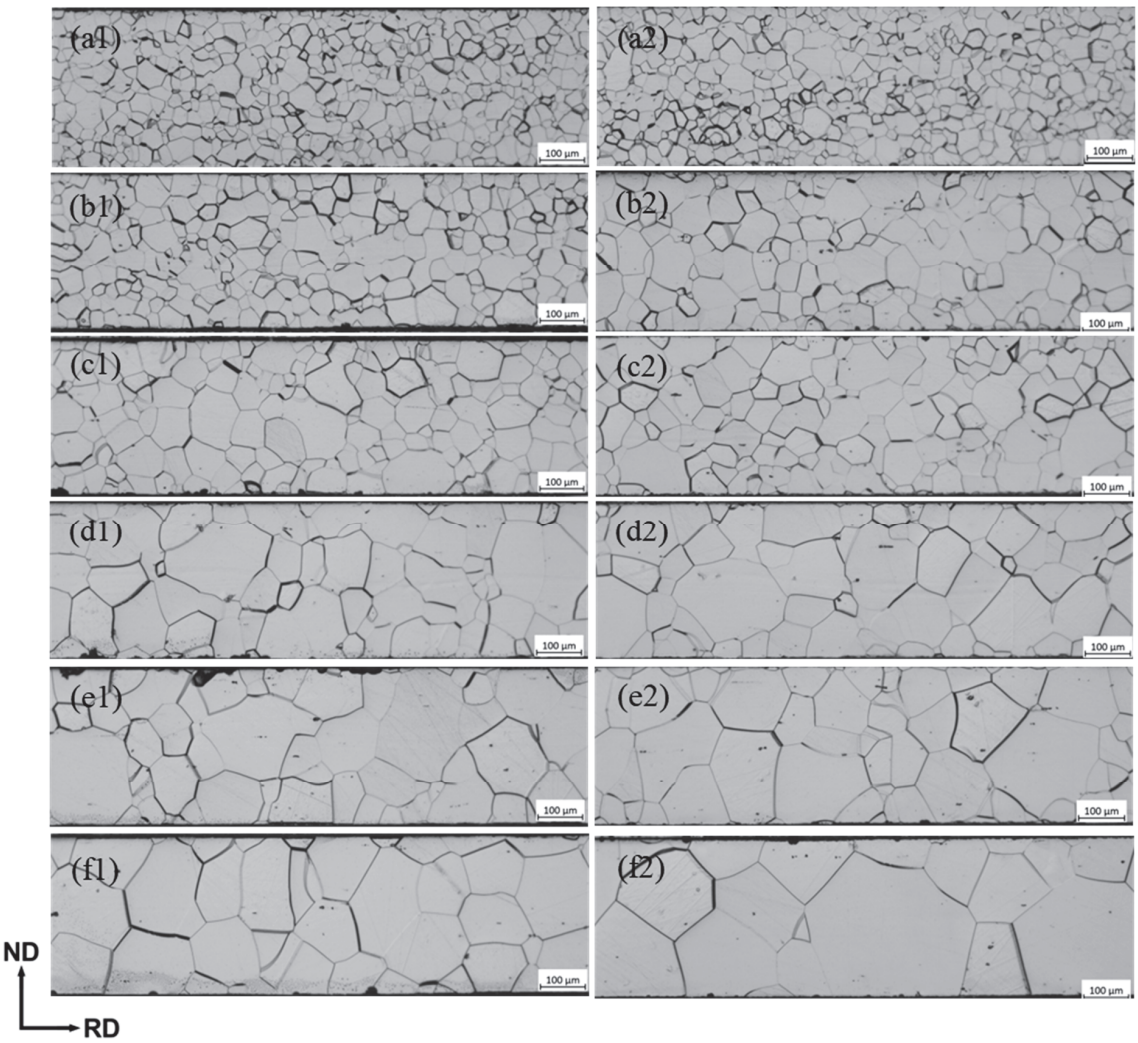

Figure 5. Microstructures of annealed sheets. (**a1**–**f1**) annealed sheets with continuous cold rolling; (**a2**–**f2**) annealed sheet with reversible cold rolling; (**a1**,**a2**) 920 °C; (**b1**,**b2**) 950 °C; (**c1**,**c2**) 980 °C; (**d1**,**d2**) 1010 °C; (**e1**,**e2**) 1040 °C; and (**f1**,**f2**) 1070 °C.

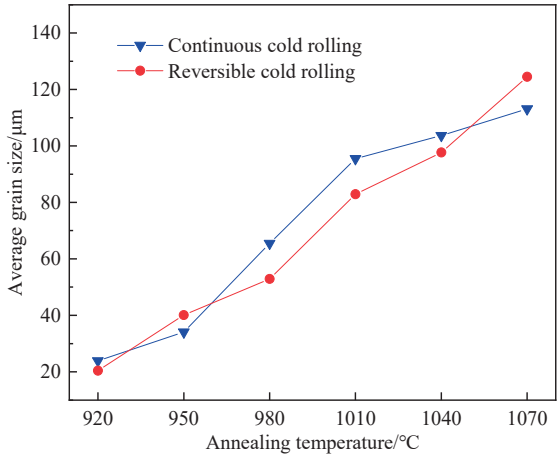

Figure 6. Average grain size of annealed sheets at different temperatures.

Table 2. Orientation distribution functions for a Φ = 45° section after annealing at different temperatures.

Temperature/°C	Cold Rolling Method	
	Continuous Cold Rolling	**Reversible Cold Rolling**
920	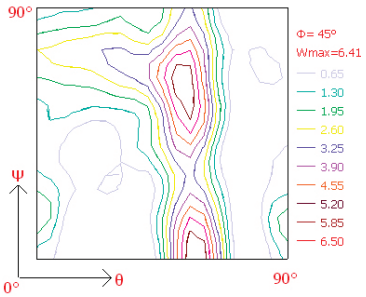	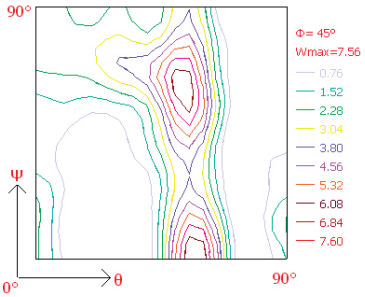
950	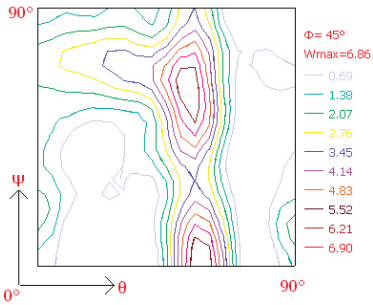	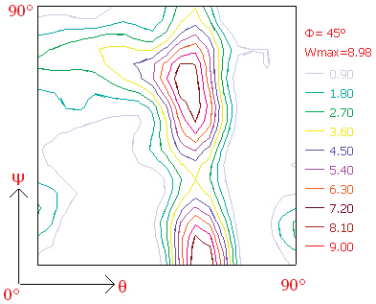
980	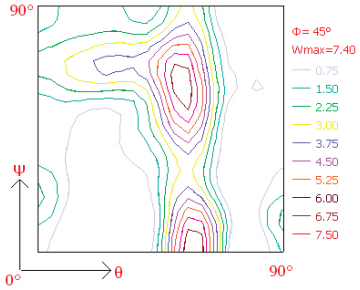	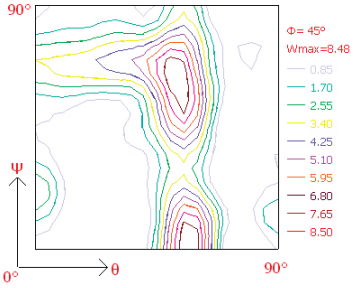
1010	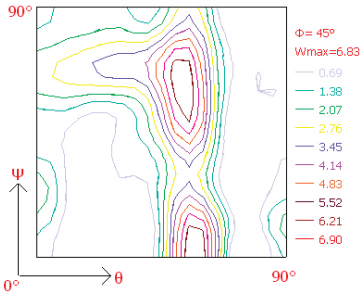	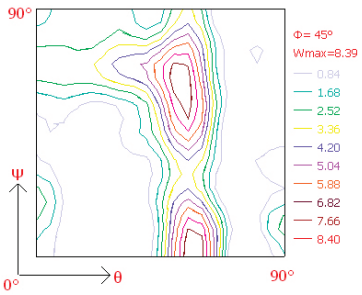
1040	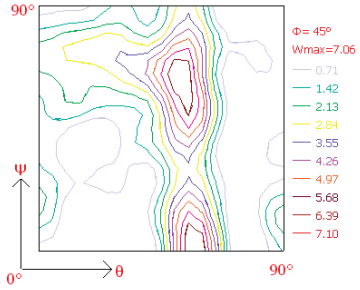	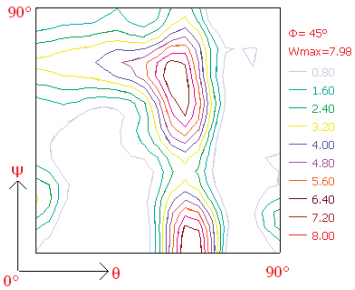

Table 2. *Cont.*

Temperature/°C	Cold Rolling Method	
	Continuous Cold Rolling	Reversible Cold Rolling
1070	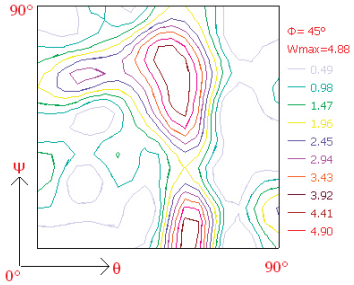	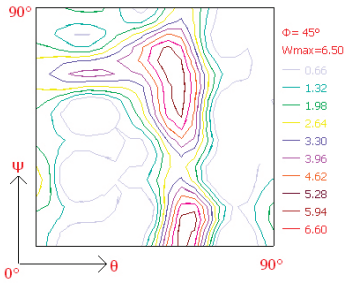

3.4. Magnetic Properties of Annealed Finished Products

Figure 7 shows the magnetic induction and iron losses of the finished products. For the finished products of continuous cold rolling, with the increase in temperature, there is only a slight fluctuation in the overall magnetic induction B_{50}, with a small variation around 1.682 T, while the iron loss $P_{1.5/50}$ decreases. The specific performance is that the iron loss decreases sharply from 3.297 W·kg^{-1} to 2.922 W·kg^{-1} when annealed at 950 °C, and then it decreases slowly to the lowest value of 2.445 W·kg^{-1}. When the temperature rises to 1070 °C, the iron loss increases slightly to 2.494 W·kg^{-1}.

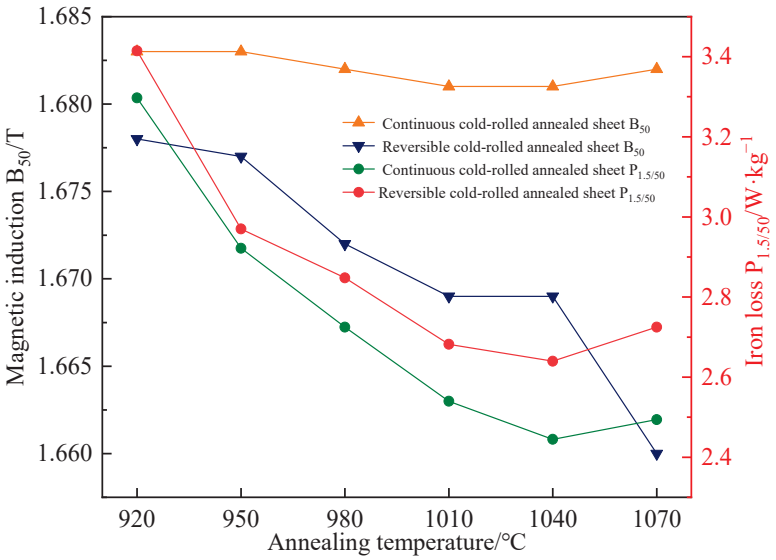

Figure 7. Iron losses $P_{1.5/50}$ and magnetic induction B_{50} of 2.4%Si non-oriented silicon steel after different annealing temperatures.

For the finished products of reversible cold rolling, the change trend of magnetic induction B_{50} is obviously different from that of continuous cold rolling. With the increase in annealing temperature, the magnetic induction B_{50} decreases slowly. When annealed at 1010 °C, the magnetic induction B_{50} decreases seriously and then tends to be stable at 1040 °C. However, when the temperature rises to 1070 °C, the magnetic induction B_{50} drops sharply to 1.660 T. The change trend of iron loss $P_{1.5/50}$ of the finished sheets of reversible cold rolling is similar to that of the finished sheets of continuous cold rolling, showing a trend of decreasing first and then increasing. The iron loss $P_{1.5/50}$ decreases slowly from 3.415 W·kg^{-1} to 2.640 W·kg^{-1}. When the annealing temperature rises to 1070 °C, the iron loss $P1_{.5/50}$ reaches 2.725 W·kg^{-1}.

Overall, the iron losses of the finished products of continuous cold rolling are lower than those of the finished products of reversible cold rolling with the increase in annealing temperature, and the magnetic induction is higher than that of the finished products of reversible cold rolling, because the crystallographic textures are important factors affecting the magnetic induction of non-oriented silicon steel, and the iron loss values are mainly determined by the grain sizes.

4. Analysis and Discussion

4.1. Effect of Cold Rolling Method on Microstructure and Texture

Plastic deformation occurs due to shear stress during the cold rolling of the normalized sheet, and the microstructure is mainly fibrous [17]. During polycrystalline rolling, deformation first occurs inside the grains. With the increase in rolling passes, the grains inside the sheet are elongated, and the dislocations are moved to the grain boundaries. The stress of the dislocations causes lattice distortion, and the internal strain-free subgrains are fibrous under the optical microscopy. The degree of tissue fibrosis is different between continuous cold-rolled sheet and reversible cold-rolled sheet due to different rolling methods. Figure 8 is a simplified diagram of the rolling deformation and stress of the polycrystalline sheet. Because the transverse direction of the sheet basically does not change, σ_{TD} is neglected. With the increase in rolling passes during continuous rolling, the influence of σ_{RD} on the deformation of the sheet during rolling is deepened, and additional shear stress is generated in the deformation zone to make each layer of metal slide along the rolling direction, so the effect of the shear stress is accumulated. In reversible rolling, the shear stress changes with the rolling direction, and the deformation effect of the shear force on the steel sheet during rolling cannot be accumulated. Therefore, under the same reduction rate, the degree of fibrosis of the transverse structure of the continuous cold-rolled sheet is less than that of the reversible cold-rolled sheet.

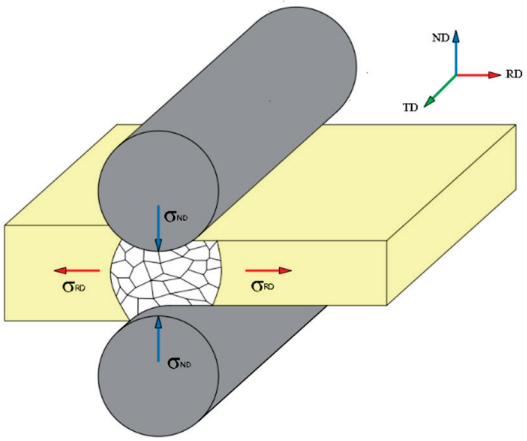

Figure 8. Simplified schematic diagram of rolling deformation and stress of polycrystalline sheet.

The shear stress effect of different rolling methods affects the grain rotation. The Bunge's symbol system was used to quantitatively analyze the texture intensity of each pass during the cross-section reduction process of the reversible cold-rolled sheet, and it is compared with the intensity of the 0.35 mm thick continuous cold-rolled sheet, as shown in Figure 9. After cold rolling with 65.91%, 70.45%, 80.91%, and 84.09% reduction, the normalized sheet formed strong α and γ fibers. The main textures in the α fiber are {001}~{112} <110>, and the main textures in the γ fiber are {111} <110> and {111} <112>. The reduction rate of the first pass of reversible cold rolling is 30.45%, the texture distribution is still relatively scattered, the grain orientation gradually gathers to the α-fiber orientation, the maximum value is near {001} <110>, and the γ-fiber intensity is weak. The second pass reduction rate is 65.91%. The strong intensity in the α fiber is near {112} <110>, and the maximum intensity in the γ fiber is near {111} <112>. The reduction rate of the third pass is

70.45%, and the grain orientations are completely concentrated near the α-fiber and γ-fiber orientations. The strong intensity at {112} <110> in the α fiber and the α fiber gradually moves to the {111} <110> orientation. The α-fiber and γ-fiber intensities increase at the same time. With the increase in the fourth pass reduction rate of 80.19% and the fifth pass reduction rate of 84.09%, the peak intensity of the reversible cold-rolled sheet appears near (0°, 15°, 45°), the intensity of {112} <110> decreases slightly, and the intensity of γ-fiber texture changes little. In the early stage of reversible cold rolling, the intensity of {001} <110> increases due to the shear stress, but the reversible cold rolling changes the direction of the surface shear stress. Therefore, with the increase in the rolling passes, the intensity of {001} <110> after rolling is weaker than that of the previous pass. The peak intensity of the α-fiber orientation of the continuous cold-rolled sheet is near {112} <110> and reaches 21. The peak intensity of the γ-fiber orientation is at {111} <110> and reaches 7.3. After the fifth pass rolling, the α-fiber intensity is significantly stronger than that of the reversible cold-rolled sheet, and the unfavorable {111} <112> is weaker than that of the reversible cold-rolled sheet [18,19].

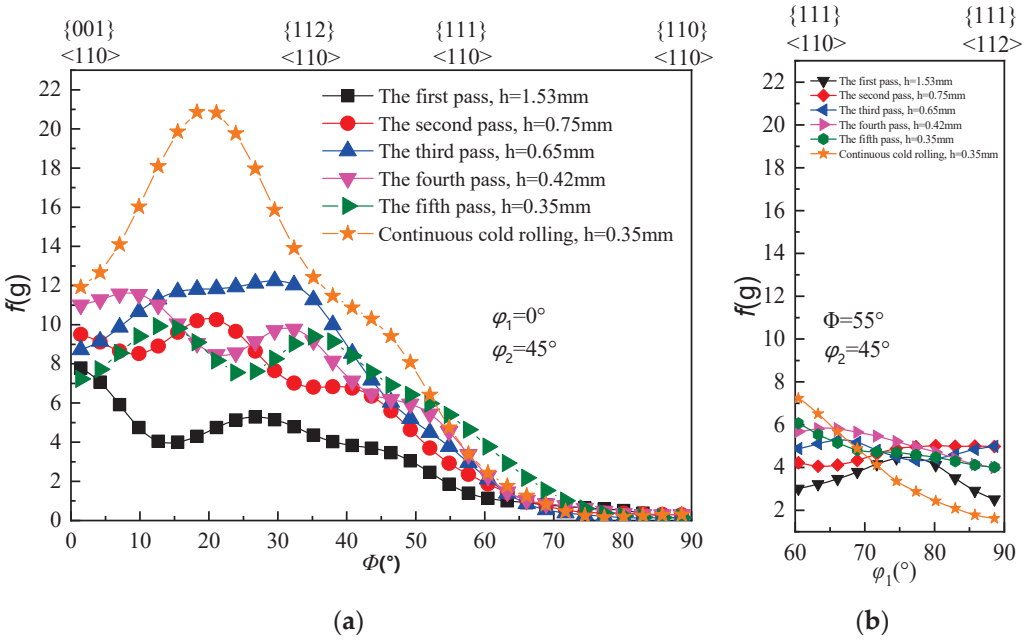

Figure 9. The density changes of α and γ fibers under different reduction rates. (**a**) The density changes of α fiber and (**b**) the density changes of γ fiber.

4.2. Effect of Annealing Temperature on Microstructure and Texture

The cold-rolled microstructures experienced recovery, recrystallization, and grain growth in the annealing stage. At the same annealing temperature, the average grain sizes of the annealed sheets are different, mainly due to the difference in rolling methods. The direction change of reversible cold rolling causes the grains to break into more shear bands, and the grains are more likely to nucleate at the shear bands during annealing. Reversible cold rolling has more nucleation points, resulting in the average grain sizes of the annealed sheets of continuous cold rolling being larger than those of the annealed sheets of reversible cold rolling [20]. However, with the increase in annealing temperature, the difference in average grain size between the two types of annealed sheets at the same temperature gradually decreases.

Figures 10 and 11 quantitatively show the variation of α-fiber and γ-fiber intensities of continuous cold-rolled sheets and reversible cold-rolled sheets with different annealing temperatures. The intensity of {00l} <110> increases first and then decreases with the increase in temperature during continuous cold rolling annealing, while it decreases rapidly and then increases slightly during reversible cold rolling annealing [21]. The main reason is that the deformation storage energy of grains is different. Due to the difference of the

microstructure and energy storage of deformed microstructure in cold-rolled sheets with different reduction rates, the order of deformation storage energy of grains with different orientations is [22] as follows: {001} < {112} < {111} < {110}.

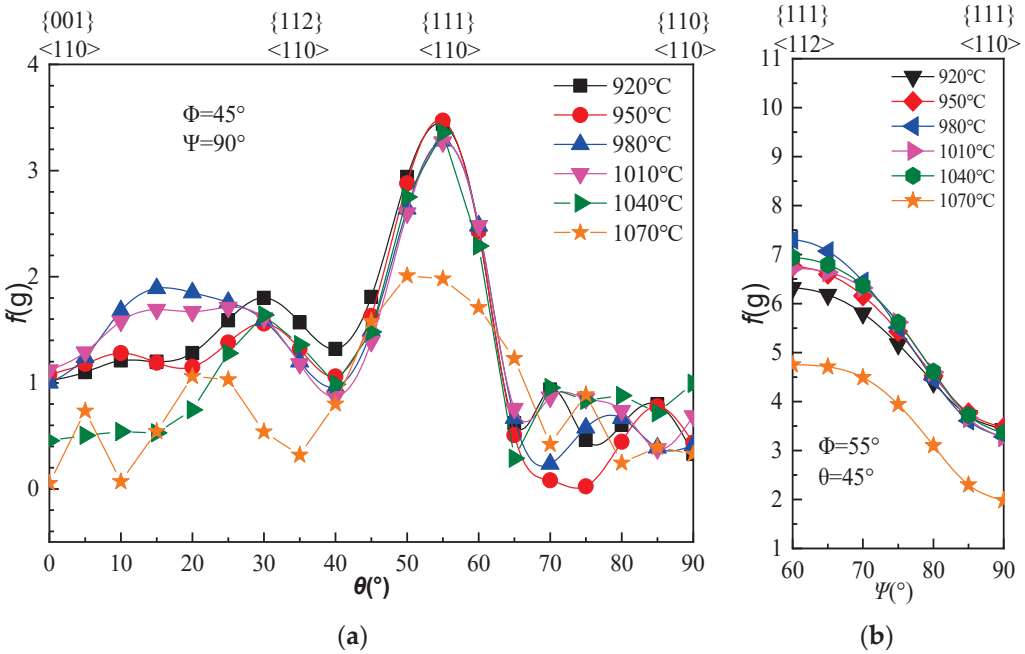

Figure 10. α and γ fibers of continuous cold-rolled sheets after different annealing temperatures. (**a**) α fiber of continuous cold-rolled sheets and (**b**) γ fiber of continuous cold-rolled sheets.

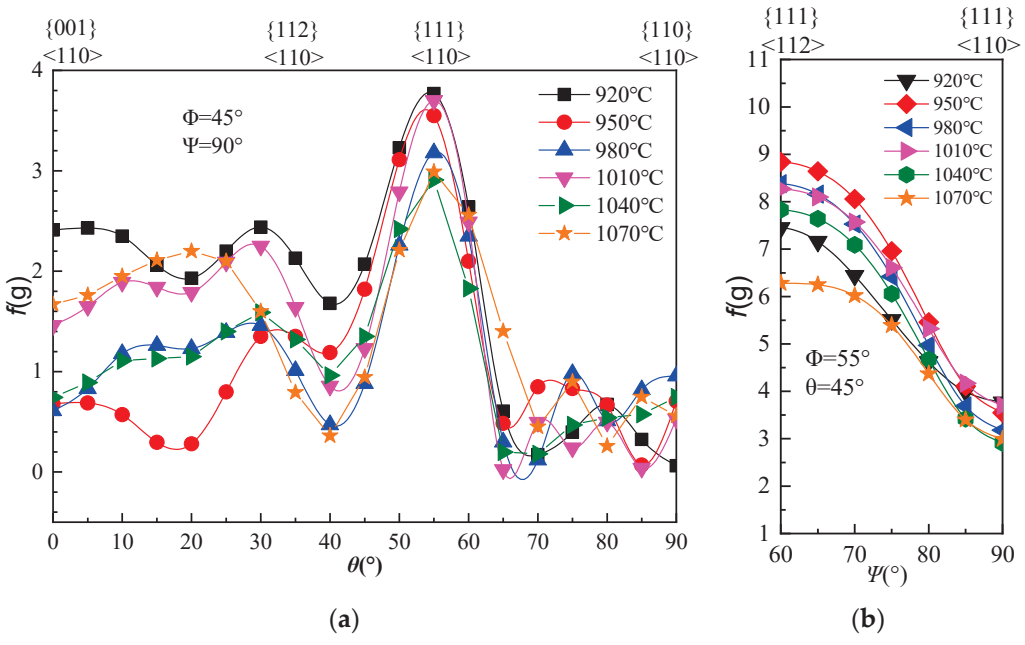

Figure 11. α and γ fibers of reversible cold-rolled sheets after different annealing temperatures. (**a**) α fiber of reversible cold-rolled sheets and (**b**) γ fiber of reversible cold-rolled sheets.

For a continuous cold-rolled sheet, after annealing at 920~1010 °C, {001} <110> grains are retained in situ recrystallization due to the low deformation storage energy, but the driving force of recrystallization is positively correlated with the annealing temperature. After annealing at 1040~1070 °C, the {001} <110> grains rotate to form other orientations, while the increase in the {001} <110> texture of the reversible cold-rolled sheet annealed at 1010 °C and 1070 °C is also due to the rotation of some grains to the {001} <110> orientation.

For both cold-rolled sheets, with the increase in annealing temperature, the α-fiber texture gradually gathers near the position of about 27° away from the <110> crystal axis due to the selective growth during recrystallization. [23]. It is not found in Figures 10 and 11 that the γ-fiber intensity increases monotonously with the increase in temperature. The main reason is that the storage energy along the γ-fiber orientation in the deformed matrix is high, and the {111} grains are recrystallized first, and the {111} texture is obviously enhanced due to the phagocytosis of the surrounding low storage energy grains. Similar results have been published for BCC Ti after cold rolling at 80% [24]. However, the preferential growth of {111} grains due to the high deformation storage energy is no longer obvious when the two cold-rolled sheets are annealed at 1070 °C and the γ-fiber intensity decreases [25].

4.3. Effect of Annealing Temperature on Magnetic Properties

{111} planes have the highest average magnetocrystalline anisotropy energy compared with {100} and {110} planes, which is one of the main factors affecting the magnetic induction [26,27]. For the non-oriented silicon steel with continuous cold rolling, combined with the findings in Figures 7 and 10, it can be seen that when the annealing temperature increases from 920 °C to 980 °C, the γ-fiber intensity increases gradually, and the α-fiber intensity remains basically unchanged, resulting in a decrease in B_{50}. When the annealing temperature rises to 1010 °C, the intensity of the {111} <110> texture remains basically unchanged, the intensity of the {111} <112> texture decreases slightly, and B_{50} increases. After annealing at 1070 °C, the γ-fiber intensity minimized more than that of the α fiber, and B_{50} increased slightly.

For reversible cold rolling (Figures 7 and 11), when the annealing temperature increases from 920 °C to 980 °C, the γ-fiber intensity increases first and then decreases, the α-fiber intensity decreases rapidly and then remains unchanged, and the intensity of {111} <110> decreases gradually, so B_{50} decreases. When the annealing temperature rises to 1070 °C, the γ-fiber intensity decreases significantly, the intensity of {111} <110> decreases and tends to be stable, and the α-fiber intensity increases slightly, but the magnetic induction B_{50} still decreases [28].

Hysteresis loss accounts for 55~75% of the power frequency iron loss $P_{1.5/50}$ of non-oriented silicon steel, which depends on the average grain size. In this work, the recrystallization of 2.4% Si non-oriented silicon steel was completed when annealed at 920 °C. With the increase in annealing temperature, the grain size increases, the area of the grain boundaries in the microstructure decreases, and the hysteresis loss decreases [29]. The grain size continues to increase, and the eddy current loss gradually increases, but the hysteresis loss still plays a leading role, and the total iron loss still decreases. When the grain size reaches the critical grain size, the magnetic domain size increases, resulting in the increase in eddy current loss and anomalous eddy current loss [30,31].

It can be seen from Figure 12 that the iron loss values of the two types of cold-rolled sheets after annealing decrease first and then increase with the increase in the average grain size. It is worth noting that for the annealed sheets of non-oriented silicon steel with two different cold rolling methods, when the average grain size is 82.9~113.1 μm, not only does the iron loss show a continuous downward trend, but it also has a high magnetic induction. When the average grain size is greater than 113.1 μm, the iron loss increases and the magnetic induction intensity decreases greatly, hence the overall magnetic properties deteriorate seriously. When the annealing temperature is between 1010 °C and 1040 °C, the iron loss $P_{1.5/50}$ tends to be stable. When the average grain size increases to a certain value, the iron loss $P_{1.5/50}$ increases. Comparing the iron losses $P_{1.5/50}$ of the two types of cold-rolled sheets after annealing, it is found that at the same annealing temperature, the average grain size of the annealed sheet of continuous cold rolling is higher than that of the annealed sheet of reversible cold rolling, so the iron loss of the annealed sheet of continuous cold rolling is slightly lower than that of the annealed sheet of reversible cold rolling, but the iron loss is not solely controlled by the size of grains. For example, after

annealing at 1070 °C, the average grain size of the annealed sheet of reversible cold rolling is higher, indicating that different rolling methods may affect the iron loss.

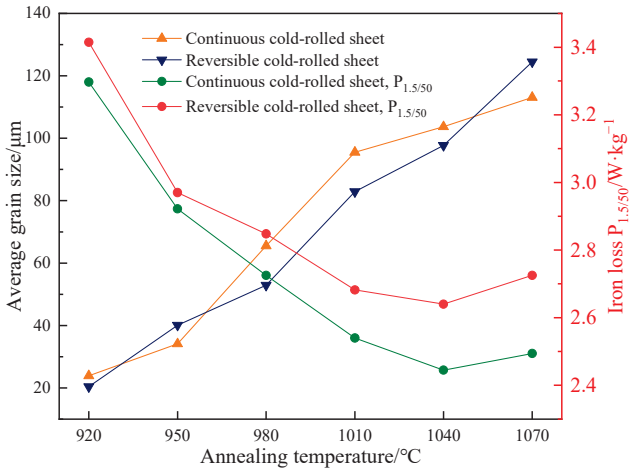

Figure 12. The average grain size and iron losses at different annealing temperatures.

5. Conclusions

(1) After the cold rolling of normalized sheets, the ferrite grains are deformed into flat or fibrous mixed structures. The surface textures of the two cold-rolled sheets are concentrated on the α-fiber and γ-fiber orientations, and the α-fiber intensity is significantly stronger than that of the γ fiber. The α-fiber intensity of the reversible cold-rolled sheet is stronger than that of the continuous cold-rolled sheet, and reversible cold rolling is more conducive to the formation of the α fiber.

(2) After annealing at 920 °C, the recrystallization process of the cold-rolled sheet is completed, and the average grain sizes increase with the increase in temperature. After annealing at different temperatures, the main recrystallization texture components are γ fiber, as well as a weak α fiber, λ fiber, and Goss texture.

(3) For two different cold-rolled non-oriented silicon steel annealed sheets, the critical grain size range should be 82.9~113.1 μm, and the overall magnetic performance is excellent. For the finished products of continuous cold rolling, the magnetic induction B_{50} fluctuates up and down at 1.682 T, and the iron loss $P_{1.5/50}$ drops to the lowest value of 2.445 W·kg^{-1}, which is annealed at 1040 °C. For the finished products of reversible cold rolling, the magnetic induction B_{50} is reduced to 1.660 T, annealed at 1070 °C, and the iron loss $P_{1.5/50}$ of the finished products is reduced to the lowest value of 2.640 W·kg^{-1}, which is annealed at 1040 °C.

(4) Under the condition of a certain chemical composition, with the increase in annealing temperature, the magnetic induction B_{50} of non-oriented silicon steel produced by reversible cold rolling is slightly lower than that of continuous cold rolling. If the product adopts continuous cold rolling, and is supplemented by a higher annealing temperature during annealing, lower amounts of iron loss can be obtained, and the comprehensive magnetic performance is the best. It is a method to improve the magnetic properties of products under the premise of certain chemical compositions. Therefore, in order to ensure the excellent electromagnetic properties of 2.36% Si non-oriented silicon steel, the continuous cold rolling method should be adopted, and the optimal annealing temperature should be controlled at 1010~1040 °C for 30 s.

Author Contributions: Conceptualization, K.S. and H.W.; methodology, Y.N and H.P.; software, J.Q.; validation, Y.N., Y.P. and H.W.; formal analysis, K.S.; investigation, K.S.; resources, Y.P.; data curation, Y.N., J.Q. and H.W.; writing—original draft preparation, K.S.; writing—review and editing, Y.N. and H.P.; visualization, H.W., Y.P. and H.P.; supervision, J.Q.; project administration, J.Q. and H.W.; and funding acquisition, H.W. All authors have read and agreed to the published version of the manuscript.

Funding: The authors acknowledge the support from the National Natural Science Foundation of China (No. 52374316), the Fund of Education Department of Anhui Province (No. 2022AH050291), the Open Project Program of Anhui Province Key Laboratory of Metallurgical Engineering & Resources Recycling (Anhui University of Technology) (No. SKF21-04 and SKF23-03), and the Jiangxi Province Major Scientific and Technological Research and Development Special Funding Project (20213AAE01009).

Data Availability Statement: The data presented in this study are available on request from the corresponding author due to privacy and ethical restrictions.

Conflicts of Interest: Authors Y.P. and J.Q. were employed by Ma'anshan Iron and Steel Co., Ltd. and Iron and Steel Research Institute Co., Ltd., respectively. The remaining authors declare that the research was conducted in the absence of any commercial or financial relationships that could be construed as potential conflicts of interest.

References

1. Zhu, C.Y.; Bao, Y.K.; Wang, Y.; Ma, J.H.; Li, G.Q. Research progress on application status and property control of non-oriented silicon steel for traction motor of new energy vehicles. *Mater. Rep.* **2021**, *35*, 23089–23096.
2. Zhu, C.Y.; Luo, X.Y.; Li, G.Q.; Feng, J.X.; Yan, Z.F. Formation mechanism analysis on magnesium-bearing inclusions in non-oriented silicon steels. *J. Chongqing Univ.* **2018**, *41*, 34–43.
3. Park, J.T.; Szpunar, J.A. Effect of initial grain size on texture evolution and magnetic properties in non-oriented electrical steels. *J. Magn. Magn. Mater.* **2009**, *321*, 1928–1932. [CrossRef]
4. Li, Z.H.; Xie, S.K.; Wang, G.D.; Liu, H.T. Dependence of recrystallization behavior and magnetic properties on grain size prior to cold rolling in high silicon non-oriented electrical steel. *J. Alloys Compd.* **2021**, *888*, 161576. [CrossRef]
5. Zhang, B.; Liang, Y.F.; Wen, S.B.; Wang, S.; Shi, X.J.; Ye, F.; Lin, J.P. High-strength low-iron-loss silicon steels fabricated by cold rolling. *J. Magn. Magn. Mater.* **2019**, *474*, 51–55. [CrossRef]
6. Fang, F.; Che, S.F.; Hou, D.W.; Zhang, Y.X.; Wang, Y.; Zhang, W.N.; Yuan, G.; Zhang, X.M.; Misra, R.D.K.; Wang, G.D. Thin-gauge non-oriented silicon steel with balanced magnetic and mechanical properties processed by strip casting. *Mater. Sci. Eng. A* **2022**, *831*, 142284. [CrossRef]
7. Li, M.; Xiao, Y.D.; Wang, W.; Zhou, J.; Wu, G.L.; Peng, Y.M. Effect of annealing parameter on microstructure and magnetic properties of cold-rolled non-oriented electrical steel. *Trans. Nonferrous Met. Soc. China* **2007**, *17*, s74–s78.
8. Kawamata, R.; Kubota, T.; Yamada, K. The effect of cold rolling parameters on the recrystallization texture of non-oriented electrical steel. *J. Mater. Eng. Perform.* **1997**, *6*, 701–709. [CrossRef]
9. Cheong, S.W.; Hilinski, E.J.; Rollett, A.D. Effect of temper rolling on texture formation in a low loss cold-rolled magnetic lamination steel. *Metall. Mater. Trans. A* **2003**, *34*, 1311–1319. [CrossRef]
10. Li, N.; Ma, L.; Xiang, L.; Qiu, S.T.; Zhao, P. Evolution of texture in a 2.8%Si non-oriented electrical steel annealed at 1100 °C. *Mater. Trans.* **2014**, *55*, 387–390. [CrossRef]
11. Kestens, L.; Jacobs, S. Texture control during the manufacturing of non-oriented electrical steels. *Texture Stress Micro.* **2008**, *2008*, 173083.
12. Zhang, S.R. Research on Rolling Force Prediction Method of Six-high Reversible Cold Rolling Mill. Master's Thesis, Xi'an University of Technology, Xi'an, China, 2021.
13. An, L.Z.; Wang, Y.P.; Song, H.Y.; Wang, G.D.; Liu, H.T. Improving magnetic properties of non-oriented electrical steels by controlling grain size prior to cold rolling. *J. Magn. Magn. Mater.* **2019**, *491*, 165636. [CrossRef]
14. Hu, C.Y.; Song, R.B.; Wang, Y.J.; Zhao, Z.Y.; Zhang, Y.C. Comprehensive influence of the normalized and final annealing process on high-strength non-oriented silicon steel. *Steel Res. Int.* **2022**, *93*, 2100641. [CrossRef]
15. Xin, Y.H.; Gao, Z.Y.; Huang, Y.Z.; Xu, H.J.; Xu, Y.B. Effect of annealing temperature on microstructure, texture and magnetic properties of non-oriented 3.2%Si steel. *Trans. Mate. Heat Treat.* **2021**, *42*, 74–80.
16. Schulte, M.; Steentjes, S.; Leuning, N.; Bleck, W.; Hameyer, K. Effect of manganese in high silicon alloyed non-oriented electrical steel sheets. *J. Magn. Magn. Mater.* **2019**, *477*, 372–381. [CrossRef]
17. Sanjari, M.; He, Y.L.; Hilinski, E.J.; Yue, S.; Kestens, L.A.I. Development of the {113}<uvw> texture during the annealing of a skew cold-rolled non-oriented electrical steel. *Scripta Mater.* **2016**, *124*, 179–183.
18. Peng, K.; Xiang, L.; Qiu, S.T.; Zhang, Y.H. Microstructure and texture of 50W470 silicon steel during reversing cold rolling process. *Heat Treat. Metals.* **2016**, *41*, 46–49.
19. Chu, S.J.; Shen, K.Y.; Sha, Y.H.; Chen, X. Orientation dependence of strain stored energy and its effect on recrystallization texture in non-oriented silicon steel. *J. Mater. Eng.* **2019**, *47*, 147–153.
20. Gupta, A.; Khatirkar, R.K.; Kumar, A.; Thool, K.; Bibhanshu, N.; Suwas, S. Microstructure and texture development in Ti-15V-3Cr-3Sn-3Al alloy–Possible role of strain path. *Mater. Charact.* **2019**, *156*, 109884. [CrossRef]
21. He, Z.Z.; Zhao, Y.; Luo, H.W. *Electrical Steel*; Metallurgical Industry Press: Beijing, China, 2012.
22. Park, J.T.; Szpunar, J.A. Evolution of recrystallization texture in non-oriented electrical steels. *Acta Mater.* **2003**, *51*, 3037–3051. [CrossRef]

23. Kestens, L.; Jonas, J.J. Modelling texture change during the static recrystallization of a cold-rolled and annealed ultra low carbon steel previously warm rolled in the ferrite region. *ISIJ Int.* **1997**, *37*, 807–814. [CrossRef]
24. Gupta, A.; Khatirkar, R.K.; Dandekar, T.; Jha, J.S.; Mishra, S. Recrystallization behavior of a cold rolled Ti–15V–3Sn–3Cr–3Al alloy. *J. Mater. Res.* **2019**, *34*, 3082–3092. [CrossRef]
25. Park, J.T.; Szpunar, J.A. Texture development during grain growth in non-oriented electrical steels. *ISIJ Int.* **2005**, *45*, 743–749. [CrossRef]
26. Huneus, H.; Günther, K.; Kochmann, T.; Plutniok, V.; Schoppa, A. Non-oriented magnetic steel with improved texture and permeability. *J. Mater. Eng. Perform.* **1993**, *2*, 199–203. [CrossRef]
27. Gheorghies, C.; Doniga, A. Evolution of texture in grain oriented silicon steels. *J. Iron Steel Res. Int.* **2009**, *16*, 78–83. [CrossRef]
28. Sidor, J.J.; Verbeken, K.; Gomes, E.; Schneider, J.; Calvillo, P.R.; Kestens, L.A.I. Through process texture evolution and magnetic properties of high Si non-oriented electrical steels. *Mater. Charact.* **2012**, *71*, 49–57. [CrossRef]
29. Jenkins, K.; Lindenmo, M. Precipitates in electrical steels. *J. Magn. Magn. Mater.* **2008**, *320*, 2423–2429. [CrossRef]
30. Salinas, J.J.; Salinas, A. Grain size and texture evolution during annealing of non-oriented electrical steel deformed in tension. *J. Mater. Eng. Perform.* **2015**, *24*, 2117–2125. [CrossRef]
31. De Campos, M.F.; Teixeira, J.C.; Landgraf, F.J.G. The optimum grain size for minimizing energy losses in iron. *J. Magn. Magn. Mater.* **2006**, *301*, 94–99. [CrossRef]

crystals

MDPI

Article

Influence Mechanisms of Cold Rolling Reduction Rate on Microstructure, Texture and Magnetic Properties of Non-Oriented Silicon Steel

Feihu Guo [1,2], Yuhao Niu [2], Bing Fu [3], Jialong Qiao [2,3,*] and Shengtao Qiu [2]

[1] School of Metallurgy, Northeastern University, Shenyang 110819, China; guofeihu2020@163.com
[2] Iron and Steel Research Institute Co., Ltd., Beijing 100081, China; niuyuhaoahut@163.com (Y.N.); qiustchina@126.com (S.Q.)
[3] Silicon Steel & Sheet Business Division, Xinyu Iron and Steel Group Co., Ltd., Xinyu 338001, China; fubing1986yj@163.com
* Correspondence: qiaojialong2015@126.com

Abstract: The effects of cold rolling reduction on the microstructure, recrystallization behavior, and magnetic properties of 3.0%Si-0.8%Al-0.3%Mn steel were studied by X-ray diffraction (XRD) and electron backscatter diffraction (EBSD). With the reduction rates of 78%, 85% and 87% in the cold rolled sheet, the width of the deformation band becomes narrower, the number of intragranular shear bands decreases, and the proportion of grain boundaries increases. The intensity of the α and γ fibers texture in the cold rolled sheet is enhanced, and the annealed sheet is dominated by the γ fibers texture and the content increases from 26.0% to 34.5%. During the recrystallization process, the Goss and γ-grains nucleate first. The λ-grains nucleate mainly at the grain boundaries of the deformed α-grains, and the α-grains ultimately recrystallize. With the increase in the cold rolling reduction rate, the γ-grains develop into the main texture due to a large amount of nucleation at the deformation band and grain boundary. The λ-grains with a high mobility do not have a numerical advantage, and the increase in the texture content is very small. The content of the unfavorable γ fiber texture in the annealed sheet increases, the magnetic induction intensity B50 decreases, Pe and Pt decrease significantly, and the critical grain size with the lowest iron loss decreases from 136.2 to 109.4 μm.

Keywords: non-oriented silicon steel; cold rolling reduction rate; recrystallization; texture; magnetic properties

1. Introduction

Non-oriented silicon steel has excellent soft magnetic materials with low iron loss characteristics and is widely used in high-end home appliances, new energy vehicle drive motors, and high-efficiency industrial motors [1,2]. In the context of carbon neutralization and energy conservation and emission reduction, improving the energy conversion efficiency of these electrical devices to reduce energy loss requires higher magnetic properties of the iron core materials [3–5]. The increasing of Si content and reducing the thickness of the product are the most effective methods to reduce the loss of non-oriented silicon steel. Especially under the condition of high frequency service, the eddy current loss is dominant, and the loss of thin silicon steel is lower and the advantage is more obvious [6–9]. Due to the manufacturing cost, work efficiency and market demand, how to adjust the cold rolling process to prepare different specifications of high silicon non-oriented silicon steel with an excellent performance by one-time cold rolling is an urgent problem to be solved. The cold rolling reduction rate is also different in the production process of non-oriented silicon steel with different specifications. The change of cold rolling reduction rate will directly affect the deformation microstructure, thus affecting the formation of recrystallized grains and then changing the magnetic properties [10].

Based on previous studies [11–14], the effects of different cold rolling reduction rates (60~95%) on the number and characteristics of micro-shear bands of cold rolled bands were proved. Under the medium reduction rate (60~70%), there are a large number of shear bands in the cold rolled band. As the reduction rate (80~95%) increases, the number and area of shear bands in the band decrease significantly until the grain fragmentation is completely replaced by the fibrous structure. The cold rolling reduction rate further analyzes the formation of the recrystallization texture by changing the deformation texture and the deformation structure including the shear band, deformation band and grain boundary region. Studies [15–17] have shown that the recrystallization texture of non-oriented silicon steel is concentrated in the Goss, α, γ and λ textures, and the competition of the texture components during recrystallization is mainly concentrated between γ and Goss. With the increase in the cold rolling reduction, the recrystallization mechanism changes from shear band nucleation to deformation band and grain boundary nucleation, resulting in the weakening of the recrystallization Goss component and the enhancement of the λ and {111}<112> recrystallization texture components [18,19]. However, the competitive relationship between the α, λ and γ texture components during recrystallization and the grain growth of the annealed sheets with different cold rolling reduction rates still needs to be systematically studied.

In this study, the effects of the cold rolling reduction on the deformation structure and texture, recrystallization texture evolution and magnetic properties of cold rolled band were studied by using 3.0%Si-0.8%Al-0.3%Mn non-oriented silicon steel 2.3 mm thick hot rolled band as raw material. By systematically analyzing the formation and growth of the recrystallized grains and their transformation with cold rolling reduction, the microstructure and texture of the annealed sheet were controlled by the annealing temperature to optimize the final magnetic properties. This provides theoretical support for improving the magnetic properties of non-oriented silicon steel with different specifications.

2. Materials and Methods

This experiment selected 2.3 mm thick non-oriented silicon steel hot-rolled sheet with the same hot rolling process conditions in the same furnace of industrial production as the experimental raw material. The main components (wt, %) were: C0.0023, Si3.11, Mn0.296, S0.0016, Al0.98, N0.0015 and Fe balance. The hot rolled sheets were subjected to a uniform normalization treatment at 950 °C for 3 min in a pure N_2 atmosphere, and then air cooled to room temperature. The heat treatment process of the normalized sheet before cold rolling was consistent. After acid washing to remove the surface oxides, the normalized sheets were rolled to 0.5, 0.35 and 0.3 mm with reduction rates of 78%, 85% and 87%, respectively. The processing schematic diagram of non-oriented silicon steel in this experiment is shown in Figure 1.

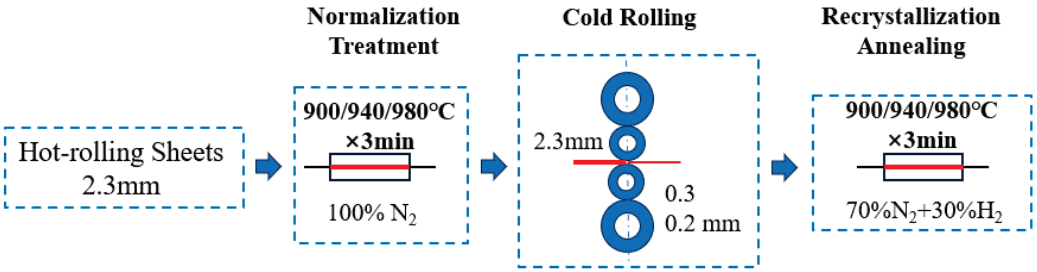

Figure 1. Processing route diagram of non-oriented silicon steel.

After standard grinding and polishing, the annealed samples were etched with 5% nitric acid alcohol solution. The metallographic structure was observed under an optical microscope (OM, DM4000, Wetzlar, Germany). The recrystallization ratio of the annealed band was estimated by Image-Pro Plus 6.0 software. The average grain size of the metallographic sample was measured according to the GB/T 6394-2002 linear intercept

method. The iron loss ($P_{1.5/50}$) and magnetic induction (B_{50}) of 30 × 300 mm single chip was measured by a magnetic measuring instrument (NIM-2000E AC, Beijing, China). The microstructure characteristics were detected by scanning electron microscopy (SEM, ZEISS SUPRA 55VP, Oberkochen, Germany) with electron backscatter diffraction system. The orientation distribution function (ODF) analysis, distribution analysis of specific orientation grains and quantitative statistics were analyzed by OIM 7.3 software. The main texture content was calculated with a deviation angle of 15°. The macroscopic texture of the sample was measured by X-ray diffraction.

3. Experimental Results

3.1. Microstructure and Texture Characteristics of Hot Rolled Sheet and Normalized Sheet

Figure 2a,c is the grain orientation diagram and macro texture of the hot rolled band. There are obvious differences in the microstructure and texture of the hot rolled sheet in the thickness direction. The surface layer is dominated by fine recrystallized grains, and the texture is dominated by a strong Goss texture, while the middle layer is dominated by deformed grains elongated along the rolling direction, and its texture is composed of strong α and λ fiber textures.

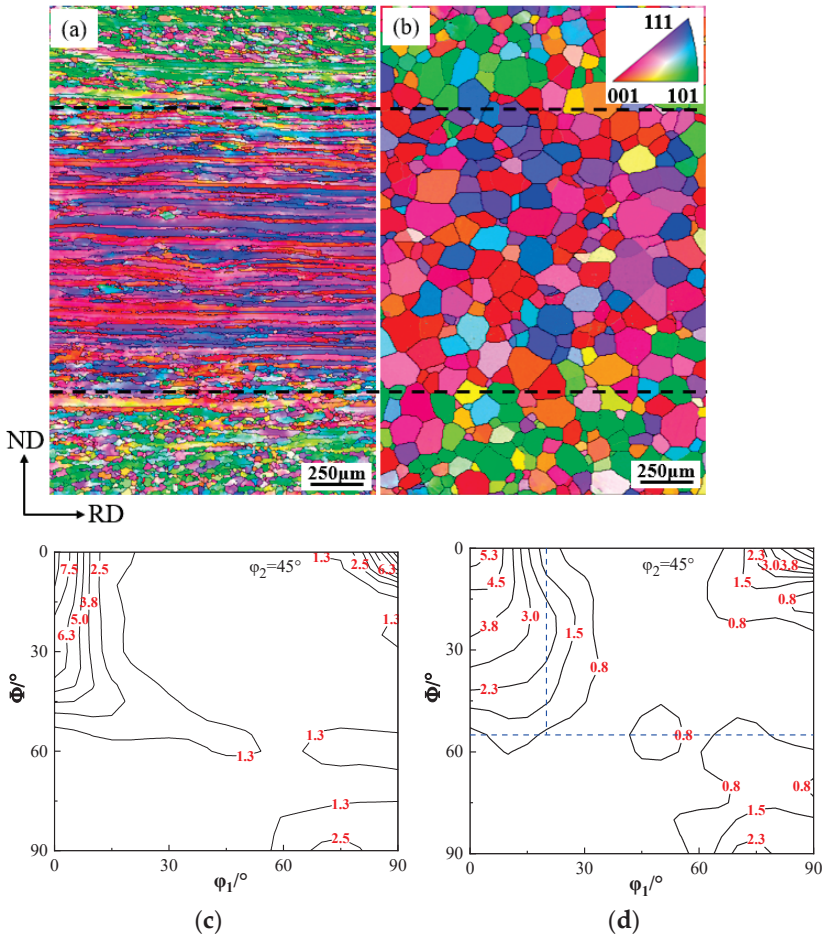

Figure 2. Grain orientation distribution and ODF section (φ_2 = 45°): (**a**,**c**) hot rolled bands; (**b**,**d**) normalized bands.

After the hot rolled sheet is normalized at 950 °C for 3 min, the fine equiaxed grains in the surface layer grow further, and the deformed microstructure in the central layer is completely recrystallized to form coarse grains. It can be seen from the grain orientation diagram of the normalized sheet in Figure 2b that the uniformity of the microstructure and the gradient of the texture in the thickness direction of the normalized sheet are improved.

The surface layer of the normalized band is mainly composed of equiaxed grains with smaller {110} orientation, while the central layer is mainly composed of grains with larger {001} and {111} orientations. The grain size distribution of the normalized sheet was 85.3 μm using the method of equivalent circle diameter. Combined with the macro texture of the normalized band in Figure 2d, the strongest texture is {100}<011>, and the texture intensity is 5.6. Compared with the hot rolled sheet, the texture intensity of the α fiber decreases, and there is a tendency to change to a α* fiber texture [20].

3.2. Microstructure and Texture Characteristics of Cold Rolled Sheet

Figure 3 is the microstructure of the cold rolled sheet with 78%, 85% and 87% reduction. The microstructure of the cold rolled sheet is mainly composed of deformed grains elongated along the rolling direction, and some of the deformed grains have shear bands with 20~35° to the rolling surface. The cold rolling reduction rate of the deformed strip has a significant effect on the characteristics of the shear band. The difference of corrosion degree of the cold rolled sheet is related to the difference of the deformation storage energy [13,17]. The deformation band has low energy storage and a low corrosion degree, which is a bright band. The grain boundary position with higher hardness and the intragranular shear band formed by the γ grains with a higher Taylor factor and flow stress [19,21], both of which have higher cold storage capacity, a greater corrosion degree and a deeper color. When the cold rolling reduction rate is 78%, there are coarse intragranular shear bands in the wider deformed grains, and the inclination angle between the shear band and the rolling direction is 29~35°. When the cold rolling reduction rate is 85%, the deformation band becomes narrower, the shear band becomes thinner, and the inclination angle with the rolling direction is reduced to 23~26°. While the cold rolling reduction rate increases to 87%, the grains are fragmented, the number of deformation bands becomes greater, thin and narrow, and the overlap between some shear bands and the grain boundaries becomes blurred, and there are still a small number of short shear bands with clear structural characteristics. For the same grain size of normalized band before cold rolling, with the increase in the cold rolling reduction rate, the dislocation density and the cold rolling energy storage in cold rolled band increase, the width of the deformation band narrows, the proportion of grain boundary increases, and the number of intragranular shear bands and the inclination angle with rolling direction decrease.

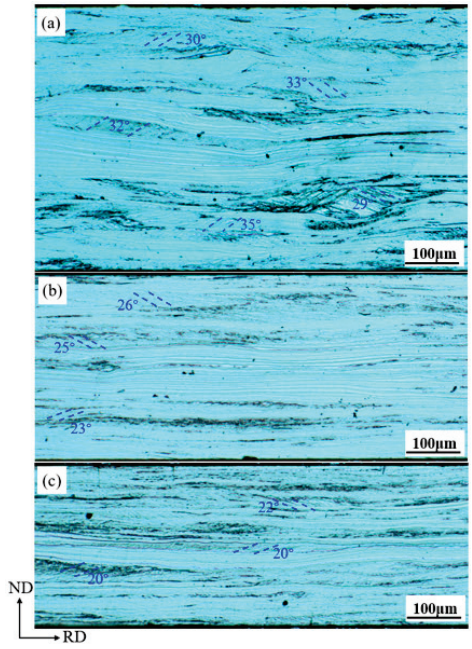

Figure 3. Microstructure of cold rolled sheets with different cold rolling reduction rates. (**a**) 0.5 mm; (**b**) 0.35 mm; (**c**) 0.3 mm.

From the macroscopic texture of the cold rolled band in Figure 4, it can be seen that the samples with different thicknesses show a strong α fiber texture and weak γ fiber texture. The α and γ fiber textures have the highest strength at the {100}<110> and {111}<112> components, respectively. With the increase in the cold rolling reduction rate, the texture strength of α and γ fibers of cold rolled sheet increases continuously.

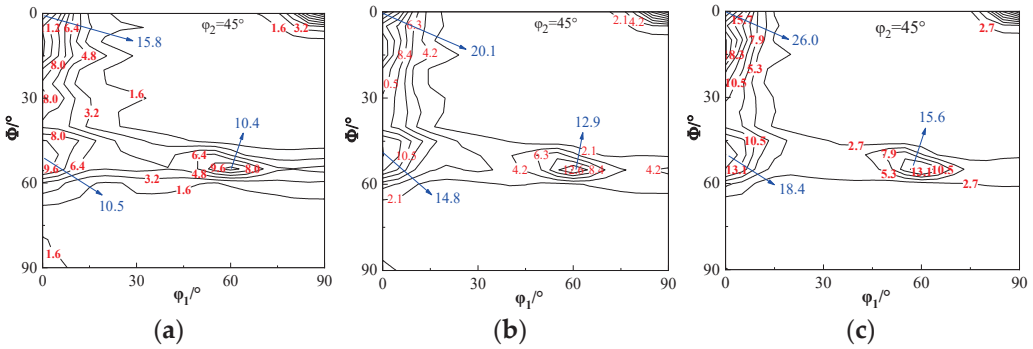

Figure 4. ODF section ($\varphi_2 = 45°$) of cold rolled sheets with different cold rolling reduction. (**a**) 0.5 mm; (**b**) 0.35 mm; (**c**) 0.3 mm.

3.3. Microstructure and Texture Characteristics of Annealed Sheet

The substructures of different deformed microstructures in cold rolled sheets caused by different cold rolling reduction rates have a significant effect on the evolution of the microstructure and texture during subsequent annealing. After annealing at 940 °C for 3 min, the recrystallized nucleus and grain growth occurred in the deformed matrix of the cold rolled sheet, and the microstructure after annealing was equiaxed ferrite grains. The special grain orientation and texture content after annealing are shown in Figures 5 and 6. The average grain sizes of the annealed sheet with thicknesses of 0.5, 0.35 and 0.3 mm are 89.7, 81.9 and 65.1 μm, respectively. The main factors affecting the microstructure of the annealed sheet are the nucleation rate (N) and grain growth rate (G) during the recrystallization process. With the increase in the cold rolling reduction rate, the accumulation of deformation energy storage and the grain boundary density of the cold rolled sheet will increase, and the energy storage driving the grain nucleation will increase, resulting in a faster increase in N and an increase in N/G. Due to the fact that the recrystallized grain size is $d \propto G/N$, the recrystallized grains are refined, meaning that the grain size is smaller under the same annealing conditions [9,22,23]. The annealed sheet is dominated by a γ fiber texture. With the increase in the cold rolling reduction, the γ texture is continuously enhanced, and the area fractions are 26.0, 31.3 and 34.5%, respectively.

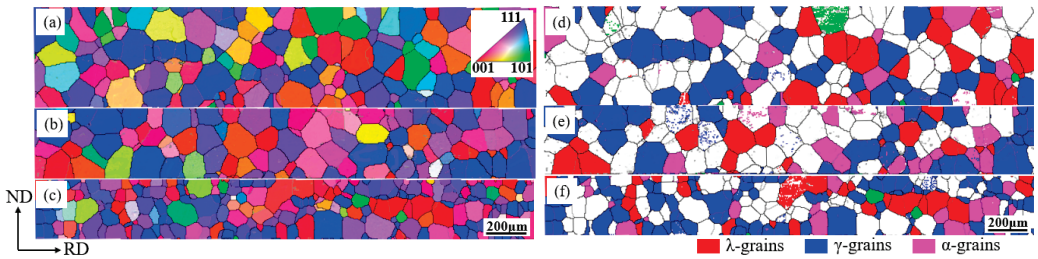

Figure 5. Grain orientation and special texture orientation of annealed sheet at 940 °C for 3 min. (**a**,**d**) 0.5 mm; (**b**,**e**) 0.35 mm; (**c**,**f**) 0.3 mm.

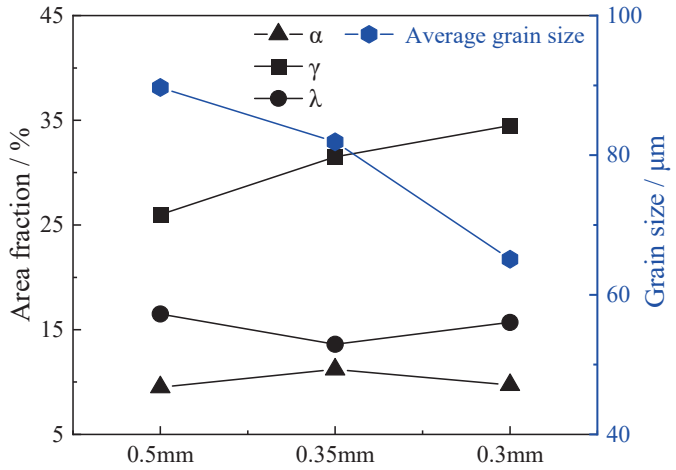

Figure 6. Changes of special texture area fraction and average grain size of annealed sheet at 940 °C for 3 min.

4. Analysis and Discussion

4.1. Recrystallization Kinetics

In order to further study the effect of the cold rolling reduction rate on the recrystallization of the deformed structure of the cold rolled sheet during annealing, the cold rolled sheet of 0.5, 0.35 and 0.3 mm were annealed in the annealing temperature range of 600~800 °C for 3 min, respectively. The recrystallization structure of the cold rolled sheet at different annealing temperatures is shown in Figure 7. After annealing at 640 °C, the cold rolled sheets of 0.5 and 0.35 mm only recovered to a certain extent, and no recrystallization occurred, while the cold rolled sheets of 0.3 mm nucleated first by a small number of small grains at the grain boundary and the intragranular shear band. When the annealing temperature is 660 °C, the 0.5 and 0.35 mm cold rolled sheets accumulate a small amount of recrystallized grains at a higher energy storage position, and the small grains previously nucleated in the 0.3 mm cold rolled sheet grow to a certain extent. Under the annealing condition of 700 °C, the recrystallization degree of the three is further expanded. At this time, with the increase in the cold rolling reduction rate, the recrystallization ratio of the cold rolled sheet increases, while the proportion and width of the deformed microstructure which is difficult to recrystallize in the band decrease. When the annealing temperature is increased to 760 °C, most of the samples are recrystallized, and there is a small amount of deformed structure surrounded by the recrystallized grains along the rolling direction in 0.5 and 0.35 mm cold rolled bands.

The purpose of annealing non-oriented silicon steel is to complete the recrystallization and grain growth in a short time at a high temperature, and the annealing time is limited. The recrystallization fraction of the microstructure at the same annealing time (3 min) and different annealing temperatures (600~800 °C) was estimated by Image-Pro software [24] as shown in Figure 8. With the increase in the cold rolling reduction, the dislocation density and energy storage increase, and the corresponding recrystallization starting temperature decreases. At the same annealing temperature, the recrystallization fraction increases with the increase in cold rolling reduction.

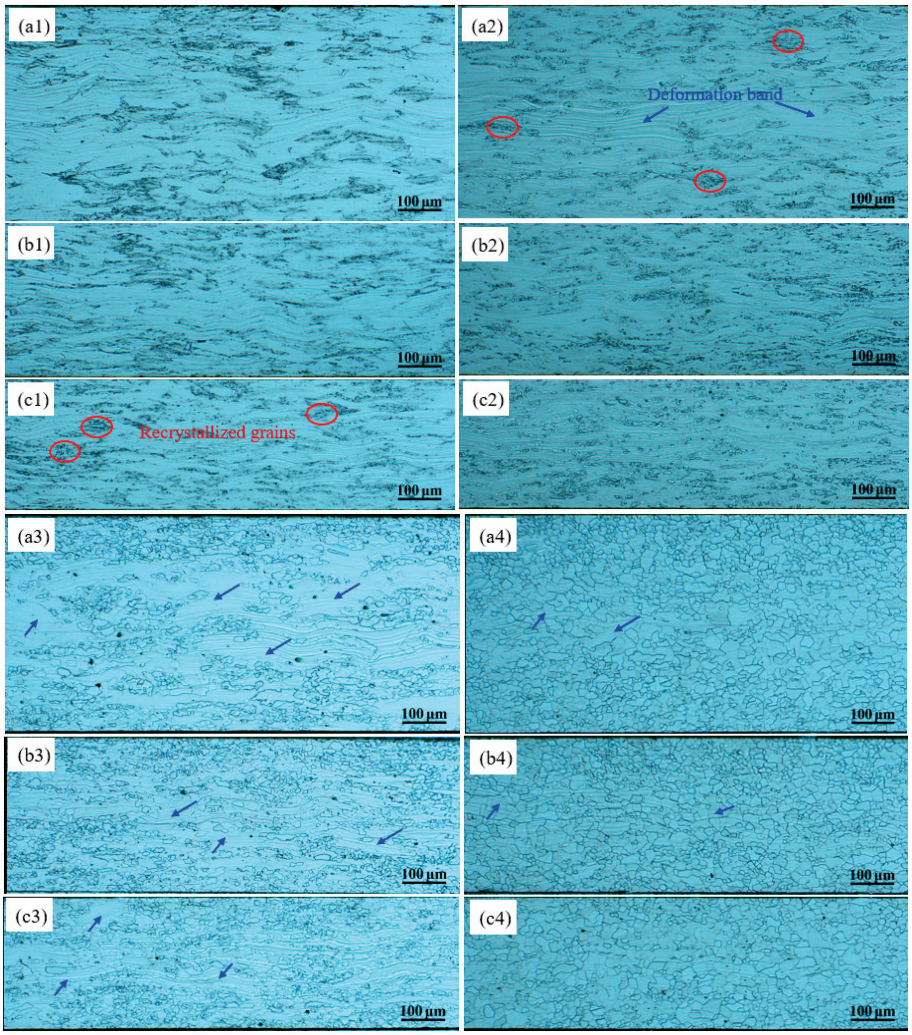

Figure 7. The recrystallization microstructure evolution of cold rolled sheets with thickness of 0.5 mm, 0.35 mm and 0.3 mm at different annealing temperatures. (**a1**,**b1**,**c1**) 640 °C × 3 min; (**a2**,**b2**,**c2**) 660 °C × 3 min; (**a3**,**b3**,**c3**) 700 °C × 3 min; (**a4**,**b4**,**c4**) 760 °C × 3 min.

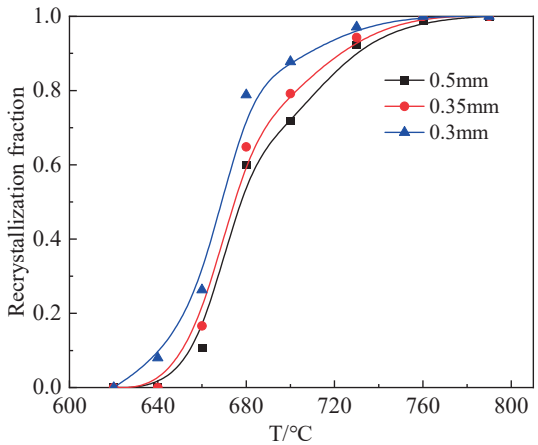

Figure 8. Recrystallization fraction of cold rolled sheets with thickness of 0.5 mm, 0.35 mm and 0.3 mm at different annealing temperatures.

4.2. Texture Evolution during Recrystallization Process

Due to the difference of microstructure and energy storage of deformed microstructure in cold rolled bands with different reduction rates, the order of deformation storage energy of grains with different orientations is: {001}<{112}<{111}<{110} [17,25], and the recrystallization rate is different during annealing. Goss and γ fiber texture storage can form recrystallized grains first, while the α fiber texture is a stable rolling texture, which is difficult to recrystallize. In order to clarify the texture transformation relationship during the recrystallization process of cold rolled bands with different reduction rates, the grain orientation images at different recrystallization stages were studied using the EBSD technique. By comparing the 680 °C for 3 min partial recrystallization annealing of the cold rolled sheets with thicknesses of 0.5 and 0.3 mm, the nucleation position and texture transformation of the recrystallized grains in the initial stage of recrystallization were analyzed. Figure 9 shows the texture characteristics at the initial stage of recrystallization and the macroscopic texture in some areas. At the early stage of the recrystallization of the cold rolled band (0.5 mm) with a reduction rate of 78%, the energy storage of the shear band of the coarse γ fiber texture is high. As a preferential nucleation site, the Goss grains will nucleate in the deformed {111}<112> shear band (I–III areas in Figure 9b). The grain boundary region of the deformed α-grains can form some new λ-grains by strain-induced grain boundary migration. For example, the {100}<012> and {100}<001> oriented new grains in the region of IV~VI nucleate near the {112}<110> and {100}<110> deformation bands [26].

With the increase in the rolling reduction, the nucleation position of the recrystallized grains changed greatly. When the rolling reduction rate is 87%, a large number of initial recrystallized grains mainly nucleate at the deformation band and grain boundary [27]. As shown in Figure 9d-I~III, the γ texture grains tend to nucleate along the deformed γ texture grain boundary and inside, and the recrystallized grains are mainly {111}<112> and a small amount of {111}<110> texture grains. The {100}<001> and {114}<481> grains nucleate at the γ-fiber texture grain boundaries (such as the d-IV region). A small amount of the Goss grains nucleated at the residual {111}<112> shear band.

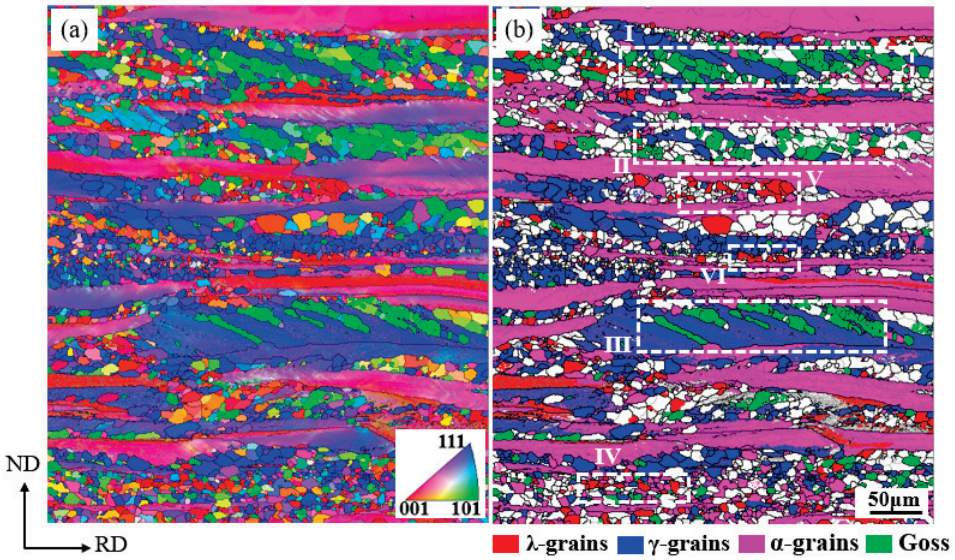

Figure 9. *Cont.*

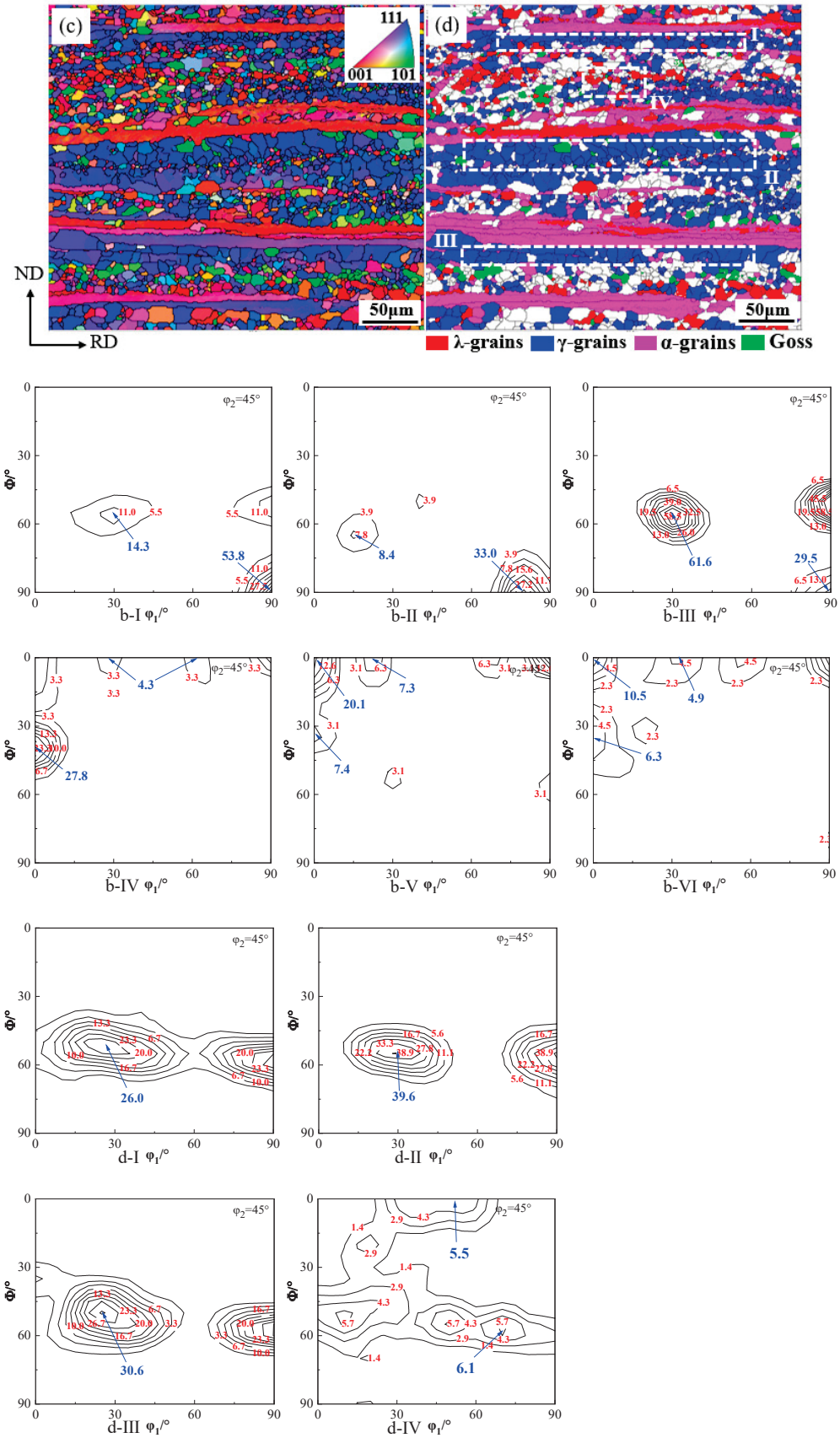

Figure 9. Recrystallization texture and ODF section (φ_2 = 45°) of cold rolled sheet after annealing at 680 °C for 3 min. (**a**,**b**) 0.5 mm; (**c**,**d**) 0.30 mm; (**b**) I–VI and (**d**) I–IV: The specific recrystallization textures of the micro regions.

Figure 10 shows the grain orientation and specific texture orientation of the partially recrystallized annealed band, with clustered recrystallized Goss grains found at the shear band position. The γ-grains have the advantage of a preferential recrystallization, with a relatively high proportion of recrystallization. The remaining deformation matrix is mainly composed of a α fiber texture. The area fractions of λ, α, γ fiber and Goss texture and recrystallized grains in annealed sheets of 0.5, 0.35 and 0.3 mm are quantitatively counted as shown in Figure 11. With the increase in the cold rolling reduction rate, the content of the Goss and α fiber texture in the corresponding annealed sheets decreases, while the content of the γ fiber texture increases significantly, from 22.5% to 37.2%.

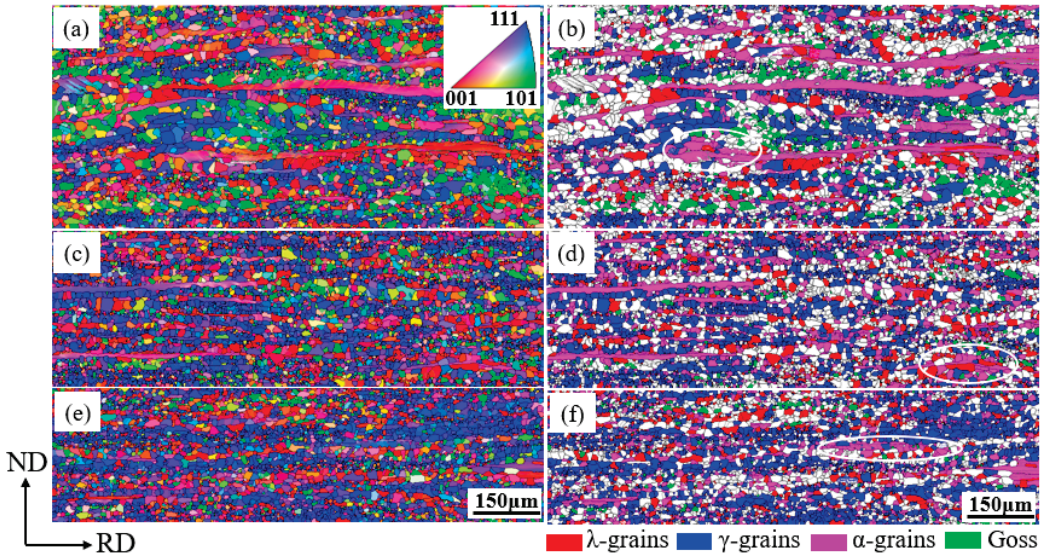

Figure 10. Grain orientation and special texture orientation diagram of partial recrystallization of annealed sheet. (**a**,**b**) 0.5 mm; (**c**,**d**) 0.35 mm; (**e**,**f**) 0.3 mm.

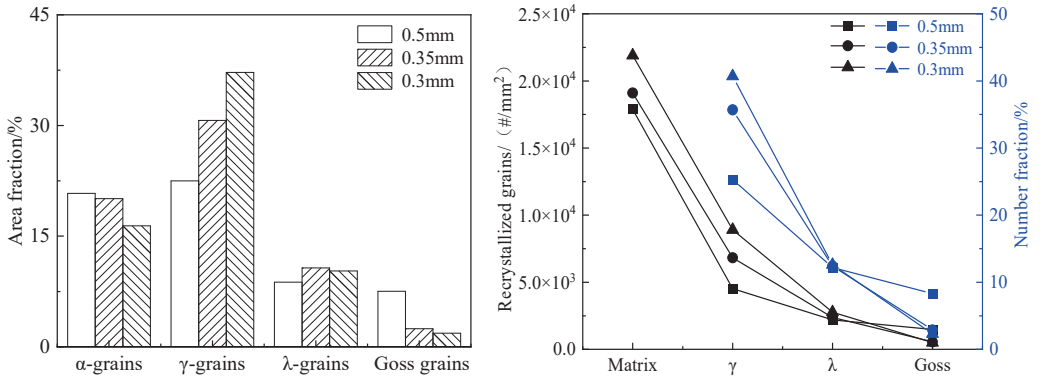

Figure 11. Partial recrystallization of annealed sheets mainly oriented grains and texture content.

With the increase in the cold rolling reduction rate, the energy storage of cold rolled sheet increases, and the temperature at the beginning of the recrystallization will decrease, which is beneficial to increase the nucleation rate of the recrystallization. The decrease in the number of shear bands in the plate leads to a reduction in the nucleation position of the Goss grains during the recrystallization process. In the early stage of recrystallization, the recrystallized γ-grains tend to nucleate at the deformed γ-grains and grain boundaries, and then aggregate and grow to occupy a numerical advantage. The high energy storage and quantity advantages provide favorable conditions for these recrystallized γ-grains to engulf adjacent deformed λ and α grains. The nucleation quantity of recrystallized λ grains at the grain boundaries of the deformed α and γ-grains is small and dispersed. However, the stored energy of the deformed α and λ grains is low, and recrystallization is

not easy to occur. In the later stage of recrystallization, partial recrystallization also occurs in the α-deformed grains, and the size of the recrystallized α-grains is generally larger than that of the matrix grains, as shown in Figure 11. Compared with the recrystallization of annealed sheets with thicknesses of 0.5, 0.35 and 0.3 mm, the number of recrystallized grains increased from 1.79×10^4 to $2.19 \times 10^4/mm^2$, the number of γ-oriented recrystallized grains increased from 4.52×10^3 to $8.91 \times 10^3/mm^2$, and the Goss recrystallized grains decreased from 1478.2 to $504.6/mm^2$ due to the increase in the proportion of the grain boundaries and the decrease in the number of shear bands in the cold rolled sheet.

When the annealing temperature is raised to 820 °C, the annealed sheet is completely recrystallized, and the grain orientation, and the grain orientation, distribution, and content of the special texture of the annealed plate are shown in Figures 12 and 13. The increase in annealing temperature leads to an increase in recrystallization activation energy (recrystallization driving force), resulting in the recrystallization of some α-deformed structure with lower energy storage. On the other hand, the migration speed of the grain boundaries increases, and the recrystallized grains grow. The recrystallized grains consume the adjacent deformed structure during the growth process, until the deformed structure in the plate is completely replaced by the recrystallized grains. With the increase in the cold rolling reduction rate, the recrystallized γ-grains have a numerical advantage and are more likely to come into contact with the deformed α-grains, providing more opportunities for the γ-grains to engulf adjacent deformed α-grains and grow. The area fraction of the recrystallized γ fibers texture increases significantly.

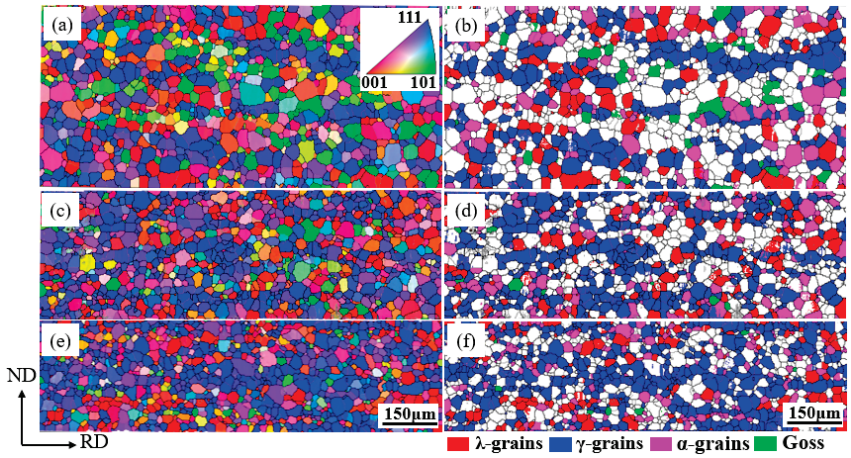

Figure 12. Grain orientation and special texture distribution diagram of annealed sheet when recrystallization is completed. (**a**,**b**) 0.5 mm; (**c**,**d**) 0.35 mm; (**e**,**f**) 0.3 mm.

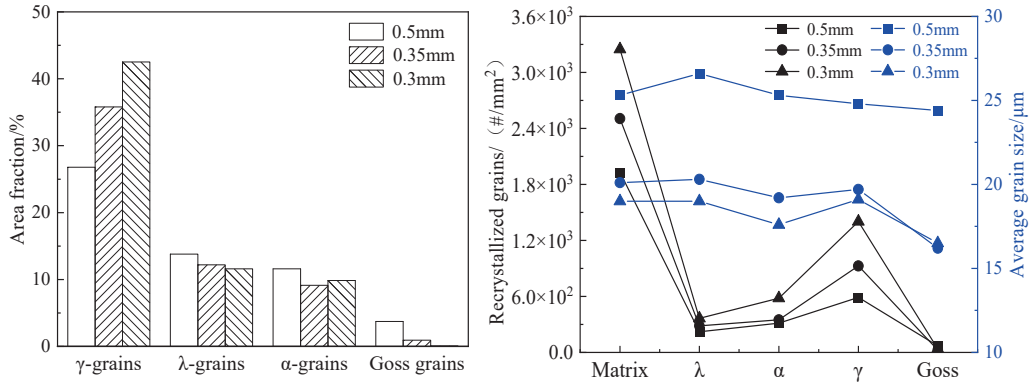

Figure 13. The main oriented grains and texture content of the annealed sheet as the recrystallization is completed.

The growth of the recrystallized grains in the annealed sheet depends on the misorientation distribution of adjacent grains. Generally, low-angle grain boundaries with misorientation less than 15° relative to the adjacent grains are considered to have a lower grain boundary mobility, while the high-angle grain boundaries with a misorientation between 15° and 40° have a higher grain boundary mobility [28]. Figure 14 shows the statistical results of the orientation deviation angles of the matrix and the main oriented grains of the fully recrystallized annealed bands with thicknesses of 0.5, 0.35 and 0.3 mm, respectively. Compared to the matrix grains, the frequency of low angle grain boundaries between adjacent grains of the γ grains is higher, while that of the λ-grains is lower.

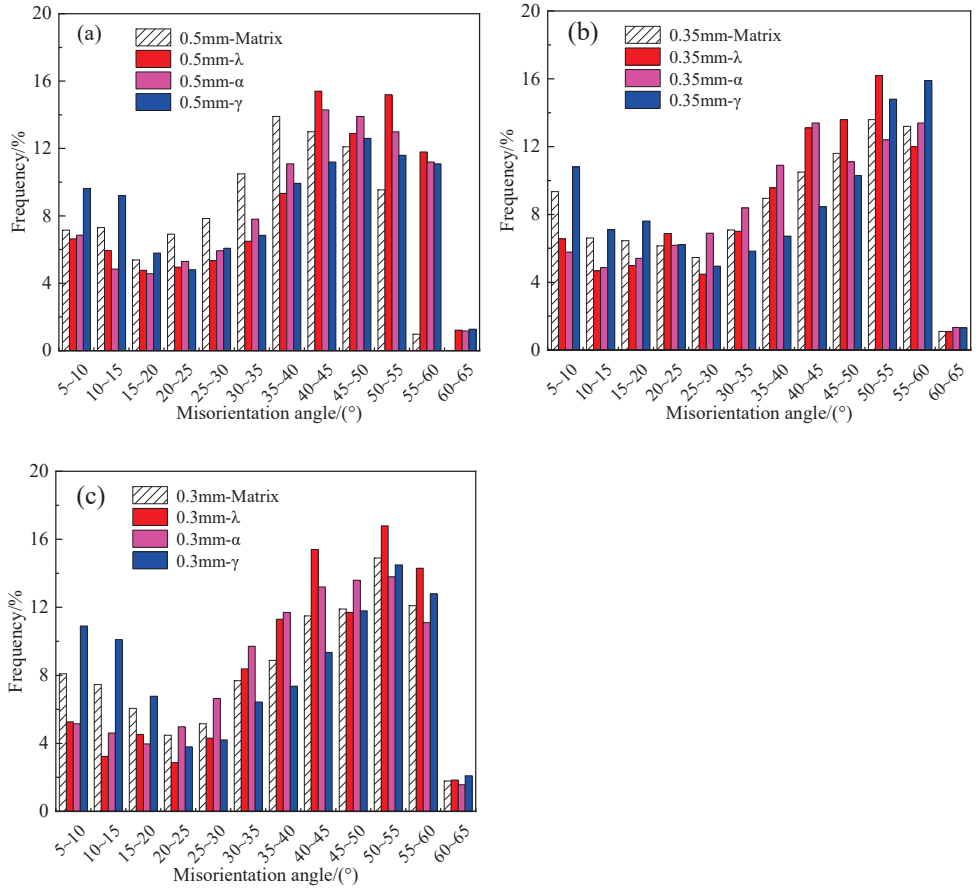

Figure 14. Distribution of orientation deviation between main oriented grains and adjacent grains in annealed sheet. (**a**) 0.5 mm; (**b**) 0.35 mm; (**c**) 0.3 mm.

With the increase in the cold rolling reduction rate, the high angle grain boundary with the orientation difference of 15~40° in the annealed band decreases from 36.1 to 32.3%, and the trend of grain growth decreases. Under the annealing process of annealing at 820 °C for 3 min, the grain size of the annealed band decreases, and the frequency of low-angle grain boundaries with an orientation difference less than 15° between the adjacent grains of γ-grains increases from 17.9 to 21.0%, and the high-angle grain boundaries with an orientation difference between 15° and 40° increase from 31.3 to 28.6%, while the frequency of low-angle grain boundaries with an orientation difference of less than 15° between adjacent grains of λ-grains increases from 12.6 to 8.5%. With the increase in the cold rolling reduction rate, the λ-grains in the fully recrystallized annealed sheet have the advantage of high mobility and grow upwards, while the γ-grains have the advantage of quantity but only have a low grain boundary mobility and are not easy to grow upwards. With the increase in the annealing temperature, the grains in the annealed sheet grow further, the content of the λ fibers texture increases and the content of the γ fibers texture decreases.

Figure 15 shows the changes in the content of λ, α and γ fibers textures in the annealed bands at annealing temperatures of 730, 820 and 940 °C, respectively. During the recrystallization process, the content of the α fibers texture in the annealed sheet decreases, and the content of the λ and γ fibers texture increases. Because of the high energy storage of deformed γ-grains and the grain boundary is the main position of γ recrystallization nucleation. With the increase in the cold rolling reduction, the γ fibers texture nucleated at the grain boundary has an obvious competitive advantage in the recrystallization process, and the γ texture is the dominant texture and the corresponding content increases. In the process of the grain growth of the annealed band, although λ-grains grow with the advantage of high mobility, there is no quantitative advantage, and the increase in the texture content is small.

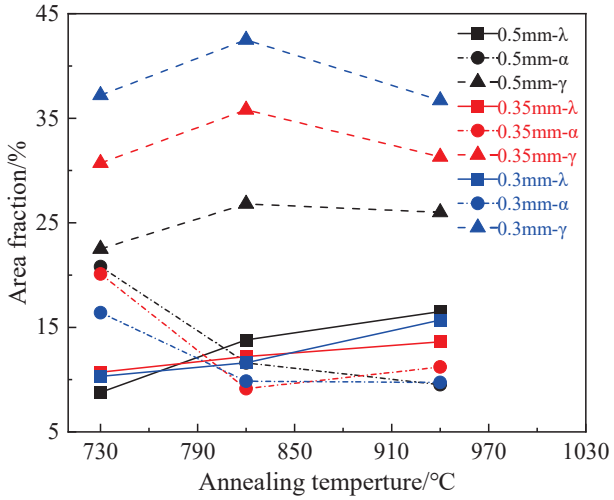

Figure 15. Variation of area fraction of specific oriented grains in annealed sheets at different annealing temperatures.

4.3. Effect of Microstructure and Texture on Magnetic Properties

The main influencing factors of magnetic induction intensity (B_{50}) of non-oriented silicon steel are chemical composition and crystal texture. In addition, the thickness of the finished sheet and grain size have a great influence on the core loss ($P_{1.5/50}$) of silicon steel. The λ fibers texture with two easy magnetization directions in the rolling plane is the ideal crystal texture of non-oriented silicon steel, while the γ fibers texture without easy magnetization direction in the rolling plane is the most unfavorable texture component for the magnetization of non-oriented silicon steel [29]. With the increase in the cold rolling reduction, the unfavorable γ texture content in the annealed sheet increases, and the corresponding magnetic induction intensity B_{50} decreases.

The iron loss (P_t) of non-oriented silicon steel is mainly determined by hysteresis loss (P_h) and eddy current loss (P_e). Among them, the empirical formula of P_h and the classical formula of P_e of thin band material derived from Maxwell's equation show that: under the same frequency test of the same material, the P_h is proportional to the maximum magnetic induction intensity, and the P_e is proportional to the square of the maximum magnetic induction intensity and the material thickness [9,30]. As the thickness of the annealed sheet decreases, the P_e decreases significantly. Thinning material thickness is an effective measure to reduce core loss. With the increase in the annealing temperature, the average grain size of the annealed band increases, the proportion of grain boundary decreases, and the P_h decreases. As the average size increases, the magnetic domain size increases, and the P_e increases. There is a suitable critical size to make P_t the lowest [19,31]. From the relationship between the grain size and magnetic properties ($P_{1.5/50}$ and B_{50}) of the annealed sheets at different annealing temperatures in Figure 16, when the annealing temperature is 1000 °C, the grain sizes of the annealed bands with thicknesses of 0.5, 0.35

and 0.3 mm are 136.2, 124.1 and 109.4 μm, respectively, the core loss is the lowest. In the smaller grain size range, the iron loss is dominated by hysteresis loss. As the grain size increases, the eddy current loss increases and becomes the main part of the iron loss.

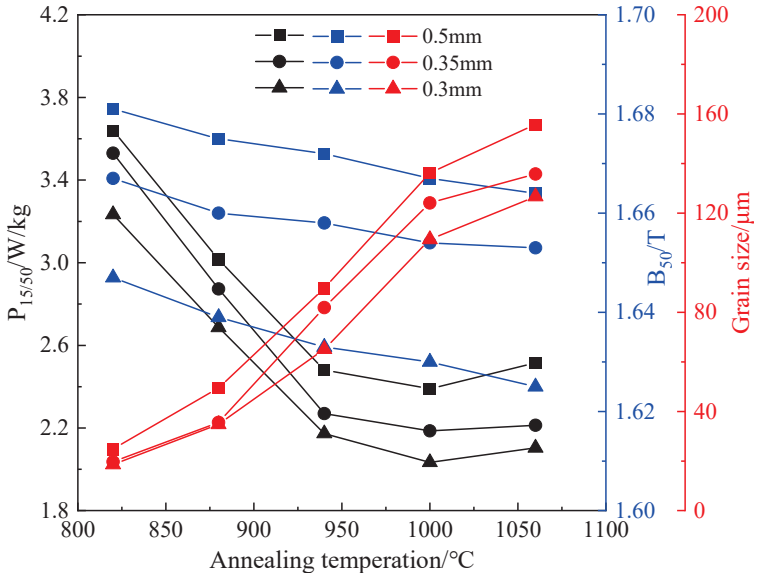

Figure 16. Grain size and magnetic properties of annealed sheets at different annealing temperatures.

5. Conclusions

(1) The microstructure of cold rolled band is mainly composed of deformed grains elongated along the rolling direction and shear bands with 20~35° to the rolling surface. With the increase in the cold rolling reduction rate, the width of the deformation band becomes narrower, the proportion of grain boundaries increases and the number of intragranular shear bands decreases. The cold rolled band is a strong α fiber texture and a weak γ fiber texture, and the annealed band is mainly a γ fiber texture. With the increase in the cold rolling reduction rate, the intensity of the α and γ fiber texture in the cold rolled sheet increases.

(2) In the early stage of recrystallization, the shear band of the coarse γ fiber texture has a high energy storage and preferential nucleation, and Goss grains will nucleate in the deformed {111}<112> shear band. The λ-grains can nucleate at the grain boundaries of the deformed α-grains. With the increase in the rolling reduction, a large number of initial recrystallized grains mainly nucleate at the deformation band and grain boundary, mainly recrystallized γ-grains.

(3) During the recrystallization process, the content of α fibers texture in the annealed sheet decreases, and the content of the λ and γ fibers texture increases. With the increase in the cold rolling reduction, the γ-grains nucleated at grain boundaries have obvious competitive advantages and become the dominant texture. In the process of grain growth, the λ-grains have a higher mobility and grow upwards. Due to the lack of a quantitative advantage, the increase in the texture content is small.

(4) With the increase in the cold rolling reduction rate, the unfavorable γ texture content in the annealed sheet increases, and the magnetic induction intensity B_{50} decreases. Thickness reduction can significantly reduce P_e and reduce core loss. In the smaller grain size range, the iron loss is dominated by the P_h. As the grain size increases, the P_e increases and becomes the main part of the iron loss. There is a critical size that makes the P_t the lowest.

Author Contributions: Conceptualization, F.G. and Y.N.; methodology, F.G.; software, J.Q.; validation, F.G., B.F. and J.Q.; formal analysis, F.G.; investigation, F.G.; resources, S.Q.; data curation, Y.N., J.Q. and S.Q.; writing—original draft preparation, F.G.; writing—review and editing, Y.N. and J.Q.; visualization, F.G. and B.F.; supervision, J.Q.; project administration, J.Q. and S.Q.; funding acquisition, S.Q. All authors have read and agreed to the published version of the manuscript.

Funding: The authors acknowledge the support from the Jiangxi Province Major Scientific and Technological Research and Development Special Funding Project (20213AAE01009) and the Jiangxi Provincial Key Laboratory of High-Performance Steel and Iron Alloy Materials (No. 2024SSY05042).

Data Availability Statement: Data available in a publicly accessible repository.

Acknowledgments: This work was supported by Xinyu Iron and Steel Group Co., Ltd., whose support is gratefully appreciated.

Conflicts of Interest: Authors J.Q. and S.Q. were employed by Iron and Steel Research Institute Co., Ltd., and Author B.F. were employed by Xinyu Iron and Steel Group Co., Ltd. The remaining authors declare that the research was conducted in the absence of any commercial or financial relationships that could be construed as potential conflicts of interest.

References

1. Oda, Y.; Kohno, M.; Honda, A. Recent development of non-oriented electrical steel sheet for automobile electrical devices. *J. Magn. Magn. Mater.* **2008**, *320*, 2430–2435. [CrossRef]
2. Lin, Y.; Wang, H.X.; Zhang, W.K.; Wang, S.J.; Sun, Y.; Wang, Y.D. Texture evolution and properties of cold rolled non-oriented silicon steel with high reduction rate. *China Metall.* **2022**, *32*, 64–70.
3. Cheng, C.Y.; Zhong, B.L.; Ni, Z.X.; Jing, W.Q.; Zhang, S.Q.; Liu, J. Research progress on the control of force and magnetic properties of high-strength non-oriented silicon steel for driving motors of new energy vehicles. *J. Eng. Sci.* **2023**, *45*, 1482–1492.
4. Zhu, C.Y.; Bao, Y.K.; Wang, Y.; Ma, J.H.; Li, G.Q. Research progress on application status and performance control of non-oriented silicon steel for drive motor of new energy vehicles. *Mater. Rep.* **2021**, *35*, 23089–23096.
5. Bian, X.H.; Zeng, Y.P.; Nan, D.; Wu, M. The effect of copper precipitates on the recrystallization textures and magnetic properties of non-oriented electrical steels. *J. Alloys Compd.* **2014**, *588*, 108–113. [CrossRef]
6. Fan, L.F.; Qin, M.M.; Yue, E.B.; Xiao, L.J.; He, J.Z. Technical challenges of new energy vehicles to non-oriented silicon steel. *Mater. Rep.* **2021**, *35*, 15183–15188.
7. De Campos, M.F.; Yonamine, T.; Fukuhara, M.; Landgraf, F.J.G.; Achete, C.A.; Missell, F.P. Effect of frequency on the iron losses of 0.5% and 1.5% Si non-oriented electrical steels. *IEEE Trans. Magn.* **2006**, *42*, 2812–2814. [CrossRef]
8. Gong, J.; Luo, H.W. Research and progress of high strength non-oriented silicon steel sheet for new energy vehicle drive motor. *J. Mater. Eng.* **2015**, *43*, 102–112.
9. He, Z.Z.; Zhao, Y.; Luo, H.W. *Electrical Steel*; Metallurgical Industry Press: Beijing, China, 2012.
10. Chu, S.J.; Shen, K.Y.; Sha, Y.H.; Chen, X. Orientation dependence of deformation energy storage and its effect on recrystallization texture of non-oriented silicon steel. *J. Mater. Eng.* **2019**, *47*, 147–153.
11. Shan, N.; Sha, Y.H.; Zhang, F.; Liu, J.L.; Zuo, L. Recrystallization texture transition in Fe-2.1 Wt Pct Si steel by different cold rolling reduction. *Metall. Mater. Trans. A* **2016**, *47*, 5777–5782. [CrossRef]
12. Yang, H.P.; Sha, Y.H.; Zhang, F.; Zuo, L. Recrystallization texture evolution of cold rolled non-oriented silicon steel with large reduction. *J. Northeast. Univ. Nat. Sci. Edit.* **2013**, *34*, 658–662.
13. Wu, S.; Jia, J.; Song, X.L.; Cheng, C.Y.; Wu, J.; Liu, J. Effect of cold rolling reduction rate on deformation microstructure and magnetic properties of high strength non-oriented electrical steel. *J. Mater. Eng.* **2024**, *52*, 158–165.
14. Jiao, H.T.; Xu, Y.B.; Xiong, W.; Zhang, Y.X.; Cao, G.M.; Li, C.G.; Niu, J.; Misra, R.D.K. High-permeability and thin-gauge non-oriented electrical steel through twin-roll strip casting. *Mater. Design.* **2017**, *136*, 23–33. [CrossRef]
15. Hawezy, D.; Birosca, S. Disparity in recrystallization of α-& γ-fibers and its impact on Cube texture formation in non-oriented electrical steel. *Acta Mater.* **2021**, *216*, 117141.
16. Sha, Y.H.; Sun, C.; Zhang, F.; Patel, D.; Chen, X.; Kalidindi, S.R.; Zuo, L. Strong cube recrystallization texture in silicon steel by twin-roll casting process. *Acta Mater.* **2014**, *76*, 106–117. [CrossRef]
17. Park, J.T.; Szpunar, J.A. Evolution of recrystallization texture in non-oriented electrical steels. *Acta Mater.* **2003**, *51*, 3037–3051. [CrossRef]
18. Sun, C.; Sha, Y.H.; Zhang, F.; Zuo, L. Effect of cold rolling reduction rate on deformation and recrystallization texture of twin-roll casting silicon steel. *J. Northeast. Univ. Nat. Sci. Edit.* **2016**, *37*, 1311–1316.
19. Li, Z.H.; Xie, S.K.; Wang, G.D.; Liu, H.T. Dependence of recrystallization behavior and magnetic properties on grain size prior to cold rolling in high silicon non-oriented electrical steel. *J. Alloys Compd.* **2021**, *888*, 161576. [CrossRef]
20. Qin, J.; Yang, J.F.; Zhang, Y.H.; Zhou, Q.Y.; Cao, Y.Y. Strong {100}<012>-{411}<148> recrystallization textures in heavily hot-rolled non-oriented electrical steels. *Mater. Lett.* **2020**, *259*, 126844.

21. Xu, H.J.; Xu, Y.B.; He, Y.L.; Jiao, H.T.; Yue, S.; Li, J.P. A quasi in-situ EBSD study of the nucleation and growth of Goss grains during primary and secondary recrystallization of a strip-cast Fe-6.5 wt% Si alloy. *J. Alloys Compd.* **2021**, *861*, 158550. [CrossRef]
22. Wang, S.J.; Li, M.; Wang, H.X.; Xu, C.X.; Lin, Y.; Wei, H.; Zhang, W.K.; Qiu, S.Y.; Wang, Y.D. Effect of grain size before cold rolling on microstructure, texture and magnetic properties of ultra-thin low-Si non-oriented silicon steel. *JOM* **2023**, *75*, 1824–1838. [CrossRef]
23. Lee, H.H.; Jung, J.; Yoon, J.I.; Kim, J.K.; Kim, H.S. Modelling the evolution of recrystallization texture for a non-grain oriented electrical steel. *Comp. Mater. Sci.* **2018**, *149*, 57–64. [CrossRef]
24. Yu, L.; Luo, H.W. Effect of partial recrystallization annealing on magnetic and mechanical properties of non-oriented silicon steel. *Acta Metall. Sin.* **2020**, *56*, 291–300.
25. Shan, N.; Liu, J.L.; Sha, Y.H.; Zhang, F.; Zuo, L. Development of through-thickness Cube recrystallization texture in non-oriented electrical steels by optimizing nucleation environment. *Metall. Mate. Trans. A* **2019**, *50*, 2486–2494. [CrossRef]
26. Dillamore, I.L.; Morris, P.L.; Smith, C.J.E.; Hutchinson, W.B. Transition bands and recrystallization in metals. *Proc. R. Soc. Lond. A Math. Phy. Eng. Sci.* **1972**, *329*, 405–420.
27. Kestens, L.; Jacobs, S. Texture control during the manufacturing of non-oriented electrical steels. *Texture Stress Microstruct.* **2008**, *2008*, 173083. [CrossRef]
28. Suehiro, R.; Hayakawa, Y.; Takamiya, T. Effect of Sn addition on evolution of primary recrystallization texture in 3% Si steel. *ISIJ Int.* **2019**, *59*, 351–358. [CrossRef]
29. Sidor, J.J.; Verbeken, K.; Gomes, E.; Schneider, J.; Calvillo, P.R.; Kestens, L.A.I. Through process texture evolution and magnetic properties of high Si non-oriented electrical steels. *Mater. Charact.* **2012**, *71*, 49–57. [CrossRef]
30. Qin, J.; Yang, P.; Mao, W.M.; Ye, F. Effect of texture and grain size on the magnetic flux density and core loss of cold-rolled high silicon steel sheets. *J. Magn. Magn. Mater.* **2015**, *393*, 537–543. [CrossRef]
31. Lee, K.M.; Park, S.Y.; Huh, M.Y.; Kim, J.S.; Engler, O. Effect of texture and grain size on magnetic flux density and core loss in non-oriented electrical steel containing 3.15% Si. *J. Magn. Magn. Mater.* **2014**, *354*, 324–332. [CrossRef]

crystals

MDPI

Article

The Influence of Process and Slag Parameters on the Liquid Slag Layer in Continuous Casting Mold for Large Billets

Zhijun Ding [1,2], Chao Wang [1], Xin Wang [3,*], Pengcheng Xiao [1,4], Liguang Zhu [5] and Shuhuan Wang [1]

[1] College of Metallurgical and Energy, North China University of Science and Technology, Tangshan 063210, China; sgdingzhijun@hbisco.com (Z.D.); chaowang202@126.com (C.W.); xiaopc@ncst.edu.cn (P.X.); wshh88@ncst.edu.cn (S.W.)
[2] HBIS Group ShiSteel Company, Shijiazhuang 050018, China
[3] Jiangyou Changcheng Special Steel Co., Ltd. of Panggang Group, Jiangyou 621701, China
[4] Yanzhao Iron and Steel Laboratory, Tangshan 063210, China
[5] College of Materials Science and Engineering, Hebei University of Science and Technology, Shijiazhuang 050018, China; zhulgts@126.com
* Correspondence: 17726531349@163.com

Abstract: In the continuous casting of special steel blooms, low casting speeds result in slow renewal of the molten steel surface in the mold, adversely affecting mold flux melting and liquid slag layer supply, which may lead to surface cracks, slag entrapment, and breakout incidents. To optimize the flow and heat transfer behavior in the mold, a three-dimensional numerical model was developed based on the VOF multiphase flow model, $k-\epsilon$ RNG turbulence model, and DPM discrete phase model, employing the finite volume method with SIMPLEC algorithm for solution. The effects of casting speed, argon injection rate, and mold flux properties were systematically investigated. Simulation results demonstrate that when casting speed increases from 0.35 m·min^{-1} to 0.75 m·min^{-1}, the jet penetration depth increases by 200 mm and meniscus velocity rises by 0.014 m·s^{-1}. Increasing argon flow rate from 0.50 L·min^{-1} to 1.00 L·min^{-1} leads to 350 mm deeper bubble penetration, 10 mm reduction in jet penetration depth, 0.002 m·s^{-1} increase in meniscus velocity, and decreased meniscus temperature due to bubble cooling. When mold flux viscosity increases from 0.2 Pa·s to 0.6 Pa·s, the average liquid slag velocity decreases by 0.006 m·s^{-1} with a maximum temperature drop of 10 K. Increasing density from 2484 kg·m^{-3} to 2884 kg·m^{-3} results in 0.005 m·s^{-1} higher slag velocity and average 8 K temperature reduction. Comprehensive analysis indicates that optimal operational parameters are casting speed 0.35–0.45 m·min^{-1}, argon flow $\leq$ 0.50 L·min^{-1}, mold flux viscosity 0.2–0.4 Pa·s, and density 2484–2684 kg·m^{-3}. These conditions ensure more stable flow and heat transfer characteristics, effectively reducing slab defects and improving casting process stability.

Keywords: low drawing speed; special steel bloom; liquid slag layer; numerical simulation

1. Introduction

Special steel refers to steel grades characterized by specific chemical compositions, unique microstructures, and properties, enabling them to meet the demands of specific applications [1–5]. Large billet continuous casting of special steel products is primarily employed in the rolling of low-alloy structural steels, heavy rail steels, hard wire steels, seamless steel pipes, medium and large H-beams, along with various bars and forgings [6–8]. The continuous casting process of special steel billets is more challenging due to their large cross-sectional dimensions and the substantial differences in composition compared to

carbon steel, necessitating a slower drawing speed for production [9]. Once the protective slag is added above the mold in continuous casting, it melts and flows onto the billet shell surface under the influence of high-temperature molten steel, providing functions such as heat transfer regulation and lubrication of the billet shell. At lower drawing speeds, the renewal of the mold liquid surface slows down, exacerbating the melting conditions of the protective slag and resulting in issues such as a thinning slag layer and inadequate slag supply. This can lead to quality defects or production accidents, such as surface cracks, slag inclusion, and steel leakage in the continuous casting billet [10,11].

Fluid dynamics has made significant advances in the field of continuous casting. Scholars have conducted extensive research by integrating numerical simulations with continuous casting processes [12–14]. For instance, Hu et al. [15] tackled the application challenges of the light pressing process at the solidification end of round billets in continuous casting. They proposed a dual-roll, triple-roll, and four-roll staggered extrusion scheme, and developed a 3D heat-force coupled model to compare and analyze the advantages and disadvantages of each scheme. Liu et al. [16] conducted numerical simulations of the magnetic-driven flow field and solidification process of high-strength low-alloy steel round billets in continuous casting, analyzing the casting surface temperature and shell thickness. Qiu et al. [17] established a 3D mathematical model to simulate molten steel flow in the continuous casting mold for small square billets. They analyzed the effects of drawing speed and submerged nozzle parameters on the flow field. An et al. [18] developed a 3D mathematical model for small square billets in continuous casting, including the effects of electromagnetic forces and heat transfer, and analyzed the impact of current strength and frequency on the flow and temperature fields. Yang J [19,20] analyzed the relationship between molten steel, protective slag, and billet shell heat transfer under ultra-high-speed continuous casting conditions, as well as the flow and heat transfer behavior within the mold. Vakhrushev et al. [21] conducted 2D simulations using an advanced multi-material model based on the new single grid method. They investigated the effects of different insulation conditions and clogging layers at submerged nozzles, finding that missing nozzle insulation could lead to parasitic solidification, while clogging promoted molten steel solidification. Both parasitic solidification and clogging together enhanced jet flow and weakened overheating transmission within the mold. Ma et al. [22] modified the heat transfer model using measured billet shell thickness and surface temperature data, achieving high accuracy in simulating the continuous casting solidification process. This model offers the potential for improved simulation of dynamic solidification processes and optimization of secondary cooling water.

In recent years, there has been significant progress in the optimization research of continuous casting large square billets. Yang et al. [23] developed a 3D real-time heat transfer model for the initial and final stages of large billet continuous casting. The model was accelerated using specific algorithms and optimization of discretization parameters, and uncertainty was minimized by calibrating thermal/physical and boundary condition parameters with experimental data. The accuracy of the model was validated through online surface temperature measurements, with calculation errors kept below ± 10 °C. Fang et al. [24] developed a 3D mathematical model for large billet continuous casting, analyzing the effects of submerged nozzle structure and installation on the flow field, temperature field, and solidification process. Ren et al. [25] developed a 3D mathematical model for large billet continuous casting to analyze the effects of current strength on the flow field, temperature field, and solidification process.

However, existing research primarily focuses on fluid field optimization, inclusion control, and other areas, with limited attention paid to the effects of process parameters on the protective slag and liquid slag layer in the mold. To gain a comprehensive under-

standing of the behavior of liquid protective slag under various operating conditions in the continuous casting mold of large billets of special steel, this study focuses on billets with cross-sections of 300 mm × 340 mm. This study considers various factors, including molten steel temperature, mold geometry, casting speed, submerged nozzle parameters, and others, to analyze their impact on the flow of protective slag in the mold.

The structure of the rest of this paper is as follows: In Section 2, a three-dimensional mathematical model for the mold is presented. Section 3 displays and discusses the simulation results, revealing the varying patterns of the flow field and temperature field of the molten steel and slag layer under different operating conditions. Finally, in Section 4, the study's findings are summarized.

2. Mathematical Models

2.1. Geometric and Algorithmic Models

2.1.1. Geometric Models

Owing to the bilateral symmetry of the geometric model, a practical 1:1 scaled three-dimensional quarter model was developed, incorporating key features such as the submerged nozzle, molten steel, and slag layers within the crystallizer. The computational domain and mesh division of the geometric model are illustrated in Figure 1. The submerged nozzle employed is a single-hole design, and the effective height of the crystallizer, initially 720 mm, was extended to 1500 mm to facilitate adequate fluid development. The mesh division adopts a hexahedral structure, with the slag layer refined to a 1 mm grid size, resulting in an overall mesh count of approximately 440,000 elements.

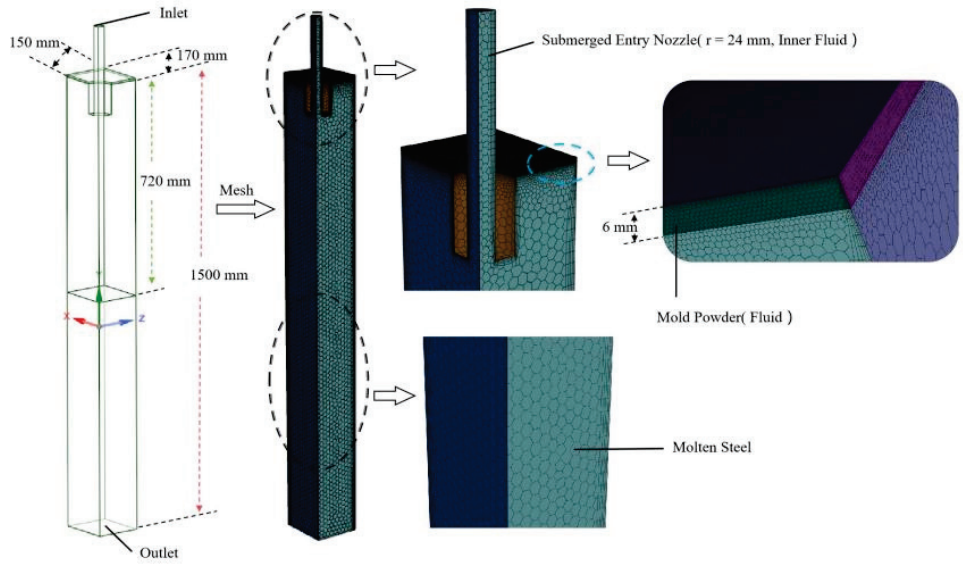

Figure 1. Computing domain and meshing.

2.1.2. Algorithm Model

This study utilizes the multiphase flow VOF (volume of fluid) model, the $k-\epsilon$ RNG (renormalization group) turbulence model, and the DPM (discrete phase model) to simulate and track fluid dynamics under varying operational conditions.

Common multiphase flow models include three primary types: the volume of fluid (VOF) model, the mixture model, and the Eulerian model. Among these, the VOF model is particularly suitable for tracking interfaces between immiscible fluids. It employs a shared momentum equation for all phases while distinguishing individual phases through volume fraction tracking. This model effectively simulates stratified flows, free-surface flows, filling processes, sloshing dynamics, and gas bubble behavior in liquids. To investigate the

three-phase interaction (molten steel, mold flux, and argon gas) in the continuous casting mold, the VOF model was adopted for phase distribution calculations. The governing equations are as follows [26]:

$$\sum_{q=1}^{n} a_q = 1 \tag{1}$$

In the equation above, q represents the phase; n denotes the total number of phases; and a_q refers to the volume fraction of the specified phase. When $a_q = 0$, it indicates that phase q is absent in the computational cell; when $0 < a_q < 1$, it signifies the coexistence of phase q and other phases in the computational cell; when $a_q = 1$, it indicates that only phase q is present in the computational cell.

When the critical Reynolds number of a flowing fluid exceeds a certain threshold, the flow transitions from laminar to turbulent, characterized by random fluctuations, enhanced diffusivity, and energy dissipation. To accurately capture turbulent phenomena—such as steel jet impingement and argon bubble-induced flow—while balancing computational efficiency and model accuracy, the $k-\epsilon$ RNG (renormalization group) turbulence model was selected. The corresponding equations are [27]:

$$\rho\frac{\partial k}{\partial t} + \rho u_i\frac{\partial k}{\partial x_i} = \frac{\partial}{\partial x_i}\left(\alpha_k \mu_{\text{eff}}\frac{\partial k}{\partial x_i}\right) + G_k + G_b - \rho\epsilon + S_k - Y_M \tag{2}$$

$$\rho\frac{\partial \epsilon}{\partial t} + \rho u_i\frac{\partial \epsilon}{\partial x_i} = \frac{\partial}{\partial x_i}\left(\alpha_\epsilon \mu_{\text{eff}}\frac{\partial \epsilon}{\partial x_i}\right) + C_{1\epsilon}\frac{\epsilon}{k}(G_k + C_{3\epsilon}G_b) - C_{2\epsilon}\rho\frac{\epsilon^2}{k} + S_\epsilon \tag{3}$$

$$\mu_{\text{eff}} = \mu_0 + \mu_t = \mu_0 + \frac{\rho C_\mu k^2}{\epsilon} \tag{4}$$

$$C_{2\varepsilon} = C'_{2\varepsilon} + \frac{C_\mu \rho \eta^3\left(1 - \frac{\eta}{\eta_0}\right)}{1 + \beta\eta^3} \tag{5}$$

$$\eta = \frac{k}{\varepsilon}\cdot\overline{S} \tag{6}$$

$$\overline{S} = \sqrt{2\cdot\overline{S_{ij}}\cdot\overline{S_{ij}}} \tag{7}$$

$$\overline{S_{ij}} = \frac{1}{2}\left(\frac{\partial\overline{u_i}}{\partial x_j} + \frac{\partial\overline{u_j}}{\partial x_i}\right) \tag{8}$$

The variables in the equations above are defined as follows: k is the turbulence kinetic energy ($m^2{\cdot}s^{-2}$); ϵ is the turbulence dissipation rate ($m^2{\cdot}s^{-3}$); ρ is the fluid density ($kg{\cdot}m^{-3}$); t represents time (s); u_i and u_j are the velocity components in the i and j directions ($m{\cdot}s^{-1}$); x_i and x_j are the coordinates in the i and j directions (m); G_k is the turbulence kinetic energy generated by the mean velocity gradient ($m^2{\cdot}s^{-2}$); G_b is the turbulence kinetic energy produced by buoyancy ($m^2{\cdot}s^{-2}$); Y_M represents the influence of fluctuating expansion on the turbulence dissipation rate; S_k, S_ϵ, $\overline{S}$, and $\overline{S_{ij}}$ are user-defined source terms. Additionally, α_k and α_ϵ are the effective Prandtl numbers for turbulence kinetic energy and turbulence dissipation rate, respectively. u_{eff} denotes the effective turbulence viscosity coefficient (Pa·s); u_0 and u_t represent the laminar and turbulent viscosities (Pa·s), respectively; β, η_0, C_μ, α_k, α_ϵ, $C_{1\epsilon}$, and $C_{2\epsilon}$ are empirical constants, where $\beta = 0.012$, $\eta_0 = 4.377$, $C_\mu = 0.0845$, $\alpha_k = \alpha_\epsilon = 1.39$, $C_{1\epsilon} = 1.42$, and $C_{2\epsilon} = 1.68$.

To account for argon bubble dispersion effects caused by turbulent velocity fluctuations, the discrete phase model (DPM) was applied to track bubble trajectories within the mold. The governing equations for bubble motion are [28]:

$$\frac{du_g}{dt} = \frac{18u}{\rho_g d_g^2} \cdot \frac{C_D R_e}{24} \cdot (u - u_g) + g_1 \frac{\rho_g - \rho}{\rho_g} + F_i \tag{9}$$

In the equation above, the variables are defined as follows: u and u_g represent the velocities of the fluid and argon bubbles (m·s^{-1}), respectively; t is time (s); ρ and ρ_g represent the densities of molten steel and argon bubbles (kg·m^{-3}), respectively; u_g is the diameter of the argon bubbles (m); C_D is the drag coefficient of the bubbles in the fluid, which is a function of the Reynolds number (Re); and F_i represents other forces acting on a unit mass of argon bubbles (kg·m^{-3}).

2.2. Model Assumptions and Boundary Conditions

2.2.1. Assumption Conditions

To ensure that the simulation results are not significantly affected, the following assumptions are made, based on the necessity for coupled calculations of complex phenomena such as fluid flow and heat transfer within the crystallizer [29]: (1) The fluid within the crystallizer is assumed to be incompressible, viscous, and homogeneous; (2) the influence of the solidifying shell inside the crystallizer is neglected; (3) the effects of vibrations and the tapering of the crystallizer are disregarded; (4) the impact of chemical reactions occurring within the crystallizer is omitted; (5) interactions between argon bubbles are neglected, and their sizes are considered constant; and (6) argon bubbles are assumed to enter the crystallizer uniformly from the nozzle outlet.

2.2.2. Boundary Conditions

1. Inlet conditions

   The inlet velocity is determined using Equation (10), which is calculated based on the casting speed of the billet, the cross-sectional dimensions, and the inner diameter of the submerged nozzle. The direction of flow is aligned along the negative Y-axis. The turbulent kinetic energy and turbulent dissipation rate at the inlet are derived from empirical formulas, specifically Equations (11) and (12). The inlet temperature corresponds to the pouring temperature of the molten steel, which is calculated using the liquidus temperature of the steel grade being cast and the overheating temperature during actual casting, as shown in Equation (13).

$$v_{\text{in}} = \frac{\left(\frac{v_0}{60}\right) \cdot (a \times b)}{\pi\left(\frac{d}{2}\right)^2} \tag{10}$$

$$k_{\text{in}} = 0.01 \cdot v_{\text{in}}^2 \tag{11}$$

$$\epsilon_{\text{in}} = \frac{k_{\text{in}}^{\frac{3}{2}}}{\frac{1}{2} \cdot D_{\text{in}}} \tag{12}$$

$$T = T_{\text{Liquid}} + \Delta T \tag{13}$$

In the equations, v_{in} represents the inlet velocity (m·s^{-1}); v_0 denotes the casting speed of the billet (m·min^{-1}); a and b refer to the width and thickness of the billet (m), respectively; d is the inner diameter of the submerged nozzle (m); k_{in} represents the inlet turbulent kinetic energy (m^2·s^{-2}); ϵ_{in} denotes the inlet turbulent dissipation rate (m^2·s^{-3}); D_{in} is the hydraulic diameter (m); T, T_{Liquid} and ΔT refer to the inlet

temperature, liquidus temperature, and overheating temperature of the molten steel (K), respectively.

2. Outlet conditions
   Due to the challenges in obtaining detailed parameters such as flow velocity and pressure at the outlet, the steel liquid outlet is defined as a free outflow type, meaning the fluid is assumed to be fully developed at the outlet.
3. Wall conditions
   The wall is modeled as a no-slip wall, and the near-wall flow field is handled using the standard wall function method. The steel liquid wall temperature near the crystallizer is set to the liquidus temperature of the molten steel. The wall temperature of the protective slag and the liquid slag near the crystallizer is set to the liquidus temperature of the protective slag. Other walls are treated as adiabatic walls.
4. Initial conditions
   The fluid is initially at rest, with the initial steel liquid temperature set to the casting temperature. The initial temperature of the slag layer is set to the liquidus temperature of the protective slag. All regions, except for the initial slag layer region, are initially set to steel liquid.
5. Free Liquid Surface
   The surface of the steel liquid is covered by liquid protective slag. The surface of the slag layer is modeled as a free liquid surface (wall), with the free liquid surface temperature set to the liquidus temperature of the protective slag.

Condition Setting Explanation:

Since the focus of this model is primarily on the slag layer, which is derived from the sintered layer and melts at the liquidus temperature of the protective slag, the initial temperature of the slag layer is set to the liquidus temperature of the protective slag. The liquidus temperature is determined by the melting point and melting rate.

2.3. Model Calculation Method and Process

2.3.1. Calculation Method

The mathematical model employs the finite volume method (FVM) and is coupled and solved using the SIMPLEC algorithm. To enhance the accuracy of the calculation results, all variables in the equations are discretized using a second-order upwind scheme. The convergence criterion for residuals is set to 10^{-5}. A typical simulation case requires approximately 8.8 h of computational time.

2.3.2. Calculation Process

The entire calculation process consists of the following steps: (1) Identify the target fluid region; (2) define the fluid state; (3) determine the grid resolution; (4) apply boundary conditions; (5) set initial parameters and initialize the solver; (6) solve the model; (7) extract the calculation results.

2.4. Model Process Parameters

Based on the actual production process of a specific plant, parameters, including the steel grade, casting speed, and the billet cross-sectional dimensions, are presented in Table 1. The composition of the molten steel is provided in Table 2.

Table 1. Process parameters.

Parameter Name	Parameter Value
Steel Grade	SFQ590
Casting Speed (m·min^{-1})	0.35, 0.45, 0.55, 0.65, 0.75
Billet Cross-sectional Dimensions (mm)	300 × 340
Nozzle Inner Diameter (mm)	48
Nozzle Outer Diameter (mm)	105
Casting Temperature (K)	1793
Slag Layer Thickness (mm)	6
Argon Flow Rate (L·min^{-1})	0.50, 0.75, 1.00
Protective Slag Viscosity (Pa·s)	0.2, 0.4, 0.6
Protective Slag Density (kg·m^{-3})	2484, 2684, 2784, 2884
Crystallizer Electromagnetic Stirring	None

Table 2. Steel liquid composition parameters (mass fraction).

C	Si	Mn	P	S	Cr	Ni	Mo	Al	V	Ti
0.38	0.6	1.45	0	0.048	0.18	0.12	0	0.015	0.13	0.02

Based on the steel composition provided in Table 2, the physical properties of the molten steel, including density, viscosity, thermal conductivity, and specific heat capacity, were calculated at 1793 K using the JMatPro-v132 software. The specific values of these properties are summarized in Table 3.

Table 3. Steel liquid physical property parameters.

Parameter Name	Parameter Value
Density (kg·m^{-3})	6.913
Viscosity (Pa·s)	0.006
Thermal Conductivity (W·m^{-1}·K^{-1})	34
Specific Heat Capacity (J·kg^{-1}·K^{-1})	821
Liquidus Temperature (K)	1762

3. Results and Discussion

The temperature field within the crystallizer significantly affects the melting behavior and flow characteristics of the protective slag. Therefore, it is crucial to investigate the variations in the temperature and flow fields within the crystallizer under different processing conditions and to analyze the metallurgical behavior of the protective slag within this environment.

3.1. Flow and Heat Transfer of Molten Steel

3.1.1. Effect of Casting Speed on Flow and Temperature Fields

The velocity distribution on the symmetry planes (narrow face and wide face) at varying casting speeds is illustrated in Figure 2. Figure 2(a1,b1,c1,d1,e1) clearly demonstrate that the casting speed significantly influences the flow field. As the casting speed increases, the impact depth of the molten steel flow gradually increases, showing a direct correlation. The impact depths of the molten steel flow at casting speeds of 0.35, 0.45, 0.55, 0.65, and 0.75 m·min^{-1} are measured at 280 mm, 330 mm, 380 mm, 430 mm, and 480 mm, respectively. For each 0.1 m·min^{-1} increase in the casting speed, the impact depth increases by 50 mm, indicating a linear relationship. Figure 2(a2,b2,c2,d2,e2) clearly illustrate that the casting speed significantly affects the distribution of molten steel backflow. As the casting

speed increases, the backflow region of the molten steel expands, the lower vortex center shrinks, and the vortex speed progressively increases.

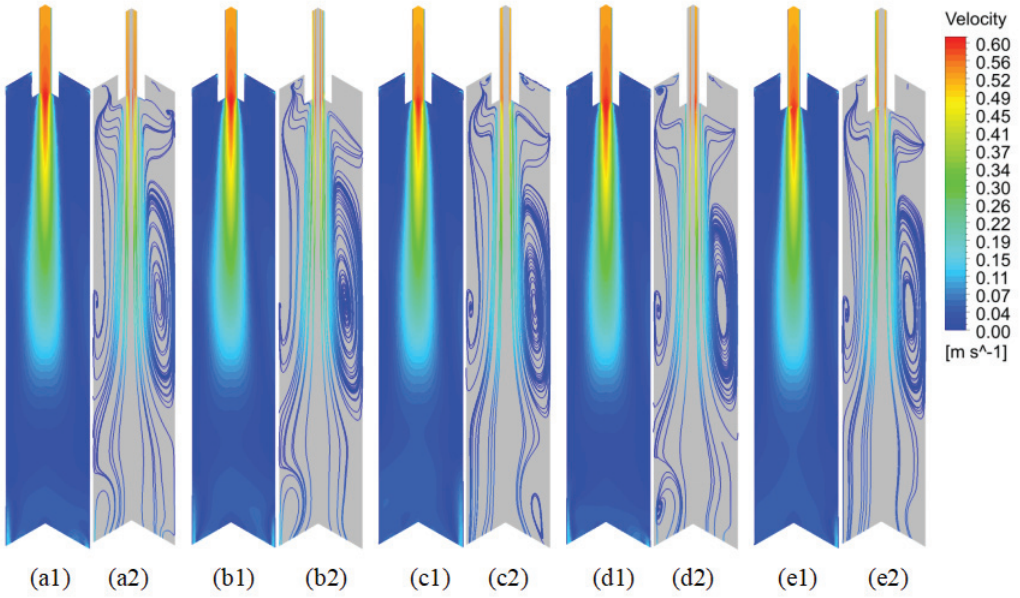

Figure 2. Velocity distribution of symmetric plane (narrow plane and wide plane) at different casting speeds. (**a1**,**a2**) 0.35 m·min^{-1}. (**b1**,**b2**) 0.45 m·min^{-1}. (**c1**,**c2**) 0.55 m·min^{-1}. (**d1**,**d2**) 0.65 m·min^{-1}. (**e1**,**e2**) 0.75 m·min^{-1}.

The surface velocity distribution of molten steel at varying casting speeds is illustrated in Figure 3. The figure indicates that the high- and low-velocity regions of the liquid surface remain relatively consistent at different casting speeds. The flow speed of molten steel near the copper and nozzle walls is relatively higher, while the speed in other areas is slower. As the casting speed increases, the average velocity of the liquid surface gradually increases in a consistent manner. The average liquid surface velocities at casting speeds of 0.35, 0.45, 0.55, 0.65, and 0.75 m·min^{-1} are 0.031 m·s^{-1}, 0.035 m·s^{-1}, 0.039 m·s^{-1}, 0.042 m·s^{-1}, and 0.045 m·s^{-1}, respectively.

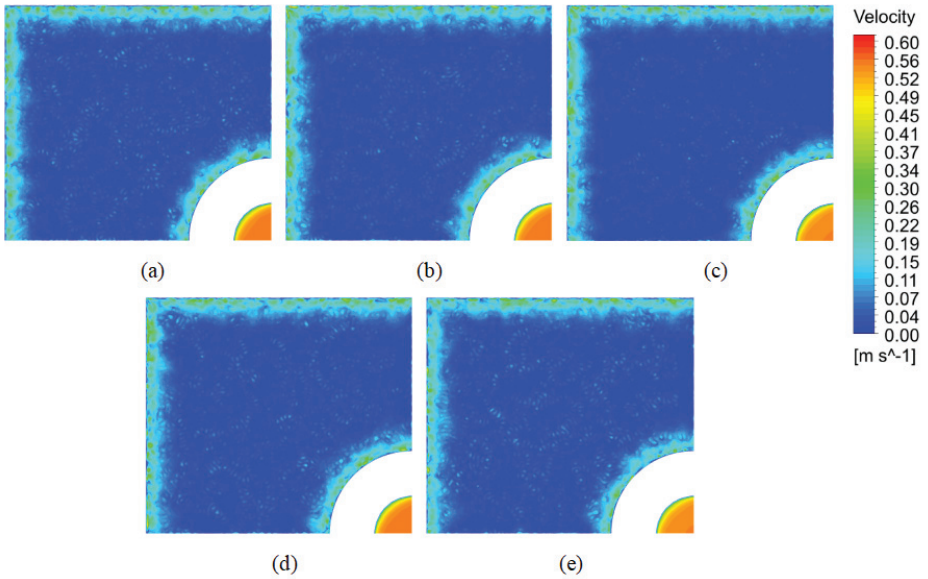

Figure 3. Surface velocity distribution of liquid steel at different casting speeds. (**a**) 0.35 m·min^{-1}. (**b**) 0.45 m·min^{-1}. (**c**) 0.55 m·min^{-1}. (**d**) 0.65 m·min^{-1}. (**e**) 0.75 m·min^{-1}.

The temperature distribution on the symmetry planes (narrow and wide faces) at various casting speeds is illustrated in Figure 4. As shown in the figure, the casting speed has a notable influence on the temperature field. With an increase in casting speed, the temperature of the molten steel in the upper section of the crystallizer gradually decreases, while the temperature of the steel flow moving downward increases, covering a broader range. Figure 5 presents the temperature distribution on the molten steel surface at various casting speeds. As observed in the figure, the casting speed has a minimal effect on the temperature distribution at the liquid surface.

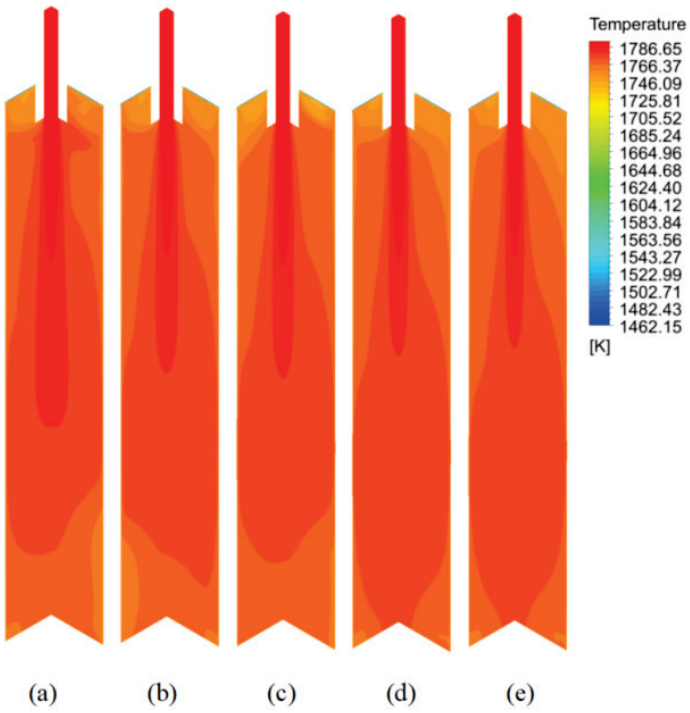

Figure 4. Temperature distribution of symmetric plane (narrow surface and wide surface) at different casting speeds. (**a**) 0.35 m·min^{-1}. (**b**) 0.45 m·min^{-1}. (**c**) 0.55 m·min^{-1}. (**d**) 0.65 m·min^{-1}. (**e**) 0.75 m·min^{-1}.

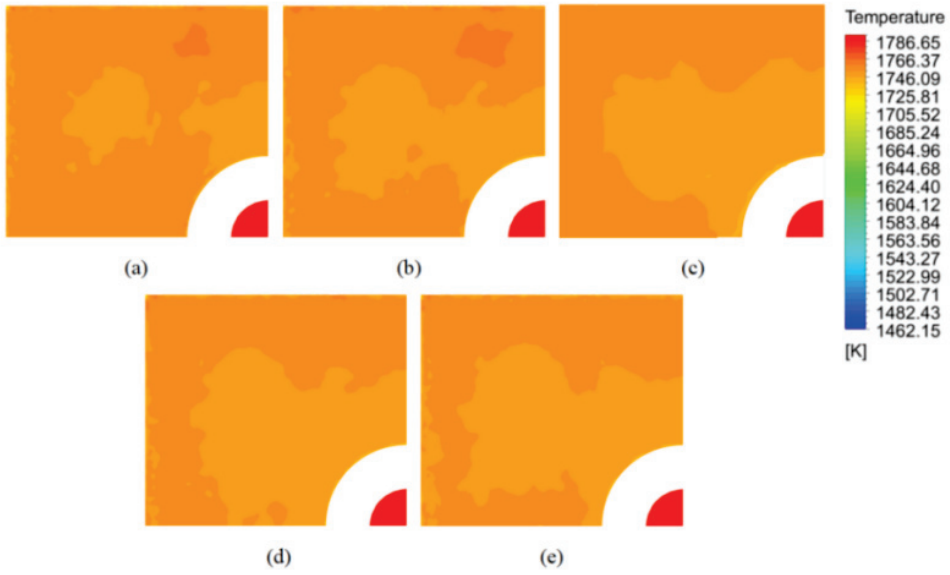

Figure 5. Temperature distribution of liquid steel surface at different casting speeds. (**a**) 0.35 m·min^{-1}. (**b**) 0.45 m·min^{-1}. (**c**) 0.55 m·min^{-1}. (**d**) 0.65 m·min^{-1}. (**e**) 0.75 m·min^{-1}.

The temperature near the nozzle on the liquid surface is comparatively lower. With an increase in the casting speed, the average temperature of the liquid surface progressively decreases. The average temperatures of the liquid surface at casting speeds of 0.35, 0.45, 0.55, 0.65, and 0.75 m·min^{-1} are 1754.32 K, 1753.62 K, 1752.97 K, 1752.46 K, and 1752.2 K, respectively. When the casting speed surpasses 0.65 m·min^{-1}, the temperature of the liquid surface stabilizes and remains nearly constant.

In conclusion, when the casting speed ranges between 0.35 and 0.45 m·min^{-1}, the impact depth and liquid surface flow velocity are moderate, which positively influences the rise of inclusions and bubbles.

3.1.2. Effect of Argon Flow Rate on the Flow Field and Temperature Field

The distribution of argon bubbles at various argon flow rates is illustrated in Figure 6. As shown in the figure, with an increase in the argon flow rate, the number of argon bubbles retained in the molten steel steadily increases. The impact of the rising bubbles on the molten steel becomes increasingly significant, and the maximum depth reached by the argon bubble flow progressively increases. At argon flow rates of 0.50, 0.75, and 1.00 L·min^{-1}, the maximum depths reached by the argon bubbles are 650 mm, 950 mm, and 1000 mm, respectively.

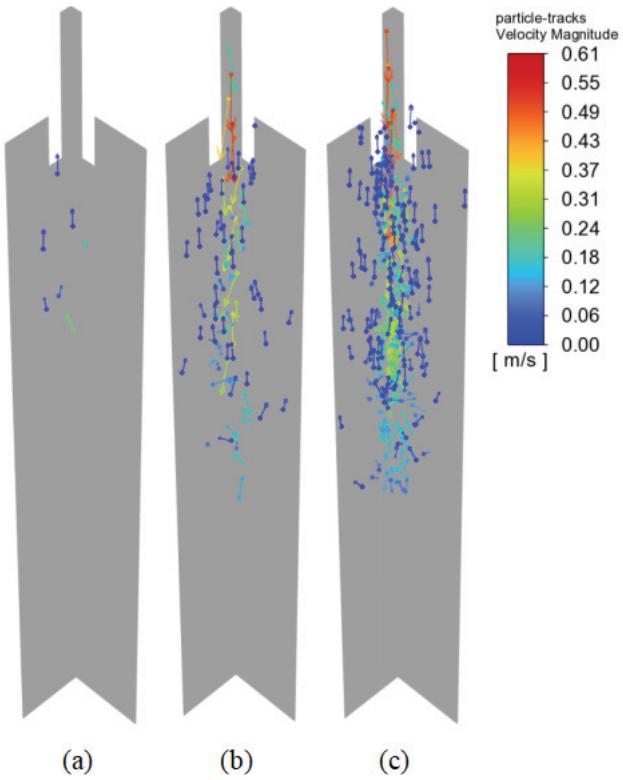

Figure 6. Argon bubble distribution at different amounts of argon blowing. (**a**) 0.50 L·min^{-1}. (**b**) 0.75 L·min^{-1}. (**c**) 1.00 L·min^{-1}.

The velocity distribution on the symmetry planes (both narrow and wide faces) at various argon flow rates is presented in Figure 7. As observed from Figure 7(a1,b1,c1), the influence of the argon flow rate on the flow field is minimal. With an increase in the argon flow rate, the impact depth of the molten steel flow gradually diminishes. At argon flow rates of 0.50, 0.75, and 1.00 L·min^{-1}, the impact depths of the molten steel flow are 330 mm, 322 mm, and 320 mm, respectively. As shown in Figure 7(a2,b2,c2), the distribution of the molten steel recirculation zone changes with varying argon flow rates. With an increase in

the argon flow rate, the molten steel flow in the upper section of the crystallizer is slightly enhanced due to the upward force exerted by the rising argon bubbles.

The distribution of molten steel surface velocity at various argon flow rates is presented in Figure 8. As observed from the figure, the effect of argon flow rate on the surface velocity distribution is minimal. The average surface velocities at argon flow rates of 0.50, 0.75, and 1.00 L·min^{-1} are 0.024 m·s^{-1}, 0.025 m·s^{-1}, and 0.026 m·s^{-1}, respectively. With an increase in the argon flow rate, the average surface velocity gradually increases.

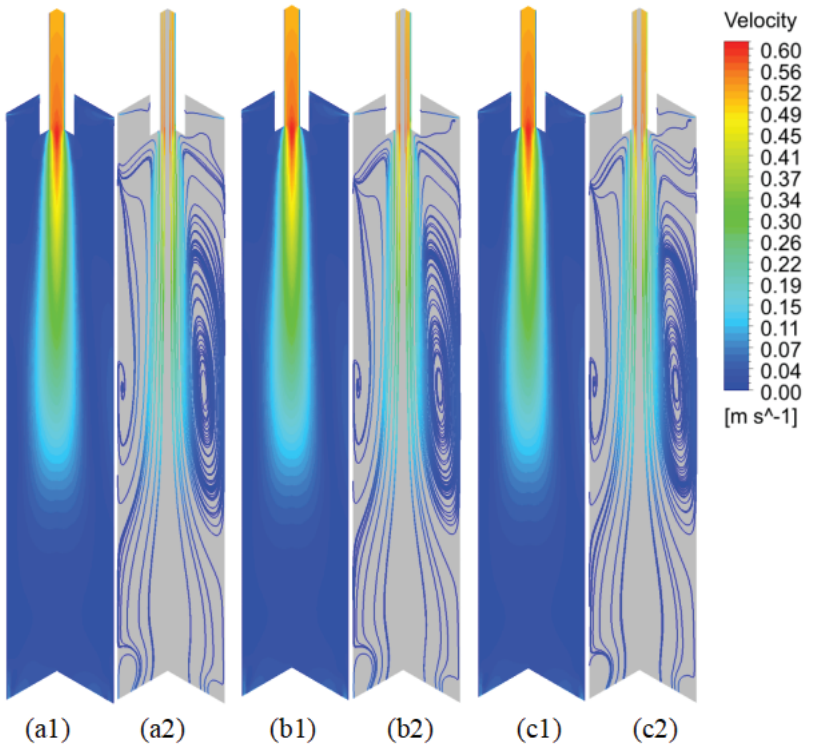

Figure 7. Velocity distribution of symmetric plane (narrow surface and wide surface) at different argon blowing quantities. (**a1**,**a2**) 0.50 L·min^{-1}. (**b1**,**b2**) 0.75 L·min^{-1}. (**c1**,**c2**) 1.00 L·min^{-1}.

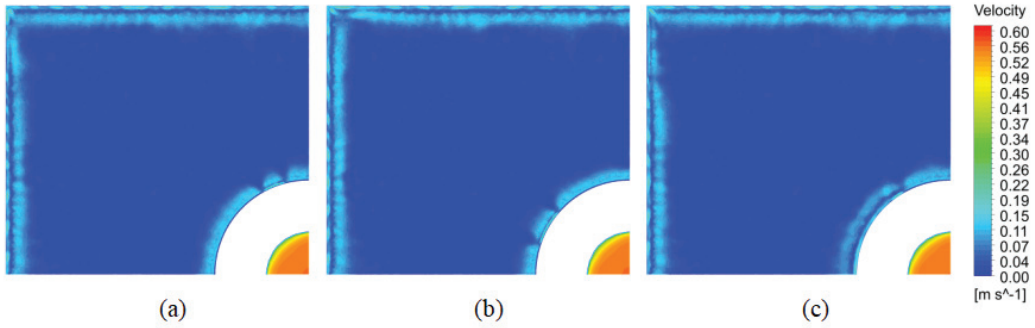

Figure 8. Surface velocity distribution of liquid steel at different argon blowing quantities. (**a**) 0.50 L·min^{-1}. (**b**) 0.75 L·min^{-1}. (**c**) 1.00 L·min^{-1}.

The temperature distribution on the symmetry planes (narrow and wide faces) at various argon flow rates is presented in Figure 9. As seen in the figure, the effect of the argon flow rate on the temperature field in different regions of the crystallizer varies: the temperature distribution in the lower part of the molten steel is less affected, whereas the upper part experiences noticeable changes. As the argon flow rate increases, the flow and escape rate of the argon bubbles accelerate, thereby modifying the molten steel flow in the upper part of the crystallizer and disrupting the kinetic energy of the upward-

flowing steel, leading to a reduction in the proportion of the high-temperature region on the crystallizer's surface.

The temperature distribution of the molten steel surface at various argon flow rates is shown in Figure 10. As observed in the figure, the argon flow rate has a notable impact on the surface temperature distribution. The average surface temperatures at argon flow rates of 0.50, 0.75, and 1.00 L·min^{-1} are 1709.45 K, 1708.33 K, and 1703.74 K, respectively. As the argon flow rate increases, the average surface temperature gradually decreases. At an argon flow rate of 1.00 L·min^{-1}, the surface temperature significantly decreases. The argon bubbles contribute to making the surface temperature distribution of the crystallizer more uniform.

If the argon flow rate is too low, it will fail to effectively remove inclusions; on the other hand, if the flow rate is too high, it will induce excessive fluctuations in the molten steel surface, which can cause slag entrapment. When the argon flow rate is between 0 and 0.50 L·min^{-1}, the flow and heat transfer of molten steel are optimized.

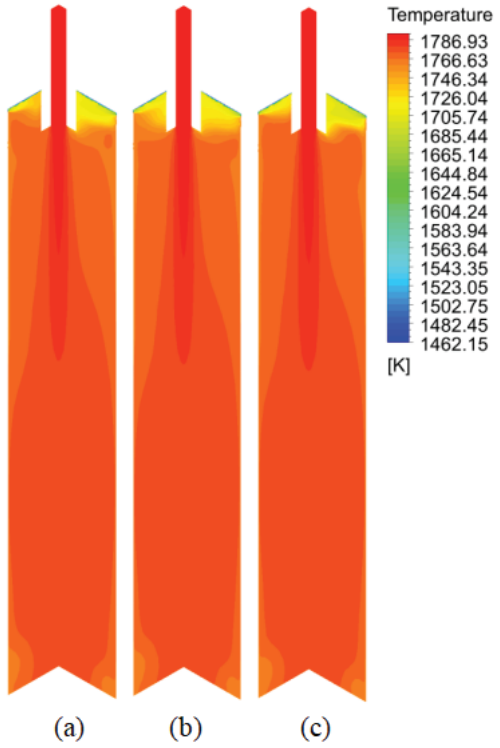

Figure 9. Temperature distribution of symmetric plane (narrow surface and wide surface) at different argon blowing quantities. (**a**) 0.50 L·min^{-1}. (**b**) 0.75 L·min^{-1}. (**c**) 1.00 L·min^{-1}.

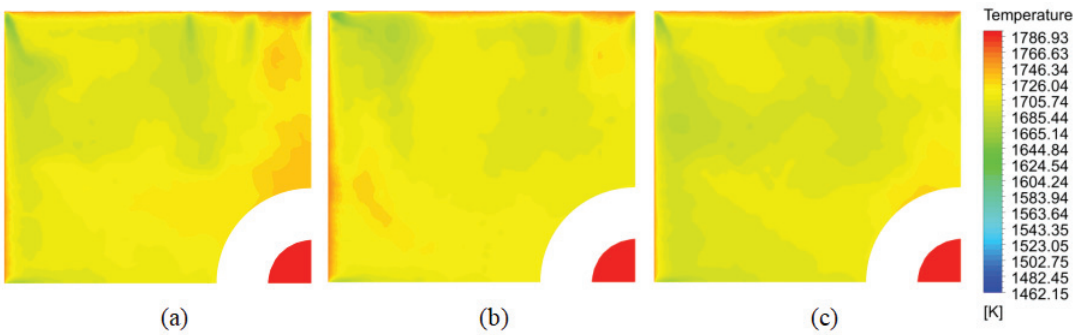

Figure 10. Temperature distribution of liquid steel surface at different argon blowing quantities. (**a**) 0.50 L·min^{-1}. (**b**) 0.75 L·min^{-1}. (**c**) 1.00 L·min^{-1}.

3.2. Flow and Heat Transfer of the Slag Layer

The optimal viscosity of the protective slag enables it to flow uniformly into the gap between the crystallizer wall and the billet shell, effectively acting as a lubricant. This reduces drawing resistance and prevents the billet shell from adhering to the crystallizer wall, thereby facilitating smooth billet demolding. Moreover, the lower density of the protective slag facilitates its smooth flow into the billet shell gap, while the increased number of internal pores helps prevent heat loss, thereby maintaining the temperature of the molten steel and promoting a more uniform solidification process. The flow of the slag layer is primarily influenced by the upper recirculation of molten steel. The behavior of the slag layer is mainly governed by the viscosity and density of the protective slag, which subsequently influences the heat transfer process and temperature distribution within the slag layer. As the properties of the protective slag change, significant changes in the behavior of the slag layer are observed.

3.2.1. Effect of Protective Slag Viscosity on the Slag Layer

Figure 11 illustrates the velocity distribution within the slag layer (1–5 mm) at varying protective slag viscosities. As shown in the figure, the effect of protective slag viscosity on the location of the velocity distribution within the slag layer is relatively minor. With an increase in the viscosity of the protective slag, both the flow velocity and fluctuations of the slag at the same height gradually decrease. As the slag layer height increases from the liquid surface, the flow velocity of the slag decreases accordingly.

Figure 12 depicts the effect of protective slag viscosity on the velocity of the slag layer. As indicated in the figure, the trend of the average velocity within the slag layer remains largely unchanged across varying protective slag viscosities. As the height of the slag layer increases from the liquid surface, the slag velocity decreases in a linear fashion. For each 1 mm increase in height, the velocity decreases by an average of 0.0015 $m \cdot s^{-1}$. As the protective slag viscosity increases, the flow velocity of the slag at the same height gradually decreases. For every 0.2 Pa·s increase in viscosity, the velocity decreases by an average of 0.003 $m \cdot s^{-1}$.

Figure 13 illustrates the temperature distribution within the slag layer (1–5 mm) at varying protective slag viscosities. As shown in the figure, the viscosity of the protective slag significantly influences the temperature distribution within the slag layer. As the height of the slag layer increases from the liquid surface, the temperature gradient within the slag layer varies with different viscosities. The slag layers with viscosities of 0.2 Pa·s, 0.4 Pa·s, and 0.6 Pa·s display distinct temperature stratification at heights of 5 mm, 3 mm, and 1 mm, respectively. With an increase in the viscosity of the protective slag, the temperature distribution at the same height becomes increasingly uneven.

Figure 14 depicts the effect of protective slag viscosity on the temperature of the slag layer. As seen in the figure, the trend of the average temperature within the slag layer varies with different viscosities. As the height of the slag layer increases from the liquid surface, the temperature of the slag gradually decreases. When the distance from the liquid surface does not exceed 3 mm, the slag temperature is lowest at a viscosity of 0.2 Pa·s and highest at a viscosity of 0.4 Pa·s. When the distance from the liquid surface exceeds 4 mm, the slag temperature decreases as the viscosity of the protective slag increases. In conclusion, when the viscosity is between 0.2 and 0.4 Pa·s, the flow and heat transfer performance of the protective slag is more efficient.

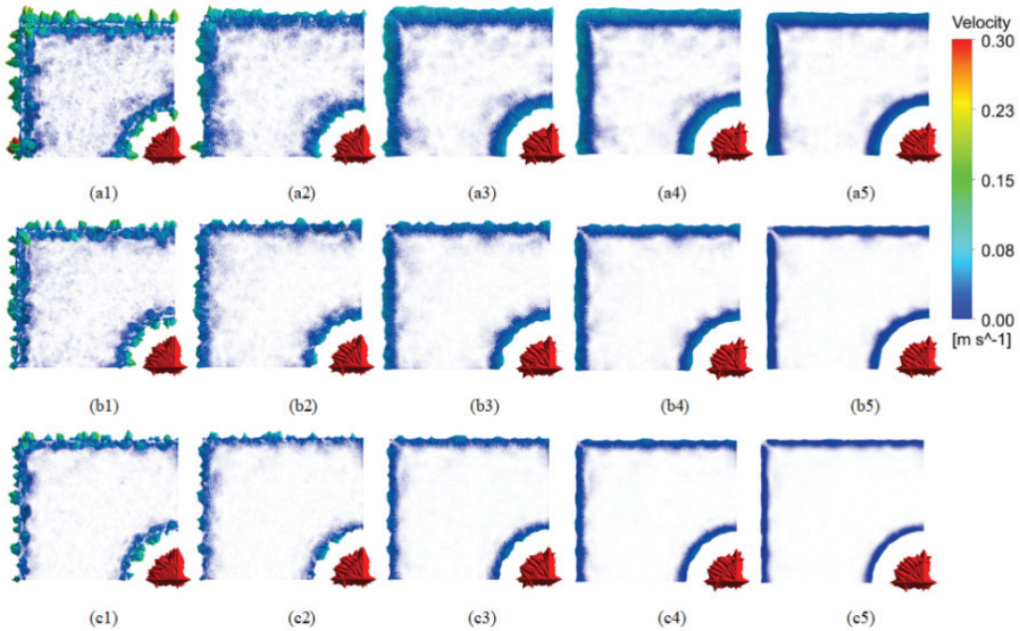

Figure 11. Velocity distribution of liquid slag layer at different viscosity levels of mold powders (different heights). (**a1**–**a5**) Corresponding to 1–5 mm at 0.2 Pa·s. (**b1**–**b5**) Corresponding to 1–5 mm at 0.4 Pa·s. (**c1**–**c5**) Corresponding to 1–5 mm at 0.6 Pa·s.

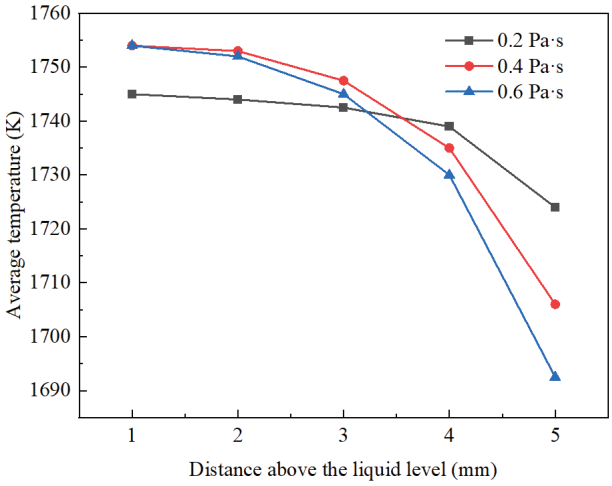

Figure 12. Effect of viscosity of mold powder on velocity of liquid slag layer.

3.2.2. The Effect of Protective Slag Density on the Slag Layer

Figure 15 illustrates the velocity distribution within the slag layer (1–5 mm) at varying protective slag densities. As observed in the figure, the velocity distribution of the slag layer remains similar across different densities. As the density of the protective slag increases, both the flow velocity and the degree of fluctuation at the same height gradually rise. As the height of the slag layer increases from the liquid surface, the flow velocity of the slag decreases.

Figure 16 depicts the effect of protective slag density on the velocity of the slag layer. As observed in the figure, the trend of the average velocity of the slag layer remains relatively constant across different densities. With an increase in the density of the protective slag, the flow velocity at the same height gradually rises. As the distance from the liquid surface increases, the slag velocity progressively decreases. In particular, within the first 1 to 2 mm above the liquid surface, the velocity decreases more rapidly, while in the range of 2 to 5 mm above the liquid surface, the velocity decreases at a slower rate.

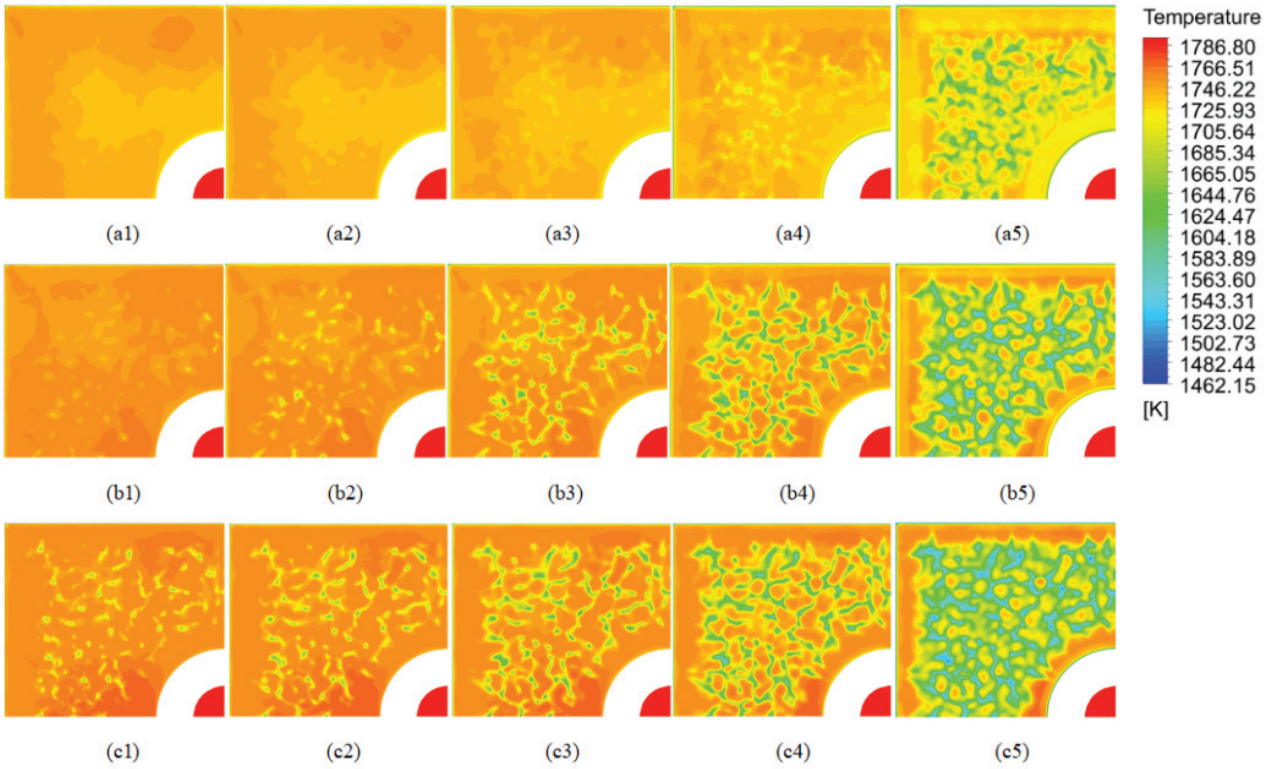

Figure 13. Temperature distribution of liquid slag layer at different viscosity levels of mold powders (different heights). (**a1**–**a5**) Corresponding to 1–5 mm at 0.2 Pa·s. (**b1**–**b5**) Corresponding to 1–5 mm at 0.4 Pa·s. (**c1**–**c5**) Corresponding to 1–5 mm at 0.6 Pa·s.

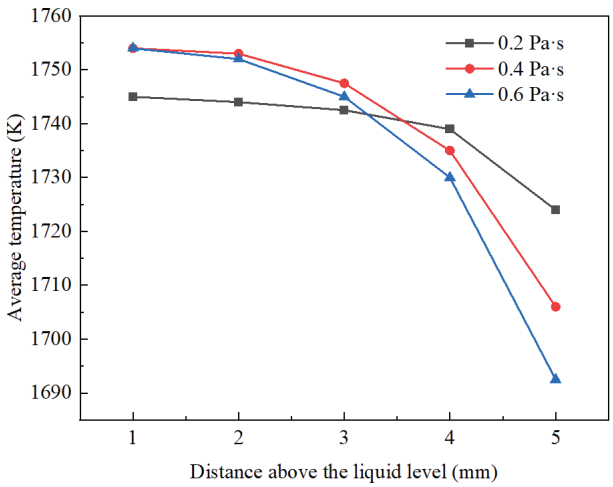

Figure 14. Effect of viscosity of mold powder on temperature of liquid slag layer.

Figure 17 illustrates the temperature distribution of the slag layer within the 1–5 mm range at varying protective slag densities. As depicted in the figure, the temperature distribution of the slag layer across different protective slag densities is relatively similar, with the slag temperature gradually decreasing as the protective slag density increases. As the slag moves further away from the liquid surface, the slag temperature continues to decrease. The temperature stratification within the slag layer remains largely unchanged under different protective slag densities.

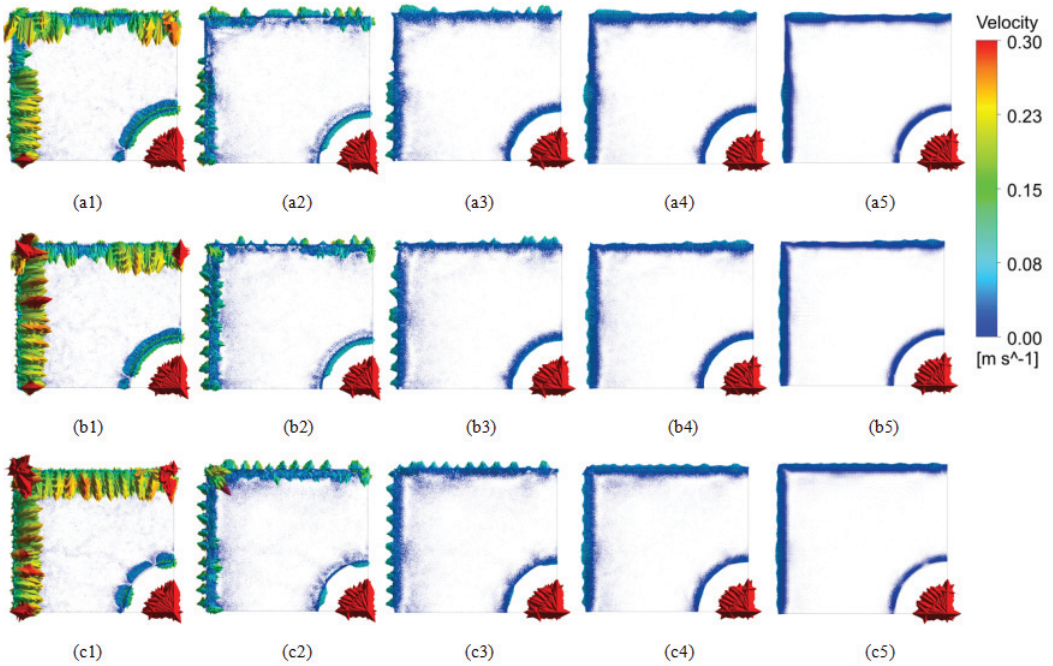

Figure 15. Velocity distribution of liquid slag layer at different density of mold powders (different heights). (**a1–a5**) Corresponding to 1–5 mm at 2484 kg·m^{-3}. (**b1–b5**) Corresponding to 1–5 mm at 2684 kg·m^{-3}. (**c1–c5**) Corresponding to 1–5 mm at 2884 kg·m^{-3}.

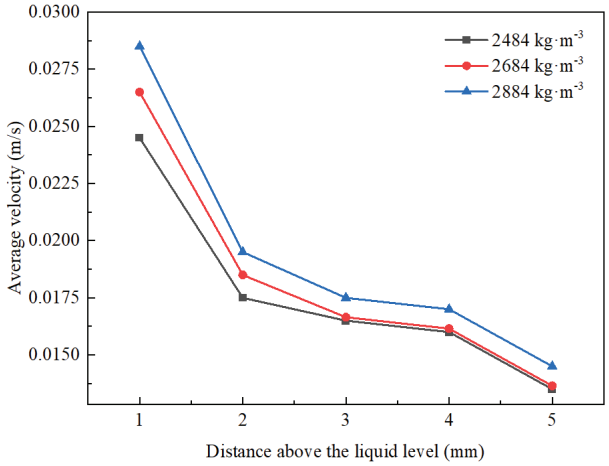

Figure 16. Effect of density of mold powder on velocity of liquid slag layer.

Figure 18 illustrates the effect of protective slag density on the temperature of the slag layer. As shown in the figure, the trend of the average temperature change within the slag layer is essentially consistent across different protective slag densities. As the protective slag density increases, the slag temperature gradually decreases, and with the increasing distance from the liquid surface, the slag temperature continues to decline. When the distance from the liquid surface is less than or equal to 3 mm, the temperature decreases more gradually; however, beyond 3 mm, the temperature decreases at a faster rate.

The flow inertia within the crystallizer and the static pressure exerted on the liquid surface vary with different protective slag densities, influencing the morphology, flow behavior, and stability of the molten steel surface. When the protective slag density ranges from 2484 to 2684 kg·m^{-3}, the flow and heat transfer behavior of the slag layer is more efficient and rational.

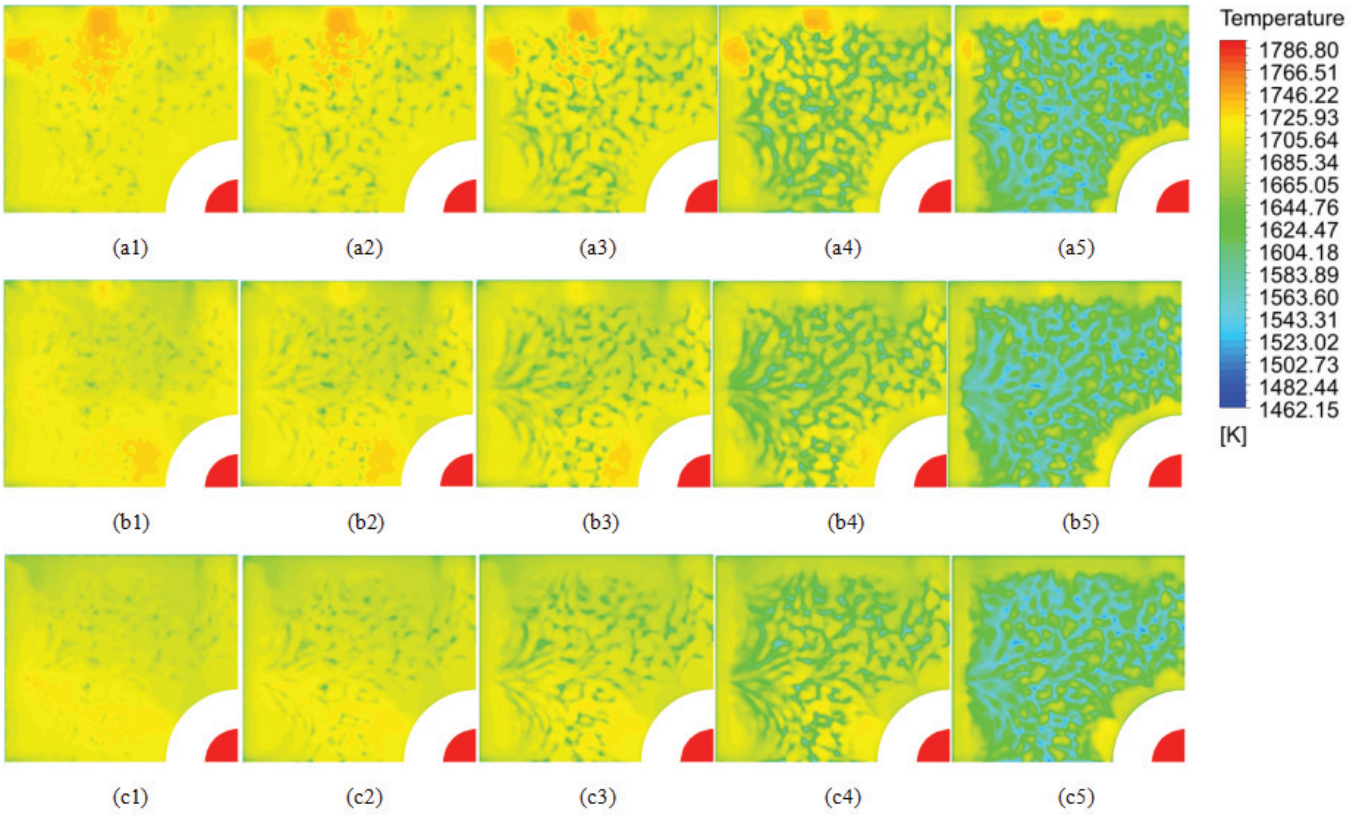

Figure 17. Temperature distribution of liquid slag layer at different density levels of mold powders (different heights). (**a1**–**a5**) Corresponding to 1–5 mm at 2484 kg·m^{-3}. (**b1**–**b5**) Corresponding to 1–5 mm at 2684 kg·m^{-3}. (**c1**–**c5**) Corresponding to 1–5 mm at 2884 kg·m^{-3}.

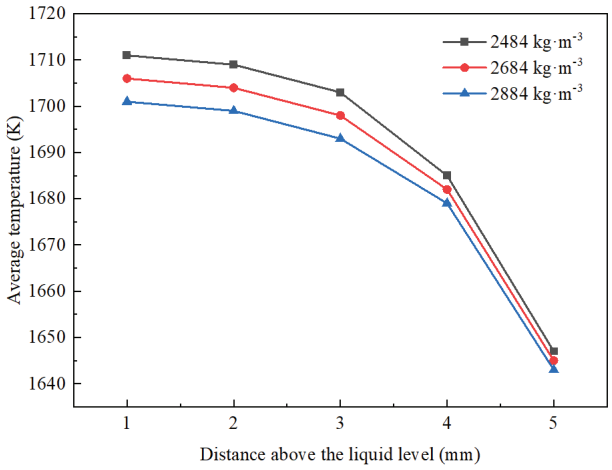

Figure 18. Effect of density of mold powder on temperature of liquid slag layer.

4. Conclusions

1. Reducing the drawing speed to 0.35–0.45 m·min^{-1} more effectively reduces the impact velocity, impact depth, surface velocity, and temperature gradient while improving the uniformity of the liquid surface temperature. This helps prevent slag entrainment at the liquid surface, inadequate slag flow and melting, as well as uneven solidification of the shell. To some extent, this also leads to a more uniform and finer internal structure in large billets of special steel;
2. The upward movement of argon bubbles disrupts the upper recirculation zone of the molten steel. As the argon injection increases, it directly alters the recirculation

trajectory of the molten steel, lowering the liquid surface temperature and increasing the risk of slag entrainment. In the continuous casting process of large billets of special steel, a smaller or even no argon flow is more beneficial for maintaining proper flow and heat transfer at the liquid surface;

3. A higher viscosity of the protective slag increases its flow resistance, resulting in an uneven temperature distribution within the slag layer and potentially causing dead zones and stratification. Lower viscosity enhances the fluidity of molten protective slag and its convective heat transfer performance; however, it also results in weaker resistance to shear deformation, which can lead to larger fluctuations on the molten steel surface and increase slag entrainment. Protective slag viscosity between 0.2 and 0.4 Pa·s ensures a more optimal flow and heat transfer within the crystallizer;
4. Protective slags with different densities exhibit varying flow inertias in the crystallizer and exert different static pressures on the molten steel surface, thereby influencing the morphology, flow state, and stability of the molten steel surface. This also impacts the temperature gradient within the slag layer and the rate of heat transfer. Protective slags with densities ranging from 2484 to 2684 kg·m^{-3} exhibit better flow and heat transfer performance.

Author Contributions: Conceptualization, Z.D., C.W., X.W. and P.X.; methodology, Z.D., C.W. and X.W.; software, C.W. and X.W.; validation, Z.D., P.X. and L.Z.; formal analysis, Z.D., P.X. and L.Z.; investigation, Z.D., P.X., L.Z. and S.W.; resources, L.Z. and S.W.; data curation, Z.D., C.W. and P.X.; writing—original draft preparation, Z.D., C.W. and X.W.; writing—review and editing, P.X., L.Z. and S.W.; visualization, Z.D., C.W. and X.W.; supervision, L.Z. and S.W.; project administration, P.X. and L.Z. All authors have read and agreed to the published version of the manuscript.

Funding: This research was supported by the National Key Fund Projects of China (No. U21A20114), the National Natural Science Foundation of China (No. 24461002D), the Hebei Provincial Science and Technology Programme of China (No. 23561007D), and the Hebei Province natural science Foundation key project (No. E2022208019).

Data Availability Statement: The data presented in this study are available on request from the corresponding author. The data are not publicly available due to privacy restrictions.

Acknowledgments: The author acknowledges the HBIS Company Limited and Steel Laboratory of Hebei Province in this study. Their generous sponsorship and technical support provided crucial resources for experiments, significantly advancing the progress and outcomes of the research.

Conflicts of Interest: Author Zhijun Ding was employed by the company HBIS Group ShiSteel Company, Xin Wang was employed by the company Jiangyou Changcheng Special Steel Co., Ltd. of Panggang Group. The remaining authors declare that the research was conducted in the absence of any commercial or financial relationships that could be construed as a potential conflict of interest.

References

1. Liu, Q.; Qu, Z.; Chen, F.; Liu, X.; Wang, G. Review of the Development of an Unbonded Flexible Riser: New Material, Types of Layers, and Cross-Sectional Mechanical Properties. *Materials* **2024**, *17*, 2560. [CrossRef] [PubMed]
2. Zhang, Z.; Wang, D.; Liu, G.; Qian, Y.; Xu, Y.; Xiang, D. Surface Modification of 42CrMo Steels: A Review from Wear and Corrosion Resistance. *Coatings* **2024**, *14*, 337. [CrossRef]
3. Dolzhenko, A.; Tikhonova, M.; Kaibyshev, R.; Belyakov, A. Microstructures and Mechanical Properties of Steels and Alloys Subjected to Large-Strain Cold-to-Warm Deformation. *Metals* **2022**, *12*, 454. [CrossRef]
4. Zaitsev, A.; Arutyunyan, N. Low-Carbon Ti-Mo Microalloyed Hot Rolled Steels: Special Features of the Formation of the Structural State and Mechanical Properties. *Metals* **2021**, *11*, 1584. [CrossRef]
5. Kozłowska, A.; Grzegorczyk, B.; Morawiec, M.; Grajcar, A. Explanation of the PLC Effect in Advanced High-Strength Medium-Mn Steels. A Review. *Materials* **2019**, *12*, 4175. [CrossRef]
6. Yang, L. China steelmaking technology progress in the 13th five-year plan and prospection. *Iron Steel* **2022**, *57*, 1–10. [CrossRef]

7. Ohno, H.; Fukushima, Y.; Matsubae, K.; Nakajima, K.; Nagasaka, T. Revealing final destination of special steel materials with input-output-based material flow analysis. *ISIJ Int.* **2017**, *57*, 193–199. [CrossRef]
8. Bjorhovde, R. Performance and design issues for high strength steel in structures. *Adv. Struct. Eng.* **2010**, *13*, 403–411. [CrossRef]
9. Xia, S.; Wang, P.; Tang, Q.; Li, W.; Hu, K.; Zhang, J. Solidified end characteristics and center quality control of bearing steel bloom. *Iron Steel* **2024**, *59*, 99–110. [CrossRef]
10. Lan, P.; Su, C.; Ai, H. Solidification Structure and Segregation in Billet Continuous Casting Under High Casting Speed for Alloyed Steel. *Metall. Mater. Trans. B* **2024**, *55*, 5093–5109. [CrossRef]
11. Fredriksson, H. On the solidification of steel ingots and continuously cast steel billets and slabs. *Can. Metall. Q.* **1991**, *30*, 235–244. [CrossRef]
12. Ma, F.; Liu, Q.; Zhang, J.; Wang, C.; Sun, J.; Li, M. Influence of jet characteristics nozzle on penetration behavior to vapor film in secondary cooling zones of continuous casting. *Iron Steel* **2022**, *57*, 101–109. [CrossRef]
13. Yuan, Z.; Zhu, L.; Wang, X.; Wang, B.; Zhang, Y. Shear-thinning property of mold flux for thin slab continuous casting with high casting speed. *Iron Steel* **2022**, *57*, 97–108. [CrossRef]
14. Liu, W.; Ren, L. Influence of outlet angle for submerged entry nozzle on fluid flow in a wide slab casting mold. *Iron Steel* **2022**, *57*, 83–92. [CrossRef]
15. Hu, W.; Ji, C.; Zhu, M. Numerical simulation of continuous casting round blooms with different solidification end reduction strategies. *Metall. Mater. Trans. B* **2021**, *52*, 4130–4140. [CrossRef]
16. Liu, H.; Chen, Y.; Qiu, H.; Wang, Z. Numerical simulation of coupled fluid flow and solidification in a curved round bloom continuous caster with a combined rotary electromagnetic stirring. *Ironmak. Steelmak.* **2022**, *49*, 506–521. [CrossRef]
17. Qiu, D.; Zhang, Z.; Li, X.; Lv, M.; Mi, X.; Xi, X. Numerical Simulation of the Flow Field in an Ultrahigh-Speed Continuous Casting Billet Mold. *Metals* **2023**, *13*, 964. [CrossRef]
18. An, H.; Bao, Y.; Wang, M.; Zhao, L. Effects of electromagnetic stirring on fluid flow and temperature distribution in billet continuous casting mould and solidification structure of 55SiCr. *Metall. Res. Technol.* **2018**, *115*, 103. [CrossRef]
19. Yang, J.; Chen, D.; Long, M.; Duan, H. Transient flow and mold flux behavior during ultra-high speed continuous casting of billet. *J. Mater. Res. Technol.* **2020**, *9*, 3984–3993. [CrossRef]
20. Yang, J.; Chen, D.; Qin, F.; Long, M.; Duan, H. Melting and Flowing Behavior of Mold Flux in a Continuous Casting Billet Mold for Ultra-High Speed. *Metals* **2020**, *10*, 1165. [CrossRef]
21. Vakhrushev, A.; Kharicha, A.; Wu, M.; Ludwig, A.; Tang, Y.; Hackl, G.; Nitzl, G.; Watzinger, J.; Bohacek, J. On Modelling Parasitic Solidification Due to Heat Loss at Submerged Entry Nozzle Region of Continuous Casting Mold. *Metals* **2021**, *11*, 1375. [CrossRef]
22. Ma, J.C.; Sun, H.Z.; Wang, X.B.; Lv, X. Numerical simulation of billet continuous casting solidification based on the measurement of shell thickness and surface temperature. *Appl. Mech. Mater.* **2011**, *80*, 81–85. [CrossRef]
23. Yang, J.; Xie, Z.; Meng, H.; Hu, Z.; Liu, W.; Ji, Z. A three dimensional real-time heat transfer model for continuous casting blooms. *ISIJ Int.* **2023**, *63*, 1360–1372. [CrossRef]
24. Fang, Q.; Ni, H.; Zhang, H.; Lv, Z. The Effects of a Submerged Entry Nozzle on Flow and Initial Solidification in a Continuous Casting Bloom Mold with Electromagnetic Stirring. *Metals* **2017**, *7*, 146. [CrossRef]
25. Ren, B.Z.; Chen, D.F.; Wang, H.D.; Long, M.; Han, Z. Numerical simulation of fluid flow and solidification in bloom continuous casting mould with electromagnetic stirring. *Ironmak. Steelmak.* **2015**, *42*, 401–408. [CrossRef]
26. Hirt, C.W.; Nichols, B.D. Volume of fluid (VOF) method for the dynamics of free boundaries. *J. Comput. Phys.* **1981**, *39*, 201–225. [CrossRef]
27. Hrenya, C.M.; Bolio, E.J.; Chakrabarti, D.; Sinclair, J.L. Comparison of low Reynolds number k-ϵ turbulence models in predicting fully developed pipe flow. *Chem. Eng. Sci.* **1995**, *50*, 1923–1941. [CrossRef]
28. Chattopadhyay, K.; Isac, M.; Guthrie, R.I.L. Considerations in using the discrete phase model (DPM). *Steel Res. Int.* **2019**, *82*, 1287–1289. [CrossRef]
29. Mingtao, X.; Min, C. Numerical Simulation for Two-Phase Flow, Heat Transfer, and Inclusion Transport in Bloom Mold Considering the Effects of Argon Gas Injection and Mold Electromagnetic Stirring. *Steel Res. Int.* **2022**, *93*, 2100848. [CrossRef]

crystals

MDPI

Article

Analysis of Fatigue Performance of Metallic Components with Gradient Microstructures

Pandi Zhao [1,2], Liheng Tuo [3], Hongrui Zhang [4,*], Zhiyan Sun [5], Shuai Ren [5], Gaihuan Yuan [6] and Zebang Zheng [1,2,*]

[1] State Key Laboratory of Solidification Processing, School of Materials Science and Engineering, Northwestern Polytechnical University, Xi'an 710072, China; zhaopandi@mail.nwpu.edu.cn
[2] Research & Development Institute, Northwestern Polytechnical University in Shenzhen, Shenzhen 518057, China
[3] State Key Laboratory of High-End Heavy-Load Robots, Midea Group Co., Ltd., China, Foshan 528311, China; tuolh1@midea.com
[4] Xi'an Institute of Optics and Precision Mechanics, Chinese Academy of Sciences, Xi'an 710119, China
[5] HBIS Materials Technology Research Institute, HBIS Group Co., Ltd., Shijiazhuang 050023, China; sunzhiyan@hbisco.com (Z.S.); renshuai@hbisco.com (S.R.)
[6] State Nuclear Baoti Zirconium Industry Co., Ltd. (SNZ), Baoji 721013, China; zzbsohu@126.com
* Correspondence: zhanghongrui@nwpu.edu.cn (H.Z.); zebang.zheng@nwpu.edu.cn (Z.Z.)

Abstract: Studying the fatigue performance of metallic components and optimizing their design from the perspectives of structure, microstructure, and service conditions has long been a critical research focus. In this study, a comprehensive analysis was conducted on the sealing performance and fatigue behavior of W-shaped metallic sealing rings with varying microstructures. A novel simulation approach is proposed that replaces explicit gradient definitions with temperature conduction to address the issue of stress concentration at interfaces in the finite element modeling of gradient structures. Based on this method, a macroscopic finite element model was developed to simulate the plastic strain accumulation and springback of the sealing ring in service. Then, taking the stress evolution at the trough position of the sealing ring during service as a boundary condition, the evolution of stored-energy density and fatigue life of rings with different microstructures, including both homogeneous and gradient configurations, was quantitatively evaluated. The findings of this work provide valuable insights for the design of structural parameters and the optimization of forming process parameters in high-performance sealing-ring applications.

Keywords: finite element; gradient microstructure; fatigue; crystal plasticity

1. Introduction

Sealing rings are critical components in engine transmission piping and pressure vessels. Their applications span a wide range of high-end equipment fields, including aerospace [1,2], deep-sea exploration [3], nuclear reactors [4,5], etc. As a novel axial self-tightening structure, the elastic metal sealing ring demonstrates exceptional adaptability to extreme service conditions such as elevated temperatures, high pressures, and intense vibration [6]. Consequently, it is widely used in aircraft engines [6,7].

During the development of elastic sealing technology, extensive research was conducted on the sealing performance of metal sealing rings, encompassing a variety of cross-sectional shapes, such as W [8], O [5], C [4], and Ω [9]. In order to improve the service performance of sealing rings, numerous studies have been conducted on the correlation among geometric structure, service conditions, and sealing performance. In terms of geometric structure, Ding [10] analyzed the effect of the outer-arc radius of the W-shaped ring

on the maximum equivalent stress and determined a reasonable range for the outer-arc radius. Jiang et al. [11] and Li et al. [12] addressed structural dimensional design by considering factors such as resilience, sealing performance, and stability under service conditions. Based on service conditions, Li et al. [8] investigated the effect of the temperature and gas pressure) on the fatigue life of W-shaped metallic sealing rings, finding that fatigue life does not vary monotonically with service temperature or pressure but exhibits a certain extremum. Bo et al. [13] and Jiang [6] proposed improvement measures such as controlling the assembly compression range and increasing the wall thickness of the sealing ring to enhance service performance. Chen et al. [7] emphasized that both sealing effectiveness and elastic stiffness should be considered during the design of sealing rings. A broad range of studies has shown that the service performance of such components is closely related to their structure and service environment [14].

In the context of a specific service environment and geometric configuration, it is imperative to consider both the inherent structure of components and the deformation history during the manufacturing process [15,16]. Taking the W-shaped metallic sealing ring as an example, a natural deformation gradient exists within the component [17], even after heat treatment following forming [18], which is often neglected when evaluating service performance. Under the influence of this deformation gradient, strain-induced dissolution behavior may occur within the microstructure, leading to the presence of gradient grain sizes or gradients in phase content [19]. The interface between fine- and coarse-grained regions in such gradient structures induces significant work hardening in the early stages of plastic deformation, thereby enhancing material strength [20]. Backstress strengthening, caused by an increased density of geometrically necessary dislocations (GNDs) within the gradient lamellae during deformation, further contributes to material strengthening [21]. Therefore, to improve the accuracy of service performance prediction, it is essential to consider the deformation gradient introduced during forming.

Certain alloys, such as titanium and aluminum alloys with gradient microstructures, have demonstrated a strength–plasticity synergy, in which strength is improved while maintaining good ductility [22,23]. At specific gradient configurations, both yield strength and impact toughness can be simultaneously enhanced, challenging the traditional notion that high strength inevitably comes at the expense of toughness [24]. Consequently, on the basis of accurate prediction of sealing-ring service performance, to further improve the sealing efficacy of ring components, a systematic investigation into the effect of material microstructure on service performance can be conducted.

In the present work, the service performance of sealing rings with gradient strain and the relationship between microstructure and fatigue are investigated. A novel macroscopic finite element modeling approach for gradient structures is first proposed to alleviate stress concentration at gradient interfaces. This model is then employed to compare the computational results of the conventional homogenized model and the proposed gradient model in evaluating the service performance of sealing rings. Subsequently, the influence of grain size within the primary deformation zone on the fatigue life of the sealing ring is investigated using a crystal plasticity model. In addition, various grain sizes are selected to construct gradient structure models, enabling a systematic analysis of the effect of grain-size gradients on the overall performance of the sealing ring. The research method presented in this paper can be applied to any other components with gradient strain, and the results can provide theoretical guidance for the microstructure design in high-performance sealing rings.

2. Materials and Methodology

2.1. Materials

The material used in this study is Inconel 718, supplied by Gaona Aero Material Co., Ltd., Beijing, China. The chemical composition is shown in Table 1. The metallic sealing rings undergo plastic deformation during forming and subsequent heat treatment prior to service. Therefore, Inconel 718 in the deformed + heat-treated state was used to study the service performance of the sealing ring in this study.

Table 1. Chemical compositions of Inconel 718 (wt %).

Element	C	Si	Mn	S	Cr	Ni	Cu	Al	Ti	Nb	Mo	Fe
Content	0.042	0.11	0.15	0.003	18.31	52.52	0.04	0.48	0.96	5.10	3.02	Bal.

2.2. Finite Element Modeling and Crystal Plasticity Modeling

Two FE models were established in this study. The first one is a uniaxial tensile model with a dog-bone shaped geometry, which is aimed at introducing the proposed temperature-controlled gradient conduct model. The second is a W-shaped cross-section model used for fatigue response and springback analysis of the sealing ring. The stress at the trough position of the sealing rings was extracted and applied as the boundary conditions in the gradient crystal plasticity model to quantify the fatigue life of the sealing ring.

A crystal plasticity model based on the thermally activated motion of dislocations is used to study the local deformation during fatigue [25,26]. The plastic deformation of crystals is generally considered to be the joint action of elastic deformation and plastic deformation. The total deformation gradient of the deformation can be expressed as

$$\boldsymbol{F} = \boldsymbol{F}^{\boldsymbol{e}}\boldsymbol{F}^{\boldsymbol{p}} \tag{1}$$

in which $\boldsymbol{F}^{\boldsymbol{p}}$ is the deformation gradient in the slip direction and $\boldsymbol{F}^{\boldsymbol{e}}$ is that generated by lattice stretching or rotation. The elastic properties of crystals are considered to be independent of crystal slip. The deformation rate gradient can be decomposed into elastic and plastic parts as

$$\dot{\boldsymbol{F}} = \dot{\boldsymbol{F}}^{\boldsymbol{e}} + \dot{\boldsymbol{F}}^{\boldsymbol{p}} \tag{2}$$

and the relation between the $\boldsymbol{F}^{\boldsymbol{p}}$ and a slip system in the crystal is

$$\dot{\boldsymbol{F}}^{\boldsymbol{p}} = \sum_{\alpha} \dot{\gamma}_p^{\alpha} \left(\boldsymbol{s}^{\boldsymbol{\alpha}} \bigotimes \boldsymbol{n}^{\boldsymbol{\alpha}} \right) \tag{3}$$

$$\dot{\gamma}_p^{\alpha} = \rho_m v_g b \tag{4}$$

where $\boldsymbol{s}^{\alpha}$ and $\boldsymbol{n}^{\boldsymbol{\alpha}}$ are the slip direction and normal of the slip surface for a given slip system; $\dot{\gamma}_p^{\alpha}$ is the plastic shear strain rate, which can be determined by the slip rule; b is the Burgers vector; ρ_m is the density of mobile dislocation; and v_g is the average dislocation slip rate. When the resolved shear stress on the slip system is higher than the corresponding critical value, plastic deformation is activated, and the plastic shear strain rate may be expressed as [27,28]

$$\dot{\gamma}_p^{\alpha} = \rho_m b^2 v_D \exp(-\frac{\Delta F}{kT}) \sinh(\frac{(\tau^{\alpha} - \tau_c^{\alpha})\Delta V^{CP}}{kT}) \tag{5}$$

in which k is the Boltzmann constant, T the temperature, v_D the frequency for dislocations attempt to cross obstacles, ΔF the activation energy, and ΔV^{CP} the activation volume.

3. Smooth Distribution of Gradient Properties in Finite Element Models via Controlled Temperature Fields

Finite element simulation of gradient properties originating from gradient microstructures remains a challenge. Taking gradient grain size as an example, to simulate the mechanical response of gradient materials characterized by three distinct grain sizes, i.e., 20 μm (referred to as Average Grain Size 1, AGS1), 70 μm (AGS2), and 180 μm (AGS3), different regions are typically assigned with corresponding material parameters, as illustrated in Figure 1a. This modeling approach may induce computational inaccuracies, particularly manifesting as stress concentrations at the interfaces between regions. To address this issue, a transitional zone may be introduced as a connective region within the gradient structure to mitigate stress concentrations. The material parameters of this transition zone (TS1 and TS2, as shown in Figure 1b) are typically interpolated based on the properties of the adjacent regions, as illustrated in the transition model in Figure 1a. While this method can alleviate some degree of stress concentration, it does not completely eliminate it.

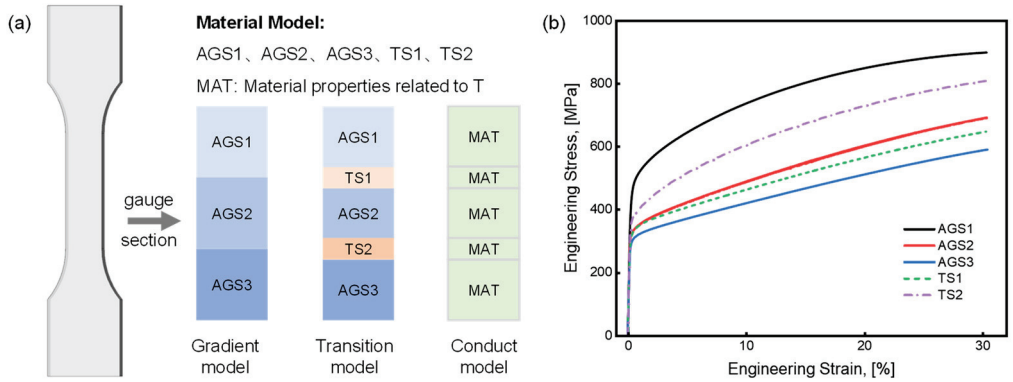

Figure 1. Different models representing the gradient microstructure. (**a**) Schematic illustration of material parameter assignment where blue represents different gradient regions, orange represents the transitional regions, and green represents the regions with uniform material parameter and (**b**) the stress–strain relationship of Inconel 718 with different grain sizes.

In this study, a novel computational strategy is proposed to replace the conventional discrete assignment of gradient properties by introducing artificially controlled temperature fields into the finite element model. It is important to emphasize that the temperature values used in this context bear no physical significance; rather, they serve solely to generate a smoothly varying gradient field. By assigning constant temperatures to the regions with uniform microstructures and allowing thermal conduction to establish a steady-state distribution, a smooth temperature gradient is formed across the model. This temperature field is then used to define spatially varying material properties corresponding to the underlying gradient structure. After the properties are assigned, the artificial temperature field can be removed, enabling subsequent simulations under various thermal conditions (either isothermal or non-isothermal) to assess the deformation behavior of materials with gradient properties. As illustrated in the conduct model in Figure 1a, we construct an integrated temperature-dependent material framework for three grain-size regimes: AGS1 (20 μm), AGS2 (70 μm), and AGS3 (180 μm), numerically corresponding to placeholder temperatures 20 °C, 70 °C, and 180 °C, respectively. These temperatures are not operating temperatures and do not have any specific physical significance. The gradient region, corresponding to the transition zone in the conventional model, is initialized with boundary temperatures that match these values. Material parameters across this region are then automatically interpolated via thermal conduction, achieving a smooth and continuous transition in mechanical behavior.

To verify the computational accuracy of the conduct model, a macroscopic finite element simulation of uniaxial tension is performed. The stress distributions obtained from the three different modeling approaches are illustrated in Figure 2a–c. It can be observed that the conduct model exhibits negligible stress concentration at the gradient junction while maintaining an overall stress field comparable to the other methods. A stress quantification analysis is further conducted along the transition path A-A′, as shown in Figure 2d. The stress differences at the AGS1/AGS2 gradient junction are found to be 165 MPa, 80 MPa, and 0 MPa for the gradient model, the transition model, and the conduct model, respectively. Similarly, at the AGS2/AGS3 interface, the corresponding differences are 103 MPa, 50 MPa, and 0 MPa. Notably, in both the gradient and transition models, the peak stress at the AGS2/AGS3 junction equals or exceeds the maximum stress in the AGS3 region, which represents a primary source of computational inaccuracy. In contrast, the stress distribution along the A-A′ path in the conduct model remains smooth and continuously elevated without abrupt fluctuations, thereby significantly improving the accuracy of the simulation.

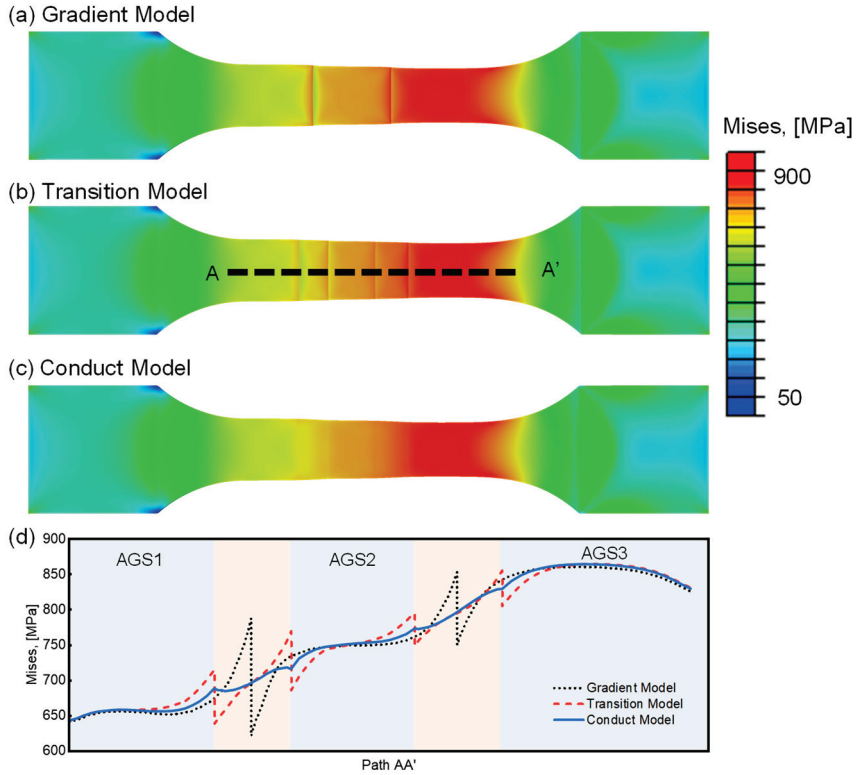

Figure 2. Stress analysis of different models after uniaxial tensile. Stress distribution contour of (**a**) gradient model, (**b**) transition model, and (**c**) conduct model; (**d**) stress distribution along A-A′ path.

Complementarily, this approach improves the computational accuracy of the gradient model and eliminates stress concentrations at the gradient interface. The construction of the model does require an independent temperature conduction step prior to deformation and the predefinition of the temperature field in order to automatically capture the corresponding properties during the subsequent deformation. However, the additional computation primarily occurs during initialization (temperature field mapping <10% of total runtime), with minimal impact on the core deformation analysis. For components like metallic sealing rings, for which predictive accuracy outweighs computational savings, this trade-off proves operationally optimal.

4. Application of the Conduct Model to Compare the Service Performance of W-Shaped Sealing Rings with Gradient and Uniform Microstructures

Due to the distinctive cross-sectional geometry of metallic sealing rings, deformation within the W-shaped section exhibits a naturally occurring gradient distribution. To alleviate residual stresses induced by the forming process, heat treatment is typically performed prior to ring installation. In existing studies, it is generally assumed that mechanical property discrepancies arising from non-uniform deformation can be mitigated by subsequent heat treatment. Accordingly, a homogenization model is often adopted to assess the service performance of W-shaped metallic sealing rings. However, our previous investigations on Inconel 718 revealed that while heat treatment can partially relieve property differences induced by plastic strain, significant variations in yield strength, tensile strength, and elongation persist due to the retained gradient strain. To further investigate the influence of gradient mechanical properties on the overall service performance of the sealing ring, both homogenized and gradient models are developed in this section. For the gradient model, the temperature conduction method introduced in Section 3 is employed to assign spatially varying material properties. This approach effectively suppresses stress concentrations at the interfaces between different gradient regions, thereby enhancing the numerical accuracy of the simulation results.

The model presented in this section is employed to simulate the service performance of metallic sealing rings. A 3 mm segment of the sealing ring was selected as the representative region for analysis, as shown in Figure 3a,b. The model is meshed using C3D20RT elements, with an average element size of 0.08 mm (The verification of grid convergence can be found in Appendix A). Based on the residual strain distribution within the W-shaped cross-section of the formed sealing rings, five distinct plastic strain levels of Inconel 718—7%, 14%, 21%, 28%, 35% (denoted as PS07, PS14, PS21, PS28, PS35)—were selected within the range of 0~40%. The stress–strain responses of these five material states are illustrated in Figure 3c. In the homogenization model, a uniform material property is applied to the entire W section. This modeling framework consists of five distinct cases, each corresponding to a specific deformation state and labeled accordingly (PS07 to PS35).

In contrast, for the gradient model, the stress–strain relationships corresponding to different plastic strain levels are integrated into a unified material framework. These are mapped onto regions within the W-shaped cross-section according to the strain gradient, which is represented through an equivalent gradient temperature field, as shown in Figure 3b. During service simulation, the sealing ring is subjected to 0.6 mm cyclic compression applied by rigid indenters on both sides, following the displacement-controlled loading profile illustrated in Figure 3d. Two key performance indicators, i.e., the springback rate (φ) and equivalent plastic strain (p), both related to fatigue deformation, are quantitatively evaluated. The springback rate φ is defined as follows:

$$\varphi = \frac{h_1 - h_0}{h - h_0} \times 100\% \tag{6}$$

in which h is the initial height of the sealing ring, h_0 is the height after compression, and h_1 is the height after unloading.

The inset in Figure 4a presents the distribution of equivalent plastic strain and displacement in the sealing ring during cyclic service. The results indicate that displacement fluctuations caused by external vibrations during operation are transmitted through the contact interface between the sealing ring and the flange. Notably, plastic deformation is concentrated at the trough region of the sealing ring, where stress localization occurs. To further investigate this behavior, the evolution of plastic strain at the trough is extracted and is also shown in Figure 4a. The plastic strain exhibits rapid accumulation during the

initial loading cycles, followed by a slower, quasi-linear growth phase. In this latter stage, the plastic strain increases linearly with the number of loading cycles. This progressive accumulation of plastic deformation leads to elastic attenuation, as demonstrated in Figure 4b. In the gradient model, the overall deformation trend remains consistent with that observed in the homogenization model. However, the deformation capacity, reflected by the rate and extent of plastic strain development, differs due to the presence of gradient mechanical properties.

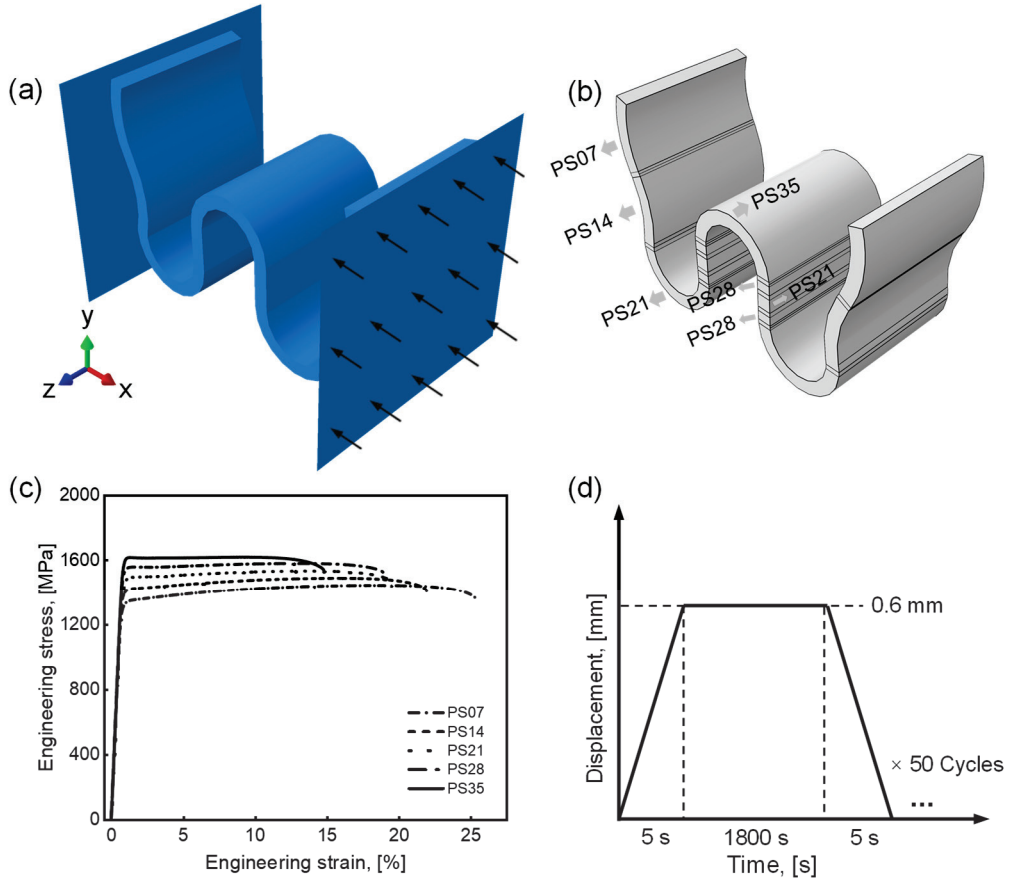

Figure 3. Finite element model to predict the performance of sealing rings. (**a**) Boundary conditions, (**b**) conduct model with gradient deformation in which the PS07, PS14, PS21, PS28 and PS35 indicates the degree of plastic strain is 7%, 14%, 21%, 28% and 35%, (**c**) the corresponding material model, and (**d**) displacement-controlled loading profile.

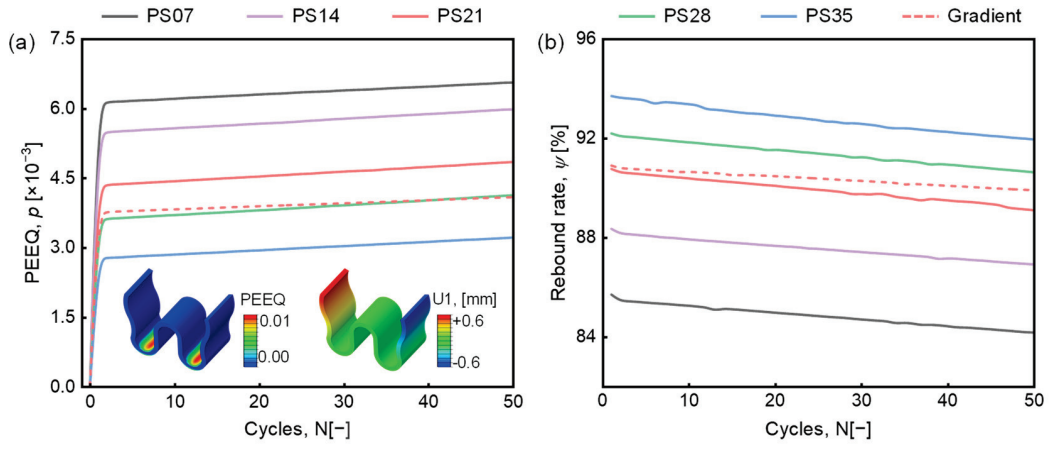

Figure 4. (**a**) Equivalent plastic strain and (**b**) springback rate in different models.

Due to the elevated internal dislocation density and enhanced mechanical properties of materials subjected to significant pre-deformation, their resistance to further plastic deformation during service is substantially improved. As a result, the homogenization models, each corresponding to different degrees of prior deformation, show that plastic strain accumulation at the trough region decreases with increasing deformation magnitude. Conversely, the springback rate exhibits a rising trend. Among these models, PS21 demonstrates performance at the trough region comparable to that of the gradient model and is therefore selected as a benchmark for comparison. As illustrated by the red solid and dashed lines in Figure 4a,b, the gradient model exhibits reduced plastic strain accumulation relative to the PS21 model. This indicates that introducing a gradient structure effectively suppresses fatigue-induced plastic strain accumulation, thereby enhancing the fatigue life of the sealing ring. Additionally, the improved springback resistance observed in the gradient model suggests superior sealing performance.

To elucidate the relationship between fatigue and sealing performance over the service duration, a linear fitting analysis is performed on the evolution of plastic strain and springback rate. The corresponding results are summarized in Table 2, where a_1 denotes the accumulation rate of plastic strain, b_1 represents the initial plastic strain in the first loading cycle, a_2 indicates the rate of elastic decay, and b_2 corresponds to the springback rate immediately after the first unloading cycle. The results reveal that the degree of deformation introduced during the forming process plays a dominant role in determining the magnitude of initial plastic strain, while exerting only a limited effect on the subsequent accumulation rate or elastic decay rate. In contrast, the gradient model exhibits a noticeably lower plastic strain accumulation rate and reduced elastic attenuation, indicating a significant enhancement in both fatigue resistance and sealing performance. These findings underscore the importance of accurately accounting for the material gradient when predicting the long-term performance of metallic sealing rings. Proper incorporation of the gradient structure is thus critical to achieving reliable fatigue life predictions and ensuring optimal service reliability.

Table 2. Fitting results of plastic strain and springback rate.

Model	Equivalent Plastic Strain, p [$\times 10^{-3}$]		Springback Rate, η [%]	
	a_1	b_1	a_2	b_2
PS07	0.00878	6.125	−0.0276	85.525
PS14	0.01029	5.469	−0.0261	88.201
PS21	0.01029	4.327	−0.0309	90.699
PS28	0.01062	3.591	−0.0304	92.144
PS35	0.00914	2.755	−0.0353	93.658
Gradient	0.00660	3.75597	−0.01873	90.837

5. Design of Gradient Microstructure at the Trough Region of Metallic Sealing Rings

According to the results presented in Section 4, the presence of a gradient structure enhances resistance to plastic deformation, mitigates elastic attenuation, and consequently extends the service life of the component when compared to a uniform structure. To further improve the performance of gradient structures, this section focuses on the trough region, which endures the majority of plastic deformation. Given the challenges of implementing gradient structures in such localized regions within a macroscopic finite element model, a microscopic modeling approach is adopted. Crystal plasticity simulations are employed, incorporating the previously established criterion for dislocation-based stored-energy density, to investigate the influence of microstructure at the trough on the service performance

of the sealing ring. Two types of crystal plasticity models are developed: one with a uniform grain size and the other with a gradient grain-size distribution. A grain-size range below 50 μm, determined based on the average grain size of the formed sealing ring, is selected to explore the relationship between grain size and the fatigue performance of the component [29,30]. Within the grain-size range of 0~50 μm, eight different grain-size combinations covering four gradient levels are then used to evaluate the effects of grain-size gradients on sealing-ring performance.

The crystal plasticity models employed in this study are quasi-three-dimensional, with dimensions of 50 μm × 50 μm × 3 μm, as illustrated in Figure 5a. As shown in Figure 5b, five uniform grain-size models with grain sizes of 10 μm, 20 μm, 30 μm, 40 μm, and 50 μm are constructed. For the gradient grain-size model, three regions with distinct grain sizes are assigned from left to right, while the overall crystal orientations are randomly distributed. The loading profile applied, depicted in Figure 5c, is extracted from the trough region of the gradient model discussed in Section 5 and used to define the boundary conditions, as shown in Figure 5a. The material properties of Inconel 718 established in our previous work [1] are used in this study, as shown in Table 3. The failure criterion based on dislocation stored-energy density, as proposed in ref. [1], is adopted here to quantify the mechanical property variations induced by grain size. This approach enables a physically grounded assessment of grain-size effects on deformation behavior and fatigue life.

The prediction of fatigue life using critical stored-energy density is conducted under the conditions of random texture as well as specific gradient region dimensions. A definite fatigue life value is derived from the results of the study. It is worth noting that the location and the evolution tendency of stored-energy density changes slightly when the grain orientation varies, and thus the predicted fatigue life value fluctuates. However, the effect of this fluctuation is negligible on the fatigue life window compared to the effect of the overall gradient or the change in grain size.

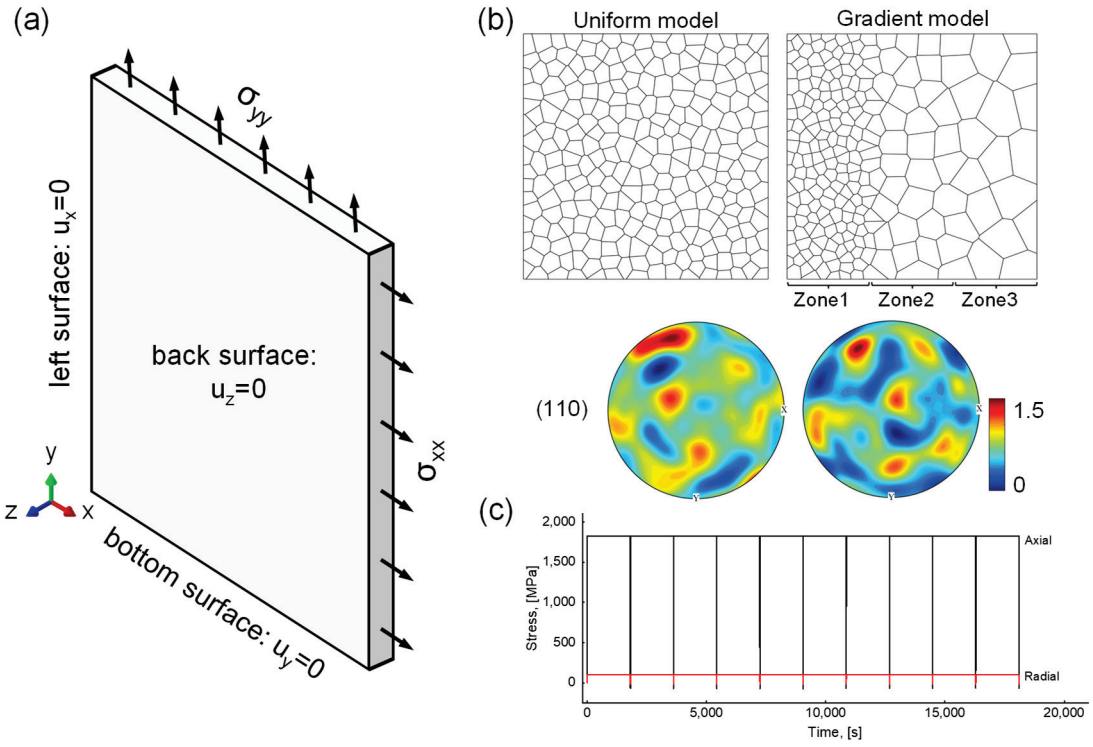

Figure 5. The crystal plasticity model with different grain sizes and gradients. (**a**) Boundary conditions, (**b**) geometry and pole figure, and (**c**) loading profile.

Table 3. Material parameters for Inconel 718 [1].

Parameter (Unit)	Value	Parameter (Unit)	Value
τ_c (MPa)	152.00	b (μm)	3.50×10^{-4}
ΔF (J)	11.00×10^{-20}	T (K)	293.00
ΔV (-)	62.86 b^3	ρ_m (μm^{-2})	5.00
ν_D (Hz)	1.00×10^{11}	k (J·K^{-1})	1.38×10^{-23}

Figure 6a illustrates the evolution of stored-energy density at the point of maximum concentration for each uniform grain-size model. As commonly observed in fatigue deformation, the stored-energy density initially increases rapidly and then enters a steady accumulation phase. The durations of this steady accumulation stage for AVG10 through AVG50 are 6, 9, 16, 18, and 20 cycles, respectively. This trend reflects the influence of grain size on plastic deformation behavior. Smaller grain sizes, with more grain boundaries, restrict dislocation motion and delay the onset of slip, leading to earlier stabilization of stored-energy accumulation. In contrast, larger grains accommodate more extensive plastic deformation, which promotes the generation of geometrically necessary dislocations (GNDs) to maintain strain compatibility, thereby resulting in higher stored-energy density.

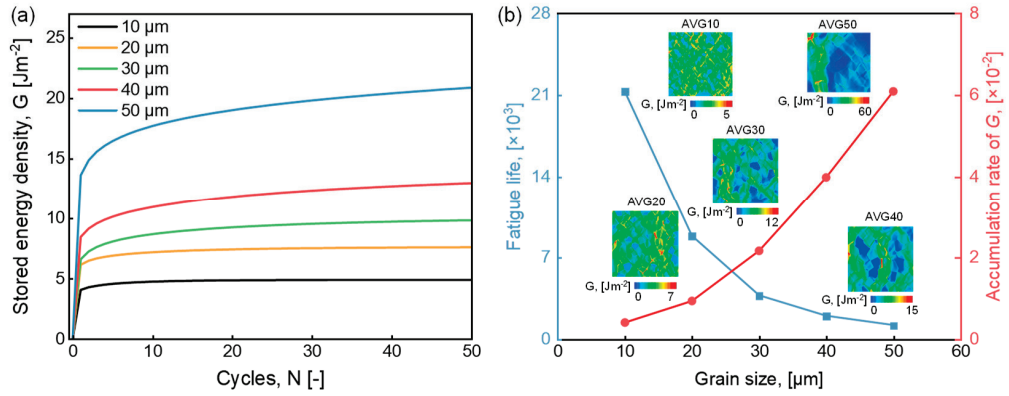

Figure 6. Simulation results of uniform grain-size model. (**a**) Evolution of stored-energy density G and (**b**) accumulation of stored-energy density and fatigue life.

The steady-state accumulation rates of stored-energy density are extracted and presented in Figure 6b. The accumulation rate increases nearly linearly with grain size, with a notably sharper rise observed when the grain size exceeds 20 μm. The fatigue life of the sealing ring is then estimated based on a previously identified critical stored-energy density threshold of 89 J m^{-2}, indicated by the blue dotted line in Figure 6b. Components with larger grain sizes exhibit significantly reduced fatigue life; for example, at a grain size of 50 μm, the predicted fatigue life drops to approximately 1100 cycles. These results underscore the importance of designing a gradient grain structure within the 0~50 μm range to ensure the reliable performance of metallic sealing rings. Properly controlling the gradient can effectively mitigate localized energy accumulation and extend service life under cyclic loading.

Subsequently, the study is extended to more complex scenarios by examining how gradient microstructures affect the accumulation of dislocation stored-energy density. Four gradient magnitudes, i.e., 5 μm, 10 μm, 15 μm, and 20 μm, were selected, and eight gradient models were established based on the grain-size configurations listed in Table 4. The mechanical response of each model was quantitatively characterized using the evolution of dislocation stored-energy density, as shown in Figure 7a.

Table 4. Matching relationship of grain size in gradient model.

Grain Size, [μm]							
Model	**Zone1**	**Zone2**	**Zone3**	**Model**	**Zone1**	**Zone2**	**Zone3**
GM1	5	10	15	GM1-1	15	20	25
GM2	5	15	25	GM2-1	15	25	35
GM3	5	20	35	GM3-1	15	30	45
GM4	5	25	45	GM4-1	15	35	55

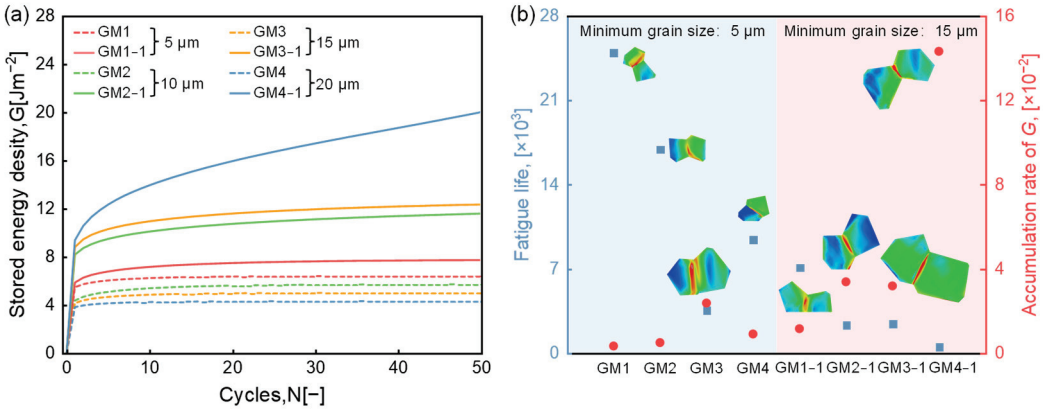

Figure 7. Simulation results of gradient grain-size model. (**a**) Evolution of stored-energy density *G* and (**b**) accumulation of stored-energy density and fatigue life.

It is observed that the accumulation of stored-energy density is primarily governed by the minimum grain size in the gradient microstructure. When the minimum grain size is sufficiently small (e.g., 5 μm), the overall stored-energy density remains relatively low. A comparison among different models further reveals that, for a minimum grain size of 5 μm, the stored-energy accumulation decreases with increasing gradient magnitude, i.e., opposite to the trend observed when the minimum grain size is 15 μm. This suggests that a pronounced grain-size gradient can better accommodate deformation incompatibility, especially when fine grains dominate the microstructure.

Figure 7b presents the accumulation rates of stored-energy density and the corresponding fatigue life across the different gradient models. The inset in Figure 7b shows that the regions of highest energy concentration are randomly distributed in the gradient microstructure. The accumulation rate is largely influenced by the maximum grain size, while smaller grains play a synergistic role in moderating the overall accumulation, as exemplified by the comparisons between GM2 and GM1-1, as well as between GM3 and GM2-1. A positive correlation is found between the energy accumulation rate and both the gradient magnitude and maximum grain size.

Moreover, the fatigue life of the sealing component tends to decline with increasing gradient magnitude. Therefore, when designing gradient microstructures, it is crucial to strike a balance: minimizing stored-energy density through deformation coordination enabled by fine grains, while avoiding excessive accumulation caused by oversized grains. Such a comprehensive design strategy is essential for optimizing the fatigue performance and sealing reliability of the component.

6. Conclusions

A new method to enhance the simulation accuracy of macroscopic finite element models for gradient structures is proposed in this study. This method is applied to evaluate the service performance of sealing rings with both uniform and gradient strain distribu-

tions. Furthermore, the correlation between grain size at the trough region and service performance is investigated using a crystal plasticity model. Based on these analyses, the mechanical behavior of gradient microstructures is systematically assessed. The main conclusions are summarized as follows:

(1) The proposed modeling approach replaces the conventional gradient-type property assignment with an artificial temperature field, which has no physical significance but is used to induce smooth material transitions. A thermal conduction zone is introduced between different regions to establish a continuous material property distribution. This approach effectively reduces stress concentrations to near-zero levels and significantly improves simulation accuracy.

(2) Neglecting gradient deformation in simulations can lead to inaccurate estimations of the service life of sealing rings. When the strain level at the trough is specified, the presence of a strain gradient enhances the resistance to plastic deformation and alleviates elastic degradation during cyclic loading.

(3) When the mechanical behavior of gradient microstructures is characterized via dislocation stored-energy density, the minimum grain size determines the energy density level, and the maximum grain size governs the accumulation rate under the same service conditions. Therefore, both factors must be jointly considered in the microstructural design of gradient materials to optimize performance.

7. Outlook

Building on this work, the proposed simulation framework quantifies macroscopic plastic strain accumulation, evaluates springback behavior, and predicts fatigue life across microstructural variants. However, the influence of multi-pass roll forming parameters on gradient strain characteristics (distribution and magnitude) in the W-section is beyond the scope of this study. Operational factors, including temperature, gas pressure, and preload, remain unexamined in the gradient microstructure performance assessment. The consideration of forming and service factors is essential for high-performance fabrication of sealing rings. In future research, on the one hand, the correlations between forming parameters and gradient strain distribution can be further explored while ensuring forming stability. The reverse optimization of forming processes will be realized based on plastic deformation and springback behavior across macro-gradient configurations. On the other hand, fatigue response in varied service environments and its governing factors can be established to enable service condition-specific microstructural design of sealing rings. Advancing this research may improve the sealing-ring springback rate, reduce leakage, and increase the service life of the sealing ring even further.

Author Contributions: Conceptualization, P.Z. and Z.Z.; methodology, P.Z. and Z.Z.; software, Z.Z. and L.T.; formal analysis and data curation, P.Z. and H.Z.; investigation, P.Z., Z.S. and S.R.; resources, G.Y.; writing—original draft preparation, P.Z.; writing—review and editing, Z.Z. and H.Z.; visualization, L.T., Z.S. and S.R.; supervision, Z.Z.; funding acquisition, Z.Z., L.T., H.Z. and P.Z. All authors have read and agreed to the published version of the manuscript.

Funding: This research was funded by the Shenzhen Science and Technology Program, grant number: GJHZ20240218114404010; the State Key Laboratory of High-end Heavy-load Robots, grant number: HHR2024010106; the Key Research and Development Program of Shaanxi Province, grant number: 2025CY-YBXM-086; and the Innovation Foundation for Doctor Dissertation of Northwestern Polytechnical University, grant number: CX2023046.

Data Availability Statement: The original contributions presented in this study are included in the article. Further inquiries can be directed to the corresponding authors.

Conflicts of Interest: Author Liheng Tuo was employed by the company Midea Group Co., Ltd., Authors Zhiyan Sun and Shuai Ren were employed by the company HBIS Group Co., Ltd., and Author Gaihuan Yuan was employed by the company State Nuclear Baoti Zirconium Industry Co., Ltd. The remaining authors declare that the research was conducted in the absence of any commercial or financial relationships that could be construed as a potential conflict of interest.

Appendix A Mesh Convergence Verification of Finite Element Model for Sealing-Ring Service Performance Prediction

Another four models with different mesh sizes (0.02 mm, 0.05 mm, 0.11 mm, 0.14 mm) were constructed to analyze the mechanical response of the sealing ring. The fitted plastic strain accumulation and springback rate calculated from different grid sizes are shown in Figure A1. The results show that the calculation results are relatively stable when the mesh size is less than 1/3 of the thickness of the sealing ring (0.3 mm), and conversely, the deviation increases. Therefore, in order to ensure the calculation efficiency and accuracy, a 0.08 mm mesh size is chosen for the service performance analysis of the sealing ring, and its size is independent of plastic strain and rebound rate.

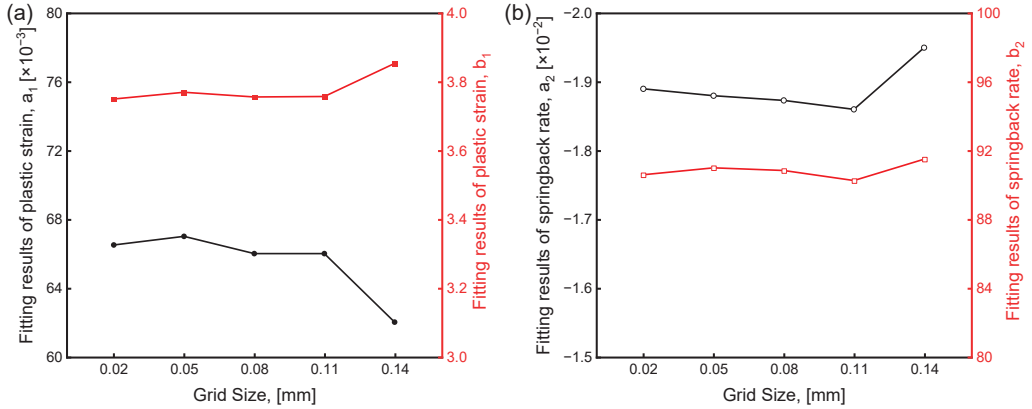

Figure A1. Fitting results of plastic strain and springback rate under different grid sizes. (**a**) a_1 and b_1 of plastic strain and (**b**) a_2 and b_2 of springback rate.

References

1. Zheng, Z.; Zhao, P.; Zhan, M.; Li, H.; Lei, Y.; Fu, M.W. Understanding of the Fatigue Crack Nucleation in Metallic Sealing Rings by Explicitly Incorporating the Deformation History from Manufacturing to Service. *Int. J. Fatigue* **2022**, *164*, 107174. [CrossRef]
2. Porter, C.; Zaman, B.; Pazur, R. A Critical Examination of the Shelf Life of Nitrile Rubber O-Rings Used in Aerospace Sealing Applications. *Polym. Degrad. Stab.* **2022**, *206*, 110199. [CrossRef]
3. Wang, Y.; Luo, W.; Liu, S.; Feng, H.; Li, J.; Wang, J. A Model for Reliability Assessment of Sealing Performance of the C-Shaped Metal Sealing Ring at the Outlet of the Subsea Tubing Hanger. *Ocean Eng.* **2022**, *243*, 110311. [CrossRef]
4. Jia, X.; Chen, H.; Li, X.; Wang, Y.; Wang, L. A Study on the Sealing Performance of Metallic C-Rings in Reactor Pressure Vessel. *Nucl. Eng. Des.* **2014**, *278*, 64–70. [CrossRef]
5. Shen, M.; Peng, X.; Xie, L.; Meng, X.; Li, X. Deformation Characteristics and Sealing Performance of Metallic O-Rings for a Reactor Pressure Vessel. *Nucl. Eng. Technol.* **2016**, *48*, 533–544. [CrossRef]
6. Jiang, Y.; Suo, S.; Wei, Y.; Wang, K.; Wang, Y. Research on Working State Stress and Compression Recovery Performance of Metallic W-Sealing Ring. *Lubr. Eng.* **2018**, *43*, 31–36.
7. Chen, J.; Wang, Y.; Li, Q.; Li, N. Analysis of Influence Factors on Sealing Effect of W-Shaped Metal Seal Ring in Aero Engine. *Adv. Aeronaut. Sci. Eng.* **2018**, *9*, 617–622.
8. Li, W.; Jia, Z.; Yin, W.; Cheng, J.; Ran, J. Fatigue Life Prediction of Multilayer Structure Metallic W-Ring Based on Thermal-Mechanical Coupling. *Hunan Daxue Xuebao/J. Hunan Univ. Nat. Sci.* **2019**, *46*, 41–47. [CrossRef]
9. Shao, G.; Li, H.; Zhang, X.; Zhan, M.; Li, Z.; Liu, Q. External-Internal Composite Spinning Technology for Forming Thin-Walled Ω-Sectioned Ring of Superalloy. *J. Mater. Process. Technol.* **2021**, *291*, 117004. [CrossRef]
10. Ding, X.Y. The Structure Optimization Design for the W-Type Metallic Sealing Ring Based on the MOGA Algorithm. *Appl. Mech. Mater.* **2015**, *727–728*, 541–545. [CrossRef]

11. Jiang, Y.; Suo, S. Comprehensive Performance Optimal Design of Metallic W-Ring under Working Conditions. *Lubr. Eng.* **2019**, *44*, 76–80. [CrossRef]
12. Li, W.; Wang, L.; Jia, Z.; Shan, X. Structure Optimization Design of Metallic W-ring Used in Aviation Engine. *Lubr. Eng.* **2019**, *44*, 12–16. [CrossRef]
13. Bo, H.; Cao, H.; Li, Y.; Yang, L. Failure Analysis and Optimized Verification of Metal W-Sealing Ring of Aero-Engine at High Temperature. *Lubr. Eng.* **2018**, *43*, 127–131. [CrossRef]
14. Skamniotis, C.; Grilli, N.; Cocks, A.C.F. Crystal Plasticity Analysis of Fatigue-Creep Behavior at Cooling Holes in Single Crystal Nickel Based Gas Turbine Blade Components. *Int. J. Plast.* **2023**, *166*, 103589. [CrossRef]
15. Zheng, Z.; Zhan, M.; Fu, M.W. Microstructural and Geometrical Size Effects on the Fatigue of Metallic Materials. *Int. J. Mech. Sci.* **2022**, *218*, 107058. [CrossRef]
16. Shen, S.; Zhan, M.; Gao, P.; Hao, W.; Dunne, F.P.E.; Zheng, Z. Microstructural Effects on Thermal-Mechanical Alleviation of Cold Dwell Fatigue in Titanium Alloys. *Crystals* **2022**, *12*, 208. [CrossRef]
17. Yan, B.; Meng, B.; Zhu, Y.; Wang, Y.; Wan, M. A Global Springback Compensation Method for Manufacturing Metallic Seal Ring with Complex Cross-Section and Submillimeter Precision. *J. Mater. Process. Technol.* **2024**, *331*, 118498. [CrossRef]
18. Shao, G.; Li, H.; Zhang, X.; Zou, J.; Huang, Z.; Zhan, M. Modelling of Ultrasonic Vibration-Assisted Forming Considering the Distribution of Ultrasonic Field with Structure Deformation. *Int. J. Plast.* **2023**, *170*, 103744. [CrossRef]
19. Chen, K.; Luo, J. Preparing Gradient Microstructure to Achieve Enhanced Performance in GH4586 Superalloy: Experiments and Models. *Mater. Sci. Eng. A* **2024**, *915*, 147231. [CrossRef]
20. Yang, L.; Chen, Z.; Ma, X.; Zhong, D.; Zhao, X.; Xiao, L.; Fang, X. Improvement of Strength and Ductility in a Gradient Structured Ni Fabricated by Severe Torsion Deformation. *Mater. Sci. Eng. A* **2021**, *826*, 141980. [CrossRef]
21. Jiang, W.; Xu, P.; Li, Y.; Wang, H.; Cai, Z.; Li, J.; Liang, Y.; Liang, Y. Effect of a Gradient Structure on the Mechanical Performance of Inconel 718 Ni-Based Superalloy at Elevated Temperatures. *J. Mater. Res. Technol.* **2023**, *23*, 2031–2042. [CrossRef]
22. Jian, S.; Wang, J.; Xu, D.; Ma, R.; Huang, C.; Lei, M.; Liu, D.; Wan, M. Gradient Microstructure and Mechanical Properties of Ti-6Al-4V Titanium Alloy Fabricated by High-Frequency Induction Quenching Treatment. *Mater. Des.* **2022**, *222*, 111031. [CrossRef]
23. Qiang, W.; Wu, Q.; Long, L. Gradient Structured Al Alloy with a Synergistic Improvement of Strength-Ductility Obtained by Friction Stir Processing. *Mater. Sci. Eng. A* **2024**, *916*, 147376. [CrossRef]
24. Shi, Y.; Shang, W.; Zhang, X.; Liang, S.; Li, S.; Chen, W.; Liu, H.; Xu, D.; Liu, X.; Lv, G.; et al. Superior Mechanical Properties and Strengthening–Toughening Mechanisms of Gradient-Structured Materials. *Mater. Sci. Eng. A* **2022**, *861*, 144365. [CrossRef]
25. Zheng, Z.; Balint, D.S.; Dunne, F.P.E. Discrete Dislocation and Crystal Plasticity Analyses of Load Shedding in Polycrystalline Titanium Alloys. *Int. J. Plast.* **2016**, *87*, 15–31. [CrossRef]
26. Zheng, Z.; Zhao, P.; Zhan, M.; Shen, S.; Wang, Y.; Fu, M.W. The Roles of Rise and Fall Time in Load Shedding and Strain Partitioning under the Dwell Fatigue of Titanium Alloys with Different Microstructures. *Int. J. Plast.* **2022**, *149*, 103161. [CrossRef]
27. Dunne, F.P.E.; Rugg, D.; Walker, A. Lengthscale-Dependent, Elastically Anisotropic, Physically-Based Hcp Crystal Plasticity: Application to Cold-Dwell Fatigue in Ti Alloys. *Int. J. Plast.* **2007**, *23*, 1061–1083. [CrossRef]
28. Gibbs, G.B. Thermodynamic Analysis of Dislocation Glide Controlled by Dispersed Local Obstacles. *Mater. Sci. Eng.* **1969**, *4*, 313–328. [CrossRef]
29. Zhang, X.; Li, H.; Xiang, Z.; Li, Z.; Zhan, M. Targeted Control of Microstructure Homogeneity of Ni-Based Superalloy Complex Component by Electric Pulse. *Mater. Lett.* **2022**, *321*, 132429. [CrossRef]
30. Li, H.; Xiang, Z.; Zhang, X.; Liu, X.; Gao, J.; Shao, G. Mechanism and Rules of Microstructure Homogenization in Non-Uniform deformed GH4738 under Pulsed Current. *J. Plast. Eng.* **2023**, *30*, 102–110. [CrossRef]

crystals

MDPI

Article

Temperature-Dependent Martensitic Transformation in Cold-Rolled AISI 304 Stainless Steel

Jaka Burja [1,2,*], Jernej Lindič [3], Barbara Šetina Batič [2] and Aleš Nagode [2]

[1] Institute of Metals and Technology, Lepi Pot 11, 1000 Ljubljana, Slovenia
[2] Faculty of Natural Sciences and Engineering, University of Ljubljana, Aškerčeva cesta 12, 1000 Ljubljana, Slovenia; barbara.setina@imt.si (B.Š.B.); ales.nagode@ntf.uni-lj.si (A.N.)
[3] SIJ Acroni d.o.o., Cesta Borisa Kidriča 44, 4270 Jesenice, Slovenia
* Correspondence: jaka.burja@imt.si

Abstract: This study investigates the influence of plastic deformation and temperature on the formation of mechanically induced martensite and the associated changes in hardness in AISI 304 austenitic stainless steel. Cold rolling was performed at three temperatures (20 °C, 0 °C, and −196 °C) and various degrees of deformation (10–70%). Microstructural changes, including the formation of ε and α′ martensite, were characterized using X-ray diffraction (XRD) and electron backscatter diffraction (EBSD). The results confirm that martensitic transformation proceeds via the $\gamma \rightarrow \varepsilon \rightarrow \alpha'$ sequence, with transformation rates and martensite fractions increasing at lower temperatures and higher strains. The stacking fault energy of 25.9 mJ/m^2 favors this transformation pathway. Transformation rates of α′ martensite fractions significantly increased at lower temperatures and higher strains, 91.8% α′ martensite was observed at just 30% deformation at −196 °C. Hardness measurements revealed a strong correlation with martensite content: strain hardening dominated at lower deformations, while martensite formation became the primary hardening mechanism at higher deformations, especially at cryogenic temperatures. The highest hardness (551 HV) was observed in samples deformed to 70% at −196 °C. The findings provide insights into optimizing the mechanical properties of AISI 304 stainless steel through controlled deformation and temperature conditions.

Keywords: austenitic stainless steel; deformation-induced martensite; microstructure; cold deformation

1. Introduction

Stainless steel can be defined as iron alloys with minimal chromium addition in the range between 10 and 12 wt. %. Chromium addition greatly improves atmospheric corrosion resistance due to the surface formation of the thin Cr_2O_3 passive film. Stainless steels can be used as structural materials where both mechanical strength and corrosion resistance are required [1].

AISI 304 (X5CrNi18-8) is the most commonly used Cr-Ni austenitic stainless steel, containing about 18% Cr and 10% Ni with a low C content (usually below 0.08%). Because it exhibits excellent corrosion resistance in the atmosphere and in fresh and seawater and has good weldability, it is widely used for modern applications in the automobile, aviation, and naval industries. Since austenitic stainless steels do not exhibit the ductile-to-brittle transition temperature, they can also be used in low temperature applications such as cryogenic pressure vessels. However, their drawback is pitting corrosion, a type of

localized surface corrosion that is confined to a very small area (pits) and is characteristic of metals with protective surface film [2–4].

Austenitic stainless steels cannot be hardened by heat treatments. But they can be hardened by cold or warm work (drawing, rolling, forging, etc.). The greater the amount of plastic strain induced, the higher the stress required to further deform the material. This is known as strain (or work) hardening [5,6]. Austenitic stainless steels are characterized by a high strain-hardening rate, which is a result of low stacking fault energy (SFE) that makes it difficult for dislocations to cross-slip easily [1]. Since the composition of AISI 304 steel corresponds to the lowest austenite stabilizing alloying element, nickel, which still ensures a fully austenitic microstructure, the austenite in AISI 304 stainless steel is less stable. However, metastable austenite can be effectively used to improve strength through mechanically induced transformation. The mechanically induced transformation from austenite to martensite can only occur at certain temperature/deformation conditions. The portion of formed martensite depends on the amount, temperature, mode of deformation, strain rate, chemical composition, crystal grain size, and crystal grain orientation [7,8]. Martensite formation results in higher hardness and strength, and better wear resistance; moreover, it is also responsible for improving the plasticity (enhanced work hardening, inhibition of necking, and increased uniform elongation) known as the transformation-induced plasticity (TRIP) effect [1,9,10].

There are two types of mechanically induced transformations of austenite into martensite: (1) stress-induced, which takes place before the plastic deformation of austenite in the Ms—Ms^{σ} temperature range, and (2) strain-induced martensite, with the plastic deformation of austenite prior to the phase transformation and occurs at higher temperatures, in the Ms^{σ}—Md range [1,9,10]. The result of the mechanically induced transformation of austenite may be ε and/or α' martensite. In the literature [11–15], two transformations, i.e., direct and indirect sequences, are described. Austenite can be directly transformed to α' martensite ($\gamma \rightarrow \alpha'$) or through an intermediate ε martensite phase ($\gamma \rightarrow \varepsilon \rightarrow \alpha'$). The direct transformation is characteristic of materials with SFE < 18 mJm^{-2} [16], while the indirect transformation occurs in materials with SFE > 18 mJm^{-2}. The occurrence of ε martensite is also favored by low deformation temperatures [17,18]. ε martensite with a hexagonal close-packed (HCP) structure originates from the stacking faults, which are created by the movement of Shockley partial dislocations in austenite, and its growth occurs by overlapping of the stacking faults on every second {1 1 1} plane [7,9,19,20]. Nucleation sites of ε martensite thus involve the intersections of shear bands and mechanical twins formed when stacking fault overlap on successive {1 1 1} planes [9], while α' martensite has a body-centered cubic (BCC) structure and forms at intersections of ε martensite plates and mechanical twins [7,11,21].

The present work aims to determine and characterize the effect of martensite obtained by different plastic deformation conditions (i.e., amount and temperature) on hardness. We studied the changes in the microstructure (with a focus on the development of ε and α' martensite) and mechanical properties (hardness) of AISI 304 austenitic stainless steel. Different temperatures of cold rolling and reductions were employed to achieve different amounts of martensite and hardness.

2. Materials and Methods

In this study, 4.1 mm thick plates of AISI 304 stainless steel with the chemical composition in Table 1 were used for the experiments. The steel samples were cold-rolled at room temperatures of 23 °C, 0 °C, and −196 °C to produce thinner strips. The roller diameters were 200 mm, and the estimated logarithmic deformation speeds were around 0.1 s^{-1}.

The samples rolled at 0 °C were soaked in a mixture of ice and water, while the −196 °C samples were submerged in liquid nitrogen, and the soaking times were 10 min.

Table 1. Chemical composition of AISI 304 in wt.%.

C	Si	Mn	Cr	Ni	Cu	Mo	N
0.042	0.31	1.51	18.2	8.38	0.39	0.35	0.048

The deformation e_h was calculated according to Equation (1).

$$e_h = \left(\frac{h_0 - h_1}{h_0}\right) \times 100 \quad (1)$$

$$h_1 = h_0 - \frac{e_h}{100} h_0 \quad (2)$$

The samples were prepared for metallographic analysis and Vickers hardness measurements, and X-ray diffraction analysis was performed. The specimens were analyzed with the light optical microscope Microphot FXA, Nikon (Nikon, Minato City, Japan), with the 3CCD video camera Hitachi HV-C20A (Hitachi, Ltd., Tokyo, Japan). Scanning electron microscopy (SEM) was performed using a Zeiss CrossBeam 550 FIB/SEM (Zeiss, Oberkochen, Germany) and a ThermoFisher Apreo 2S (Thermo Scientific, Waltham, MA, USA). Electron backscatter diffraction (EBSD) was conducted with a HikariSuper EBSD detector (Ametek, Berwyn, PA, USA). For EBSD measurements, an accelerating voltage of 15 keV and beam currents ranging from 10 to 15 nA were used to ensure high-quality pattern acquisition. Data analysis and visualization were carried out using OIM Analysis 8 software.

X-ray diffraction analysis was performed using Panalytical X'Pert Pro (Panalytical, Malvern, UK) instrument with Cu anode, operated at 45 kV and 40 A. Hardness (Vickers hardness HV10, Wilson Instruments, Norwood, MA, USA) was measured using an Instron Tukon 2100B Vickers hardness measurement instrument (Wilson Instruments, Norwood, MA, USA). The Vickers HV1 method was used with a 1 kgf (9.807 N) load and 10 s dwelling time.

The stacking fault energy can be calculated from the chemical composition using Equation (3) [22].

$$\begin{aligned} \mathrm{SFE} = 39 &+ 1.59(\%\mathrm{Ni}) - 1.34(\%\mathrm{Mn}) + 0.06(\%\mathrm{Mn})^2 - 1.75(\%\mathrm{Cr}) + 0.01(\%\mathrm{Cr})^2 \\ &+ 15.21(\%\mathrm{Mo}) - 5.59(\%\mathrm{Si}) - 60.69\sqrt{(\%\mathrm{C} + 1.2(\%\mathrm{N}))} \\ &+ 26.27(\%\mathrm{C} + 1.2(\%\mathrm{N}))\sqrt{(\%\mathrm{Cr} + \%\mathrm{Mn} + \%\mathrm{Mo})} \\ &+ 0.61\sqrt{(\%\mathrm{Ni}(\%\mathrm{Cr} + \%\mathrm{Mn})} \end{aligned} \quad (3)$$

3. Results

The rolled samples were measured, and their achieved deformation was measured. The sample that was rolled at −196 °C to 70% deformation developed severe cracking, and no metallographic samples were extracted from it. The results of the cold rolling deformation are presented in Table 2.

Table 2. Deformation and thickness of strip samples cold-rolled at different temperatures.

h_1 (mm)	e_h (%)	T (°C)
3.69	10	23
2.90	29.3	23
2.03	50.5	23
1.20	70.7	23

Table 2. *Cont.*

h_1 (mm)	e_h (%)	T (°C)
3.70	9.8	0
2.85	30.5	0
2.06	49.8	0
1.25	69.5	0
3.70	9.8	−196
2.90	29.3	−196
2.02	50.7	−196
1.26	69.3	−196

3.1. Microstructural Analysis

Metallographic analysis shows different martensite contents in the samples. The initial microstructure consisted of equiaxed austenite and some delta ferrite, as seen in Figure 1.

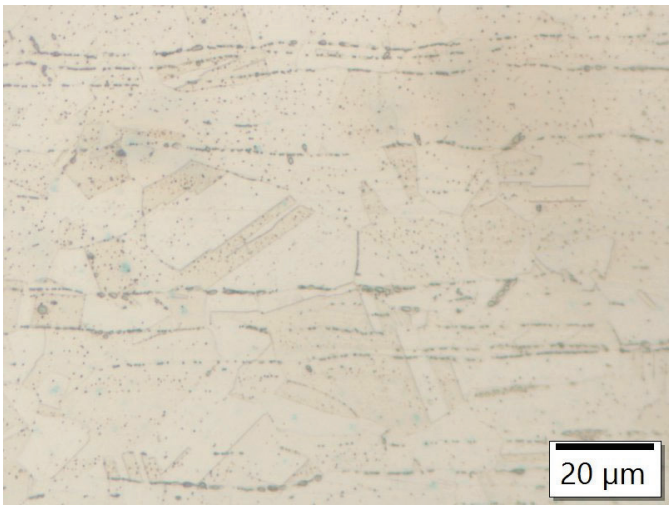

Figure 1. The initial microstructure of AISI 304 consists of equiaxed austenite grains and delta ferrite stringers.

As the deformation is applied, deformation bands start to form. Figures 2–5 show the increasing deformation in the material from 10 to 70% deformation at room temperature.

The EBSD phase analysis gave limited results, as indexation was possible only up to 30% deformation and 50% for 0 °C. At higher deformation, the microstructure is too deformed to produce usable patterns for indexation. The results of the volume fraction of the phases are given in Tables 3–6.

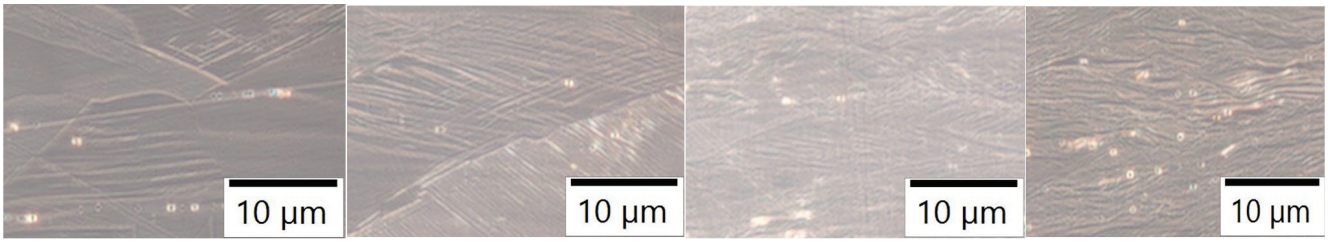

Figure 2. Microstructure under increasing cold deformation at room temperature.

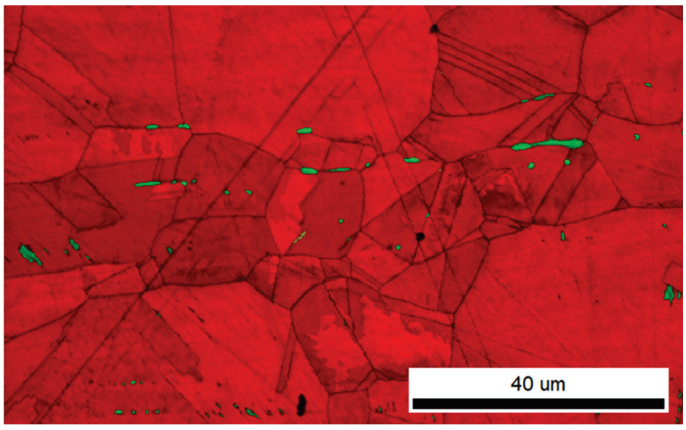

Figure 3. EBSD of the initial microstructure. Austenite is marked with red, and delta ferrite is marked with green.

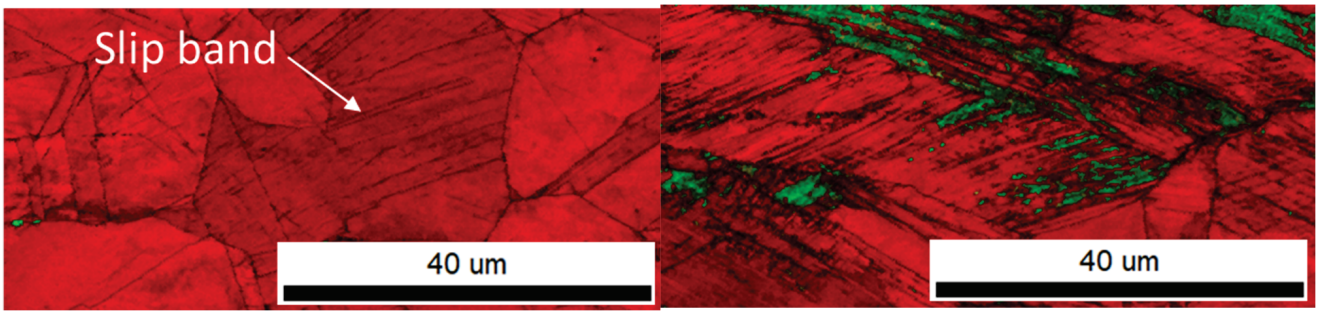

(**a**) (**b**)

Figure 4. Slip bands appear before martensite formation takes place. (**a**) EBSD of the sample with slip bands; 10% deformation at room temperature; austenite is marked with red and delta ferrite green. (**b**) EBSD of the sample with α′ martensite; 30% deformation at room temperature; austenite is marked with red, and α′ martensite is marked with green. Epsilon martensite only appears at lower temperatures.

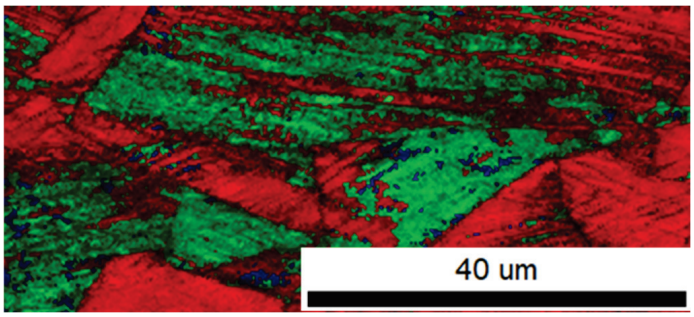

Figure 5. The formation of ε martensite takes place on the slip bands, where it is transformed to α′martensite upon further deformation. EBSD of the sample with ε martensite; 30% deformation at 0 °C; austenite is marked with red, α′ martensite green, and ε martensite blue.

Table 3. Volume fraction of austenite and delta ferrite in the initial microstructure, EBSD analysis.

Phase	Vol.%
austenite	99.6
δ-ferrite	0.4

Table 4. Volume fraction of austenite in samples, EBSD analysis.

	Temperature (°C)		
Deformation (%)	20	0	−196
10	0	0.4	5.1
30	3.0	3.1	6.3
50		17.6	

Table 5. Volume fraction of ε martensite in samples, EBSD analysis.

	Temperature (°C)		
Deformation (%)	20	0	−196
10	0	0.4	5.1
30	3.0	3.1	6.3
50		17.6	

Table 6. Volume fraction of α′ martensite in samples, EBSD analysis.

	Temperature (°C)		
Deformation (%)	20	0	−196
10	0	1.1	25.1
30	11.4	22.4	91.8
50		49.2	

In addition to phase analysis, EBSD gave a good insight into the microstructural evolution during different processing conditions, as can be seen in Figure 6.

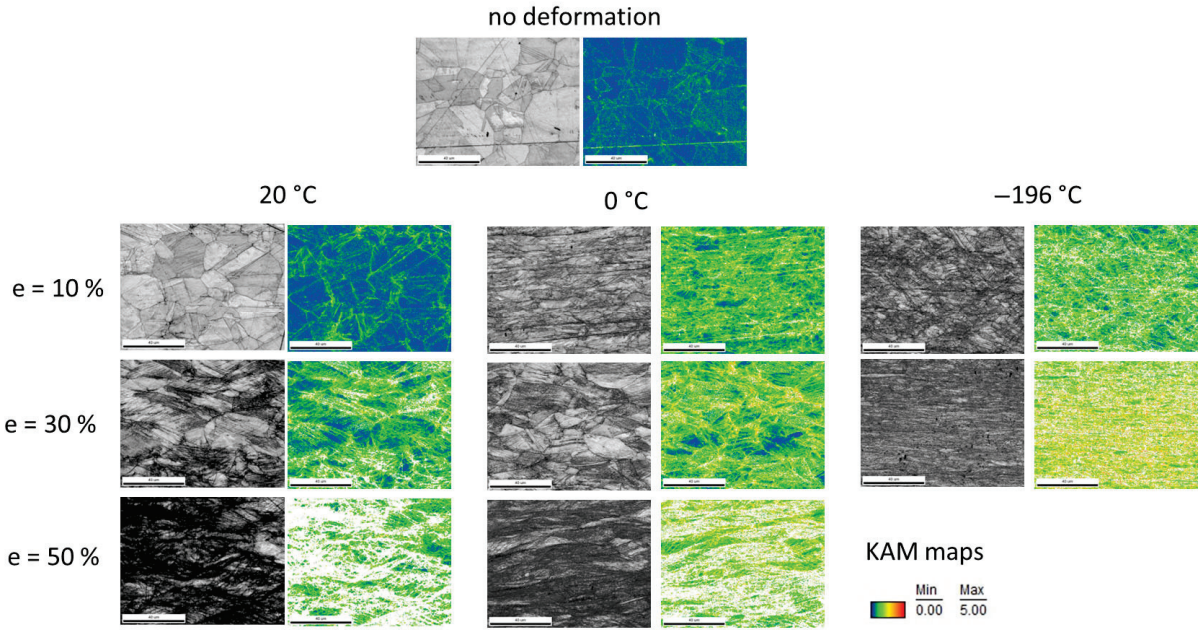

Figure 6. EBSD IQ and KAM maps for different processing conditions.

3.2. XRD Analysis

We additionally determined the presence of austenite, ε martensite, and α′ martensite in the microstructure, based on XRD analysis. We compared the intensity of the peaks of

the phases at the same degree of deformation and different temperatures. The results are shown in Figures 7–10. Black dots and their corresponding peaks indicate the presence of austenite, red dots belong to α′ martensite and δ-ferrite, while green dots mark ε martensite.

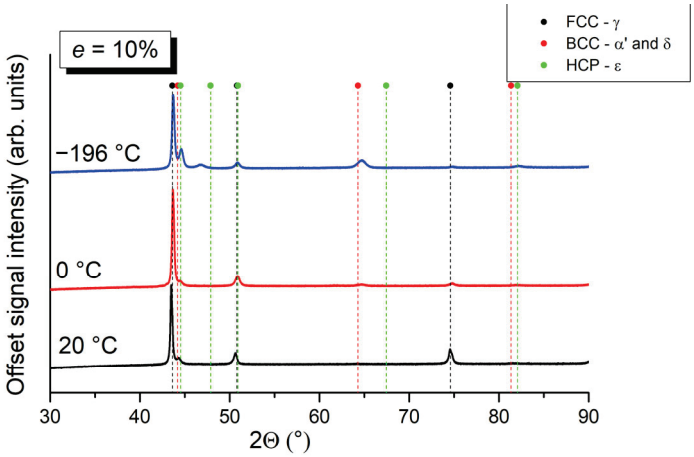

Figure 7. Comparison of XRD analysis results of microstructural constituents in samples deformed at temperatures of 20 °C, 0 °C, and −196 °C and a 10% degree of deformation.

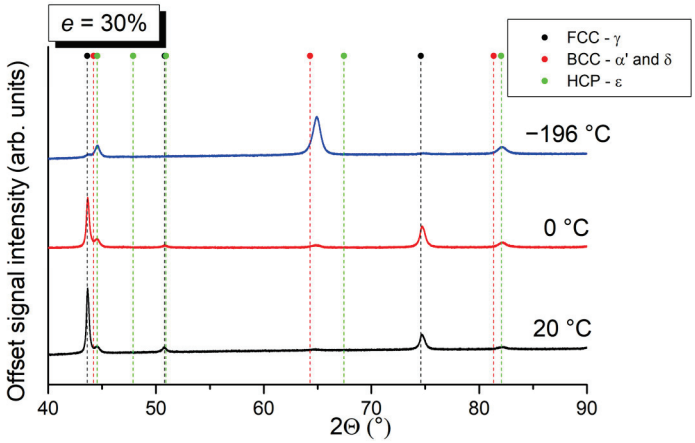

Figure 8. Comparison of XRD analysis results of microstructural constituents in samples deformed at temperatures of 20 °C, 0 °C, and −196 °C and a 30% degree of deformation.

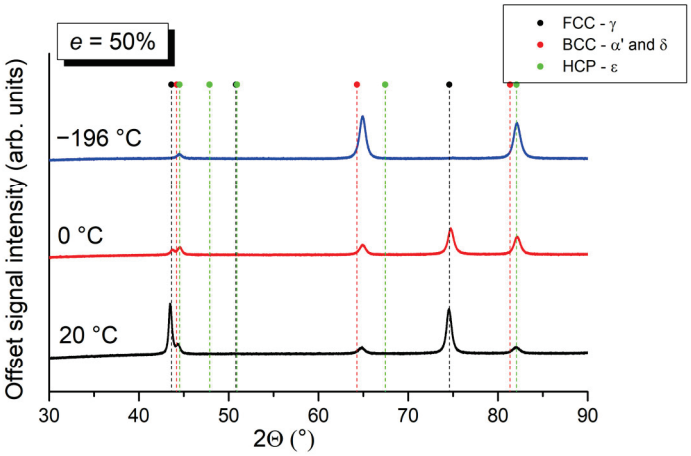

Figure 9. Comparison of XRD analysis results of microstructural constituents in samples deformed at temperatures of 20 °C, 0 °C, and −196 °C and a 50% degree of deformation.

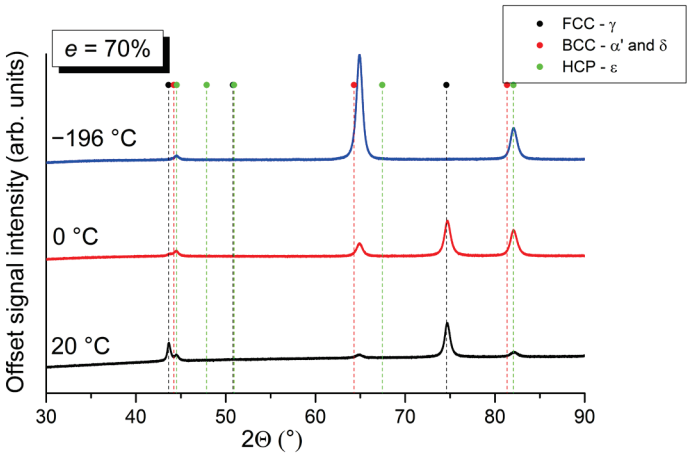

Figure 10. Comparison of XRD analysis results of microstructural constituents in samples deformed at temperatures of 20 °C, 0 °C, and −196 °C and a 70% degree of deformation.

At 10% deformation, a decrease in the intensity of austenite diffraction peaks is evident with a decrease in the deformation temperature. With an increase in deformation to 30, 50, and 70%, the intensities of the austenite peaks decreased further at all deformation temperatures. At a 70% deformation, the austenite peaks can still be observed at deformation temperatures of 20 and 0 °C, but at −196 °C, they disappear above a 30% deformation. With the decrease in austenite diffraction peaks, the peaks belonging to ε martensite and α′ martensite increased. Peaks of ε martensite and α′ martensite first appear at the temperature of 20 °C and 30% deformation. At 0 and −196 °C, they are already present at a 10% deformation. At 70% deformation and temperature of −196 °C, a distinct peak belonging to α′ martensite is observed at a diffraction angle of 64.30°.

The results of the XRD analysis are comparable to those obtained by EBSD analysis. The changes in the intensity of the peak signals belonging to a specific phase are consistent with the changes in the fractions of individual phases determined by EBSD analysis and compiled in Tables 3–6.

3.3. Vickers Hardness

Hardness measurements are presented in Figure 11. The hardness is increased by the degree of deformation. The lower the temperature at which the deformation took place, the higher the resulting hardness.

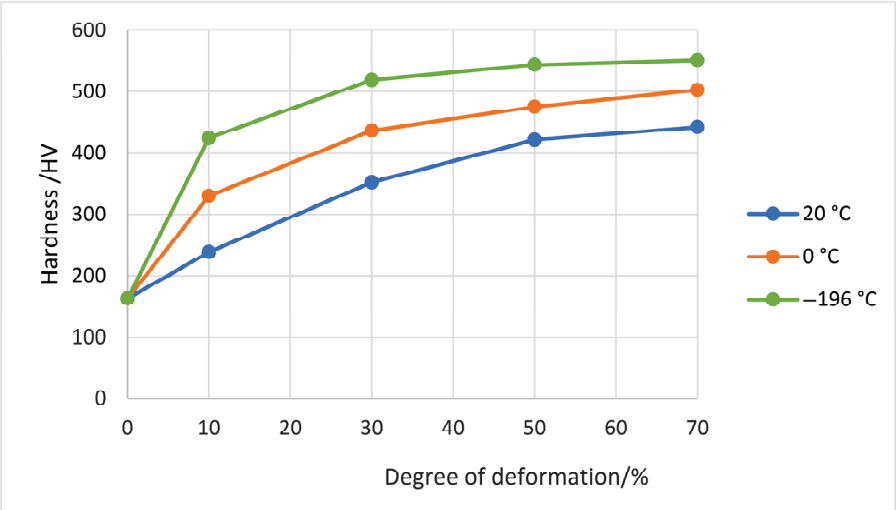

Figure 11. Hardness of samples depends on different degrees of deformation at different temperatures.

3.4. Stacking Fault Energy

The stacking fault energy (SFE) of the investigated steel is 25.9 mJ/m^2. It was calculated using empirical Equation (3), which, in addition to the chemical composition of the steel, also considers the interactions between the individual elements. The SFE values between 20 and 50 mJ/m^2 favor the transformation of austenite into martensite through the intermediate epsilon phase ($\gamma \rightarrow \varepsilon \rightarrow \alpha'$) [23,24]. This was observed in the microstructural analysis, but only in low-temperature samples.

$$\text{SFE} = 39 + 1.59(8.38) - 1.34(1.51) + 0.06(1.51)^2 - 1.75(18.20) + 0.01(18.20)^2 + 15.21(0.35) - 5.59(0.31) - 60.69(0.042 + 1.2(0.048)) + 26.27(0.042 + 1.2(0.048))\sqrt{(18.20 + 1.51 + 0.35)} + 0.61\sqrt{(8.38(18.20 + 1.51))}$$

4. Discussion

The microstructural change during cold deformation (10, 30, 50, and 70%) of austenitic stainless steel 304 at three different temperatures (20, 0, and −196 °C) showed a profound influence on the final properties. The lower degrees of deformation resulted in fewer slip bands in the crystal grains. However, at cryogenic temperatures, martensite forms even at low deformations.

At a 10% degree of deformation (Figure 12a), the number of shear bands within the austenite grains is low, and they are parallel to each other. With an increase in the degree of deformation, the number of shear bands within the grains also increased (Figure 12b).

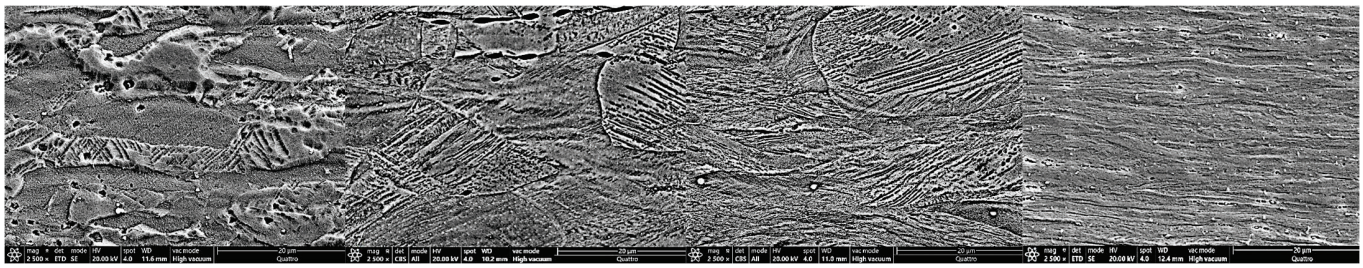

(**a**) (**b**) (**c**) (**d**)

Figure 12. Microstructure of samples deformed at 0 °C: (**a**) 10% deformation, (**b**) 30% deformation, (**c**) 50% deformation, (**d**) 70% deformation.

As the degree of deformation increases, the dislocation density and the number of mutual interactions in the steel increase. Most dislocations in FCC crystal systems are dissociated into Shockley partial dislocations, which are not capable of cross-slip and climb. Due to the reduction in mobility, cross-slip systems are activated, leading to intersections between shear bands, as seen at a 30% degree of deformation. At a 50% degree of deformation (Figure 12c), the number of shear bands is lower, as their intersections act as nucleation sites for the formation of ε martensite and α′ martensite. At a 70% degree of deformation (Figure 12d), most of the microstructure has already been overgrown by martensite. Higher deformations result in a microstructure where single grains cannot be identified.

The martensitic transformation proceeded via the reaction $\gamma \rightarrow \varepsilon \rightarrow \alpha'$, which is consistent with the literature [25] on AISI 304 steel, where it was found that with increasing degree of deformation, the fractions of ε martensite and α′ martensite initially increase. The fraction of ε martensite increases more slowly and also reaches lower values than α′ martensite, as ε martensite also acts as a nucleation site for the formation of α′ martensite. In contrast to the previously mentioned research, in our case, the fraction of ε martensite increased at all temperatures and degrees of deformation, although according to reference [25], it should reach a maximum at a certain temperature and degree of deformation, after which

its fraction would begin to decrease due to the formation of α′ martensite. This underlines ε martenite's consistent presence as a precursor.

The martensitic transformation reaction is also consistent with previous research [18], where it was found that for a calculated stacking fault energy value of SFE = 25.87 mJ/m^2, the transformation of austenite to α′ martensite occurs via the formation of ε martensite.

At low deformation temperatures, the stacking fault energy is also lower, which causes an increasing number of perfect dislocations to decompose into Shockley partial dislocations that are not capable of climb and cross-slip. Due to the limited mobility, cross-slip systems are activated, leading to intersections between shear bands. The intersections act as nucleation sites for the formation of ε martensite and α′ martensite. With the growth of martensite, the number of shear bands decreased, which is evident from the microstructure image at a deformation temperature of 0 °C (Figure 13a). At −196 °C, most of the microstructure is martensitic (Figure 13b).

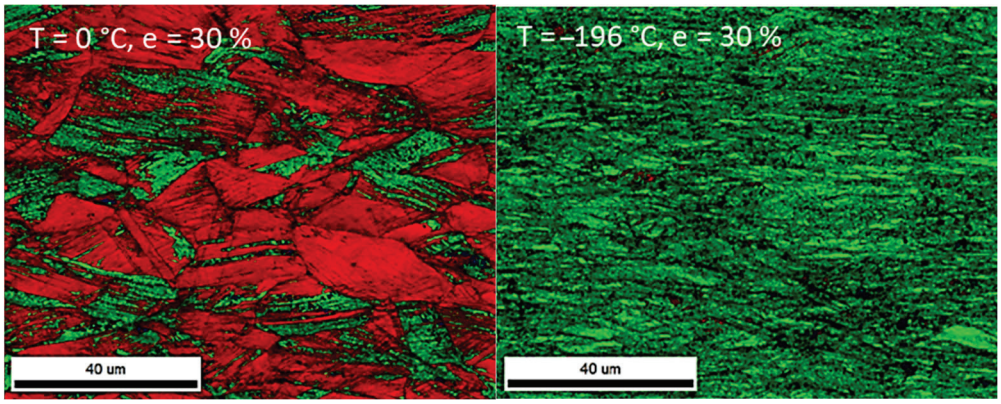

(**a**) (**b**)

Figure 13. The formation of α′martensite largely depends on the deformation temperature. EBSD mappings where austenite is marked with red, and α′martensite is marked with green; (**a**) 30% deformation at 0 °C, partial martensitic microstructure, and (**b**) 30% deformation at −196 °C, predominantly martensitic microstructure.

While α′ martensite is indeed the primary phase responsible for the significant increase in hardness, the $\gamma \rightarrow \epsilon \rightarrow \alpha'$ transformation sequence is not merely a pathway but an intrinsic and crucial mechanism that enables and enhances this hardening, especially at lower temperatures.

In materials with SFE > 18 mJ/m^2 (AISI 304 with 25.9 mJ/m^2), ε martensite forms first from stacking faults in the austenite. These ε martensite plates, particularly their intersections with each other or with mechanical twins, act as preferential nucleation sites for the harder α′ martensite [24,26].

Without this preceding ε martensite phase, the nucleation of α′ directly from austenite would be much more difficult, requiring higher driving forces (more deformation, lower temperatures) or a different crystallographic mechanism, thus affecting the efficiency of α′ formation and subsequently the hardening rate.

The formation of ε-martensite itself induces local stresses and lattice distortions, which contribute to the overall work hardening [27].

The transformation from ε to α′ involves additional lattice shear and rearrangements. This dynamic process during deformation continuously introduces new defects (dislocations, boundaries) and refines the microstructure, further increasing the steel's resistance to plastic flow. This "dynamic" aspect of transformation is key to the TRIP effect.

We studied the influence of temperature and the degree of deformation on hardening based on the results of Vickers hardness measurements (Figure 12) and the fractions of

α′ martensite. We did not consider the fraction of ε martensite in this analysis. Since there is significantly less ε martensite than α′ martensite in the microstructure, only small deviations are expected. First, we converted the engineering strains (e) into true strains (ε) using Equation (4).

$$\varepsilon = \ln(1 + e) \tag{4}$$

The rate of α′ martensite formation was calculated according to Equation (5).

$$\text{Rate of } \alpha' \text{ martensite formation} = \frac{(f_{\alpha'_1} - f_{\alpha'_0})}{\varepsilon} \tag{5}$$

where $f_{\alpha'_1}$ represents the fraction of α′ martensite at a given deformation, and $f_{\alpha'_0}$ represents the fraction of α′ martensite at the previous deformation.

The difference in hardness was calculated according to Equation (6):

$$\Delta H = H_1 - H_0 \tag{6}$$

where H_1 represents the hardness at the given deformation and H_0 represents the hardness at the previous deformation.

The fraction of α′ martensite increases with increasing deformation, and a decreasing deformation temperature can be observed from diagrams in Figure 14a,c,e. Consequently, as the fraction of α′ martensite increases, the hardness also increases. This increase in the α′ martensite fraction is more rapid at lower temperatures, reaching higher overall values. Correspondingly, with the increasing fraction of α′ martensite, the hardness increases rapidly at lower deformations. At higher deformations, the rate of increase in the α′ martensite fraction slows, and the hardening effect also diminishes. The diagrams in Figure 14a,c show that hardness increased with deformation even before the formation of α′ martensite in the microstructure. This initial increase in hardness can be attributed to the strain hardening of the steel, resulting from the increased dislocation density and consequently shorter free slip paths. The effect of strain hardening is more pronounced at lower temperatures (Figure 14e), where the lower stacking fault energy leads to an increased decomposition of perfect dislocations into Shockley partial dislocations with limited mobility. Figure 14f illustrates that after most of the austenite has transformed into α′ martensite, the hardness increases minimally.

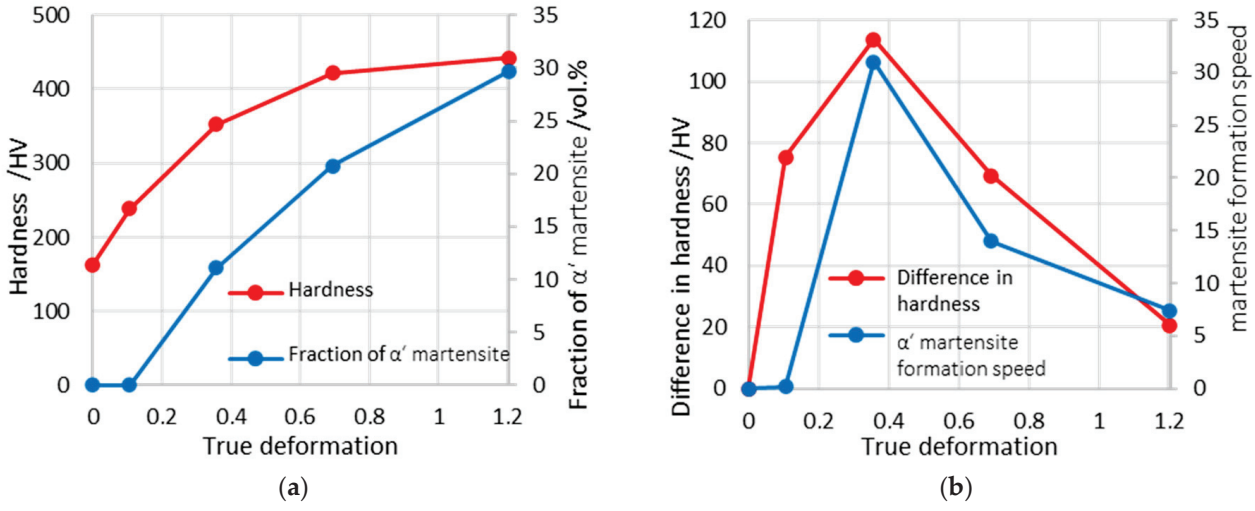

Figure 14. *Cont.*

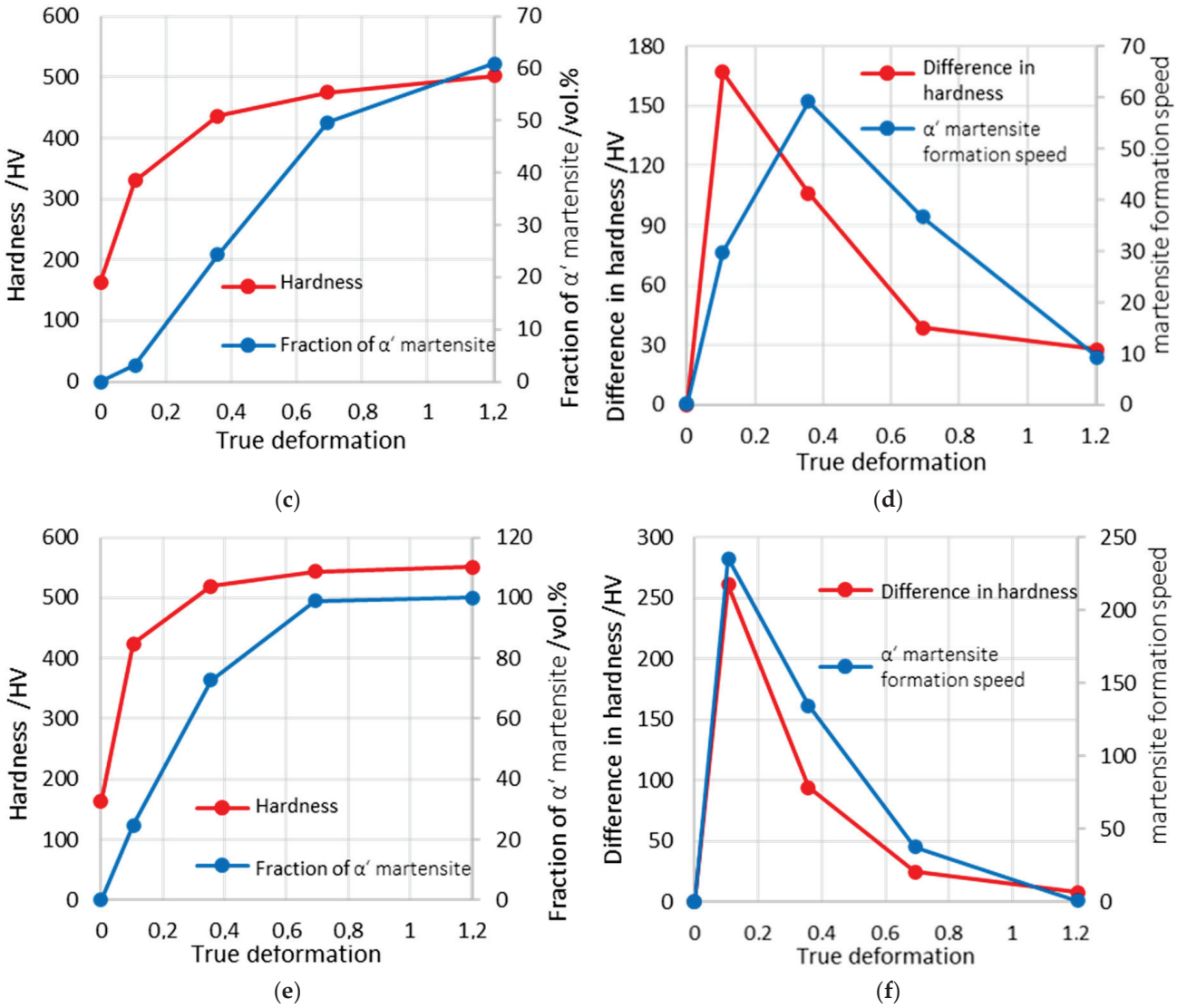

Figure 14. Diagrams of hardness and α′ martensite fractions (**a**) 20 °C, (**c**) 0 °C, (**e**) −196 °C at different true deformations. Diagrams of difference in hardness and martensite formation rate (**b**) 20 °C, (**d**) 0 °C, (**f**) −196 °C at different true deformations.

At low deformations, both the difference in hardness and the rate of α′ martensite formation increase, as presented by the diagrams in Figure 14b,d,f. They reach a maximum at a certain deformation level, after which both values decrease with further deformation. In Figure 14b,f, the curve representing the hardness difference closely follows the curve representing the rate of α′ martensite formation. Following the maximum, which occurs at approximately the same deformation, the rate of α′ martensite formation decreases, and the hardening effect also diminishes. This decrease in rate occurs as the fraction of α′ martensite in the steel increases. The closer we are to the maximum fraction of α′ martensite at a given deformation temperature, the lower the rate of α′ martensite formation. In Figure 14d, a slight shift is observed between the maximums of the hardness difference and the rate of α′ martensite formation, indicating that hardness increased more rapidly at lower deformations. This rapid increase in hardness at low deformations is attributed to the strain hardening of the steel.

The martensite formation rates are the greatest at cryogenic temperatures, where they reach peak rates at 0.1 true deformation, while 20 and 0 °C peak at around 0.3 true deformation, as seen in Figure 15.

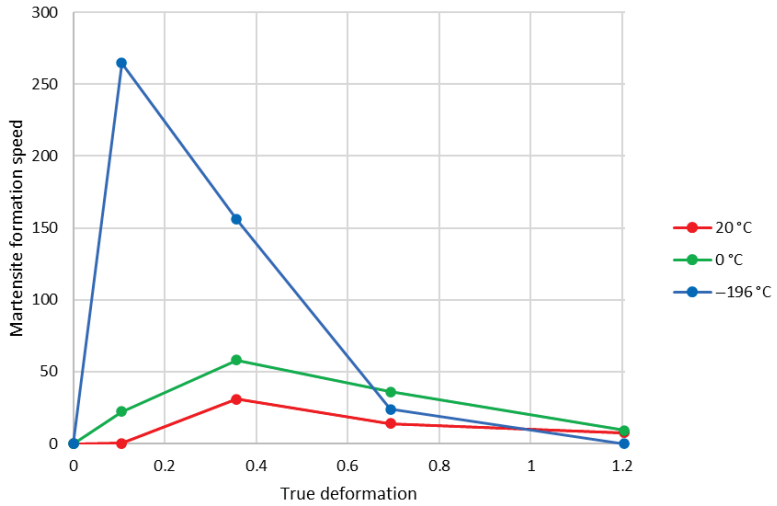

Figure 15. Martensite formation rate at different true deformations for 20, 0, and −196 °C.

Therefore, the $\gamma \rightarrow \varepsilon \rightarrow \alpha'$ sequence is not merely a crystallographic pathway but a critical aspect of the mechanical response and hardening mechanism in AISI 304. The formation of ε martensite from stacking faults, while itself contributing to initial hardening, primarily serves as a high-density nucleation platform for the significantly harder α' martensite.

Furthermore, the increased ease of ε formation and its rapid subsequent transformation to α' at lower temperatures explain the dramatically higher rates of α' formation and corresponding hardness increases observed, particularly at −196 °C.

Beyond the strain hardening of austenite, the continuous formation of ε martensite and its subsequent transformation to α' martensite during deformation provides a robust, dynamic hardening mechanism. The lattice strains and defect generation associated with the $\varepsilon \rightarrow \alpha'$ transformation contribute significantly to the observed increase in hardness, enhancing the TRIP effect by continually presenting new obstacles to dislocation motion.

While α' martensite is the principal hard phase, the efficiency of its nucleation via the ε intermediate phase dictates the overall rate and extent of hardening. The observed rapid increase in hardness at cryogenic temperatures is a direct consequence of the accelerated ε formation and its efficient conversion to α' under these conditions.

Additionally, the calculated SFE of 25.9 mJ/m^2 indeed favors the $\gamma \rightarrow \varepsilon \rightarrow \alpha'$ transformation pathway. This implies that the presence of ε martensite is a prerequisite for a more pronounced α' formation in this steel, directly influencing its mechanical behavior. Thus, the SFE not only dictates the pathway but also the potential for strain-induced hardening through this specific two-step transformation.

5. Conclusions

This study effectively demonstrates the significant influence of cold rolling temperature and deformation degree on the mechanically induced martensitic transformation in AISI 304 stainless steel.

Upon deformation, shear bands form, increasing with strain. These bands, particularly their intersections, act as nucleation sites for martensite. Martensite (both ε and α′) forms at lower deformation levels with decreasing temperature (e.g., at 10% deformation at 0 °C and −196 °C, versus 30% at 20 °C).

The deformation-induced transformation primarily follows the $\gamma \rightarrow \varepsilon \rightarrow \alpha'$ pathway. Lower temperatures and higher deformation degrees accelerate the formation and increase the fraction of both ε and α′ martensite, with α′ martensite showing a more rapid increase.

Critically, hardness directly correlates with martensite content. Initial hardening at lower deformations is due to strain hardening. However, as martensite forms, it becomes the dominant hardening mechanism. The highest hardness (551 HV) was achieved at −196 °C and 70% deformation, where martensite formation was maximized. The rate of martensite formation significantly influences the hardening effect, with faster transformation leading to greater hardness increases.

Author Contributions: Conceptualization, J.B. and A.N.; methodology, J.L., B.Š.B. and A.N.; validation, J.B., B.Š.B. and A.N.; formal analysis, J.L. and B.Š.B.; investigation, J.L. and B.Š.B.; resources, J.B.; data curation, J.B. and B.Š.B.; writing—original draft preparation, J.B. writing—review and editing, J.B., B.Š.B. and A.N.; visualization, J.B. and J.L.; supervision, J.B. and A.N. All authors have read and agreed to the published version of the manuscript.

Funding: Funding was provided by the Slovenian Research Agency ARRS program P2-0050 (C).

Data Availability Statement: The original contributions presented in the study are included in the article; further inquiries can be directed to the corresponding author.

Conflicts of Interest: Author Jernej Lindič was employed by the company SIJ Acroni d.o.o. The remaining authors declare that the research was conducted in the absence of any commercial or financial relationships that could be construed as a potential conflict.

References

1. De Cooman, B.C.; Speer, J.G. *Fundamentals of Steel Product Physical Metallurgy*; AIST, Association for Iron & Steel Technology: Warrendale, PA, USA, 2011.
2. Chakraborty, A.; Singh, J.K.; Sen, D.; Pityana, S.; Manna, I.; Krishna, S.; Dutta Majumdar, J. Microstructures, Wear and Corrosion Resistance of Laser Composite Surfaced Austenitic Stainless Steel (AISI 304 SS) with Tungsten Carbide. *Opt. Laser Technol.* **2021**, *134*, 106585. [CrossRef]
3. Desu, R.K.; Nitin Krishnamurthy, H.; Balu, A.; Gupta, A.K.; Singh, S.K. Mechanical Properties of Austenitic Stainless Steel 304L and 316L at Elevated Temperatures. *J. Mater. Res. Technol.* **2016**, *5*, 13–20. [CrossRef]
4. Cui, C.Y.; Cui, X.G.; Zhang, Y.K.; Zhao, Q.; Lu, J.Z.; Hu, J.D.; Wang, Y.M. Microstructure and Corrosion Behavior of the AISI 304 Stainless Steel after Nd:YAG Pulsed Laser Surface Melting. *Surf. Coat. Technol.* **2011**, *206*, 1146–1154. [CrossRef]
5. Milad, M.; Zreiba, N.; Elhalouani, F.; Baradai, C. The Effect of Cold Work on Structure and Properties of AISI 304 Stainless Steel. *J. Mater. Process. Technol.* **2008**, *203*, 80–85. [CrossRef]
6. Zhang, X.; Xiao, Y.; Cai, Y. Effect of Ni Element on Microstructure and Properties of Cold-Rolled 316 L Austenitic Stainless Steel. *Mater. Res. Express* **2024**, *11*, 036521. [CrossRef]
7. Gilapa, L.C.M.; de Oliveira, C.A.S.; da Silva, M.R. Effect of Copper on the Formation of Strain-Induced Martensite in Two Austenitic Stainless Steels AISI 304. *Mater. Sci. Eng. A* **2015**, *622*, 212–218. [CrossRef]
8. Solomon, N.; Solomon, I. Deformation Induced Martensite in AISI 316 Stainless Steel. *Rev. Metal.* **2010**, *46*, 121–128. [CrossRef]
9. Sohrabi, M.J.; Naghizadeh, M.; Mirzadeh, H. Deformation-Induced Martensite in Austenitic Stainless Steels: A Review. *Arch. Civ. Mech. Eng.* **2020**, *20*, 124. [CrossRef]
10. Denkena, B.; Breidenstein, B.; Dittrich, M.-A.; Wichmann, M.; Nguyen, H.N.; Fricke, L.V.; Zaremba, D.; Barton, S. Setting of Deformation-Induced Martensite Content in Cryogenic External Longitudinal Turning. *Procedia CIRP* **2022**, *108*, 170–175. [CrossRef]
11. Pun, L.; Soares, G.C.; Isakov, M.; Hokka, M. Effects of Strain Rate on Strain-Induced Martensite Nucleation and Growth in 301LN Metastable Austenitic Steel. *Mater. Sci. Eng. A* **2022**, *831*, 142218. [CrossRef]
12. Das, A.; Tarafder, S. Experimental Investigation on Martensitic Transformation and Fracture Morphologies of Austenitic Stainless Steel. *Int. J. Plast.* **2009**, *25*, 2222–2247. [CrossRef]
13. Lecroisey, F.; Pineau, A. Martensitic Transformations Induced by Plastic Deformation in the Fe-Ni-Cr-C System. *Metall. Trans.* **1972**, *3*, 391–400. [CrossRef]
14. Das, A.; Sivaprasad, S.; Ghosh, M.; Chakraborti, P.C.; Tarafder, S. Morphologies and Characteristics of Deformation Induced Martensite during Tensile Deformation of 304 LN Stainless Steel. *Mater. Sci. Eng. A* **2008**, *486*, 283–286. [CrossRef]
15. Choi, J.Y.; Jin, W. Strain Induced Martensite Formation and Its Effect on Strain Hardening Behavior in the Cold Drawn 304 Austenitic Stainless Steels. *Scr. Mater.* **1997**, *36*, 99–104. [CrossRef]
16. Shen, Y.F.; Li, X.X.; Sun, X.; Wang, Y.D.; Zuo, L. Twinning and Martensite in a 304 Austenitic Stainless Steel. *Mater. Sci. Eng. A* **2012**, *552*, 514–522. [CrossRef]

17. Olson, G.B.; Cohen, M. Kinetics of Strain-Induced Martensitic Nucleation. *Metall. Trans. A* **1975**, *6*, 791–795. [CrossRef]
18. Talonen, J.; Hänninen, H. Formation of Shear Bands and Strain-Induced Martensite during Plastic Deformation of Metastable Austenitic Stainless Steels. *Acta Mater.* **2007**, *55*, 6108–6118. [CrossRef]
19. Yang, H.; Liu, Y. Factors Influencing the Stress-Induced Fcc ↔ Hcp Martensitic Transformation in Co-32Ni Single Crystal. *Acta Mater.* **2006**, *54*, 4895–4904. [CrossRef]
20. Alves, J.M.; Brandão, L.P.; Dos Santos Paula, A. Mechanically Induced Martensitic Transformation of Hot Rolled and Annealed 304L Austenitic Stainless Steel at Room and Cryogenic Temperatures. *Mater. Res.* **2019**, *22*, e20190150. [CrossRef]
21. Yang, H.; Zhang, J.H.; Xu, Y.; Meyers, M.A. Microstructural Characterization of the Shear Bands in Fe-Cr-Ni Single Crystal by EBSD. *J. Mater. Sci. Technol.* **2008**, *24*, 819–828.
22. Dai, Q.-X.; Wang, A.-D.; Cheng, X.-N.; Luo, X.-M. Stacking Fault Energy of Cryogenic Austenitic Steels. *Chin. Phys.* **2002**, *11*, 596. [CrossRef]
23. Weiß, A.; Gutte, H.; Scheller, P.R. Deformation Induced Martensite Formation and Its Effect on Transformation Induced Plasticity (TRIP). *Steel Res. Int.* **2006**, *77*, 727–732. [CrossRef]
24. Kowalska, J.; Witkowska, M. The Influence of Cold Deformation and Annealing on Texture Changes in Austenitic Stainless Steel. *Adv. Sci. Technol. Res. J.* **2024**, *18*, 143–158. [CrossRef] [PubMed]
25. De, A.K.; Speer, J.G. Deformation-Induced Phase Transformation and Strain Hardening in Type 304 Austenitic Stainless Steel. *Metall. Mater. Trans. A* **2005**, *37A*, 1875–1886. [CrossRef]
26. He, C.; Zhu, X.; Hu, C.; Dong, H.; Wan, X.; Liu, E.; Li, G.; Wu, K. Processing an 18Cr-8Ni Austenitic Stainless Steel Without the Dilemma of the Strength and Ductility Trade-Off. *JOM* **2024**, *76*, 829–842. [CrossRef]
27. Bachani, M.; Hayoune, A.; Fajoui, J.; Dubos, P.-A. Phase Transformations in Cold-Rolled 304L Stainless Steel by Dilatometry. *Bull. Mater. Sci.* **2024**, *47*, 64. [CrossRef]

crystals

MDPI

Article

Analysis of Inclusions in the Entire Smelting Process of High-Grade Rare Earth Non-Oriented Silicon Steel

Liqiang Xue [1,2,†], Xiangyu Li [1,†], Tao Wang [1,3], Qi Zhao [1], Haozheng Wang [1], Jia Wang [4], Wanming Lin [1], Xiaofeng Niu [1], Wangzhong Mu [5,6] and Chao Chen [1,*]

[1] College of Materials Science and Engineering, Taiyuan University of Technology, Taiyuan 030024, China; xueliqiang421@sina.com (L.X.); 2023520466@link.tyut.edu.cn (X.L.); wangtao0314@link.tyut.edu.cn (T.W.); zhaoqi0825@link.tyut.edu.cn (Q.Z.); 15135730921@163.com (H.W.)
[2] No. 2 Steelmaking Plant, Shanxi Taigang Stainless Steel Co., Ltd., Taiyuan 030030, China
[3] Key Laboratory of Electromagnetic Processing of Materials (Ministry of Education), Northeastern University, Shenyang 110819, China
[4] College of Architecture and Arts, Taiyuan University of Technology, Taiyuan 030024, China
[5] Department of Materials Science and Engineering, KTH Royal Institute of Technology, SE-100 44 Stockholm, Sweden
[6] Engineering Materials, Department of Engineering Science and Mathematics, Luleå University of Technology, SE-971 87 Luleå, Sweden
* Correspondence: chenchao@tyut.edu.cn
† These authors contributed equally to this work.

Abstract: Rare earth can modify inclusions in non-oriented silicon steel which is harmful to magnetic properties. This study focused on the 3.1% Si non-oriented silicon steel under industrial production conditions. Samples were taken during the stages before and after addition of rare earth ferrosilicon alloy in Ruhrstahl-Heraeus (RH) unit, different pouring time in tundish, and continuous casting slab. This study systematically examined the morphology, composition, and size distribution of inclusions throughout the smelting process of non-oriented silicon steel by scanning electron microscopy with energy-dispersive spectroscopy (SEM/EDS), and thermodynamic analysis at liquid steel temperature and thermodynamic analysis of equilibrium solidification. The research results demonstrated that the rare earth treatment ultimately modifies the original Al_2O_3 inclusions in the non-oriented silicon steel into $REAlO_3$ and RE_2O_2S inclusions, while also aggregating AlN inclusions to form composite inclusions. After rare earth modification, the average size of the inclusions decreases. In the RH treatment process, the inclusions before the addition of rare earth ferrosilicon alloy are mainly AlN and Al_2O_3. After the addition of rare earth ferrosilicon alloy, the inclusions are mainly RES and $REAlO_3$. In the tundish and continuous casting, the rare earth content decreased, and the rare earth inclusions transform into RE_2O_2S and $REAlO_3$. For the size of inclusions, after adding rare earth ferrosilicon alloy, the average size of inclusions rapidly decreased from 16.15 μm to 2.65 μm and reach its minimum size 2.16 μm at the end of RH treatment. When the molten steel entered the tundish, the average size of inclusions increased slightly and gradually decreased with the progress of pouring. The average size of inclusions in the slab is 5.79 μm. Phase stability diagram calculation indicates the most stable rare earth inclusion is Ce_2O_2S in molten steel. Thermodynamic calculations indicated that Al_2O_3, Ce_2O_2S, Ce_2S_3, AlN, and MnS precipitate sequentially during the equilibrium solidification process of molten steel.

Keywords: non-oriented silicon steel; rare earth inclusions; thermodynamic calculation

1. Introduction

With the continuous advancement of electric vehicle (EV) technology [1–3], in China, EV sales are projected to increase six to eight times in 2025 compared to 13.10 million in 2022 [2]. The policies [3] and willingness of customers [1] made this happen. One of the important components in sustainable new energy EVs is the drive motors. And the non-oriented silicon steel is widely used in those drive motors. Besides, the silicon steel has been widely used in household appliances (such as air conditioners, refrigerator compressors), industrial motors, power transmission and transformation equipment. Therefore, the performance of silicon steel directly determines the efficiency and quality of products [4–7]. Inclusions in non-oriented silicon steel inhibit grain growth by pinning grain boundaries, resulting in fine grain size of the finished product, and also hinder the rotation of magnetic domains and increase hysteresis loss [8,9]. Therefore, inclusions in silicon steel can deteriorate magnetic properties, the cleanliness of steel should be improved as far as possible and the harm of inclusions should be reduced. At present, the inclusions control methods include vacuum refining [10–13], calcium treatment, rare earth treatment [14–16] and so on.

The current production process of cold-rolled non-oriented silicon steel is basically as follows [15,17,18]: blast furnace → pretreatment → converter steelmaking → Ruhrstahl-Heraeus (RH) vacuum degassing → tundish → continuous casting. Deoxygenation and desulfurization are carried out in the vacuum refining stage, and ferroalloy are added to control components. During the production process, various factors may introduce impurities into the molten steel and form inclusions [19–21]. In the vacuum refining, during deoxidation and alloying, deoxidizers and alloys react with dissolved oxygen in the molten steel to generate a large amount of oxide inclusions. The inclusions in the vacuum refining are mainly Al_2O_3 produced by aluminum deoxidation, SiO_2 and MnO inclusions appear during the alloying process [22,23]. When the molten steel enters the tundish, it undergoes secondary oxidation due to contact with air, resulting in an increase in oxide inclusions in the molten steel and an increase in the size of the inclusions [24]. During the continuous casting, with the temperature gradually decreases, the solubility of nitrogen and sulfur elements in the molten steel decreases, and they precipitate in the form of nitrides (AlN) and sulfides (MnS, CuS) [25], further increasing the number of inclusions in the slab. Through experiments and thermodynamic calculations, a large number of studies have shown that AlN and MnS inclusions not precipitate in the molten steel. These inclusions only precipitate when the temperature is below the solidification point [26–28]. Moreover, these nitrides and sulfides are mostly fine inclusions smaller than one micron, which pose the greatest threat to the magnetic properties of non-oriented silicon steel [29,30]. In addition to the above mentioned methods of introducing inclusions, slag entrapment in molten steel and the detachment of refractory materials will also introduce inclusions into the molten steel [31].

Rare earth elements have more active chemical properties due to their unique outer electronic structure. By adding rare earths to the molten steel, both deoxidation, desulfurization, and modification of inclusions can be achieved simultaneously. On the one hand, rare earth elements have a stronger binding ability with oxygen and sulfur. By generating high melting point rare earth inclusions, rare earths can play a role in deoxidation and desulfurization. Numerous studies have shown that the addition of rare earth elements significantly reduces the oxygen and sulfur content of molten steel [32,33]; On the other hand, rare earths can modify oxide inclusions into rare earth inclusions [34–39]. Rare earths transform irregularly shaped inclusions into spherical or nearly spherical rare earth inclusions [40–45]. Japanese steel companies such as Kawasaki Steel and Nippon Steel have conducted research on adding rare earth to silicon steel production and developed the JNA series silicon steel [46–48]. In current research, researchers have found that after

adding rare earths to silicon steel, not only can the inclusions be modified [49–51], but the microstructure of the silicon steel can also be improved [52–55], and the magnetic properties of the silicon steel can be enhanced [56,57]. Ren et al. [15] found that high-grade non oriented silicon steel with 3% Si-0.5% Al after adding Ce-Mg-Si alloy, the rare earth content in the sample gradually decreased as the smelting process progressed, and the rare earth inclusions changed from Ce_2O_2S to $CeAlO_3$ and Ce_2O_2S. And there is relatively little research on the changes in inclusions throughout the entire production process of non-oriented silicon steel after rare earth treatment. Ren et al. [15], Wang et al. [18], and Wang et al. [58] reported different types of rare earth inclusions after rare earth treatment of non-oriented silicon steel in industrial production. However, in the industrial production of non-oriented silicon steel, the stable application of rare earth elements faces challenges such as unstable yield rates and poor production continuity. When the rare earth addition amount enables stable production, there remains a lack of relevant research on the types and evolution of inclusions in each processing stage. Therefore, this article systematically investigates the evolution patterns of inclusions at each processing stage during stable production with rare earth ferrosilicon alloy addition, through comprehensive analysis of specimens collected throughout the entire smelting process of non-oriented silicon steel, thereby providing a theoretical foundation for the practical industrial application of rare earth elements in non-oriented silicon steel production.

2. Materials and Methods

The production process of non-oriented silicon steel 23W1700 in a steelmaking plant is as follows: 80 tons of BOF steelmaking → 80 tons of Ruhrstahl-Heraeus (RH) vacuum refining → tundish → continuous casting. The converter adopts boiling steelmaking, and the molten steel is transported to the vacuum refining(RH) for deep decarburization. The RH unit operation is crucial for the steelmaking of the silicon steel [10,12]. In RH operation, aluminum pellets with an aluminum content of 99.99% are added to the molten steel for deoxidation. After deoxidation, ferrosilicon alloy and ferromanganese alloy are added to adjust the composition of the molten steel. Thereafter the rare earth ferrosilicon alloy are added. The composition of the rare earth ferrosilicon alloy used is as follows: Ce + La: 25 wt%, Si: 43–46 wt%, Fe: 20 wt% [49]. Finally, the CaO-CaF_2 desulfurizer was added to achieve deep desulfurization. Before the finishing of RH treatment, the temperature of the molten steel is 1585 °C. The temperature of the molten steel in the tundish decreases slightly to 1548 °C. The liquid stream is protected by a ladle shroud. The tudnish flux is CaO-SiO_2 based with a small content of MgO and Al_2O_3. When molten steel is transferred from the tundish to the mold, the molten steel stream is protected by the submerged entry nozzle. The mold powder is SiO_2-CaO-Al_2O_3-Na_2O-Li_2O-MgO based system. The dimensions of the slab are 1160 mm in width and 220 mm in thickness. The casting speed is 0.65 m/min.

The sampling procedure is shown in Figure 1. The composition of molten steel is shown in Table 1. A detailed sampling schedule was made in the RH unit during operation stages. Those stages are (1) after adding aluminum, (2) after adding ferrosilicon and ferromanganese alloy (before addition of rare earth alloy), (3) after adding rare earth ferrosilicon alloy and (4) after adding desulfurizer. Samples were taken at the different time during tundish pouring, e.g., 10, 25 min and the end of pouring. The sampling method for the RH and tundish samples are as follows: a sampling gun with a barrel sampler attached to one end is inserted into the molten steel. And the barrel samplers are water quenched. The solidified silicon steel samples were extracted from the barrel samplers. Finally samples were cut directly from the inner surface at 1/4 and 1/2 of the width direction of the slab. All the samples are cut into 10 mm cubic specimens. The specimens surface were sequentially

ground with 60–2000 grit SiC abrasive paper, followed by polishing with a polishing machine to prepare metallographic samples for inclusion observation.

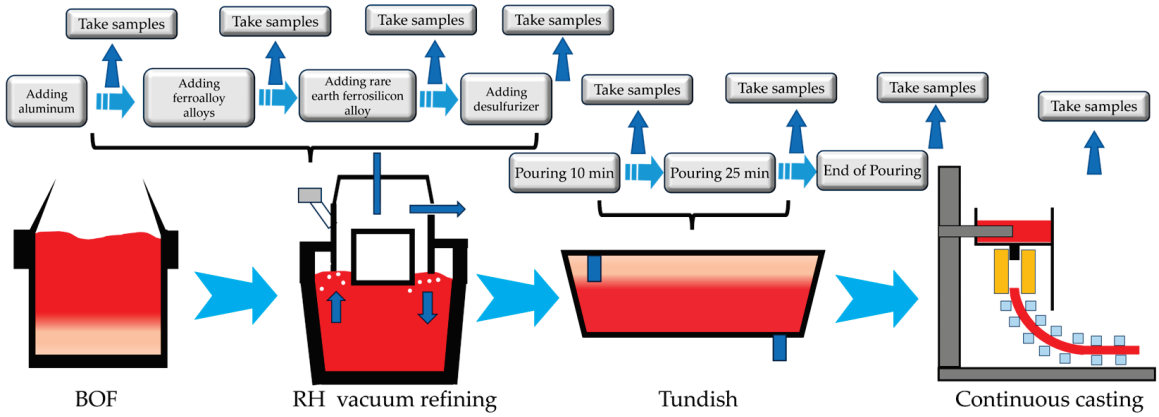

Figure 1. Schematic diagram of sampling process.

Table 1. Composition of molten steel.

Element	C	Si	Mn	P	S	Al	O	Ce	La	N	Cr
RH	0.0032	3.144	0.281	0.0128	0.0021	0.8797	0.0025	0.0047	0.0022	0.0016	0.0147
Tundish	0.0029	3.114	0.281	0.0125	0.0013	0.8644	0.0007	0.0011	0.0005	0.0016	0.0147

In this experiment, scanning electron microscopy (JSM-IT500) was used to analyze the component and size of inclusions. Multiple fields of view were selected for each sample to observe inclusions. The average size was calculated after measuring the size of inclusions. Based on the EDS scanning results, the composition and element distribution of inclusions were determined. The proportion of each element in the inclusions was analyzed through point scanning results, and the component content of inclusions is calculated through atomic pairing to obtain the specific composition of each composite inclusion.

The phase stability zone diagram of rare earth inclusions was mapped by Wagner model. The thermodynamic calculation software Thermo-calc (version 2024b) along with the iron-based database TCFE12 was used to calculate the precipitation of inclusions during solidification of molten steel.

3. Results and Discussion

This section is arranged as follows: the inclusions evoluations in the RH process, tundish, and slab via SEM/EDS technique are analysized in Sections 3.1–3.3 , respectively. A summary of the inclusions type/morphologies and size distribution are presented in Sections 3.4 and 3.5, respectively. Thermodynamic calculation on the inclusions formation is presented in Section 3.6. And finally is the Section 3.7.

3.1. Analysis of Inclusions in the RH Process

Figures 2 and 3 show typical inclusions after adding Al in the RH, with Al_2O_3 and composite inclusions of different shapes being the main inclusions. Figure 2b shows Al_2O_3·CaO composite inclusion with a size of around 50 μm, which Al_2O_3 accounts for about 80–90% and the remaining composition is CaO. It can be concluded from the results of SEM that in the Al_2O_3·CaO composite inclusion, the mass fraction of CaO at the edge of inclusion is 20%, and the mass fraction inside the inclusion is 10%. This phenomenon indicates that Al reacts with O in the molten steel to form Al_2O_3 after adding Al, then Al_2O_3 inclusions continuously aggregate to form lager-sized inclusions. At the same time, Al_2O_3 inclusions also aggregate with CaO in the molten steel to form large inclusions.

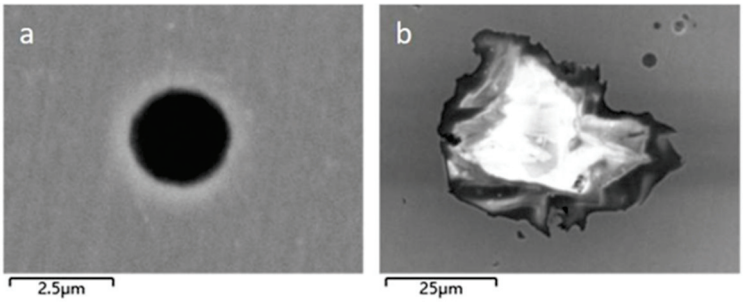

Figure 2. Typical inclusion after adding Al: (**a**) Al_2O_3; (**b**) Al_2O_3·CaO.

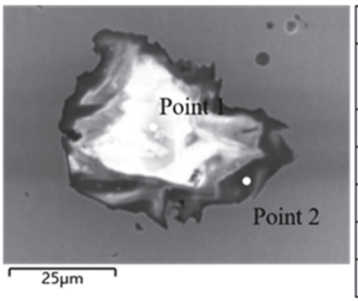

Point 1		Point 2	
Element	Mass percentage	Element	Mass percentage
Al	57.2	Al	50.1
O	34.8	O	30.7
Ca	7.1	Ca	17.8
Mg	0.8	Mg	0.9
S	0.1	S	0.4

Figure 3. Point scanning results of Al_2O_3·CaO inclusion.

Figures 4 and 5 show typical inclusions before adding rare earth ferrosilicon alloy in the RH process. The inclusions are mainly Al_2O_3 inclusions with a size of about 2.5 μm and composite inclusions, Figure 4b shows a large-sized Al_2O_3 inclusion. From Figure 4, it can be seen that the inclusions are continuously agglomerated in the molten steel, large-sized inclusions are formed eventually. However, according to the analysis of the inclusions size change, the average size of inclusions in this stage is relatively small, so the removal effect of large-sized inclusions is better in this stage. Figure 5 shows Al_2O_3·CaS composite inclusion with a size of around 2.5 μm. According to EDS scanning analysis, the mass fraction of Al_2O_3 in Al_2O_3·CaS composite inclusion is around 70%, the mass fractiont of CaS is around 15%, the AlN is 10%, there is also a small fraction of MnS.

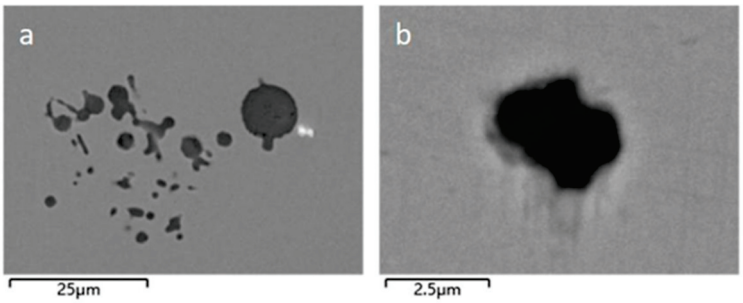

Figure 4. Typical inclusion before adding rare earth ferrosilicon alloy: (**a**) Al_2O_3; (**b**) Al_2O_3·CaS.

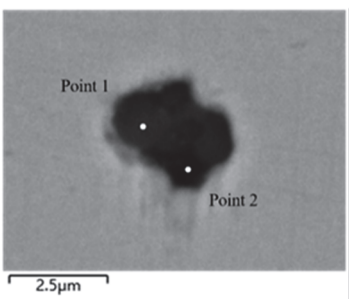

Point 1		Point 2	
Element	Mass percentage	Element	Mass percentage
Al	59.0	Al	69.3
S	12.6	O	10.7
O	12.0	S	8.4
N	7.5	Si	4.5
Mn	3.5	Ca	3.1
Ca	2.4	N	1.8
Si	2.0	Mn	1.4
Mg	0.9	Mg	0.8

Figure 5. Point scanning results of Al_2O_3·CaS inclusion.

Figures 6 and 7 show typical inclusions after adding rare earth ferrosilicon alloy in the RH process. The inclusions are mainly small-sized rare earth composite inclusions with a size of 2.5 μm, and only a small proportion of AlN inclusions are observed. Figure 7 shows rare earth composite inclusions, Figure 7a is Al_2O_3-MgS-$REAlO_3$ composite inclusion with the mass fraction of Al_2O_3 is 71%, the mass fraction of $REAlO_3$ is 23%, and a small portion of MgS. The EDS scanning results are shown in Figure 8. Figure 7b shows the AlN-MgS-RES composite inclusion, where the light part at the center of the inclusion is MgS-RES, and AlN is the dark part wrapping around the outside of MgS-RES. The surface scanning results are shown in Figure 9. Figure 7c shows the Al_2O_3-CaS-$REAlO_3$-RES composite inclusion. The dark part on the left is Al_2O_3-$REAlO_3$, the dark part on the right is CaS-RES, and the light part on the right is RES. The surface scanning results are shown in Figure 10. From Figures 6 and 7a, it can be seen that after adding rare earth ferrosilicon alloy, the polygonal AlN inclusions are modified into spherical composite inclusions, and the rare earth elements also play a role in aggregating inclusions.

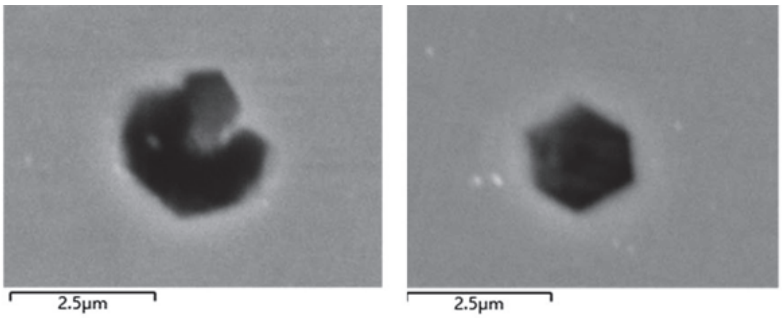

Figure 6. Typical AlN inclusions after adding rare earth ferrosilicon alloy.

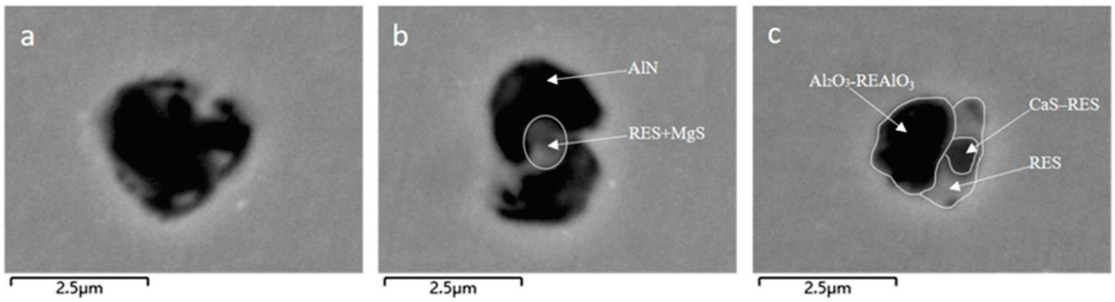

Figure 7. Typical rare earth composite inclusions after adding rare earth ferrosilicon alloy: (**a**) Al_2O_3-MgS-$REAlO_3$; (**b**) AlN-MgS-RES; (**c**) Al_2O_3-CaS-$REAlO_3$-RES.

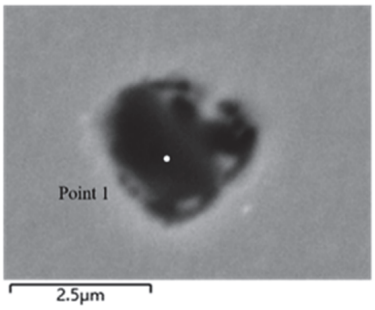

Point 1	
Element	Mass percentage
Al	43.3
O	29.5
Ce	14.1
La	3.8
Mg	2.7
S	2.6
Ca	2.1
Si	1.8

Figure 8. Point scanning results of Al_2O_3-MgS-$REAlO_3$ composite inclusions.

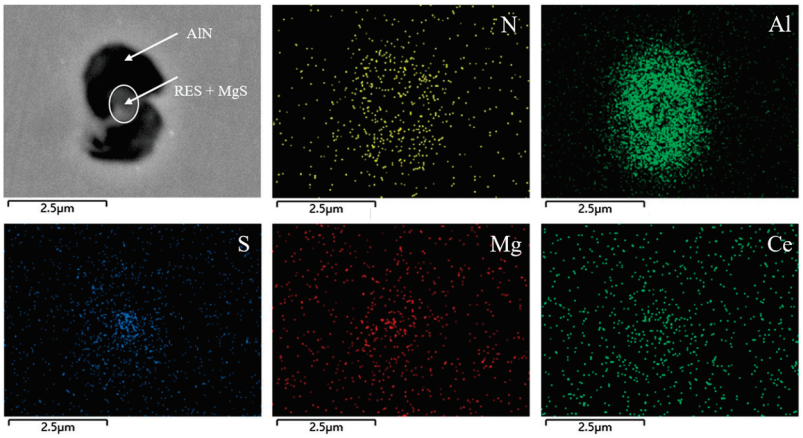

Figure 9. Surface scanning results of AlN-MgS-RES composite inclusions.

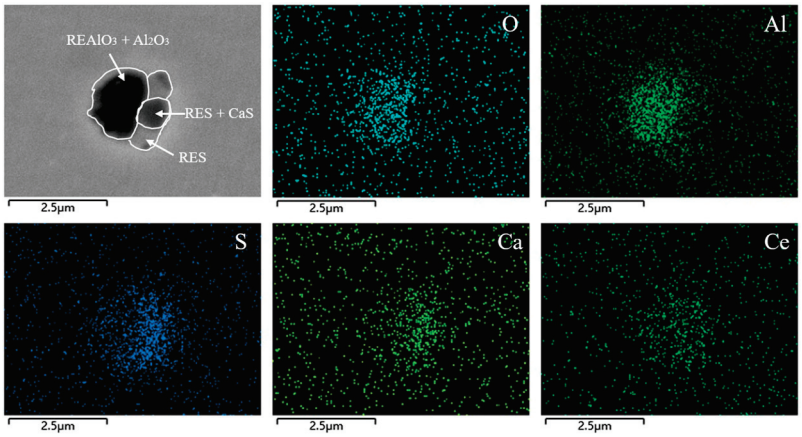

Figure 10. Surface scanning results of Al_2O_3-CaS-$REAlO_3$-RES composite inclusion.

Figure 11 shows the inclusions after adding desulfurizer. At this stage, the inclusions in molten steel are mainly small-sized rare earth composite inclusions with a size of 2.5 μm, and a small proportion of AlN, typical inclusions are shown in Figure 11a,b. Figure 11a shows single phase AlN inclusion, and Figure 11b shows AlN-RES composite inclusion, with the mass fraction of AlN is 80% and the mass fraction of RES is 20%. The EDS scanning results are shown in Figure 12. Figure 11c shows a large composite inclusion with a size of around 100 μm, where the central part is Al_2O_3, CaO, and $REAlO_3$, the outer edge is wrapped with a layer of CaS, and the EDS surface scanning results are shown in Figure 13.

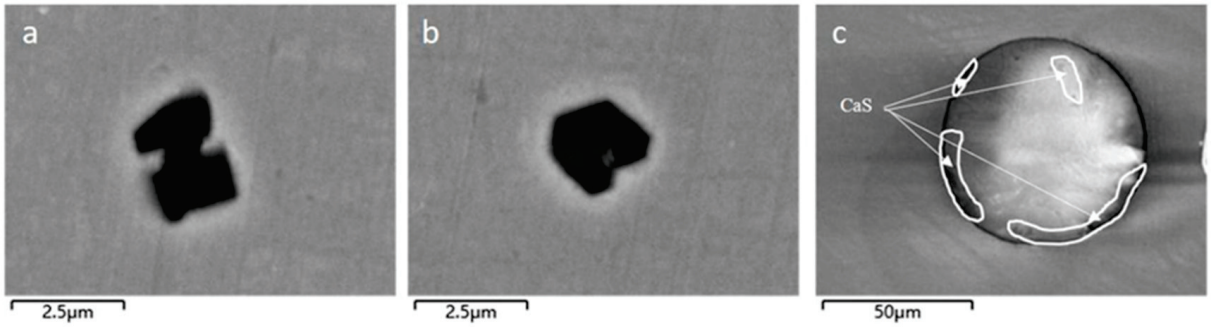

Figure 11. Typical inclusions after adding desulfurizer: (**a**) AlN; (**b**) AlN-RES; (**c**) Al_2O_3-CaO-CaS-$REAlO_3$.

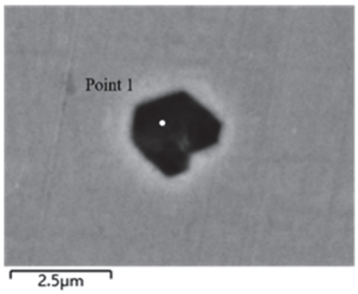

Point 1	
Element	Mass percentage
Al	59.0
N	12.6
Ce	12.0
La	7.5
S	3.5
Si	2.4
Ca	2.0
Mn	0.9

Figure 12. Point scanning results of AlN-RES composite inclusion.

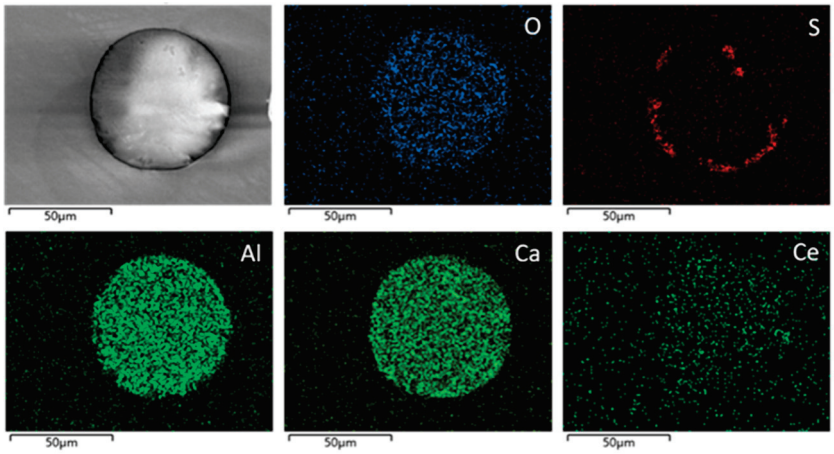

Figure 13. Surface scanning results of Al_2O_3-CaO-CaS-$REAlO_3$ composite inclusion.

3.2. Analysis of Inclusions in the Tundish

Figure 14 shows typical inclusions in the tundish after pouring 10 min. At this stage, the inclusions are mainly rare earth composite inclusions with a size of about 5 μm, and a small proportion of smaller single-phase AlN inclusions and single-phase MgS inclusions, as shown in Figure 14a,b. Figure 14c shows the AlN-CaS-RE_2O_2S composite inclusions. In the rare earth composite inclusions, the darkest parts is AlN, the darker part in the middle circular area is CaS, and the light part is RE_2O_2S. The EDS surface scanning results are shown in Figure 15. Multiple petal shaped composite inclusions are observed in the sample, with the central of these inclusions being RE_2O_2S and CaS or MgS, and AlN on the outer side. Figure 14d shows the Al_2O_3-MgO-AlN-$REAlO_3$ composite inclusion, with the light part on the right being $REAlO_3$, the dark part on the left being Al_2O_3·MgO, and the upper and lower dark parts of the inclusion being Al_2O_3·AlN. The EDS surface scanning results are shown in Figure 16.

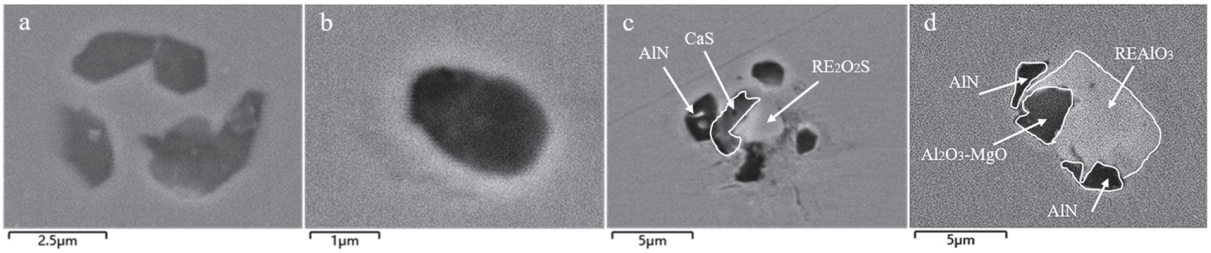

Figure 14. Typical inclusions in the tundish for pouring 10 min: (**a**) AlN; (**b**) MgS; (**c**) AlN-CaS-RE_2O_2S; (**d**) Al_2O_3-MgO-AlN-$REAlO_3$.

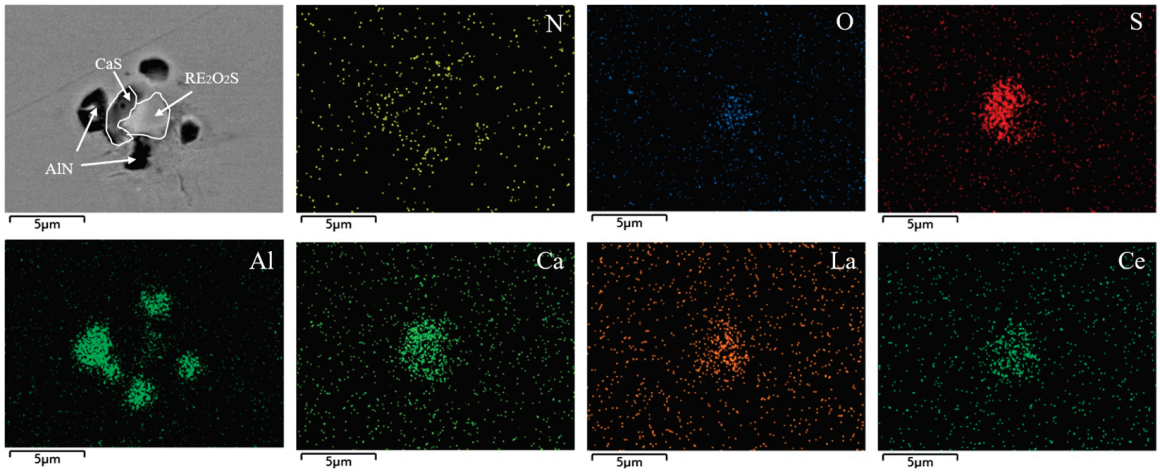

Figure 15. Surface scanning results of AlN-CaS-RE_2O_2S composite inclusion in tundish for pouring 10 min.

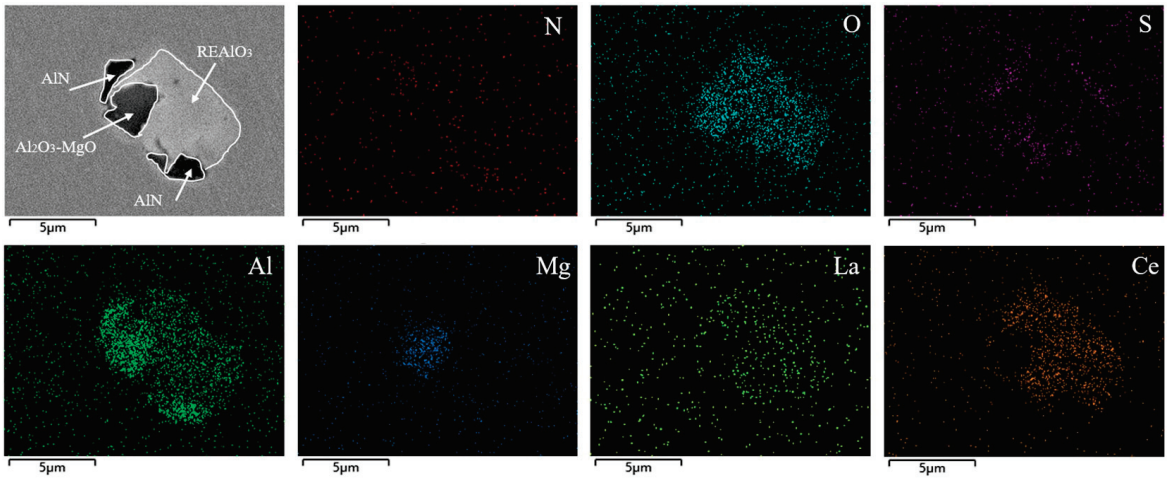

Figure 16. Surface scanning results of Al_2O_3-MgO-AlN-$REAlO_3$ composite inclusion in tundish for pouring 10 min.

Figure 17 shows typical inclusions in tundish after pouring 25 min. The single-phase inclusions in this stage are slightly larger in size than those in the previous stage. Figure 17a,b show single-phase AlN inclusions and single-phase MgS inclusions. Figure 17c shows a rare earth composite inclusion, with RE_2O_2S in the central light area and Al_2O_3-MgO-AlN in the outer dark area. The EDS surface scanning results are shown in Figure 18. According to the surface scanning results, the center of the inclusion is RE_2O_2S which wrapped with a layer of Al_2O_3·MgO, and the outermost layer is AlN. Most of the rare earth inclusions in this stage are RE_2O_2S, which are wrapped with Al_2O_3·MgO and AlN. Figure 17d shows the $REAlO_3$ composite inclusion, with the center being $REAlO_3$. Similar to other composite inclusions in this stage, the inclusion core is wrapped with Al_2O_3·MgO and AlN. The EDS surface scanning results are shown in Figure 19.

At the end of the tundish pouring, there are still small-sized single-phase inclusions, and inclusions are mainly rare earth composite inclusions, as shown in Figure 20. Figure 20a shows single-phase AlN inclusion; Figure 20b shows the composite inclusions MgS-RES-AlN-Al_2O_3. The central dark part is MgS-RES-Al_2O_3. The mass fraction of MgS is 60%, RES is around 25%, Al_2O_3 is around 15%, and the peripheral strip or block shaped inclusions are AlN. The EDS point scanning results are shown in Figure 21. Figure 20c shows a composite inclusion with $REAlO_3$ as the core and the left side of the central region being $REAlO_3$-Al_2O_3-MgO-CaS. The dark part at the edge are AlN inclusions. The EDS surface scanning

results are shown in Figure 22. Figure 20d shows a composite inclusion with RE_2O_2S as the core, Al_2O_3·MgO·CaS inclusion below the central region, and AlN inclusions at the edge of the composite inclusion. The EDS surface scanning results are shown in Figure 23.

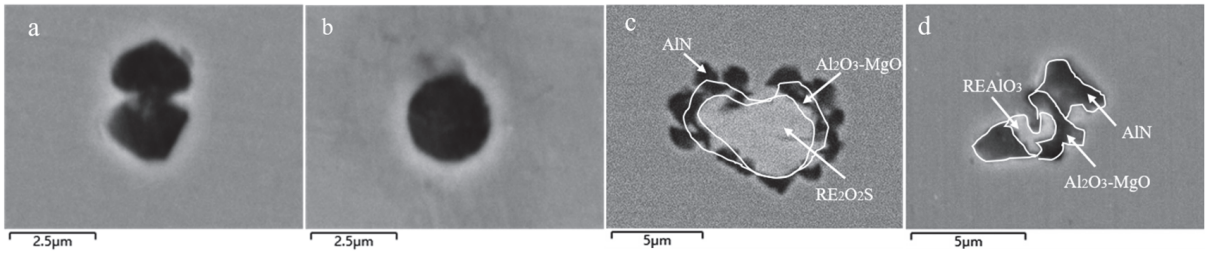

Figure 17. Typical inclusions in the tundish for pouring 25 min: (**a**) AlN; (**b**) MgS; (**c**) Al_2O_3-MgO-AlN-RE_2O_2S; (**d**) Al_2O_3-MgO-AlN-$REAlO_3$.

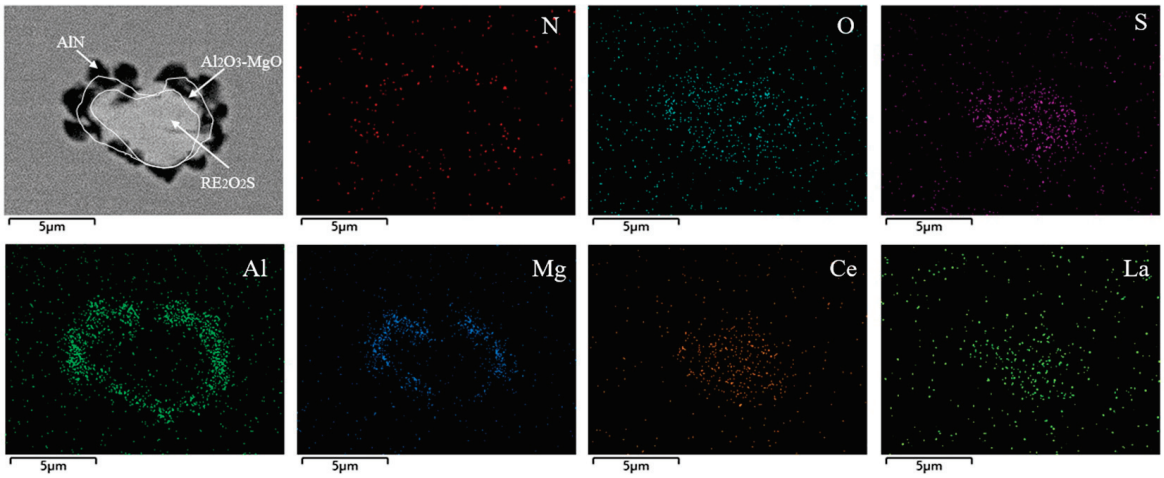

Figure 18. Surface scanning results of Al_2O_3-MgO-AlN-RE_2O_2S composite inclusion in the tundish for pouring 25 min .

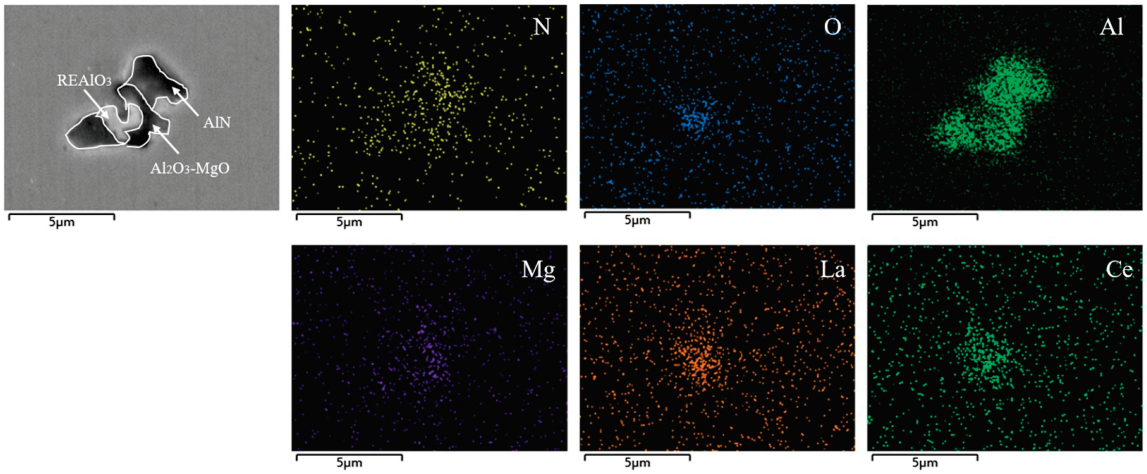

Figure 19. Surface scanning results of Al_2O_3-MgO-AlN-$REAlO_3$ composite inclusion in tundish for pouring 25 min.

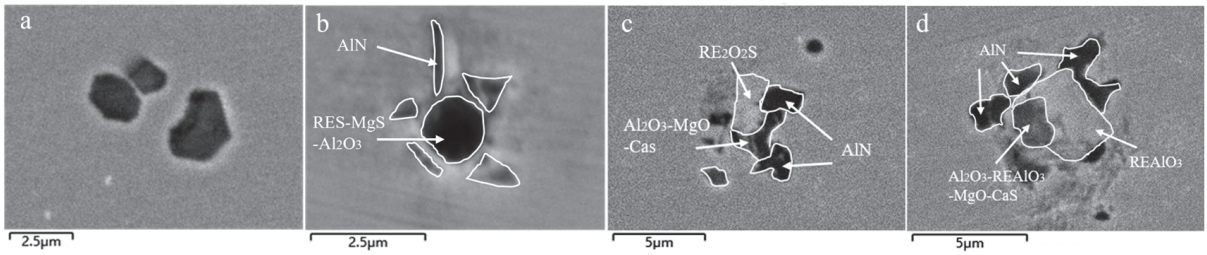

Figure 20. Typical rare earth composite inclusions at the end of tundish pouring: (**a**) AlN; (**b**) AlN-Al_2O_3-MgS-RES; (**c**) AlN-Al_2O_3-MgO-CaS-RE_2O_2S; (**d**) AlN-Al_2O_3-MgO-CaS-$REAlO_3$.

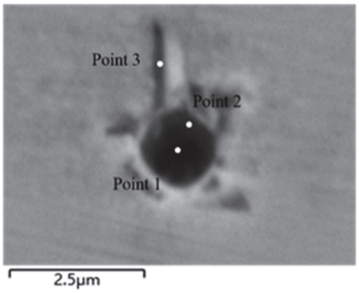

Point 1		Point 2		Point 3	
Element	Mass percentage	Element	Mass percentage	Element	Mass percentage
S	36.3	S	41.4	Al	48.3
Mg	22.1	Mg	23.9	N	29.0
Ce	18.2	Ce	14.3	Si	11.0
O	11.2	Al	8.1	Mn	3.7
Al	5.7	N	5.5	S	3.0
Si	2.8	O	2.9	Ce	2.5
N	2.0	Si	2.2	Mg	1.9
Ca	0.9	La	1.3	La	0.6

Figure 21. Point scanning results of AlN-Al_2O_3-MgS-RES composite inclusion.

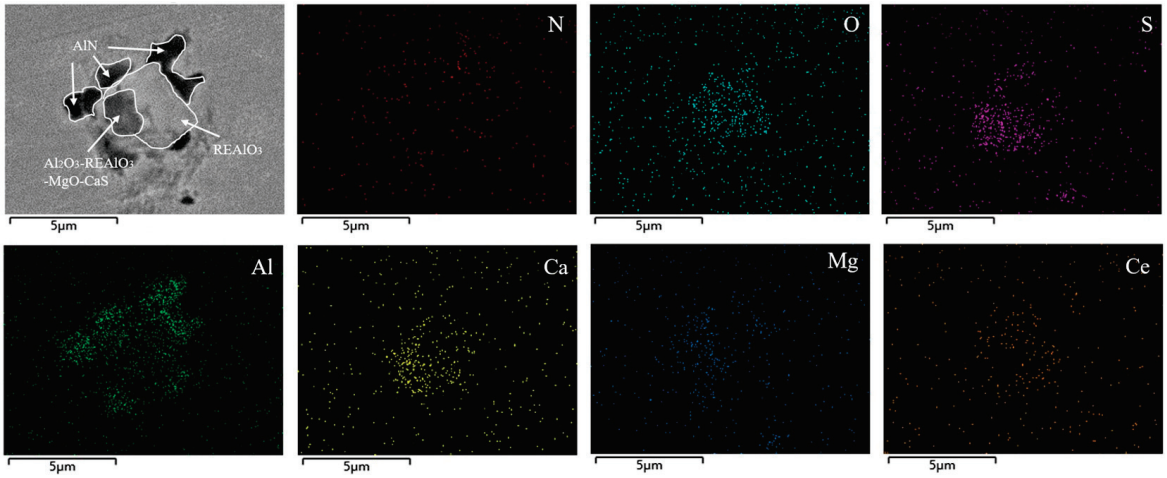

Figure 22. Surface scanning results of AlN-Al_2O_3-MgO-CaS-$REAlO_3$ composite inclusion at the end of tundish pouring.

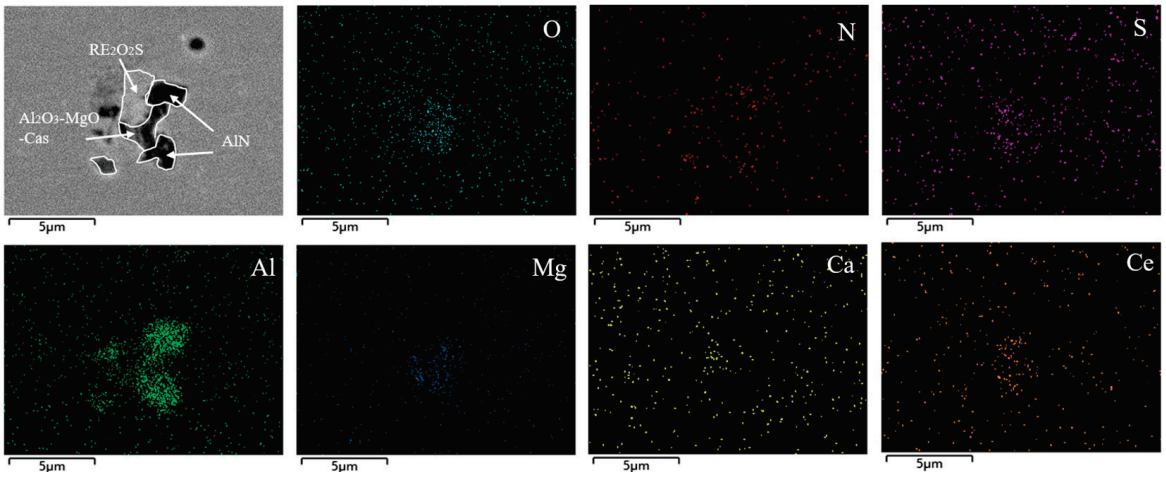

Figure 23. Surface scanning results of AlN-Al_2O_3-MgO-CaS-RE_2O_2S composite inclusion at the end of tundish pouring.

3.3. Analysis of Inclusions in Slab

In the slab, inclusions are mainly single-phase AlN and rare earth composite inclusions. Figures 24 and 25 are typical inclusions in the slab. Figure 24 shows AlN with different shapes and sizes. The size of AlN is around 2 μm and the size of aggregated AlN is around 5 μm. Figure 25 shows the rare earth composite inclusions with a size of around 7 μm in the slab. Figure 25a shows a composite inclusion, with AlN-Al_2O_3-MgO-$REAlO_3$ on the left side of the inclusion. The composition on the right side of the inclusion is Al_2O_3-CaO-CaS-RE_2O_2S, and its EDS surface scanning results are shown in Figure 26. Figure 25b shows the composite inclusion of AlN and Al_2O_3-$REAlO_3$. The center of the inclusion is Al_2O_3-$REAlO_3$ and the outer is AlN. The EDS surface scanning results are shown in Figure 27. Figure 25c shows the composite inclusion of AlN and Al_2O_3-MgO-CaS-RE_2O_2S, with the center light part being Al_2O_3-MgO-CaS-RE_2O_2S and the outer dark part being AlN. The EDS surface scanning results are shown in Figure 28.

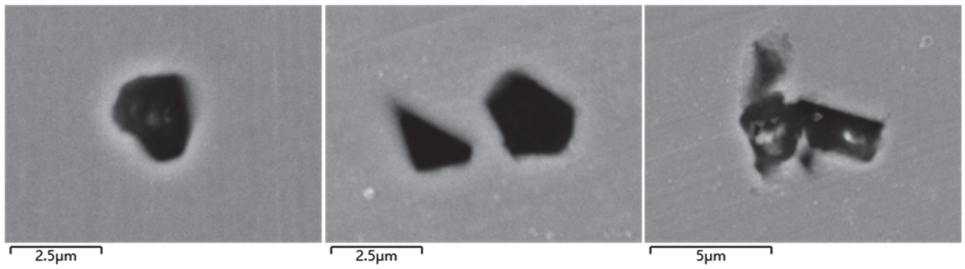

Figure 24. Typical AlN inclusions in slab.

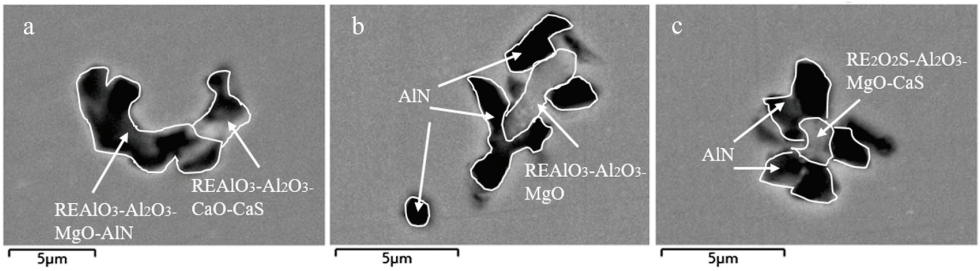

Figure 25. Typical rare earth composite inclusions in slab: (**a**) AlN-Al_2O_3-MgO-CaO-CaS-$REAlO_3$-RE_2O_2S; (**b**) AlN-Al_2O_3-MgO-$REAlO_3$; (**c**) AlN-Al_2O_3-MgO-CaS-RE_2O_2S.

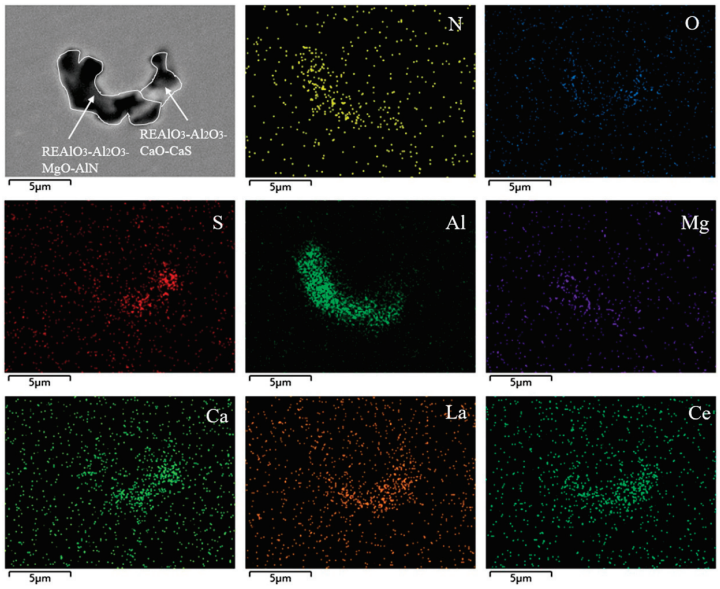

Figure 26. Surface scanning results of AlN-Al_2O_3-MgO-CaO-CaO-CaS-$REAlO_3$-RE_2O_2S composite inclusion in slab.

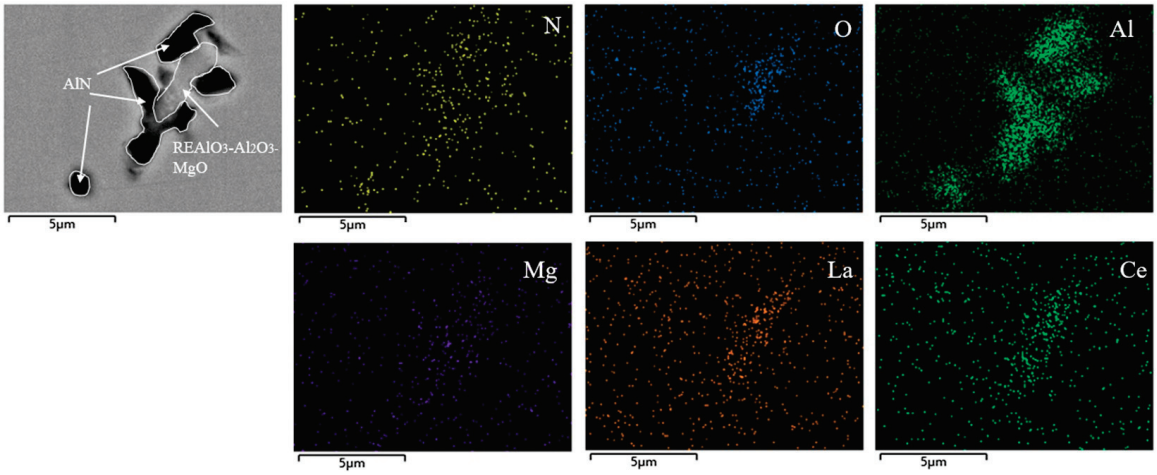

Figure 27. Surface scanning results of AlN-Al_2O_3-MgO-$REAlO_3$ composite inclusion in slab.

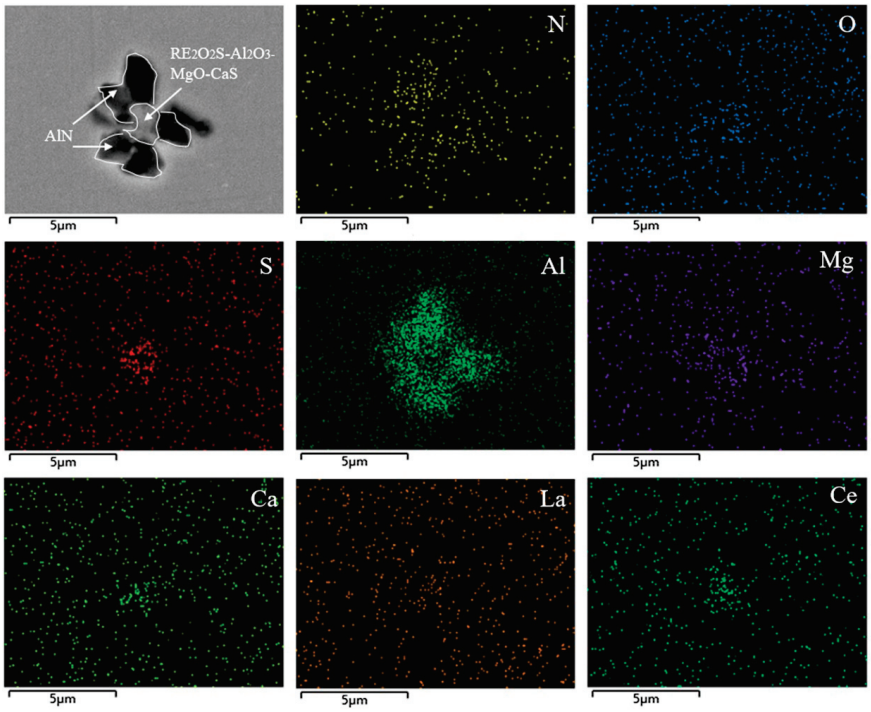

Figure 28. Surface scanning results of AlN-Al_2O_3-MgO-CaS-RE_2O_2S composite inclusion in slab.

3.4. Analysis of the Evolution of Inclusions Throughout the Entire Process

Figure 29 shows the evolution of inclusions in non-oriented silicon steel treated with rare earth ferrosilicon alloy during the entire smelting process. Among them, blue represents AlN or Al_2O_3 inclusions, dark yellow represents RES and its composite inclusions, yellow represents RE_2O_2S and its composite inclusions, light yellow represents $REAlO_3$ and its composite inclusions, and purple represents CaS inlusions. Red represents MgS inclusions.

After RH deoxidation, the inclusions in the molten steel are mainly large-sized AlN and Al_2O_3 inclusions. A small proportion of large-sized Al_2O_3·CaO composite inclusions are observed, too. After adding rare earth ferrosilicon alloy to the molten steel, a large number of rare earth inclusions appears, the main type of rare earth inclusions are RES and $REAlO_3$. After the addition of desulfurizer, RES and $REAlO_3$ inclusions are the main type of inclusions, and large-sized $REAlO_3$ composite inclusions appear, with a layer of CaS inclusions wrapping around the outside of the inclusions.

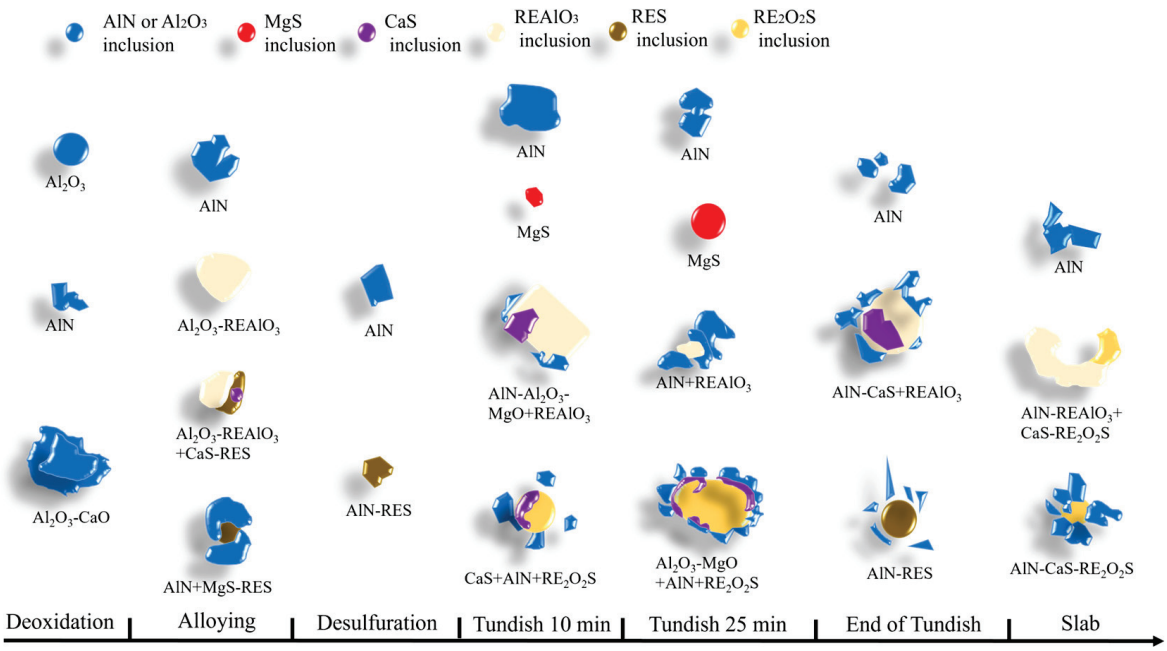

Figure 29. Schematic diagram of the evolution of inclusions in the entire smelting process.

During the tundish pouring for 10 min, single-phase MgS and RE_2O_2S composite inclusions are found in the molten steel. In the RE_2O_2S composite inclusions, the center of the inclusion is RE_2O_2S and wrapped by CaS, the center is surrounded by AlN. In the $REAlO_3$ composite inclusions, the center of the inclusions is $REAlO_3$. A small proportion of AlN and Al_2O_3·MgO are formed on the outside. After tundish pouring for 25 min, the same type of inclusions are found. The rare earth inclusions are wrapped with Al_2O_3·MgO and AlN. At the end of the tundish pouring, except the rare earth inclusions mentioned above, very few RES composite inclusions are found. In the composite inclusions $REAlO_3$ and RE_2O_2S, a certain proportion of Al_2O_3-MgO-CaS wraps around the outer part of the rare earth inclusion core, and AlN on the edge. In the RES composite inclusion, the center is Al_2O_3-MgO-RES, and the mass fraction composition of RES accounts for only about 25%.

In the slab, some larger size single-phase AlN inclusions are observed. Rare earth inclusions are mainly $REAlO_3$ and RE_2O_2S, but there are differences from previous stages. The center of composite inclusions are $REAlO_3$ and RE_2O_2S and Al_2O_3·MgO, and some inclusions also have a small proportion of CaS. There are two forms of rare earth inclusion combination, with $REAlO_3$ inclusion on the left and RE_2O_2S inclusion on the right. The inclusion also include a certain proportion of oxides, sulfides, and nitrides.

AlN inclusions are observed in the entire production process. Single-phase Al_2O_3 inclusions generate after the addition of Al and single-phase MgS inclusions generate in the tundish. Due to the shedding of refractory materials in the tundish, some Mg impurities enter the molten steel and form MgS and MgO inclusions. The modification trend of rare earth inclusions is: $REAlO_3$ and RES(RH) → $REAlO_3$ and RE_2O_2S (tundish and slab).

3.5. Analysis of Inclusion Size

Figure 30 shows the average size of inclusions in the entire process. As shown in Figure 30, after adding aluminum, the average size of inclusions is the largest, i.e., 16.15 μm. As RH treatment continues, the average size of inclusions gradually decreases, and there is a significant decrease in size after adding rare earth ferrosilicon alloy. This is due to the reasons that (1) the large-sized inclusions float up and are removed in RH treatment, and (2) rare earth modifies large-sized alumina inclusions into smaller-sized rare earth inclusions. At the end of RH treatment, the average size of inclusions in the molten steel

reaches its minimum value, i.e., 2.16 μm. When the molten steel enters the tundish, the average size of inclusions significantly increases to 4.57 μm. This is possibly due to the re-oxidation of the molten steel after entering the tundish, which generates a large number of large-sized rare earth composite inclusions. With the tundish continuously pouring, the average size of inclusions in the tundish gradually decreases, which mainly due to the reduced level of re-oxidation in the molten steel, and the tundish flux has a removal effect on inclusions. At the end of the tundish pouring, the average size of inclusions in the molten steel decreases to a lower level, i.e., 3.5 μm. However, in the slab, the average size of inclusions rapidly increases to 5.79 μm. This change may be due to the precipitation of second phase AlN inclusions. When the temperature drops, AlN precipitate with the rare earth inclusions as nucleation cores to form composite inclusions during the cooling process, resulting in an increase in average size. At the same time, AlN aggregate during the solidification process, which also lead to an increase in the size of inclusions.

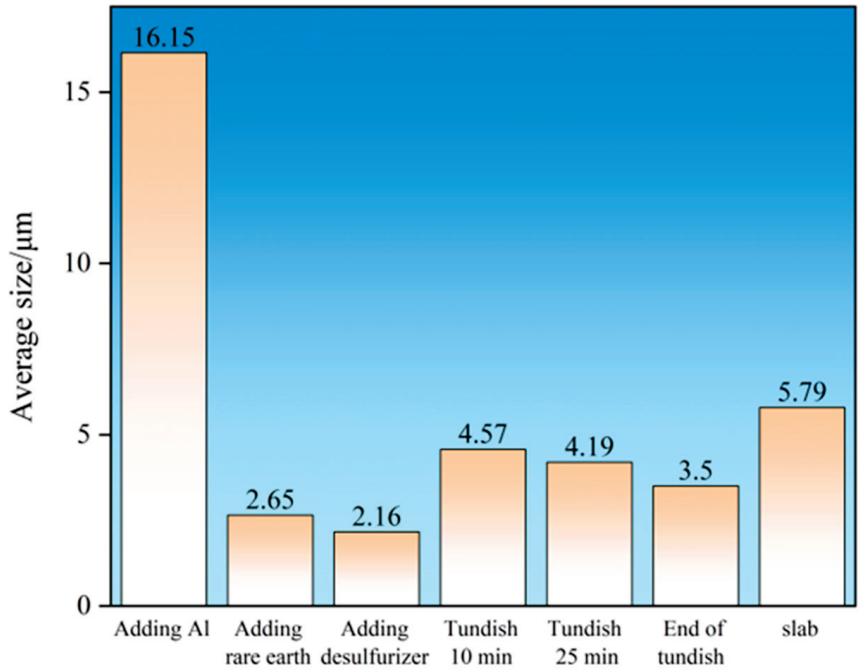

Figure 30. Average size of inclusions of the entire process.

Figure 31 shows the size distribution of inclusions throughout the entire production process. After adding aluminum, the sizes of inclusions in the molten steel are mainly in the ranges of 2–3 μm and 3–5 μm. The proportions of these two size categories are 29.7% and 24.3% respectively. The proportion of small—sized inclusions of 1–2 μm is relatively small, accounting for 13.5%. The proportions of inclusions of 5–10 μm and greater than 10 μm are 18.9% and 13.6% respectively. After deoxidation by adding aluminum, a large number of large—sized inclusions are generated in the steel. After adding rare earth, the original large—sized Al_2O_3 inclusions are modified into small-sized rare earth inclusions. At this stage, the sizes of the inclusions are mainly 2–3 μm and 3–5 μm, accounting for 42.9% and 32.1% respectively. In addition, the proportion of inclusions with a size of 5–10 μm is 19%. From the addition of rare earth onwards, there are almost no large-sized inclusions larger than 10 μm in the samples.

After adding the desulfurizer, the change in the proportion of inclusion sizes is relatively small compared to the stage that after adding rare earths. Need to clarify is that the very large inclusion with a size of around 100 μm (Figures 11c and 13) is not counted since this is random exogenous inclusion and will cause errors for comparison. It

is manifested in the increase in the proportion of inclusions with a size of 1–2 μm (to 11%), and the proportion of inclusions with a size of 2–3 μm increases by 7.1% to 50%. However, the proportions of inclusions with sizes of 3–5 μm and 5–10 μm decrease by 15.9% and 2.3%, to 22.2% and 16.7% respectively. After adding the desulfurizer, the sizes of inclusions in the sample are further reduced.

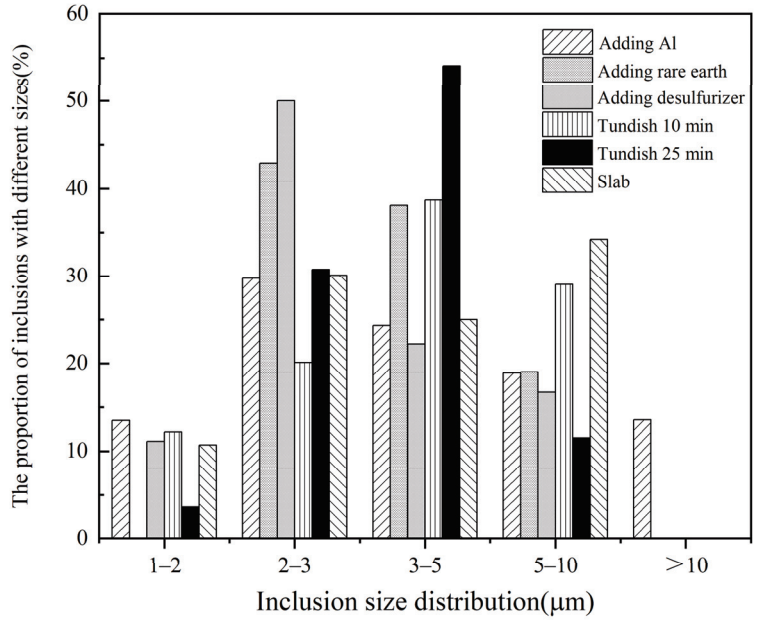

Figure 31. The proportion of inclusions with different sizes of the entire process.

After the heat of liquid steel are pouring into the tundish at 10 min, the size of inclusions increases due to secondary oxidation. The proportion of inclusions with a size of 1–2 μm remains relatively unchanged, while the proportion of those with a size of 2–3 μm decreases by 29.9% to 20.1%. The proportions of inclusions with sizes of 3–5 μm and 5–10 μm increase to 38.7% and 29% respectively. As casting proceeds in the tundish, the sizes of inclusions concentrate in the ranges of 2–3 μm and 3–5 μm. After 25 min of tundish casting, the proportions of these two types of inclusions are 30.8% and 54.1% respectively, the proportion of small -sized inclusions (1–2 μm) decreases to 3.6%, and the proportion of large-sized inclusions (5–10 μm) drops to 11.5%.

In the slab, due to the slower cooling rate in the mold compared to that of the molten steel sampling, inclusions are fully precipitated and grow. At this stage, the types with higher proportions are those of 2–3 μm and 5–10 μm, accounting for 30.1% and 34.2% respectively. The proportion of inclusions with a size of 1–2 μm is 10.7%, and that of inclusions with a size of 3–5 μm is 25%.

3.6. Thermodynamic Calculation

3.6.1. Thermodynamic Calculation of Phase Stability Zone Diagram

The Gibbs free energy for the formation and transformation of rare earth inclusions in molten steel was calculated using the Wagner model with first-order interaction coefficients. Table 2 shows the standard Gibbs free energy for the formation of rare earth inclusions.

The Gibbs free energy of rare earth inclusion transformation was calculated and used as the boundary line in the phase stability zone diagram. As an example, the calculation process of $CeAlO_3$ transform to Ce_2O_2S is as follows.

$$CeAlO_3 + 2[Ce] + \frac{3}{2}[S] = \frac{3}{2}(Ce_2O_2S) + [Al]\ \Delta G^{\theta} = -536420 + 163.86T\left(\frac{J}{mol}\right) \quad (1)$$

Therefore, the coefficient K can be expressed by temperature T as:

$$lgK = \frac{34503.3}{T} - 6.9044 \quad (2)$$

And the coefficient K can also be expressed by activity a of each elements as:

$$K = \frac{a_{Ce_2O_2S}^{1.5} \times a_{Al}}{a_{CeAlO_3} \times a_{Ce}^{2} \times a_{S}^{1.5}} \quad (3)$$

$$lgK = \frac{3}{2}lga_{Ce_2O_2S} + lga_{Al} - lga_{CeAlO_3} - 2lga_{Ce} - \frac{3}{2}lga_{S}^{1.5} \quad (4)$$

Activity a is the product of activity coefficient f and element mass fraction, therefore, the above equation can be transformed into:

$$lgK = lgf_{Al} + lg[\%Al] - 2(lgf_{Ce} + lg[\%Ce]) - \frac{3}{2}(lgf_{S} + lg[\%S])$$

After inputting the mass fraction and activity coefficients of each element, the relationship between Ce and S mass fraction can be obtained. This equation represents the boundary between phase $CeAlO_3$ and phase Ce_2O_2S in the phase stability zone diagram.

$$lg[\%Ce] = -\frac{3}{4}lg[\%S] - 7.26907$$

Table 2. The standard Gibbs free energy for the formation of rare earth inclusions.

Rare Earth Inclusion	Gibbs Free Energy
$[Ce] + [O] + \frac{1}{2}[S] = \frac{1}{2}(Ce_2O_2S)$	$\Delta G_1^\theta = -675,700 + 165.5T(J/mol)$
$[Ce] + [Al] + 3[O] = (CeAlO_3)$	$\Delta G_2^\theta = -1366,460 + 364.3T(J/mol)$
$[Ce] + \frac{3}{2}[O] = \frac{1}{2}(Ce_2O_3)$	$\Delta G_3^\theta = -714,380 + 179.74T(J/mol)$
$[Ce] + [S] = (CeS)$	$\Delta G_4^\theta = -422,100 + 120.38T(J/mol)$
$[Ce] + \frac{3}{2}[S] = \frac{1}{2}(Ce_2S_3)$	$\Delta G_5^\theta = -536,420 + 163.86T(J/mol)$

The calculation method for the other boundary lines are the same, and the calculation results are shown in Table 3.

Table 3. Reaction formulas of rare earth inclusions in RH and tundish.

Chemical Equation	RH	Tundish
$CeAlO_3$-Ce_2O_2S	$lg[\%Ce] = -\frac{3}{4}lg[\%S] - 7.26907$	$lg[\%Ce] = -\frac{3}{4}lg[\%S] - 7.39596$
Ce_2O_2S-CeS	$lg[\%Ce] = -\frac{3}{2}lg[\%S] - 4.09282$	$lg[\%Ce] = -\frac{3}{2}lg[\%S] - 4.79783$
CeS-Ce_2S_3	$lg[\%S] = -1.10162$	$lg[\%S] = -1.1921$
Ce_2O_2S-Ce_2O_3	$lg[\%Ce] = -\frac{3}{2}lg[\%S] - 9.8306$	$lg[\%Ce] = -\frac{3}{2}lg[\%S] - 10.3056$
$CeAlO_3$-Ce_2O_3	$lg[\%Ce] = -4.70754$	$lg[\%Ce] = -4.48637$

According to Table 3, the phase stability zone diagram of rare earth inclusions ($CeAlO_3$, Ce_2O_2S, CeS, Ce_2S_3, Ce_2O_3) are drawn using lg[%Ce] and lg[%S] as the y-axis and x-axis, respectively, as shown in Figure 32.

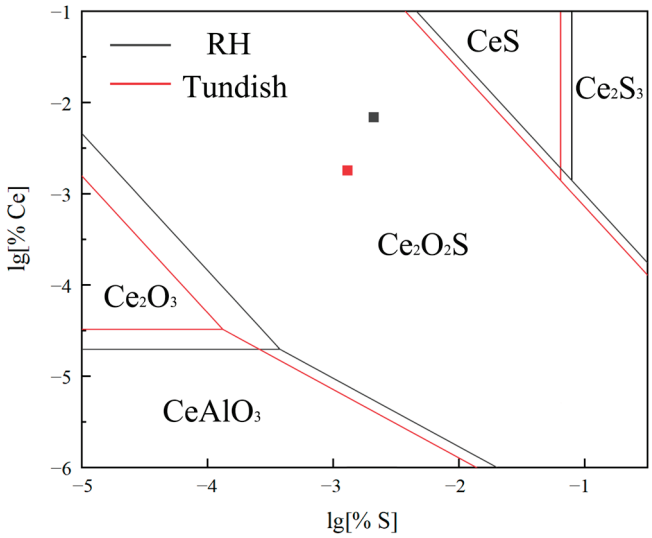

Figure 32. Phase stability diagram of molten steel in RH and tundish.

Figure 32 shows the phase stability zone diagram of rare earth inclusions in the molten steel. The two points in the figure represent the composition of the molten steel at the end of RH treatment and in the tundish. As shown in Figure 32, the stable rare earth inclusion in RH and tundish is RE_2O_2S, which is similar to the obtained inclusion types in Sections 3.1 and 3.2.

According to the analysis of inclusions, there are more $REAlO_3$ and RES composite inclusions in the RH, and more $REAlO_3$ and RE_2O_2S inclusions in the tundish and slab. This is probably due to the uneven distribution of rare earth elements. After adding rare earth ferrosilicon alloy, locally rare earth elements in molten steel being too high or too low makes $REAlO_3$ and RES inclusions generate. In the tundish, the rare earth elements are well mixed, resulting in a large proportion of RE_2O_2S inclusions. Due to the influence of re-oxidation in the tundish, the rare earth content in the molten steel decreases, making it easier to form $REAlO_3$ inclusions.

3.6.2. Thermodynamic Calculation of Second Phase Precipitation in Molten Steel

Figures 33 and 34 show the mass fraction changes of each phase during the equilibrium solidification process obtained by calculating the composition of molten steel in RH and tundish using Thermo- calc.

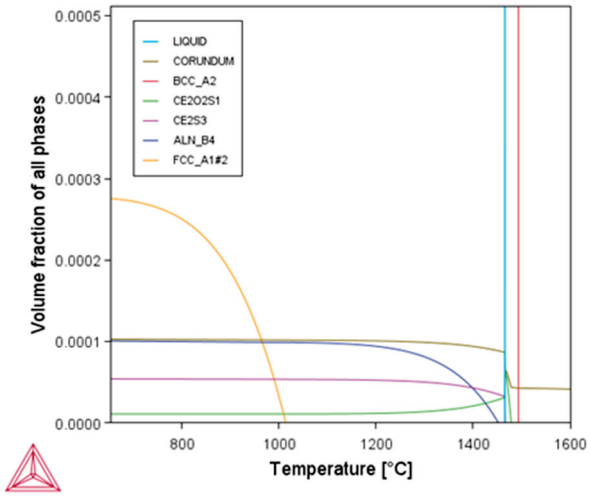

Figure 33. Calculation of second phase precipitation of molten steel in RH.

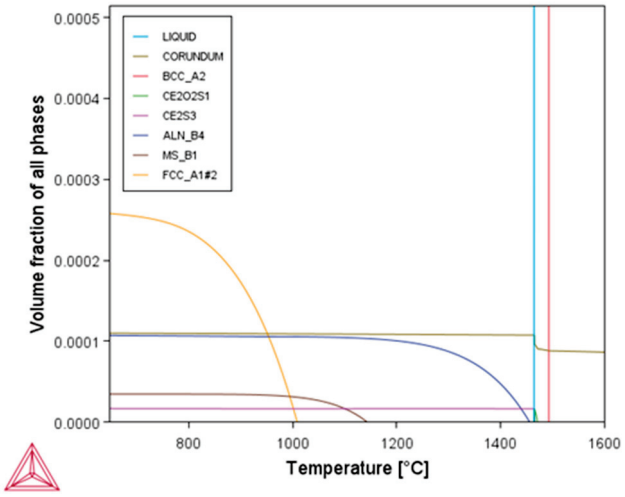

Figure 34. Calculation of second phase precipitation of molten steel in tundish.

As shown in Figure 33, during the solidification process of the molten steel, Al_2O_3 exists in the molten steel. When temperature reaches the critical solidification temperature, Al_2O_3 rapidly precipitates. When the molten steel is completely solidified, the precipitation of Al_2O_3 slows down, and the overall quality change is not significant. During the cooling process of molten steel, as the temperature decreases, Ce_2O_2S begins to precipitate. After the molten steel is completely solidified, a portion of Ce_2O_2S transforms into Ce_2S_3, and the content of Ce_2O_2S gradually decreases with the decrease of temperature, while the content of Ce_2S_3 gradually increases. When the temperature drops to 1450 °C, AlN begins to precipitate. As the temperature decreases, its content continues to increases. When the temperature is around 1000 °C, its content approaches that of Al_2O_3. In Section 3.1, a large number of RES inclusions and RE_2O_2S inclusions were observed in both the samples after rare earth added and those after desulfurizer added, which is consistent with the calculation results. The AlN inclusions in the samples also exist either alone or in combination with rare earth inclusions.

From Figure 34, it can be seen that Al_2O_3 also exists in the molten steel in the tundish, which rapidly precipitates during the solidification process and slowly precipitates during the cooling process. However, compared to the RH, the increases in Al_2O_3 precipitation from the molten steel in the tundish is slightly lower. But as the molten steel gradually cools, the amount of Ce_2O_2S is relatively small. When the molten steel is completely solidified, the Ce_2O_2S is completely transformed into Ce_2S_3. During the cooling process of the slab, its content will not change significantly. The precipitation of AlN is similar to that of AlN in RH, but MnS begins to precipitate when the slab temperature drops to 1150 °C, and the MnS content tends to stabilize at 950 °C.

In the tundish, the content of alumina decreases significantly, and the Al in the molten steel is transferred from Al_2O_3 to AlN. This is manifested in that AlN begins to continuously and massively precipitate at around 1000 °C, and the precipitation gradually slows down at around 700 °C. The calculated type of rare earth inclusions is RE_2O_2S, and there is no RE_XS_Y. In the observation results of inclusions in the tundish in Section 3.2, the types of rare earth inclusions are RE_2O_2S and $REAlO_3$.

3.7. Discussions

In industrial research on the modification of inclusions in silicon steel by rare earths, La-Ce mixed rare earths are the most commonly used rare earth additives [52,58,59]. To ensure production continuity, the content of rare earths added in industrial tests is generally small. As shown in Table 4, the final rare earth content in the molten steel is around 20 ppm.

In addition, as the smelting process proceeds, the rare earth content in the molten steel will gradually decrease, which corresponds to the evolution of rare earth inclusions, whose types will change with the smelting process. Eventually, the types of rare earth inclusions are basically $REAlO_3$ and RE_2O_2S.

Table 4. Research on the application of rare earths in silicon steel production.

Name	The Type of Rare Earth	The Content of Rare Earth (wt%)	Research Conclusions
Song, C. et al. [52]	La-Ce	21, 34, 58 ppm	As the content of RE increases, the inclusions transform from Al_2O_3 to $REAlO_3$ and RE_2O_2S, and the number density of inclusions first decreases and then increases with the increase of RE content.
Ren, Q. et al. [15]	SiMgCe	23 ppm	Ce modifies $MgO \cdot Al_2O_3$ inclusions into Ce_2O_2S inclusions and Ce-Al-Mg-Ca-S-O inclusions. As the Ce content in the molten steel decreases, the inclusions in the tundish are Ce_2O_2S and $CeAlO_3$.
Wang, H.J. et al. [58]	La-Ce	25 ppm	After the addition of rare earths, the main rare earth inclusions in the RH and tundish are $REAlO_3$. Rare earths promote the agglomeration of inclusions, resulting in an increase in the number of inclusions with a size of 1.0~3.5 μm, and the average size of the inclusions is 2.66 μm.
Cui, L.X et al. [59]	La-Ce	25 ppm	Rare earths slightly reduce the sulfur content and modify the original $Al_2O_3 \cdot MgO$ inclusions into RES and RE_2O_2S.

In this study, the rare earth content in the molten steel decreased from 69 ppm to 18 ppm from the time of rare earth alloy addition during RH treatment to sampling at the tundish. As the rare earth content in the molten steel decreases, the types of rare earth inclusions from $REAlO_3$ and RES in RH to $REAlO_3$ and RE_2O_2S in the tundish and slab. The final rare earth content is 18 ppm, and the types of rare earth inclusions are $REAlO_3$ and RE_2O_2S. The type of inclusions in this study is similar to the studies by Song et al. [52] and Ren et al. [15] The averaged size in this study is slightly higher than the results of Wang et al. [58].

Additionally, the addition of rare earth elements generates a large number of fine rare earth inclusions, which can lead to nozzle clogging and disrupt production continuity. Among common rare earth inclusions, $REAlO_3$ tends to aggregate and dominate the clogging layer [60]. In this study, the rare earth inclusions observed in the slab were RE_2O_2S and $REAlO_3$. Adjusting the rare earth addition amount is required to modify the types of inclusions in the steel and mitigate nozzle clogging caused by rare earth inclusions. While this requires future studies.

4. Conclusions

1. In the RH treatment process, AlN, Al_2O_3, and their composite inclusions are the main type of inclusions before the addition of rare earth ferrosilicon alloy. After adding rare earth ferrosilicon alloy, single phase inclusions are mainly AlN, while rare earth inclusions are mainly RES composite inclusions and $REAlO_3$ composite inclusions. Only a very large CaO-CaS based inclusion with a size of around 100 μm was found after adding desulfurizer. For the inclusions in tundish and slab, single phase MgS inclusions are found. Rare earth inclusions are mainly composed of RE_2O_2S and $REAlO_3$. All rare earth inclusions contain small amounts of CaS or MgS.

2. During the RH treatment process, the average size of inclusions rapidly decreases after the addition of rare earth ferrosilicon alloy and reach its minimum size at the end of RH process. After the molten steel enters the tundish, the average size of inclusions increases slightly and gradually decreases with the progress of pouring. Due to the slow cooling rate, inclusions have fully grown, the average size of inclusions in the slab is the lagerest.

3. According to thermodynamic calculations, the most stable rare earth inclusion type in molten steel is RE_2O_2S in both RH and tundish. During the equilibrium solidification process of the molten steel, Al_2O_3, Ce_2O_2S, Ce_2S_3, AlN, and MnS precipitate successively, which is basically similar to the observed inclusion types in experiments.

Author Contributions: Conceptualization, L.X., W.L. and C.C.; methodology, L.X., W.L., W.M. and J.W.; software, T.W., J.W., W.M. and X.N.; validation, L.X., X.L. and H.W.; formal analysis, L.X., W.M., Q.Z., X.L. and H.W.; investigation, X.L., Q.Z. and T.W.; resources, J.W., W.L. and X.N.; data curation, X.L., Q.Z., H.W. and T.W.; writing—original draft preparation, L.X., T.W. and X.L.; writing—review and editing, L.X., T.W., Q.Z. and X.L.; visualization, Q.Z., X.L. and H.W.; supervision, W.M., C.C. and X.N.; project administration, C.C., X.N. and W.L.; funding acquisition, H.W., J.W. and C.C. All authors have read and agreed to the published version of the manuscript.

Funding: This research was funded by Applied Fundamental Research Programs of Shanxi: 202303021221036; Applied Fundamental Research Programs of Shanxi: 202403021222046; Undergraduate Innovation and Entrepreneurship Training Program of Shanxi Province (20250176).

Data Availability Statement: Date are contained within the article.

Conflicts of Interest: Author Liqiang Xue was employed by the company Shanxi Taigang Stainless Steel Co., Ltd., The remaining authors declare that the research was conducted in the absence of any commercial or financial relationships that could be construed as a potential conflict of interest.

Abbreviations

The following abbreviations are used in this manuscript:

RH	Ruhrstahl-Heraeus
RE	Rare earth
EDS	Energy Dispersive X-ray Spectroscopy

References

1. Irfan, M. Assessing Consumers' Behavioral Intention and Willingness to Pay for Electric Vehicles: An Evidence from China. *J. Compr. Bus. Adm. Res.* **2024**, *1*, 2–11. [CrossRef]
2. Li, W.; Cui, K.; Wu, L.; Zheng, B. Users' Perceived Value of Electric Vehicles in China: A Latent Class Model-Based Analysis. *World Electr. Veh. J.* **2025**, *16*, 461. [CrossRef]
3. Zuo, L.; Zhou, S.; Wang, M.; Zhang, S. Research on the Impact of Fiscal Subsidies on High-Quality Development of New Energy Vehicle Companies Based on Threshold Effects. *J. Compr. Bus. Adm. Res.* **2025**, 1–13. [CrossRef]
4. Kubota, T. Recent Progress on Non-oriented Silicon Steel. *Steel Res. Int.* **2005**, *76*, 464–470. [CrossRef]
5. Oda, Y.; Kohno, M.; Honda, A. Recent development of non-oriented electrical steel sheet for automobile electrical devices. *J. Mag. Mag. Mater.* **2008**, *320*, 2430–2435. [CrossRef]
6. Ouyang, G.Y.; Chen, X.; Liang, Y.F.; Macziewski, C.; Cui, J. Review of Fe-6.5 wt% Si high silicon steel-A promising soft magnetic material for sub-kHz application. *J. Mag. Mag. Mater.* **2019**, *481*, 234–250. [CrossRef]
7. Xu, N.; Liang, Y.F.; Zhang, C.Y.; Wang, Z.; Wang, Y.L.; Ye, F.; Lin, J.P. Development of strong Goss texture in ultra-thin high silicon steel with excellent magnetic properties fabricated by two-stage rolling. *Int. J. Miner. Metall. Mater.* **2025**, *32*, 1595–1606. [CrossRef]
8. Wang, J.Y.; Ren, Q.; Luo, Y.; Zhang, L.L. Effect of non-metallic precipitates and grain size on core loss of non-oriented electrical silicon steels. *J. Mag. Mag. Mater.* **2018**, *451*, 454–462. [CrossRef]
9. Dijkstra, L.J.; Wert, C. Effect of inclusions on coercive force of iron. *Phys. Rev.* **1950**, *79*, 979–985. [CrossRef]
10. Wang, H.J.; Xu, R.; Ling, H.T.; Zhong, W.; Chang, L.Z.; Qiu, S.T. Numerical simulation of fluid flow and alloy melting in RH process for electrical steels. *J. Iron Steel Res. Int.* **2022**, *29*, 1423–1433. [CrossRef]

11. Wang, J.H.; Ni, P.Y.; Chen, C.; Ersson, M.; Li, Y. Effect of gas blowing nozzle angle on multiphase flow and mass transfer during RH refining process. *Int. J. Miner. Metall. Mater.* **2023**, *30*, 844–856. [CrossRef]
12. Xue, L.Q.; Zhao, Y.S.; Wang, J.; Wang, H.; Miao, Z.; Xiong, R.X.; Xu, Z.B.; Lin, W.M.; Niu, X.F.; Chen, C. The flow performance of combined gas blowing at the vacuum chamber and up-snorkel in the ruhrstahl–heraeus (RH) degasser for electrical steel production. *Processes* **2025**, *13*, 448. [CrossRef]
13. Xu, Z.B.; Ouyang, X.; Chen, C.; Li, Y.H.; Wang, T.Y.; Ren, R.J.; Yang, M.M.; Zhao, Y.S.; Xue, L.Q.; Wang, J. Numerical simulation of the density effect on the macroscopic transport process of tracer in the ruhrstahl–heraeus (RH) vacuum degasser. *Sustainability* **2024**, *16*, 3923. [CrossRef]
14. Liu, X.J.; Yang, J.C.; Ren, H.P.; Jia, X.B.; Zhang, M.Y.; Yang, C.Q. Effect of solute Ce, Mn, and Si on mechanical properties of silicon steel: Insights from DFT calculations. *J. Iron Steel Res. Int.* **2024**, *31*, 700–709. [CrossRef]
15. Ren, Q.; Zhang, L.F.; Hu, Z.Y.; Cheng, L. Transient influence of cerium on inclusions in an Al-killed non-oriented electrical steel. *Ironmak. Steelmak.* **2020**, *48*, 191–199. [CrossRef]
16. Ren, Q.; Hu, Z.Y.; Liu, Y.X.; Zhang, W.C.; Gao, Z.Q.; Zhang, L.F. Effect of lanthanum on inclusions in non-oriented electrical steel slabs. *J. Iron Steel Res. Int.* **2024**, *31*, 1680–1691. [CrossRef]
17. Cao, J.Q.; Chen, C.; Xu, L.Q.; Li, Z.; Zhao, J.; Lin, W.M. Analysis of the inclusions in the whole smelting process of non-oriented silicon steel DG47A. *Iron Steel* **2023**, *58*, 61–71. [CrossRef]
18. Wang, T.; Chen, C.; Mu, W.Z.; Xue, L.Q.; Cao, J.Q.; Lin, W.M. Analysis of inclusions in whole smelting process of non-oriented silicon steel 23W1700 by rare earth treatment. *Iron Steel* **2024**, *59*, 92–103. [CrossRef]
19. Kong, W.; Chen, Y.F.; Cang, D.Q. A statistical study of inclusions in medium-grade non-oriented silicon steel. *Meter. Res. Technol.* **2019**, *116*, 207. [CrossRef]
20. Zhang, F.; Li, G.Q.; Miao, L.D. Effects of chemical composition systems on non-metallic inclusions in non-oriented silicon steel sheets. *J. Iron Steel Res.* **2012**, *24*, 40–44.
21. Zhu, C.Y.; Liu, Y.L.; Xiao, Y.; Yan, W.; Li, G.Q. A new review on inclusion and precipitate control in grain-oriented silicon steels. *JOM* **2022**, *74*, 3141–3161. [CrossRef]
22. Pindar, S.; Pande, M.M. Assessment of Si-O equilibria and nonmetallic inclusion characteristics in high silicon steels. *Steel Res. Int.* **2023**, *94*, 2300115. [CrossRef]
23. Pindar, S.; Pande, M.M. Investigation of Inclusion Characteristics in Ferrosilicon Killed High Silicon Steels. *Steel Res. Int.* **2024**, *95*, 2400331. [CrossRef]
24. Li, X.A.; Wang, N.; Chen, M.; Ma, T.Y. Tracking Large-size Inclusions in Al Deoxidated Tinplate Steel in Industrial Practice. *ISIJ Int.* **2021**, *61*, 2074–2082. [CrossRef]
25. Ueshima, Y.; Sawada, Y.; Mizoguchi, S.; Kajioka, H. Precipitation behavior of MnS during δ/γ transformation in Fe−Si alloys. *Metall Mater. Trans. A* **1989**, *20*, 1375–1383. [CrossRef]
26. Ito, Y.M.; Masumitsu, N.; Matsubara, K.; Komatsubra, M. Formation of MnS-type inclusion in steel. *Tetsu Hagane* **1980**, *66*, 647–656. [CrossRef] [PubMed]
27. Zhou, B.; Zhu, C.Y.; Li, G.Q.; Luo, Z.; Gao, Y.Z.; Bao, S.Q.; Schneider, J. Effect of sulphur and acid soluble aluminium content on grain oriented silicon steel. *Mater. Sci. Technol.* **2015**, *31*, 1809–1817. [CrossRef]
28. Takamiya, T.; Obare, T.; Muraki, M.; Komatsubara, M. Influence of sulfur content and deformation temperature on precipitation behavior of MnS in 3% Si steel. *Tetsu Hagane* **2003**, *89*, 518–523. [CrossRef]
29. Wu, S.J.; Wang, W.L.; Yue, C.X.; Qian, H.W.; Li, H.L. Effect of Annealing Stress on the Magnetic Properties of High-Grade Non-oriented Electrical Steel. *Metall. Mater. Trans. A.* **2024**, *55*, 2602–2608. [CrossRef]
30. Ren, Q.; Hu, Z.Y.; Cheng, L.; Zhang, L.F. Effect of rare earth elements on magnetic properties of non-oriented electrical steels. *J. Magn. Magn. Mater.* **2022**, *560*, 169624. [CrossRef]
31. Song, J.T.; Chen, C.; Guo, Z.J.; Geng, M.J.; Rong, Z.R.; Wang, T.Y.; Wang, J.; E, D.; Fan, J.P.; Sun, Y.H. Analysis of Flow Field, Temperature, and Inclusion Evolution in a 12-Strand Tundish During Ladle Changeover Process. *Metall. Mater. Trans. B* **2025**, *56*, 2700–2714. [CrossRef]
32. Liu, P.; Cai, Z.Z.; Zhu, M.Y. Effect of La Treatment and Al–La Composite Treatment on Sulfur-Containing Peritectic Steel. *Metall. Mater. Trans. B* **2025**, *56*, 4114–4124. [CrossRef]
33. Zhang, L.F.; Wei, H.; Duan, S.C. Effect of Gadolinium on Inclusions in a High-Sulfur Free-Cutting Steel and Converting Two-Dimensional to Three-Dimensional Morphology of Inclusions Through Matlab Programming. *Metall. Mater. Trans. B* **2024**, *55*, 4759–4774. [CrossRef]
34. Ren, Q.; Zhang, L.F. Effect of cerium content on inclusions in an ultra-low-carbon aluminum-killed steel. *Metall. Mater. Trans. B* **2020**, *51*, 589–600. [CrossRef]
35. Cao, J.Q.; Li, Y.; Lin, W.M.; Che, J.L.; Zhou, F.; Tan, Y.F.; Li, D.L.; Dang, J.; Chen, C. Assessment of inclusion removal ability in refining slags containing Ce_2O_3. *Crystals* **2023**, *13*, 202. [CrossRef]

36. Ren, P.; Wang, H.; Zhao, Y.; Zhu, X.; Shi, C.B.; Lan, P. Effect of Cerium on Solidification Structure and Eutectic Carbides in Electroslag Remelted S136 Tool Steel. *Metall. Mater. Trans B* **2024**, *55*, 5080–5092. [CrossRef]
37. Zhao, Y.; Wang, H.; Liu, J.; Zhu, X.; Zhang, H.; Shi, C.B. Effect of Cerium on Solidification Structure and Eutectic Precipitates in Electroslag Remelted Cr–W–Co Martensitic Heat-Resistant Steel. *Metall. Mater. Trans. B* **2024**, *55*, 4915–4928. [CrossRef]
38. Liang, Y.Y.; Ni, P.Y.; Liu, Q.L.; Li, Y. Effect of Rare Earth Metal Alloying on Inclusion Evolution in High-Strength Oil Casing Steel. *Metall. Mater. Trans. B* **2024**, *55*, 3158–3173. [CrossRef]
39. Yu, Z.; Liu, C.J. Modification mechanism of spinel inclusions in medium manganese steel with rare earth treatment. *Metals* **2019**, *9*, 804. [CrossRef]
40. Liu, J.R.; Cui, H.; Wang, Z.D.; Fan, L.F. Evolution of Inclusions in Low-Alloy Wear-Resistant Steel with Ce-Ca Combined Treatment. *Metall. Mater. Trans. B* **2025**. [CrossRef]
41. Wang, L.C.; Tian, J.L.; Ren, J.; Jiang, C.G.; Jiang, Z.H.; You, Z.M. Effect of Mg–Ce Treatment on the Inclusion Evolution of Al Pre-deoxidized M50 Aerospace Bearing Steel During Vacuum Induction Melting Process. *Metall. Mater. Trans. B* **2025**, *56*, 3997–4009. [CrossRef]
42. Liu, T.; Ma, H.; Liu, Y.; Li, D.Z. Effect of Aluminum-Oxygen (Al-O) Enrichment on Inclusion Evolution During Cerium Treatment. *Metall. Mater. Trans. B* 2025. [CrossRef]
43. Kang, J.; Yu, Y.C.; Zhang, J.L.; Chen, C.; Wang, S.B. Effect of rare earth on inclusion evolution in industrial production of HRB500E steel. *Metall. Res. Technol.* **2021**, *118*, 220. [CrossRef]
44. Zhao, L.; Yang, J.C.; Fu, X.Y. Effect of Ce content on modification behavior of inclusions and corrosion resistance of 316L stainless steel. *Materials* **2025**, *18*, 69. [CrossRef] [PubMed]
45. Zhuo, C.; Liu, R.; Zhao, Z.R.; Zhang, Y.L.; Hao, X.S.; Wu, H.J.; Sun, Y.H. Effect of rare earth cerium content on manganese sulfide in U75V heavy rail steel. *Metals* **2022**, *12*, 1012. [CrossRef]
46. Takashima, M.; Ono, S.M.; Nishimura, K. Low iron loss non-oriented electrical steel for high-efficiency Motor "RAM series". *Kawasaki Steel Gihou* **1997**, *29*, 185.
47. Kono, M.; Ozaki, Y.; Honda, A. Non-Oriented Silicon Steel Sheet Excellent in Magnetic Property after Stress Relieving Annealing and Its Production. Patent Abstracts of Japan JPH10212556A, 28 July 2003.
48. Takashima, M.; Kono, M. Method for Producing Semiprocess Non-Oriented Magnetic Steel Sheet with Excellent Iron-Loss Characteristic. Patent Abstracts of Japan JP2006169577A, 29 June 2006.
49. Li, X.Y.; Chen, C.; Wang, T.; Guo, Z.J.; Wang, H.Y.; Wang, H.Z.; Xue, L.Q.; Tian, J.; Sun, Y.H. Inclusions and phases in Fe-RE-Si steelmaking alloys and their effect on evolution of inclusions in non-oriented silicon steels. *J. Rare Earths* **2025**. [CrossRef]
50. Wang, H.J.; Niu, Y.; Ling, H.T.; Qiao, J.L.; Zhang, Y.L.; Zhong, W.; Qiu, S.T. Effects of rare earth La–Ce alloying treatment on modification of inclusions and magnetic properties of W350 non-oriented silicon steel. *Metals* **2023**, *13*, 626. [CrossRef]
51. Li, N.; Wang, Y.Q.; Qiu, S.T.; Li, X. Effect of Ce on the evolution of recrystallization texture in a 1.2%Si-0.4%Al non-oriented electrical steel. *ISIJ Int.* **2016**, *56*, 1256–1261. [CrossRef]
52. Song, C.; Xiang, L.; Shi, C.; Qiao, J.L.; Liu, J.F.; Qiu, S.T. Effect of rare earth La-Ce on solidification structure of 3.2%Si-0.9%Al non-oriented silicon steel. *ISIJ Int.* **2024**, *64*, 1347–5460. [CrossRef]
53. Qin, J.; Zhao, H.B.; Wang, D.S.; Wang, S.L.; Yang, Y.W. Effect of Y on recrystallization behavior in non-oriented 4.5 wt% Si steel sheets. *Materials* **2022**, *15*, 4227. [CrossRef]
54. Fan, L.F.; Zhu, R.; He, J.Z.; Lu, B. Effect of rare earth element La on texture and inclusion of non-oriented electrical steel produced by thin slab casting and rolling process. *ISIJ Int.* **2018**, *58*, 2348–2353. [CrossRef]
55. Zhao, L.; Yang, J.C.; Hu, H.G.; Fu, X.Y. Effect of rare-earth Ce on the texture of non-oriented silicon steels. *High Temp. Mater. Process.* **2024**, *43*, 20220321. [CrossRef]
56. Hou, C.K.; Liao, C.C. Effect of cerium content on the magnetic properties of non-oriented electrical steels. *ISIJ Int.* **2008**, *48*, 531–539. [CrossRef]
57. Wan, Y.; Chen, W.Q.; Wu, S.J. Effect of lanthanum content on microstructure and magnetic properties of non-oriented electrical steels. *J. Rare Earths* **2013**, *3*, 727–733. [CrossRef]
58. Wang, H.J.; Niu, Y.H.; Ling, H.T.; Qiao, J.L.; Zhang, Y.L.; Zhong, W.; Qiu, S.T. Modification of rare earth Ce on inclusions in W350 non-oriented silicon steel. *Metals* **2023**, *13*, 453. [CrossRef]
59. Cui, L.X.; Liu, Y.B.; Ren, Q.; Hu, Z.Y.; Zhang, L.F. Effect of La-Ce mixed rare earth on inclusions in high-grade non-oriented silicon steel. *Steelmaking* **2025**, *41*, 53–64.
60. Ma, F.X.; Gu, Q.; Liu, G.Q.; Zhang, Y.; Li, H.X. A systematic study of carbon-free oxide-based lining for preventing submerged entry nozzle clogging in continuous casting of rare earth steel. *J. Iron Steel Res. Int.* **2025**, *32*, 1584–1595. [CrossRef]

crystals

MDPI

Article

Characterization of Cobalt-Based Composite Multilayer Laser-Cladded Coatings

Iasmina-Mădălina Anghel [1], Alexandru Pascu [2], Iosif Hulka [3,*], Dino Horst Woelk [1], Ion-Dragoș Uțu [1,*] and Gabriela Mărginean [4]

[1] Department of Materials Engineering and Manufacturing, Politehnica University Timisoara, Bulevardul Mihai Viteazul Nr.1, 300222 Timisoara, Romania; iasmina.anghel@student.upt.ro (I.-M.A.)
[2] Materials Engineering and Welding Department, Transilvania University of Brașov, Eroilor Blvd 29, 500036 Brașov, Romania; alexandru.pascu@unitbv.ro
[3] Research Institute for Renewable Energie, Politehnica University of Timisoara, G. Muzicescu 138, 300501 Timisoara, Romania
[4] Institute of Mechanical Engineering, Westphalian University of Applied Sciences Gelsenkirchen Bocholt Recklinghausen, Neidenburger Str. 43, 45897 Gelsenkirchen, Germany; gabriela.marginean@w-hs.de
* Correspondence: iosif.hulka@upt.ro (I.H.); dragos.utu@upt.ro (I.-D.U.)

Abstract: Laser cladding is an essential method for strengthening and restoring component surfaces. To increase its efficacy and provide a reliable surface treatment technique, it is necessary to optimize process parameters, enhance material adhesion, and guarantee high-quality, reliable coatings. These measures help to extend the lifespan of components. In this study, the surfaces of AISI 904L stainless steel samples were cladded to prepare various Co-based composite coatings with single and multiple layers reinforced with WC–CoCr–Ni powder. The phases within the newly developed layers were investigated using X-ray Diffraction (XRD), while the microstructure was examined using Scanning Electron Microscopy (SEM) and Energy Dispersive X-ray Spectroscopy (EDX). Further tests were performed to assess the hardness, wear resistance and corrosion performance of the deposited coatings. Analyzing and comparing the coatings, it was observed that the coating performance increased with increasing thickness and generally due to a lower amount of Fe present within the microstructure.

Keywords: laser cladding; CoCr-based coatings; wear; corrosion; hardness

1. Introduction

Cobalt-based (Co-based) alloys are widely recognized for their superior mechanical strength, thermal stability, and excellent wear and corrosion resistance under harsh service environments. These alloys are particularly valuable for components operating in aerospace, petrochemical, and power generation sectors, where elevated temperature and corrosive media can severely degrade conventional steels. The outstanding performance of Co-based alloys originates from their γ–Co solid solution matrix strengthened by carbides such as M_7C_3, $M_{23}C_6$, and η phases, which provide high hardness and thermal stability [1]. Nevertheless, their intrinsic brittleness and the possibility of solidification defects during processing limit their direct application. To overcome these challenges, laser cladding (LC) has become a prominent surface engineering technique capable of producing dense, metallurgically bonded coatings with controlled dilution and tailored microstructures [2,3].

Laser cladding provides rapid solidification and localized heat input, resulting in fine-grained, defect-free microstructures with strong adhesion to the substrate. Zhou and

Kong demonstrated that Ti_3AlC_2-reinforced Co-based coatings fabricated by LC exhibited improved frictional stability and oxidation resistance at elevated temperatures due to the formation of continuous tribo-oxide layers [4]. Similarly, Zhang et al. reported that Stellite3–Ti_3SiC_2–Cu composite coatings developed on Inconel 718 achieved nearly double the hardness of the substrate and exhibited excellent high-temperature oxidation resistance, attributing these enhancements to the synergistic effect between the MAX-phase reinforcement and the ductile Cu addition [5]. Furthermore, Chen et al. fabricated WC–Cu/Co composite coatings via laser cladding and found a 70% increase in hardness and a significant reduction in wear rate, emphasizing the beneficial dual effect of hard carbide phases and a lubricating metallic matrix [6]. Numerous studies have also examined the role of rare-earth oxides and refractory elements in improving coating integrity. Li et al. observed that the addition of CeO_2 and graphite to Co-based plasma-cladded coatings refined the dendritic structure, decreased porosity, and increased both hardness and corrosion resistance in chloride media [7]. Similarly, Liu et al. investigated Ta-reinforced Co-based coatings fabricated by direct laser deposition, reporting that in situ TaC particles contributed to microstructural stabilization and enhanced erosion resistance [8]. These results indicate that the chemical composition and type of reinforcement have a profound influence on coating performance by modifying solidification dynamics and carbide formation behavior.

In recent years, the concept of multilayer laser-cladded coatings has gained increasing attention as a means to further enhance coating quality and reduce dilution. Multilayer architectures enable the formation of compositional and thermal gradients that help mitigate interfacial stress, improve metallurgical bonding, and enhance wear and corrosion performance. Li et al. reported that multilayer Co-based coatings exhibited reduced dilution and higher microhardness than single-layer coatings due to improved remelting control and heat dissipation [9]. Likewise, Zhang et al. demonstrated that WC–CoCr–Ni multilayer coatings provided superior wear resistance and lower friction coefficients compared to single-layer coatings, mainly because of a reduced Fe diffusion from the substrate and the formation of uniform carbide networks [10].

Despite these advances, a detailed understanding of the relationship between Fe diffusion from the substrate into the coating, coating thickness, and reinforcement distribution in multilayer Co-based systems remains incomplete. Excessive dilution of Fe from the substrate into the Co-based layer can deteriorate mechanical and corrosion properties by altering the phase composition and matrix stability [11–14]. Consequently, controlling dilution and compositional uniformity is a key objective in optimizing coating performance.

In our previous study [15], Co-based composite coatings containing 0–30 wt.% WC–CoCr–Ni particles were deposited by laser cladding onto AISI 904L stainless steel. That work systematically analyzed the influence of WC content on the microstructure, phase composition, hardness, and tribo-corrosion performance of the coatings. The results indicated that the coating with Co + 30 wt.% WC exhibited the most balanced combination of wear resistance and corrosion stability, despite showing a relatively high Fe dilution from the substrate due to single-layer deposition. Building upon these findings, the present research utilizes the optimized Co + 30 wt.% WC composition from the previous work to fabricate single-, double-, and triple-layer Co-based coatings. The aim is to investigate how increasing the number of deposited layers influences Fe dilution within the Co matrix and consequently affects the mechanical, wear, and corrosion performance of the coatings. Through this approach, the study provides new insights into the optimization of multilayer Co-based composite systems fabricated by laser cladding for improved surface reliability in industrial applications.

2. Materials and Methods

Three different laser cladding layers were manufactured using a mechanical dry mixture of Amdry MM509B-C Co-based powder (Oerlikon Metco, Langenfeld, Germany) and WC–CoCr powder (Thermico GmbH, Dortmund, Germany), with the latter added in an amount of 30 wt%. The Co-based powder exhibited a particle size distribution of 45–125 μm, while the WC–CoCr powder (WC) had a particle size distribution in the range of 45–106 μm. The mixture was deposited on AISI 904L stainless steel and labeled as Sample 1 (single layer cladding), Sample 2 (dual layer cladding), and Sample 3 (triple layer cladding). The cladding was carried out using a Coherent 100F diode laser equipped with a water-cooled Precitec YC50 gun (Precitec GmbH & Co. KG, Gaggenau, Germany), operated by a six-axis robot from CLOOS. The cladding parameters used in this study have been reported in previous work [15] and were laser power of 720 W, cladding speed of 22 cm/min, and a powder feed rate of 6 g/min. Argon was used as the carrier gas for powder feeding, at a flow rate of 14 L/min. Metallographic samples were cut using a liquid-cooled cutting machine to avoid microstructural changes within the layers. After cutting, the samples were embedded in epoxy resin via hot mounting and subsequently ground with SiC abrasive papers up to 4000P grit, followed by polishing on cloths down to 1 μm. A scanning electron microscope (SEM, TESCAN VEGA, TESCAN Group, Brno, Czech Republic) was employed to examine the morphology of the etched samples, equipped with an energy-dispersive X-ray (EDX) spectrometer for local compositional analyses. The phase composition was identified by X-ray diffraction (Philips X'Pert Diffractometer, Panalytical, The Netherlands) method using a Cu Kα radiation, a scanning width of 2θ in the range of 20–100°, with a step size of 0.02° and a counting time of 0.2 s/step. The X-ray tube was operated at 40 kV and 40 mA at room temperature. The microhardness of the layers was evaluated by the Vickers method using a FALCON 600G2 hardness tester (INNOVATEST Europe BV, Maastricht, The Netherlands). Indentations were performed on the cross-sections of the specimens under a load of 300 gf with a dwell time of 15 s. The sliding wear properties of the coatings were evaluated using the pin-on-disk method with a CSM tribometer (CMS Instruments, Lausanne, Switzerland). The ASTM G99-17 standard [16] was employed for the measurements using a normal force (F) of 10 N, a wear radius of 3 mm, and a linear speed of 10 cm/s, with 10,000 laps performed. A WC-Co ball with a 6 mm diameter was used as the counterbody. Material loss volume was determined by measuring depth profiles for each track. A SP-150 potentiostat/galvanostat (Biologic, Seyssinet-Pariset, France) was used to test the corrosion performance of the layers at room temperature. The sample being investigated served as the working electrode (WE) in a standard three-electrode electrochemical cell. The 1 cm^2 test area was submerged in a 3.5% NaCl solution by weight.

Before performing the wear and corrosion tests, all coating surfaces were ground and polished to obtain a metallic mirror finish with an average surface roughness of approximately 0.2 μm. Therefore, the effect of surface roughness on wear and corrosion behavior was minimized, ensuring that the measured performance differences are primarily attributed to the coating microstructure and composition rather than surface irregularities.

3. Results and Discussions

3.1. Microstructure

Figure 1 presents the cross-sectional macrographs of the fabricated coatings. The coatings exhibit a dense structure, indicating good metallurgical bonding, as no delamination was observed at the coating–substrate interface. All samples display WC carbide agglomeration, represented by the white particles randomly dispersed within the coatings. Macro-pores are absent in the layer structures. The coating thickness varies, particularly in

samples 2 and 3, due to multiple passes, with sample 3 being the thickest as a result of the overlapping of three layers.

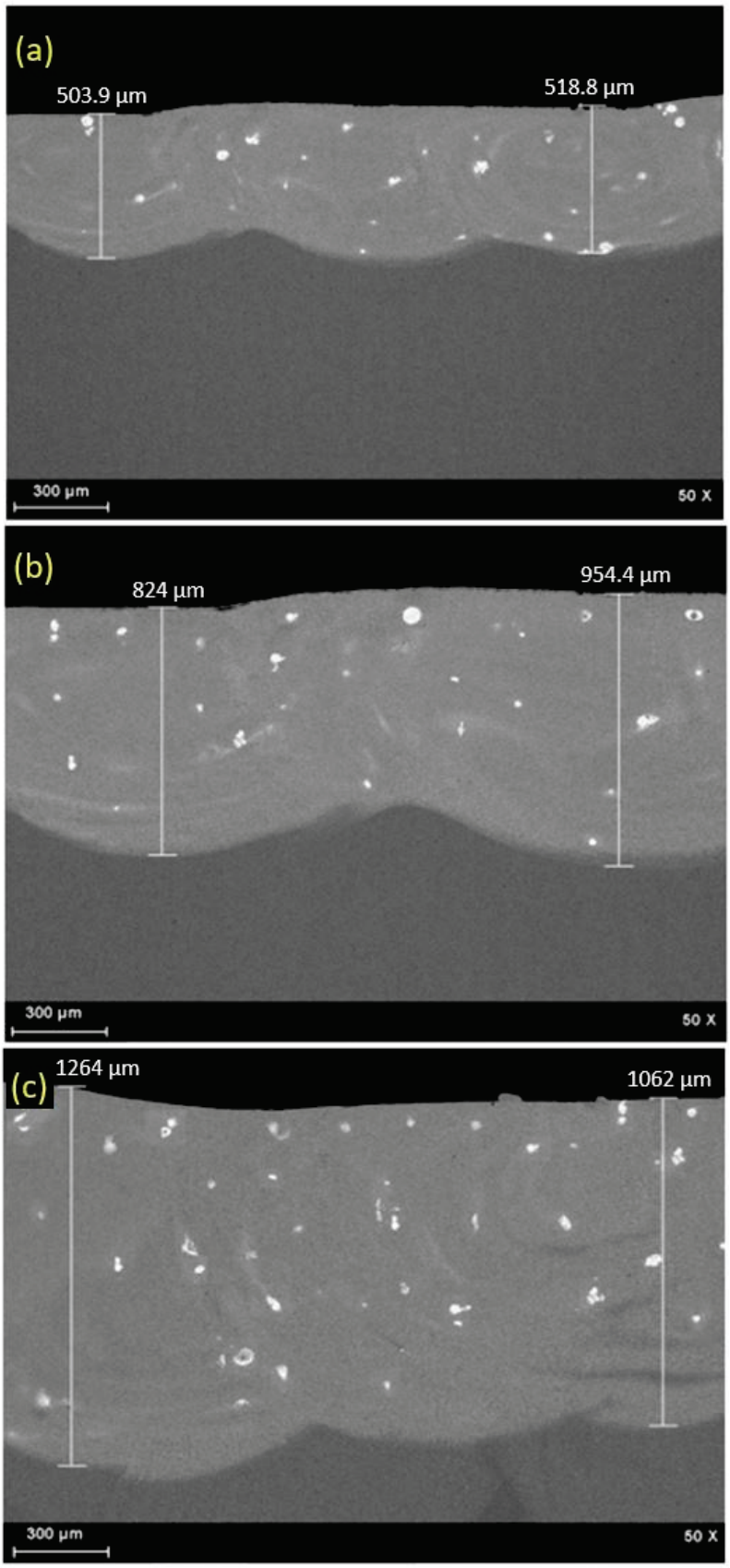

Figure 1. SEM images of cross-sections of the investigated samples: (**a**) Sample 1; (**b**) Sample 2, and (**c**) Sample 3.

The chemical investigation was performed on the upper part of each sample, and the corresponding spectra are presented in Figure 2. In all samples, the major alloying elements detected were Cr, Co, Fe, and Ni, followed by W and C. No other elements were detected, most likely due to their low concentrations, which were below the detection limit of the technique. However, a difference can be observed in the case of Fe, identified by its major K-line peak at ~6.4 keV. With increasing coating thickness, the intensity of the Fe peak decreases. This can be attributed to the high solubility of Fe with elements such as Ni, Co, and Cr, which allows it to easily diffuse and mix into the molten pool during cladding. Therefore, iron is more abundant in Sample 1, which was prepared with a single layer. As the deposition process continues with two or three passes, as in Sample 3, the iron content decreases. In a previous study [17], an increase in Fe content within the laser-clad coating led to microstructural changes and a reduction in hardness, which was attributed to the presence of a higher number of softer phases in the composition of WC–Co/NiCrB-based coatings.

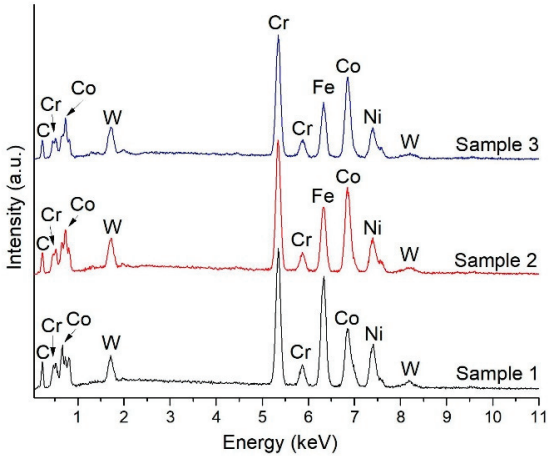

Figure 2. EDX spectrum of samples collected in the upper region of the layers.

Based on the quantification presented in Table 1, the Fe content decreases from approximately 28 wt.% in Sample 1 to about 16 wt.% in Sample 3 as the coating thickness increases. A comparative analysis reveals that Sample 2 contains roughly 35% less Fe than Sample 1, while Sample 3 exhibits an even greater reduction, with about 43% less Fe relative to Sample 1. The increase in Co% is primarily attributed to reduced substrate dilution with increasing coating thickness, which limits Fe incorporation and enriches the coating in Co derived from the feedstock powder, while the concentrations of other alloying elements remain nearly unchanged. Similar observations were reported by Xiao et al. when investigating the effect of dilution on FeCoNiCrNb high-entropy alloy coatings fabricated with different numbers of layers [18]. Their results showed that as the number of layers increased, a reduction in Fe content was observed in the upper layers.

Table 1. Chemical composition determined by EDX for the investigated samples.

Element	Sample 1	Sample 2	Sample 3
Fe [wt.%]	28.65	18.39	16.33
Cr [wt.%]	22.53	23.28	24.28
Co [wt.%]	18.19	30.19	31.28
Ni [wt.%]	16.17	13.75	13.55
C [wt.%]	11.04	10.24	9.98
W [wt.%]	2.67	4.14	4.57

Figure 3, it can be observed that the samples exhibit a similar microstructure, which has been described previously in more detail [2]. The SEM micrographs and EDX mapping performed in cross-section at high magnification reveal various areas. The metallic matrix consists of a solid solution rich in Co, Cr, Fe, and Ni, with dark gray regions corresponding to Cr-rich areas. The white particles are WC, in some cases surrounded by light gray regions that represent W_2C, which forms due to the partial melting of WC during laser cladding. In all cases, the morphology of WC particles appears slightly rounded, indicating partial dissolution, as described by Bolelli et al. [19].

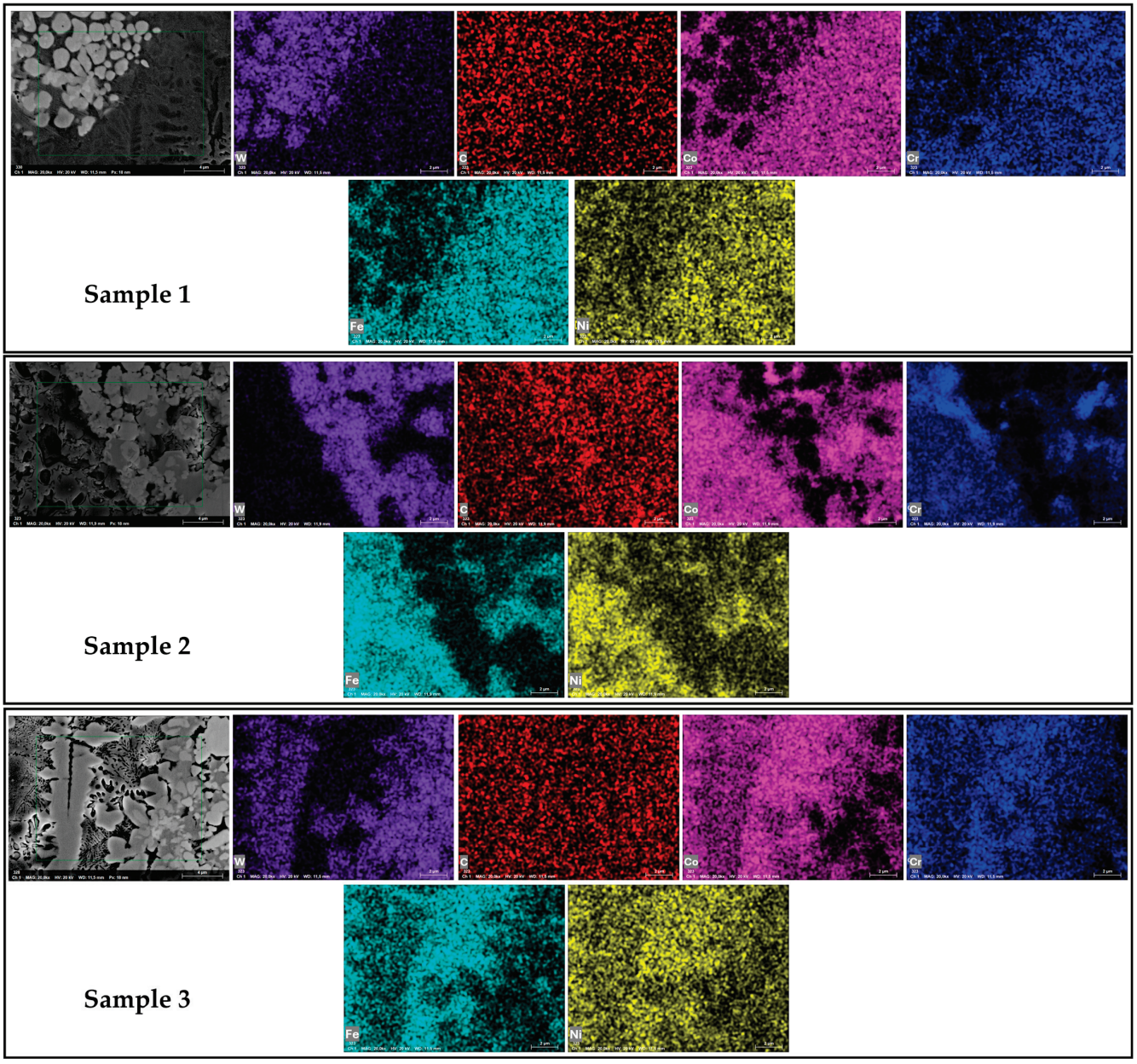

Figure 3. SEM and EDX element distribution of the investigated samples.

3.2. Phase Composition

Figure 4 presents the X-ray diffraction spectra of the coatings produced by laser cladding. The spectra indicate that the layers exhibit similar patterns, with the main peaks corresponding to the metallic binder, composed of NiFe and containing metallic Co and Cr. Minor peaks corresponding to hard carbides, such as WC and Cr_7C_3, are also observed, along with small peaks attributed to W_2C secondary carbide. The decarburization transfor-

mation occurs in the WC-based coatings because carbon is burned from WC during deposition [20]. The partial dissolution of Cr in the melt pool and its reaction with carbon from the partially decomposed WC leads to the formation of Cr_7C_3. According to Venkatesh et al., Cr_7C_3 is a stable carbide phase that forms during cladding due to rapid heating and cooling, and it is found together with the Ni-rich metallic phase in the interdendritic regions [21]. It is known that the hardness of W_2C is about 30 GPa, much higher than that of WC (HV = 17 GPa). Since hardness and wear resistance are usually correlated, the presence of W_2C within WC-CoCr-based coatings in a certain amount can enhance their wear performance [22].

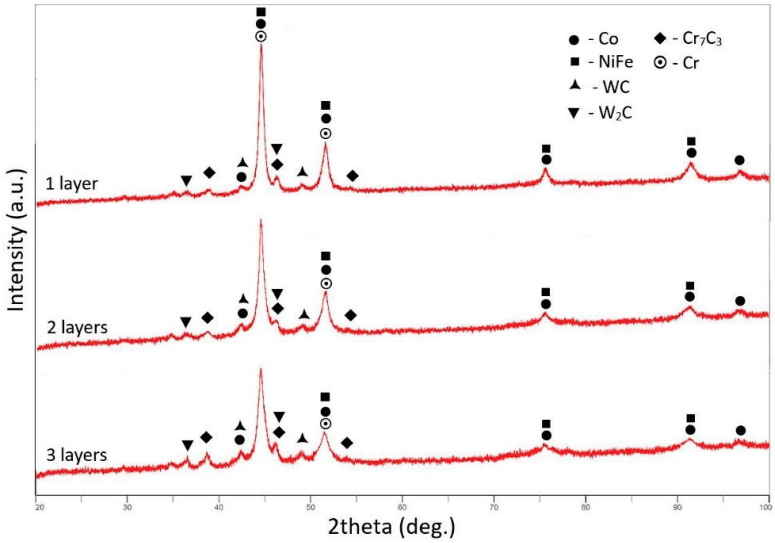

Figure 4. XRD patterns for the laser-clad layers.

3.3. Hardness Evaluation

The starting hardness of the coating was about 825 HV03, as obtained in our previous study [2]. The measurements were conducted exclusively in the upper part of the coating, as the objective was to assess hardness variations in cross-section at a depth of approximately 2 mm from the surface. For each sample, six measurements were performed, and the average values are presented in Table 2. An increase in coating thickness was found to correlate with higher hardness values. This enhancement in hardness can be attributed to the reduction in Fe, which promotes grain refinement in the microstructure, as reported by Liu et al. [23]. Comparable findings were also reported by Li et al., who investigated the influence of Fe content on the microstructure and wear resistance of AlCoCrFeNi coatings produced by laser cladding [24].

Table 2. Hardness values (measured at the top of the laser-clad coatings).

Co + 30 wt.% WC	HV 0.3
1 layer (sample 1)	825 ± 18
2 layers (sample 2)	866 ± 35
3 layers (sample 3)	879 ± 70

3.4. Wear Performance

Figure 5 presents the evolution of the coefficient of friction (COF) for the different coating configurations. In all cases, a distinct rise in COF is observed during the initial stage of testing. This increase can be attributed to the limited real contact area between the polished surface of the coating and the unaltered counter ball at the beginning of the test. The small initial contact area concentrates the applied load, producing higher frictional

forces, localized wear, and fluctuations in the COF [25]. As sliding continues, both the coating and the counter ball undergo progressive wear, generating debris that becomes entrapped within the contact interface. The presence of this debris initiates abrasive wear, leading to intermittent COF fluctuations as the system transitions toward a more stable contact condition.

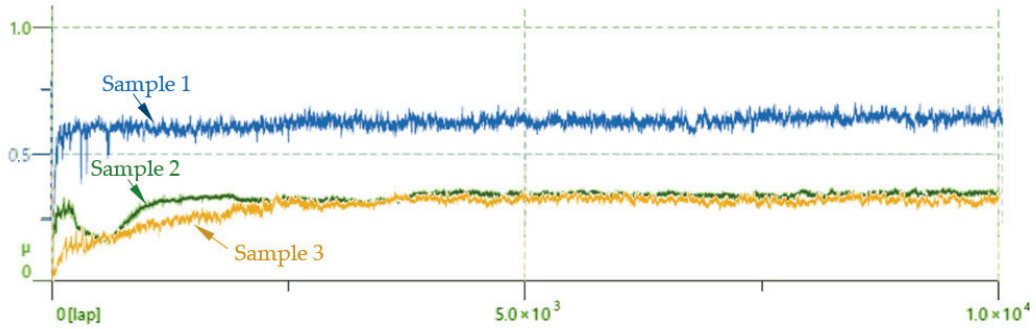

Figure 5. COF recorded for the investigated samples.

Among the tested samples, the single-layer coating exhibited the highest average COF (μavg = 0.621), while the double-layer (μavg = 0.323) and triple-layer (μavg = 0.318) coatings demonstrated substantially lower values. The improved frictional performance of the multilayer coatings can be associated with their enhanced structural integrity and reduced WC decomposition, which favors the formation of a higher fraction of W_2C carbide. This phase contributes to increased hardness and wear resistance, thereby stabilizing the frictional response throughout the test.

Figure 6 illustrates the corresponding wear rates for the single-layer (sample 1), double-layer (sample 2), and triple-layer (sample 3) coatings, which are 0.19, 0.16, and 0.15×10^{-8} $mm^3/N{\cdot}m$, respectively. A clear trend is observed in which wear resistance improves with increasing coating thickness. This behavior can be primarily attributed to the direct correlation between wear resistance and hardness [26]. Multilayer coatings typically possess a higher density of carbides and secondary hard phases within their microstructure, which not only enhances hardness but also improves load-bearing capacity and resistance to plastic deformation. Consequently, the multilayer architecture effectively mitigates material loss and contributes to superior overall tribological performance [25].

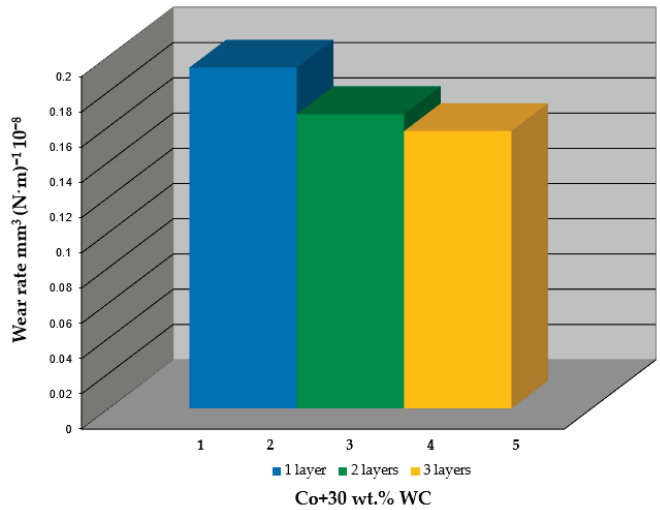

Figure 6. Wear rate values of the laser-clad coatings.

3.5. Corrosion Performance

The electrochemical tests were carried out in a 3.5% NaCl solution, which is a standard medium for evaluating the corrosion resistance of metallic coatings. Before conducting the experiments, the OCP values were measured during a 30 min monitoring period. Figure 7 illustrates the polarization curves in semilogarithmic form, obtained using the Tafel extrapolation method. The graph shows the relationship between the measured potential and the logarithm of the current density. It is derived from linear polarization curves by applying a logarithmic transformation to the current density values. From these plots, key corrosion parameters—namely, the corrosion potential (E_{corr}) and corrosion current density (i_{corr})—were determined.

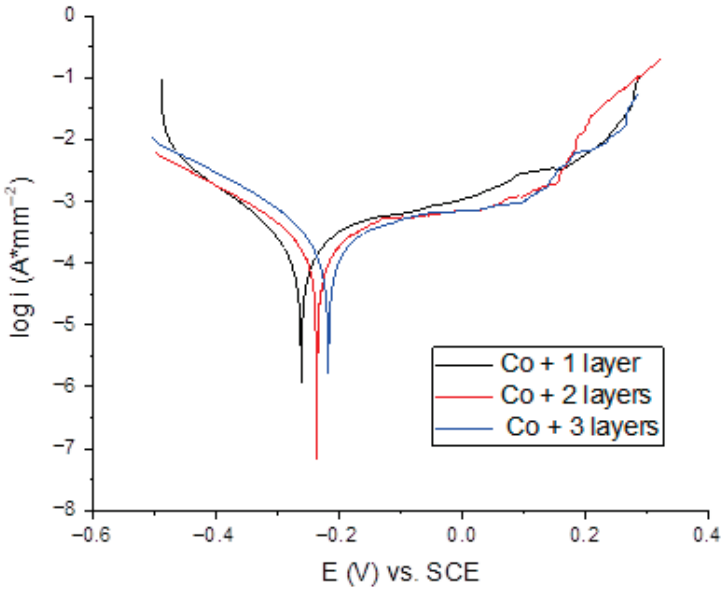

Figure 7. Potentiodynamic polarization curves.

Analysis of the polarization curves shown in Figure 7, together with the electrochemical parameters listed in Table 3, indicates that the coating with the triple-layer structure exhibited the best corrosion resistance. This is evidenced by its lowest corrosion current density values (0.091 μA·cm^{-2}) compared with single- (0.105 μA·cm^{-2}), and double-layer (0.117), demonstrating improved protective performance. Moreover, for sample 3, the corrosion potential shifted towards more positive values (to the right on the E vs. log i curve), indicating a more noble material. This behavior is consistent with the lower iron content in the triple-layer coating, since iron is more electrochemically active and thus prone to anodic dissolution.

Table 3. Electrochemical test results.

Sample	i_{corr} (μA·cm^{-2})	E (mV)
Co + 1 layer	0.117	−259.22
Co + 2 layers	0.105	−237.61
Co + 3 layers	0.091	−218.22

The reduced Fe proportion likely promotes the formation of a denser and more stable passive film, enhancing the barrier properties of the coating [27]. Consequently, the triple-layer coating demonstrates a more stable electrochemical behavior and better durability in chloride-containing environments.

4. Conclusions

Co-based composite coatings reinforced with WC–CoCr–Ni powder were successfully deposited by laser cladding onto AISI 904L stainless steel substrates in single-, double-, and triple-layer configurations. The experimental investigation focused on evaluating the effect of the number of deposited layers on the microstructure, hardness, sliding wear resistance, and electrochemical behavior. Based on the obtained results, the following conclusions can be drawn:

- The dilution effect inherent to laser cladding led to an increased Fe content in the bottom region of the first layer. As the number of layers increased, the Fe concentration gradually decreased toward the surface.
- All coatings exhibited partial decarburization of WC, leading to the formation of W_2C. This phenomenon was more pronounced in the triple-layer coating due to the higher cumulative heat input.
- The multilayer coatings had significantly lower coefficients of friction than the single-layer coating due to their improved structural integrity and reduced WC decomposition. The lower Fe content and higher W_2C fraction that results enhances hardness and wear resistance, leading to a more stable frictional response during testing.
- A lower iron content in the coating improved the corrosion resistance, as evidenced by the lowest corrosion current density. This iron reduction promoted the formation of a denser and more stable passive film, resulting in the most stable electrochemical behavior.

Overall, it can be concluded that the Co-based composite coating with a triple-layer structure produced by laser cladding exhibited the most favorable combination of corrosion resistance and wear performance among all the investigated configurations.

Author Contributions: Conceptualization, I.-M.A. and I.-D.U.; methodology, A.P. and I.H.; software, D.H.W. and I.-M.A.; validation, I.-D.U. and G.M.; formal analysis, I.H. and D.H.W.; investigation, I.-M.A., D.H.W. and A.P.; resources, I.-D.U. and A.P.; data curation, I.-M.A., I.H. and I.-D.U.; writing—original draft preparation, I.-M.A., I.H. and I.-D.U.; writing—review and editing, I.-D.U., I.H. and G.M.; visualization, I.-M.A., A.P., I.H., D.H.W., I.-D.U. and G.M.; supervision, I.-D.U., I.H. and G.M. All authors have read and agreed to the published version of the manuscript.

Funding: This research received no external funding.

Data Availability Statement: The data presented in this study are available on request from the corresponding author.

Conflicts of Interest: The authors declare no conflicts of interest.

References

1. Davis, J.R. *Surface Engineering for Corrosion and Wear Resistance*; ASM International: Novelty, OH, USA, 2001.
2. Bartkowski, D.; Młynarczak, A.; Piasecki, A.; Dudziak, B.; Gościański, M.; Bartkowska, A. Microstructure, microhardness and corrosion resistance of Stellite-6 coatings reinforced with WC particles using laser cladding. *Opt. Laser Technol.* **2015**, *68*, 191–201. [CrossRef]
3. Poloczek, T.; Lont, A.; Górka, J. The structure and properties of laser-cladded Inconel 625/TiC composite coatings. *Materials* **2023**, *16*, 1265. [CrossRef] [PubMed]
4. Zhou, J.; Kong, D. Friction–wear performances and oxidation behaviors of Ti_3AlC_2 reinforced Co–based alloy coatings by laser cladding. *Surf. Coat. Technol.* **2021**, *408*, 126816. [CrossRef]
5. Zhang, S.-Y.; Liu, X.B.; Zhu, Y.; Liu, Y.F.; Meng, Y.; Liang, J.; Zhang, S.H. Stellite3–Ti_3SiC_2–Cu composite coatings on IN718 by laser cladding. *Surf. Coat. Technol.* **2022**, *446*, 128766. [CrossRef]
6. Chen, G.-D.; Liu, X.-B.; Zhang, F.-Z.; Liu, Q.-S.; Ou, H.-Z.; Zhang, S.-H. Fabrication and tribological properties of laser cladding WC–Cu/Co-based composite coatings. *Surf. Coat. Technol.* **2023**, *472*, 129930. [CrossRef]

7. Li, D.; Zhang, Z.; Cui, X.; Feng, L.; Zhang, D.; Jin, G.; Liu, J.; Zheng, W. Effect of graphite/CeO_2 on microstructure and tribological property of plasma cladded Co-based coatings. *Mater. Chem. Phys.* **2022**, *280*, 125756. [CrossRef]
8. Liu, Y.; Ding, T.; Lv, H.; Hu, D.; Zhang, Y.; Chen, H.; Chen, Y.; She, J. Microstructure and properties of Ta-reinforced cobalt based composite coatings processed by direct laser deposition. *Surf. Coat. Technol.* **2022**, *447*, 128874. [CrossRef]
9. Li, M.; He, Y.; Sun, G. Microstructure and wear resistance of laser clad cobalt-based alloy multi-layer coatings. *Appl. Surf. Sci.* **2004**, *230*, 108802.
10. Angelastro, A.; Campanelli, S.L.; Casalino, G.; Ludovico, A.D. Optimization of Ni-Based WC/Co/Cr Composite Coatings Produced by Multilayer Laser Cladding. *Adv. Mater. Sci. Eng.* **2013**, *2013*, 615464. [CrossRef]
11. Xu, Z.; Wang, Z.; Chen, J.; Qiao, Y.; Zhang, J.; Huang, Y. Effect of Rare Earth Oxides on Microstructure and Corrosion Behavior of Laser-Cladding Coating on 316L Stainless Steel. *Coatings* **2019**, *9*, 636. [CrossRef]
12. Costa, J.M.; Porto, M.B.; Amancio, R.J.; Almeida Neto, A.F. Effects of Tungsten and Cobalt Concentration on Microstructure and Anticorrosive Property of Cobalt-Tungsten Alloys. *Surf. Interfaces* **2020**, *20*, 100626. [CrossRef]
13. Zhai, Y.; Guo, X.; He, Y.; Li, Z. Corrosion resistance and mechanical properties of electrodeposited Co–W/ZrO_2 composite coatings. *Int. J. Electrochem. Sci.* **2023**, *18*, 100015. [CrossRef]
14. Ding, L.; Hu, S. Effect of Nano-CeO_2 on Microstructure and Wear Resistance of Co-Based Coatings. *Surf. Coat. Technol.* **2015**, *276*, 256–257. [CrossRef]
15. Anghel, I.-M.; Uțu, I.-D.; Pascu, A.; Hulka, I.; Woelk, D.H.; Mărginean, G. Microstructure and properties of Co-based laser cladded composite coatings. *Mater. Test.* **2024**, *66*, 665–674. [CrossRef]
16. *ASTM G99-17*; Standard Test Method for Wear Testing with a Pin-on-Disk Apparatus. ASTM International: West Conshohocken, PA, USA, 2017.
17. Hulka, I.; Utu, D.; Serban, V.A.; Negrea, P.; Lukáč, F.; Chráska, T. Effect of Ti Addition on Microstructure and Corrosion Properties of Laser Cladded WC-Co/NiCrBSi(Ti) Coatings. *Appl. Surf. Sci.* **2020**, *504*, 144349. [CrossRef]
18. Xiao, D.; Jiang, F.; Song, T.; Wei, C.; Zhang, Y.; Liang, P.; Yang, F. Impact of Dilution on the Microstructural Evolution and Corrosion Behavior in High-Entropy Alloy Coatings Applied via Laser Cladding on Marine Engineering Equipment. *Eng. Fail. Anal.* **2025**, *171*, 109337. [CrossRef]
19. Bolelli, G.; Hulka, I.; Koivuluoto, H.; Lusvarghi, L.; Milanti, A.; Niemi, K.; Vuoristo, P. Properties of WC—FeCrAl Coatings Manufactured by Different High Velocity Thermal Spray Processes. *Surf. Coat. Technol.* **2014**, *247*, 74–89. [CrossRef]
20. Korobov, Y.; Alwan, H.; Soboleva, N.; Makarov, A.; Lezhnin, N.; Shumyakov, V.; Antonov, M.; Deviatiarov, M. Cavitation Resistance of WC-10Co_4Cr and WC-20CrC-7Ni HVAF Coatings. *J. Therm. Spray Technol.* **2022**, *31*, 234–246. [CrossRef]
21. Venkatesh, L.; Samajdar, I.; Tak, M.; Doherty, R.D.; Gundakaram, R.C.; Prasad, K.S.; Joshi, S.V. Microstructure and Phase Evolution in Laser Clad Chromium Carbide-NiCrMoNb. *Appl. Surf. Sci.* **2015**, *357*, 2391–2401. [CrossRef]
22. Wang, H.; Li, Y.; Gee, M.; Zhang, H.; Liu, X.; Song, X. Sliding Wear Resistance Enhancement by Controlling W2C Precipitation in HVOF Sprayed WC-Based Cermet Coating. *Surf. Coat. Technol.* **2020**, *387*, 125533. [CrossRef]
23. Liu, W.; Li, L.; Mi, G.; Wang, J.; Pan, Y. Effect of Fe Content on Microstructure and Properties of Laser Cladding Inconel 625 Alloy. *Materials* **2022**, *15*, 8200. [CrossRef] [PubMed]
24. Li, Y.; Shi, Y.; Li, S.; Yan, X.; Wang, S.; Zhuo, X. Effect of Fe Content on the Microstructure and Wear Resistance of AlCoCrFeNi High-Entropy Alloy Coating Prepared by Laser Cladding. *Appl. Surf. Sci.* **2025**, *685*, 162019. [CrossRef]
25. Yu, Y.; Ding, W.; Wang, X.; Mo, D.; Chen, F. Study on Microstructure and Wear Resistance of Multi-Layer Laser Cladding Fe901 Coating on 65 Mn Steel. *Materials* **2025**, *18*, 3505. [CrossRef]
26. Zhu, H.; Ouyang, M.; Hu, J.; Zhang, J.; Qiu, C. Design and Development of TiC-Reinforced 410 Martensitic Stainless Steel Coatings Fabricated by Laser Cladding. *Ceram. Int.* **2021**, *47*, 12505–12513. [CrossRef]
27. Potgieter, J.H. Alloys cathodically modified with noble metals. *J. Appl. Electrochem.* **1991**, *21*, 471–482. [CrossRef]

MDPI AG
Grosspeteranlage 5
4052 Basel
Switzerland
Tel.: +41 61 683 77 34

Crystals Editorial Office
E-mail: crystals@mdpi.com
www.mdpi.com/journal/crystals

Academic Open
Access Publishing

mdpi.com

ISBN 978-3-7258-6132-3